



**HAL**  
open science

## Développement de filaments composites coaxiaux

Muhammad Ali Afzal

► **To cite this version:**

Muhammad Ali Afzal. Développement de filaments composites coaxiaux. Autre. Université de Haute Alsace - Mulhouse; National Textile University (Pakistan), 2016. Français. NNT : 2016MULH0599 . tel-02388508

**HAL Id: tel-02388508**

**<https://theses.hal.science/tel-02388508>**

Submitted on 2 Dec 2019

**HAL** is a multi-disciplinary open access archive for the deposit and dissemination of scientific research documents, whether they are published or not. The documents may come from teaching and research institutions in France or abroad, or from public or private research centers.

L'archive ouverte pluridisciplinaire **HAL**, est destinée au dépôt et à la diffusion de documents scientifiques de niveau recherche, publiés ou non, émanant des établissements d'enseignement et de recherche français ou étrangers, des laboratoires publics ou privés.

UNIVERSITÉ DE HAUTE ALSACE, FRANCE  
ÉCOLE NATIONALE SUPÉRIEURE D'INGÉNIEURS SUD ALSACE  
LABORATOIRE DE PHYSIQUE ET MÉCANIQUE TEXTILES

&

NATIONAL TEXTILE UNIVERSITY, PAKISTAN

# THESIS

To obtain the title of

**DOCTEUR DE L'UNIVERSITÉ DE HAUTE ALSACE**

DISCIPLINE : MÉCANIQUE

To

**Muhammad Ali AFZAL**

## **DEVELOPMENT OF A COAXIAL COMPOSITE FIBER**

Defended on 17 November 2016 in front of following Jury:

Professor Manuel José DOS SANTOS SILVA	Universidade da Beira Interior, Portugal	Reviewer
Doctor (HDR) Xavier LEGRAND	Université de Lille, ENSAIT, France	Reviewer
Doctor (HDR) François BAUER	AIFP Saint Louis, France	Examiner
Doctor Arman SHAFI	Softwood Pvt. Ltd., Pakistan	Examiner
Doctor Nabyl KHENOUSI	Université de Haute Alsace, France	Invited Examiner
Professor Niaz Ahmad AKHTAR	University of Engineering and Technology, Taxila, Pakistan	Co-supervisor
Doctor HDR Omar HARZALLAH	Université de Haute Alsace, France	Co-supervisor
Professor Jean Yves DREAN	Université de Haute Alsace, France	Supervisor
Professor Laurence SCHACHER	Université de Haute Alsace, France	President



## **DEDICATION**

I dedicate all my work and efforts to my beloved parents for always supporting me. They are the driving force in my career and life. I can't find myself at this position without their prayers and wishes. They motivated and actively supported me throughout my life in my determination to find and realize my potential.





## ACKNOWLEDGEMENT

This work is a part of Joint PhD Degree program (Cotutelle) between Université de Haute Alsace, France and National Textile University, Pakistan. The work has been carried out in Laboratoire de Physique et Mécanique Textiles (LPMT) of Université de Haute Alsace at Ecole Nationale Supérieure d'Ingénieurs Sud Alsace (ENSISA) in Mulhouse, France.

I highly thank to the PhD supervisor, Mr. Jean Yves DREAN, Professor in LPMT at Mulhouse to give me the opportunity to work under his supervision. The technical guidance and support provided by him can't be elaborated in words. I appreciate his insightful advices and motivation at every step of my work.

I am thankful to Mr. Omar HARZALLAH, Maitre de conférences HDR in LPMT at Mulhouse and co-supervisor of this PhD study, for all his efforts and support. The guidance and support given in characterization of polymers and coaxial composite filaments are remarkable.

I am also thankful to Mr. Nabyl KHENOUSSE, Maitre de conférences in LPMT at Mulhouse for his dedication and guidance provided in this study. I acknowledge his support at every step during the whole program.

I acknowledge the support provided by Mr. Niaz Ahmad AKHTAR, Professor in University of Engineering and Technology, Taxila, Pakistan, worked as Ex-Rector of National Textile University, Faisalabad, Pakistan and co-supervisor of this study for his guidance and support. I acknowledge his efforts to take this joint PhD degree program up to the end.

I acknowledge the technical support provided by Mr. Christian PIDANCIER, technician in mechanical workshop in LPMT at Mulhouse for machining of extrusion dies.

I am grateful for the support of Mr. Abdel Aziz LALLAM, LPMT and Mr. Gaetan GARREFFA, LPIM for their support in polymer characterization.

I acknowledge Mr. François BAUER, Doctor in Sciences and chief executive of Advices in Ferrorelaxor Polymer in Saint Louis in providing polymers and technical support during the study.

The am thankful to National Textile University, Faisalabad, Pakistan for providing the financial assistance to carry out this research work in France.

I also acknowledge the financial support provided by Fondation Pierre et Jeanne SPIEGEL in Mulhouse in this study. This funding was useful for completion of interested research work.

I also acknowledge the moral support of my family, friends and colleagues whom I always find at my side at every difficult position particularly during experimental steps of this study. I acknowledge the moral support provided by Mr. Suleman BUTT, Mrs. Humairah SULEMAN, Miss Munazza AFZAL, Mr. Umer AFZAL, Miss Imen BOUGHAMOURA, Mr. Arman SHAFI, Mr. Sheraz AHMAD, Mr. Ahsan NAZIR and particularly my father, Mr. Ch. Muhammad AFZAL. I am extremely thankful to my father who keeps my spirits high in every moment of life and have equivalent share in accomplishment of this thesis by his prayers.

## TABLE OF CONTENTS

Dedication .....	i
Acknowledgement.....	iii
Table of Contents .....	v
List of Figures .....	xi
List of Tables.....	xix
List of Equations .....	xxi
List of Abbreviations.....	xxiii
1        CHAPTER 1 GENERAL INTRODUCTION.....	1
I    Research problem.....	1
II   Significance of proposed research.....	2
III  Specific objectives of the study.....	2
2        CHAPTER 2 BASIC INTRODUCTION .....	3
I    Introduction .....	3
II   Smart textiles.....	3
III  Composite fibre .....	3
A        Types of composite fibre.....	4
1        Structure morphology.....	5
1.1    Heterogeneous structure .....	5
1.2    Homogeneous structure .....	8
2        Electrical Conductivity.....	8
2.1    Conductive composite filament.....	8
2.2    Non-conductive composite filament.....	11
B        Coaxial composite fibre.....	11
1        Materials used for coaxial composite fibre .....	17
1.1    Fibres .....	17
1.2    Metals .....	17
1.3    Foreign particles .....	17
1.4    Polymers .....	17
2        Application areas of coaxial composite filament.....	18
3        Manufacturing techniques of coaxial composite filament .....	18
3.1    Fibre spinning .....	18
3.2    Extrusion.....	18
3.3    Drawing .....	21
IV   Process design and development.....	22
A        Extrusion dies .....	22
1        Die designs .....	22
1.1    Mono-extrusion dies .....	22
1.2    Co-extrusion dies .....	27

2	Design methods .....	35
2.1	Traditional method.....	35
2.2	Computer added method.....	35
3	Construction types of extrusion die designs.....	36
3.1	Plate dies.....	36
3.2	Streamlined dies.....	36
4	Types of die construction methods.....	37
4.1	Core-plate technique.....	37
4.2	Torpedo technique .....	38
5	Phenomenon affecting die designs .....	38
5.1	Rheology and kinematics of flow .....	38
5.2	Wall slip.....	39
5.3	Extrusion instabilities .....	40
5.4	Material degradation and residence time.....	45
5.5	Extrusion swell .....	46
5.6	Draw down.....	47
5.7	Thermal effects .....	47
6	Strategies and approaches for die design .....	48
6.1	Flow balancing.....	48
6.2	Land dimension for streamline dies.....	49
6.3	Avoid-cross-flow strategy .....	49
6.4	Flow separators.....	50
6.5	Neutralization of extrudate swell.....	50
7	General die design rules .....	51
B	Process modification .....	53
V	Characterization of polymer.....	53
A	Thermal characterization of polymer .....	53
1	Diffraction scanning calorimetry analysis.....	53
B	Rheological characterization of polymer .....	54
1	Melt flow rate analysis .....	55
2	Shear rate analysis .....	55
2.1	Constant shear rate.....	55
2.2	Variable shear rate .....	55
VI	Morphological characterization of coaxial composite filament.....	55
A	Cross-sectional cutting technique.....	55
B	Surface morphology .....	56
VII	Mechanical characterization of coaxial composite filament.....	57
A	Tensile test.....	57
VIII	Tribology characterization .....	58
IX	Piezoelectric sensors.....	59

X	Conclusion.....	59
3	CHAPTER 3 EXPERIMENTAL.....	61
I	Introduction .....	61
II	Materials.....	61
A	Conductive filament .....	61
B	Spinneret material.....	62
C	Tubing material .....	62
D	Polymers.....	63
III	Equipment and methods .....	65
A	Polymer sample preparation equipment.....	65
B	Characterization of polymer.....	66
1	Thermal characterization .....	66
2	Rheological characterization .....	66
3	Analytical characterization.....	68
C	Modification of melt extrusion process.....	68
1	Development of new designs .....	69
1.1	Spinneret design.....	69
1.2	Core filament passage.....	71
2	Modification of process design .....	71
2.1	Piston bore modification.....	71
2.2	Modification of cooling process .....	72
3	Optimization of extrusion parameters .....	72
D	Development of coaxial composite filament.....	73
E	Characterization of coaxial composite filament.....	73
1	Physical characterization .....	73
2	Morphological characterization.....	74
2.1	Cross-sectional surface morphology.....	74
2.2	Linear surface morphology.....	76
3	Mechanical characterization.....	77
4	Tribology characterization .....	77
5	Bending characterization.....	78
F	Conclusion.....	79
4	CHAPTER 4 RESULTS AND DISCUSSION.....	81
I	Introduction .....	81
II	Modification of melt extrusion process.....	81
A	Development of spinneret design .....	81
1	Evaluation of flow stability .....	81
2	Material performance calculation.....	82
3	Spinneret Prototypes.....	83
3.1	Full length spinneret design.....	83

	3.2	Fragmented spinneret design .....	92
B		Modification of machine design.....	106
	1	Introduction of tube .....	106
	2	Piston modification.....	108
	2.1	Type 1 .....	108
	2.2	Type 2 .....	109
	2.3	Type 3 .....	111
	3	Cooling chamber .....	112
	3.1	Forced counter airflow.....	113
	3.2	Increase in length.....	113
III		Characterization of polymers .....	114
A		Thermal characterization.....	114
	1	Differential scanning calorimetry.....	114
B		Rheological characterization .....	120
	1	Melt flow index .....	120
	2	Shear rate analysis .....	120
C		Analytical characterization.....	123
IV		Optimization of melt extrusion process.....	124
A		Optimization of spinning parameters .....	124
B		Optimization of filament cutting method .....	126
C		Optimization of spinneret design .....	128
	1	Conventional simple spinneret .....	128
	2	Prototype 1-4 .....	128
	3	Prototype 5 .....	128
	4	Prototype 6 .....	128
	5	Prototype 7 .....	129
	6	Prototype 8 .....	130
	6.1	Effect of number of holes on geometrical structure of composite filament.....	133
	6.2	Effect of tube position on geometrical structure of composite filament.....	134
	6.3	Effect of spinneret exit diameter on geometrical structure of composite filament.....	135
	6.4	Effect of tube inner diameter on geometrical structure of composite filament.....	136
	7	Prototype 9 .....	136
	8	Prototype 10 .....	137
D		Optimization of modifications in machine design .....	137
	1	Selection of tube .....	137
	2	Piston lower end .....	138
	2.1	Conventional design .....	138
	2.2	Type 1 .....	138

2.3	Type 2 .....	138
2.4	Type 3 .....	138
3	Cooling chamber .....	139
V	Characterization of coaxial composite filament.....	140
A	Physical characterization .....	140
1	Linear density .....	140
2	Diameter of composite filaments .....	143
B	Morphological characterization.....	145
1	Cross-sectional surface morphology .....	145
2	Linear surface morphology .....	148
C	Mechanical characterization.....	149
1.1	Tenacity .....	154
1.2	Breaking extension .....	158
1.3	Modulus .....	159
1.4	Work of rupture .....	160
D	Tribology characterization .....	161
E	Bending characterization .....	162
VI	Development of coaxial ferroelectric filament.....	165
A	Characterization of PVDF-TrFE composite filament .....	168
VII	Conclusion.....	171
5	CHAPTER 5 CONCLUSION.....	173
6	FUTURE PLANS .....	177
7	REFERENCES.....	179
8	ANNEXURE.....	191





## LIST OF FIGURES

Figure 1.	Cross-sectional shapes of different composite filaments .....	4
Figure 2.	Images of composite metallic core cotton yarns .....	12
Figure 3.	Cross sectional view of bicomponent fiber .....	14
Figure 4.	Schematic image of copper and polypyrrole coated para-aramid fiber..	15
Figure 5.	Cross sectional view of the composite fiber.....	16
Figure 6.	Systematic illustration of melt extrusion process.....	19
Figure 7.	Diagrammatical representation of molecular chain arrangement in molten polymer.....	20
Figure 8.	Geometrical design measurements of circular exit die .....	23
Figure 9.	Schematic illustration of centre fed mandrel support die structure.....	24
Figure 10.	Schematic design illustration of screen pack die.....	26
Figure 11.	Mandrel of side fed die with, (a. coathanger manifold, b. heart shape manifold) .....	26
Figure 12.	Spiral extrusion dies, (a. star shaped melt distribution with radial bore holes, b. ring shaped melt distribution with axial boreholes).....	27
Figure 13.	Flat-slit dual-slot co-extrusion die.....	28
Figure 14.	Fixed adaptor feed block die for flat sheets extrusion.....	29
Figure 15.	Flit slit feed block die with sliding adaptor .....	30
Figure 16.	Flat slit feed block die with vane adaptor.....	30
Figure 17.	Feed block dies with, (1) outside layer adaptor and (2) inside layer adaptor .....	31
Figure 18.	Melt extrusion used for the development of three layered coaxial composite filament .....	31
Figure 19.	Cross-sectional view of three layered coaxial composite filament .....	31
Figure 20.	Revolving adaptor for changing order of layers.....	32
Figure 21.	Multi-manifold dies for co-extrusion .....	33
Figure 22.	Schematic illustration of co-extrusion spinning die designs (a. side-side design, b. coaxial design, c. hollow fibre design, d. multi-layered design, e. circular stream plate mixer design) .....	33
Figure 23.	Schematic illustration of extrusion die for monofilament coaxial spinning process .....	34
Figure 24.	Schematic illustration of core sheath spinneret die .....	34
Figure 25.	Schematic illustration of extrusion die, (a. section and isometric die design, b. coaxial die exit shape, c. die exit diameter with electro-polishing effect).....	35
Figure 26.	Schematic representation of co-extrusion die, (a. exploded view, b. material streamlines view).....	36
Figure 27.	Schematic illustration of die cavity regions in streamline die.....	37
Figure 28.	Schematic illustration of combined plate-torpedo construction of extrusion die .....	38
Figure 29.	Flow through circular cross-section, (a. stable flow; b. unstable inlet zone; c. melt fracture) .....	41
Figure 30.	Rearrangement of interface in melt co-extrusion of polystyrene .....	42
Figure 31.	Rearrangement of interface in co-extrusion of two different grades of PE .....	43
Figure 32.	Instability build-up in interface of coextruded films.....	43

Figure 33.	Schematic illustration of model for explanation of adhesion at interface .....	44
Figure 34.	Stress-strain curve for PET fibre at different draw ratios .....	57
Figure 35.	Desiccator for conditioning .....	65
Figure 36.	Differential scanning calorimeter (a. operating chamber, b. sample preparation fixture).....	66
Figure 37.	Extrusion plastometer.....	67
Figure 38.	Physica MCR modular rheometer .....	67
Figure 39.	XRD used for analytical analysis of polymers.....	68
Figure 40.	Melt extrusion machine .....	69
Figure 41.	Lathe machine with parts .....	70
Figure 42.	Geared head drill press with parts .....	70
Figure 43.	High precision weighing balance .....	73
Figure 44.	Blade types used in the study .....	74
Figure 45.	Gold coating metalizer .....	75
Figure 46.	Scanning electron microscope.....	76
Figure 47.	Atomic force microscope .....	76
Figure 48.	MTS tensile strength tester.....	77
Figure 49.	Device arrangement used to measure friction coefficient by twist method .....	78
Figure 50.	KES - Single hair stiffness tester.....	79
Figure 51.	Schematic illustration of outer part of full length spinneret design prototype 1, (a. solid front view, b. transparent front view, c. inclined top view, d. inclined bottom view).....	84
Figure 52.	Schematic illustration of inner part of full length spinneret design prototype 1 inclined views, (a. solid view, b. transparent view, c. top view, d. bottom view).....	85
Figure 53.	Schematic illustration of full length spinneret prototype 1 solid views, (a. top view, b. bottom view, c. inclined top view, d. inclined bottom view) .....	85
Figure 54.	schematic illustration of transparent bottom view of full length spinneret prototype 1, (a. inclined view, b. magnified inclined view).....	86
Figure 55.	Schematic illustration of outer part of full length spinneret prototype 2, (a. solid front view, b. transparent front view, c. inclined top view, d. inclined bottom view).....	87
Figure 56.	Schematic illustration of inner part of full length spinneret prototype 2, (a. solid front view, b. transparent front view, c. inclined top view, d. inclined bottom view).....	87
Figure 57.	Schematic illustration of full length spinneret prototype 2 solid view, (a. top view, b. bottom view, c. inclined top view, d. inclined bottom view) .....	88
Figure 58.	Schematic illustration of full length spinneret prototype 2 transparent view, (a. full inclined view, b. magnified inclined view).....	88
Figure 59.	Schematic illustration of inner view of full length spinneret prototype 3, (a. solid view, b. transparent view) .....	89
Figure 60.	Schematic illustrations of full length spinneret prototype 3 solid views, (a. top view, b. bottom view, c. inclined top view, d. inclined bottom view) .....	90
Figure 61.	Schematic illustrations of full length spinneret design prototype 3 transparent views, (a. full view, b. magnified view) .....	90

Figure 62.	Schematic illustration of inner view of full length spinneret prototype 4, (a. solid view, b. transparent view) .....91
Figure 63.	Schematic illustrations of full length spinneret prototype 4 solid view, (a. top view, b. bottom view, c. inclined top view, d. inclined bottom view) .....91
Figure 64.	Schematic illustrations of full length spinneret prototype 4 transparent view, (a. inclined full view, b. inclined magnified view).....92
Figure 65.	Schematic illustration of upper part of prototype 5, (a. top view of main body, b. magnified top view of tube, c. magnified front view of tube)..93
Figure 66.	Schematic illustrations of solid view of upper part prototype 5, (a. top view, b. bottom view, c. inclined top view, d. magnified top view) .....93
Figure 67.	Schematic illustration of front view of lower part of prototype 5, (a. solid view, b. transparent view) .....94
Figure 68.	Schematic illustration of extrusion process design .....95
Figure 69.	Schematic illustration of front view of upper part of prototype 6, (a. solid view, b. transparent view) .....95
Figure 70.	Schematic illustrations of top and bottom views of prototype 6, (a. top view, b. bottom view, c. inclined top view, d. inclined bottom view, e. inclined top transparent view, f. inclined bottom transparent view).....96
Figure 71.	Schematic illustration of front view of prototype 6, (a. solid view, b. transparent view) .....96
Figure 72.	Schematic illustrations of top and bottom views of lower part of prototype 6, (a. top view, b. bottom view, c. inclined top view, d. inclined bottom view).....97
Figure 73.	Schematic illustrations of complete spinneret set of prototype 6, (a. solid front view, b. transparent front view, c. top inclined solid view, d. top inclined transparent view) .....97
Figure 74.	Schematic illustrations of top and bottom view of prototype 6 spinneret set, (a. top view, b. bottom view) .....98
Figure 75.	Schematic illustrations of top and bottom view of upper part of prototype 7, (a. top view, b. bottom view, c. top inclined transparent view) .....99
Figure 76.	Schematic illustration of front view of upper part of prototype 8, (a. solid view, b. transparent view) .....99
Figure 77.	Schematic illustrations of top and bottom view of upper part of prototype 8, (a. top solid view, b. bottom solid view, c. top transparent view, d. bottom transparent view, e. top inclined solid view, f. bottom inclined solid view) ..... 100
Figure 78.	Schematic illustrations of front view of lower spinneret part of prototype 8, (a. solid view, b. transparent view) ..... 100
Figure 79.	Schematic illustrations of top and bottom view of lower part of prototype 8, (a. top view, b. bottom view, c. inclined top view, d. inclined bottom view)..... 101
Figure 80.	Schematic illustrations of front and inclined view of prototype 8 complete spinneret set, (a. front solid view, b. front transparent view, c. top inclined solid view, d. top inclined transparent view)..... 102
Figure 81.	Schematic illustrations of top and bottom view of prototype 8 complete spinneret set..... 102
Figure 82.	Schematic illustrations of upper part of prototype 9, (a. solid view, b. transparent view) ..... 103

Figure 83.	Schematic illustration of top and bottom views of upper part of prototype 9, (a. top solid view, b. bottom solid view, c. top inclined view, d. bottom inclined view, e. top inclined transparent view, f. bottom inclined transparent view) .....	103
Figure 84.	Schematic illustration of front view of lower part of prototype 9, (a. solid view, b. transparent view) .....	104
Figure 85.	Schematic illustrations of top and bottom view of lower part of prototype 9, (a. top view, b. bottom view, c. top inclined view, d. bottom inclined view).....	104
Figure 86.	Schematic illustrations of complete set of prototype 9, (a. front solid view, b. front transparent view, c. top inclined solid view, d. top inclined transparent view) .....	105
Figure 87.	Schematic illustrations of top and bottom views of upper part of prototype 10, (a. top view, b. bottom view, c. top inclined view, d. bottom inclined view).....	106
Figure 88.	Schematic illustration of the melt extrusion process comparison, (a, conventional process, b. modified process).....	107
Figure 89.	Schematic illustration of fixation of tube in the spinneret set prototype 8, (a. solid inclined view, b. transparent inclined view).....	108
Figure 90.	Schematic illustration of front view of piston lower part type 1, (a. solid view, b. transparent view) .....	109
Figure 91.	Schematic illustrations of top and bottom view of piston lower end type 1, (a. top view, b. bottom view, c. top inclined view, d. bottom inclined view).....	109
Figure 92.	Schematic illustration of parts of piston lower end type 2, (a. front opened view, b. side opened view, c. top view of discs, d. bottom view of discs) .....	110
Figure 93.	Schematic illustrations of front view of piston lower end type 2, (a. solid view, b. transparent view) .....	111
Figure 94.	Schematic illustrations of top and bottom views of piston lower end type 2, (a. top view, b. bottom view, c. top inclined view, d. bottom inclined view).....	111
Figure 95.	Schematic illustration of front view of piston lower end type 3, (a. solid view, b. transparent view) .....	112
Figure 96.	Schematic illustrations of top and bottom views of piston lower end type 3, (a. top view, b. bottom view, c. top inclined view, d. bottom inclined view).....	112
Figure 97.	Arrangement of fan arrays in cooling chamber.....	113
Figure 98.	Change in column length of melt extrusion machine, (a. small column length, b. large column length).....	114
Figure 99.	DSC thermogram of PET in chips form.....	116
Figure 100.	DSC thermogram of PET in composite filament .....	116
Figure 101.	DSC thermogram comparison of PET in chips and composite filament .....	117
Figure 102.	DSC thermogram of low molecular weight PVDF-TrFE copolymer in chips form.....	118
Figure 103.	DSC thermogram of low molecular weight PVDF-TrFE copolymer in composite filament .....	119
Figure 104.	DSC thermogram comparison of low molecular weight PVDF-TrFE in chips and composite filament .....	119

Figure 105.	Viscosity Vs shear rate for polyester at different temperatures .....	121
Figure 106.	Viscosity vs shear rate of polyester chips and filament at 280 °C .....	122
Figure 107.	Viscosity vs shear rate of PVDF-TrFE copolymer of different molecular weights at different temperatures .....	122
Figure 108.	X-ray diffraction patterns for polyester in chips and composite filament form .....	123
Figure 109.	X-ray curves obtained for PVDF-TrFE copolymer in chips and composite filament form .....	124
Figure 110.	SEM cross-sectional images of composite filament developed at different piston speeds, (a. 3 mm/min, b. 5 mm/min, c. 7 mm/min).....	125
Figure 111.	SEM cross-sectional images of composite filament at different winding speeds, (a. 100 rpm, b. 120 rpm, c. 140 rpm).....	126
Figure 112.	SEM cross-sectional images of polyester coaxial composite filaments cut by different techniques, cutting at room temperature (a) scissor, (b) paper cutting blade, (c) Hamaguri grind blade, (d) single bevel grind blade, (e) Zero ground saber blade; cutting at $-10 \pm 3$ °C (f) zero ground saber blade .....	127
Figure 113.	SEM cross-sectional image of composite filament through conventional spinneret .....	128
Figure 114.	SEM cross-sectional image of composite filament through prototype 6 .....	129
Figure 115.	SEM cross-sectional image of composite filament with prototype 7... 129	
Figure 116.	SEM cross-sectional image of composite filament using prototype 8. 130	
Figure 117.	Schematic illustration of different number of holes in upper part for characterization, (a. 4 holes, b. 3 holes, c. 2 holes).....	131
Figure 118.	Schematic illustration of tube position with respect to upper part bottom level for characterization, (a. position 0 mm, b. position 2 mm) .....	131
Figure 119.	Schematic illustrations of different spinneret exit diameters in lower part for characterization, (a. diameter 1 mm, b. diameter 2 mm).....	132
Figure 120.	Schematic illustration of different tube internal diameters for characterization .....	132
Figure 121.	SEM cross-sectional images of composite filaments developed by different number of holes in prototype 8, (a. 2 holes, b. 3 holes, c. 4 holes, d. 4 holes) .....	134
Figure 122.	SEM cross-sectional image of composite filament developed with different position of tube in spinneret, (a. 0 mm, b. 2 mm) .....	135
Figure 123.	SEM cross-sectional images of composite filament developed with different spinneret exit diameters, (a. 1 mm, b. 2 mm) .....	135
Figure 124.	SEM cross-sectional images of composite filament developed with different tube inner diameters, (a. 254 $\mu$ m, b. 508 $\mu$ m, c. 762 $\mu$ m).....	136
Figure 125.	SEM cross-sectional image of composite filament by spinneret prototype 9.....	137
Figure 126.	SEM cross-sectional view of composite filament developed at different cooling chamber length, (a. short length, b. large length).....	139
Figure 127.	Graphical representation of filament linear density of different sample codes.....	140
Figure 128.	Actual and theoretical linear density with error percentage of polyester composite filament .....	143
Figure 129.	Graphical representation of mean diameter of samples vs sample codes .....	144

Figure 130.	Theoretical and experimental diameter comparison with error percentage of Polyester composite filament .....	144
Figure 131.	Geometrical characterization codes for composite filament .....	145
Figure 132.	Graphical representation of mean diameter uniformity ratio vs sample code .....	146
Figure 133.	Graph between mean standard deviation of diameter within sample vs sample code .....	147
Figure 134.	Eccentricity of core filament graph of samples .....	147
Figure 135.	Longitudinal 3D surface morphology of composite filament at different magnification levels .....	148
Figure 136.	Surface roughness amplitude of composite filaments at different magnification levels .....	149
Figure 137.	Failure of composite filaments as necking during tensile test.....	150
Figure 138.	Failure of composite filaments as breakage during tensile test.....	150
Figure 139.	Specific load-extension curves obtained for sample code 1.....	151
Figure 140.	Specific load-extension curves of copper filament without thermal treatment.....	151
Figure 141.	Specific load-extension curves of polyester filament.....	152
Figure 142.	Graphical representation of tenacity of samples .....	155
Figure 143.	Estimation of area around core in different shaped composite filaments .....	156
Figure 144.	Graphical representation of breaking extension in percentage .....	159
Figure 145.	Graphical representation of elastic modulus of samples .....	159
Figure 146.	Graphical representation of work of rupture of different samples .....	160
Figure 147.	Graphical representation of specific work of rupture of samples .....	160
Figure 148.	Force verse extension graph obtained for sample code 1.....	161
Figure 149.	Mean friction coefficient difference values of different sample codes	161
Figure 150.	Experimental bending curves of different shaped filaments .....	163
Figure 151.	Experimental bending curves obtained for different sample codes .....	164
Figure 152.	Graphical representation of bending modulus of samples .....	165
Figure 153.	Cross-sectional view of Cu/PVDF-TrFE core/sheath coaxial composite filament.....	166
Figure 154.	Graphical representation of eccentricity of core in PVDF-TrFE composite filaments .....	166
Figure 155.	Graphical representation of mean diameter uniformity ratio of PVDF-TrFE composite filaments .....	167
Figure 156.	Graphical representation of standard deviation within samples of PVDF-TrFE composite filaments .....	167
Figure 157.	Specific load vs extension curves of Cu/PVDF-TrFE core/sheath coaxial composite filament .....	168
Figure 158.	Force verses displacement curve obtained during frictional testing of composite filament .....	169
Figure 159.	Friction coefficient difference values of low and high molecular weight PVDF-TrFE composite filaments.....	170
Figure 160.	Experimental bending curves for low and high molecular weight coaxial composite Cu/PVDF-TrFE filaments.....	171
Figure 161.	Chemical structure of poly (ethylene terephthalate) .....	192
Figure 162.	Schematic diagram of continuous polyester manufacturing process ...	193
Figure 163.	Chemical reactions for the preparation of bis-(2-hydroxyethyl) terephthalate .....	194

Figure 164.	Polycondensation reaction for second step of PET manufacturing.....	194
Figure 165.	Morphological variations observed by change in spin line parameters during melt spinning.....	199
Figure 166.	Morphological transformation in filament during spin-line process....	200
Figure 167.	Morphological illustration of polyester fibre showing various features .....	201
Figure 168.	Graphical representation of draw ratio as a function of molecular orientation induced during spinning.....	202
Figure 169.	Interactive graph between typical forces acting upon spinning thread-line vs winding speed .....	202
Figure 170.	Schematic illustration of relation between cooling rate line of different cooling rates and temperature dependent different crystallization rate curve .....	203
Figure 171.	Mandrel support system .....	204
Figure 172.	DSC thermogram of high molecular weight PVDF-TrFE copolymer in chips form.....	205
Figure 173.	DSC thermogram of high molecular weight PVDF-TrFE copolymer in composite filament .....	205
Figure 174.	DSC thermogram comparison of high molecular weight PVDF-TrFE copolymer chips and composite filament.....	206
Figure 175.	DSC thermogram comparison of high and low molecular weight PVDF-TrFE copolymer in chips form .....	206
Figure 176.	DSC thermogram comparison of high and low molecular weight PVDF-TrFE copolymer in composite filament.....	207
Figure 177.	Specific load-extension curves of sample code 2.....	208
Figure 178.	Specific load-extension curves of sample code 3.....	208
Figure 179.	Specific load-extension curves of sample code 4.....	209
Figure 180.	Specific load-extension curves of sample code 5.....	209
Figure 181.	Specific load-extension curves of sample code 6.....	210
Figure 182.	Specific load-extension curves of sample code 7.....	210
Figure 183.	Specific load-extension curves of sample code 8.....	211
Figure 184.	Specific load-extension curves of sample code 9.....	211
Figure 185.	Specific load-extension curves of sample code 10.....	212
Figure 186.	Specific load-extension curves of sample code 11.....	212
Figure 187.	Specific load-extension curves of sample code 12.....	213
Figure 188.	Specific load-extension curves of thermally treated copper filament (C-HS).....	213
Figure 189.	DSC thermogram of Nylon 6,6 in chips form .....	215
Figure 190.	Viscosity vs shear rate curves of polyamide at different temperatures	215
Figure 191.	SEM cross-sectional image of Cu/Nylon 6,6 core/sheath composite filament.....	216





## LIST OF TABLES

Table 1.	Technical specifications of copper monofilament.....	61
Table 2.	Chemical composition (%) of elements used to form brass.....	62
Table 3.	Mechanical characterization of brass .....	62
Table 4.	Specifications of stainless steel and ceramic tubes .....	63
Table 5.	Characteristics data of 100 $\mu\text{m}$ thin film of PVDF-TrFE copolymer ....	64
Table 6.	Thermal properties of polyester in chips and composite filament form .....	115
Table 7.	Thermal properties of PVDF-TrFE copolymer in chips and composite filament form.....	118
Table 8.	Melt flow rate of polymers .....	120
Table 9.	Design of experiments for optimization of spinning parameters .....	125
Table 10.	Design of experiments for characterization of spinneret design .....	133
Table 11.	Calculated linear density for different samples .....	142
Table 12.	Tensile properties of different samples .....	153
Table 13.	Area calculations of different shaped filaments .....	156
Table 14.	Comparison of theoretical and experimental tenacity values of composite filaments .....	158
Table 15.	Experimental data of bending properties of different samples.....	162
Table 16.	Tensile properties of Cu/PVDF-TrFE core/sheath coaxial composite filament.....	169
Table 17.	Experimental data of bending properties of PVDF-TrFE coaxial composite filament .....	170
Table 18.	Major properties of polyester polymer .....	191
Table 19.	Comparison of some semi crystalline polymeric material's properties	197
Table 20.	Comparison of ceramic materials and standard piezoelectric polymer properties .....	198
Table 21.	Properties of Nylon 6, 6 .....	214



## LIST OF EQUATIONS

<u>Equation 1</u> .....	39
<u>Equation 2</u> .....	40
<u>Equation 3</u> .....	45
<u>Equation 4</u> .....	46
<u>Equation 5</u> .....	48
<u>Equation 6</u> .....	48
<u>Equation 7</u> .....	49
<u>Equation 8</u> .....	50
<u>Equation 9</u> .....	54
<u>Equation 10</u> .....	55
<u>Equation 11</u> .....	57
<u>Equation 12</u> .....	66
<u>Equation 13</u> .....	78
<u>Equation 14</u> .....	81
<u>Equation 15</u> .....	82
<u>Equation 16</u> .....	126
<u>Equation 17</u> .....	140
<u>Equation 18</u> .....	140
<u>Equation 19</u> .....	141
<u>Equation 20</u> .....	141
<u>Equation 21</u> .....	141
<u>Equation 22</u> .....	141
<u>Equation 23</u> .....	142
<u>Equation 24</u> .....	145
<u>Equation 25</u> .....	145
<u>Equation 26</u> .....	145
<u>Equation 27</u> .....	146
<u>Equation 28</u> .....	157
<u>Equation 29</u> .....	164



## LIST OF ABBREVIATIONS

$\overline{\mu_s - \mu_k}$	Average frictional coefficient difference
$\mu$	Shear viscosity / friction coefficient
$\mu_0$	Consistency coefficient
$\mu_k$	Frictional coefficient at stick
$\mu_s$	Frictional coefficient at slip
2HB	Moment of hysteresis
AFM	Atomic Force Microscope
B	Bending rigidity
C. V %	Coefficient of variation percent
C-HS	Thermal treated core filament
C-NHS	Non-thermal treated core filament
CNT	Carbon nanotubes
CPC	Conductive polymer composites
Cu	Copper
D	Diameter
$D_a$	Actual diameter
$D_c$	Calculated diameter
DSC	Diffraction scanning calorimetry
E	Eccentricity
$E_B$	Bending modulus
$E_y$	Modulus
F	Force
$F_k$	Force in stick
$F_s$	Force in slip
Hi MW	High molecular weight
ICP	Inherent conductive polymers
K	Curvature
KES	Kawabata Evaluation System
L	Length
Lo MW	Low molecular weight
m	Index in Navier slip law
M	Bending momentum per unit width
M	Mass
$M_n$	Molecular weight
n	Number of divisions
n	Power Law index
$\eta$	Intrinsic viscosity
$\bar{\eta}$	Melt viscosity
$N_1$	First normal stress difference
NP	Nanoparticles
PANI	Polyaniline
PET	Polyethylene terephthalate polymer
PVDF	Polyvinylidene fluoride polymer
PVDF-TrFE	Polyvinylidene fluoride-trifluoroethylene copolymer
S	Cross-sectional area
S. S	Stainless steel
SEM	Scanning Electron Microscope

T	Temperature
$T_{cc}$	Cold crystallization temperature
$T_{dr}$	Drawing temperature
$T_g$	Glass transition temperature
$T_m$	Melting temperature
$t_{res}$	Residence time field
Tt	Linear density
$Tt_a$	Actual Linear density
$Tt_c$	Calculated Linear density
v	Volume
V%	Volume percent (v/v)
Vol.	Volume
w	Weight
W%	Weight percent (w/w)
wEDM	Wire electric discharge machining
$W_{pl}$	Specific work of rupture
X	Diameter uniformity ratio
XRD	X-Ray diffraction
$\alpha$	Angle between two surfaces
$\Delta H_c$	Enthalpy of crystallization
$\Delta H_{cc}$	Enthalpy of cold crystallization
$\Delta H_m$	Enthalpy of fusion
$\varepsilon_f$	Breaking extension
$\lambda$	Stretching ratio
$\rho$	Density
$\rho_c$	Composite density
$\sigma$	Standard deviation
$\sigma_B$	Experimental tenacity
$\sigma_{id}$	Standard deviation of sample intra-diameter
$\sigma_{th}$	Theoretical tenacity
$\tau$	Shear stress
v	Velocity
$\chi$	Crystallinity
$\omega$	Symbol of capillary wall

## **CHAPTER 1**

### **GENERAL INTRODUCTION**

Fibres and filaments are the basic elements of textile structures. A number of different types of filaments are developed with different cross-sectional shapes and structures to achieve particular properties in desired application areas. The world of textiles is changing day by day, which introduces incorporating electronic devices in textile structure. The branch of textile which deals with electronics and interaction with environment is studied under SMART textiles, e-textiles and intelligent textiles. These branches of textiles use very particular filament and fibres for their functionalities. One of the key and fundamental filament type being used in these branches is called as coaxial composite filaments. These filaments have a core with a sheath around it. These filaments are extensively explored for textile based sensors and actuators. They looked like an electric wire having conductive core with insulating sheath. In fact, these filaments are quite different from commercially available electric wires, because of very small size of core at central axial position of the filament.

The problem being faced in this field of textiles is the production and development of these coaxial composite filaments. The filaments having metal as core is only the best solution for being use in these fields. No literature is being available except the work carried out in this laboratory for the manufacturing of metal core coaxial composite filaments. The manufacturing technique previously developed in this laboratory for the manufacturing of these coaxial composite filaments can't help to scale up the production at industrial level. The problems and short comings needed to be addressed are: to make the process robust and industrially acceptable for the manufacturing and development of these composite filaments.

#### ***I Research problem***

The development of coaxial monofilament using the metallic core is difficult to develop and process. That is one of the reason that less literature is available in this field. The previous spinneret designed was too expensive and vulnerable to be choked with polymer. There is no other spinneret available to produce coaxial composite filaments having very small diameter metallic core at central axial position of the filament.



## ***II Significance of proposed research***

The so-called SMART textiles available now is the integration of technologies in conventional textile substrates rather than developing with wholly functional monofilaments. The intelligent monofilaments are the backbone of the SMART textiles and beyond doubt be the significant first step towards the SMART applications.

The development of intelligent monofilament using the metallic core is more efficient in its conductive properties as compared with conductive polymers or doped polymers. Considering its advantages, this field need to be advanced to move forward for better functionality and improved efficiency of the SMART materials.

## ***III Specific objectives of the study***

The main objective of this study is to develop a new spinneret design for the manufacturing of desired coaxial composite filament which can be used for development of sensors. In addition, modification of machine design, process and investigation of parameters affecting product quality in all respects. Furthermore, characterization of polymer and performance of developed coaxial composite filaments need also to be investigated.

## **CHAPTER 2**

### **BASIC INTRODUCTION**

#### ***I Introduction***

The chapter includes the introduction of composite filaments and its types. The constituent materials of composite filament reported in literature were also briefly introduced. The spinneret types available and their design configurations were explained. The die design rules for the development of industrially acceptable dies were briefly outlined. The polymer and filament characterization techniques previously reported in literature for composite filaments were also elaborated.

#### ***II Smart textiles***

The textiles which can sense and react at some external stimuli are called as smart textiles. Electrically conductive textiles are one of the basic areas of smart textile. Conductive textiles are the upcoming high tech field of textiles in regards of performance, application and uses. This area finds its application in fields such as electromagnetic shielding, antistatic, microelectronics, heat generation and textile sensors etc. composite filaments are used for the development of textile sensors to measure temperature or pressure parameters. This work has been focused to develop composite fibre for intended application in sensors, actuators and electrical signal transmission in wearable electronics.

#### ***III Composite fibre***

Fibre is a textile raw material having characteristic fineness and flexibility and have high length to thickness ratio of at least 100 value [1-3]. The filament is the continuous form of the fibre which have length to thickness ratio of infinity value [3]. Composite is defined as a material composed of two or more components having different composition or form on a macro-scale and have two or more distinct phases with recognizable interfaces between them [4].

A composite fibre is such a material which may have two or more different materials, such as polymers, metals, fibres etc., in a single fibre structure. Composite fibres and yarns with combinations of different materials like metal filaments [5], conventional polymers [6], advanced technical polymers [7, 8], conventional fibres [9, 10], high performance fibres [11, 12], nanoparticles [13, 14] and different metal coatings [13, 15] were produced,

out of which some are commercially available as well [16]. The composite fibres can have various value added properties such as electrical conductivity [17], thermal conductivity [18], UV protection, antimicrobial [19], flame retardancy [20], self-cleaning etc. which depends upon the material characteristics which is used.

### A Types of composite fibre

Composite filament manufacturing technology was initially developed to enhance the properties of the conventional filaments and production of microfibers at economical values [21]. The most widely known composite filament types are shown in Figure 1. Usually two polymer components are used for fabrication of composite filaments. The exception lies for coaxial, twisted, coated and doped structures, where some external material is used as the second component. In other composite filaments, an external material may also be used along with two polymeric components like in conjugated structures. The composite filaments are classified according to their morphological structure and their detailed explanation for each composite filament is as under:

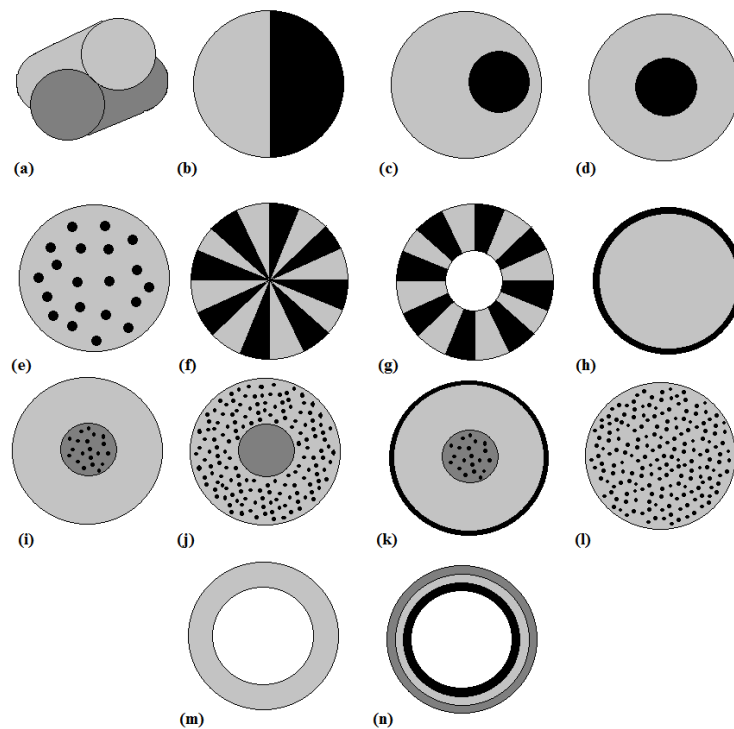


Figure 1. Cross-sectional shapes of different composite filaments

## ***1 Structure morphology***

Structure morphology explains the morphological characteristics of the fibre which includes the cross-sectional shape, homogeneity and uniformity of material. The composite fibres can be divided into two different structures based on their morphological characteristics, heterogeneous structure and homogeneous structure.

### ***1.1 Heterogeneous structure***

The composite fibres which have non-uniformity of constituent material concentration at different macromolecular regions is classified as heterogeneous structure. These structures comprise large volume of composite fibres. This structure is further divided into subclasses based on their shape and degree of localization of constituent materials.

#### ***1.1.1 Twisted structure***

These composite structures are developed by twisting two different material types as shown in Figure 1(a). This plied structure may use conventional textile fibres or filaments with technical fibres or filaments to develop intelligent textile material [22, 23]. These structures are commonly fabricated on ring spinning process [24]. The most common example of this structure is the twisted composite yarn developed by twisting cotton roving and polyester multifilament [25].

#### ***1.1.2 Side-side structure***

The composite filament structure in which different polymers shared along the length in two or more distinct region as shown in Figure 1(b) [26]. The polymers having different physical properties but same chemical nature are used for fabrication of this composite filament. The change of physical properties is caused by variation in molecular weight. For instance, two different molecular weight polyester polymers can be used for the manufacturing of this filament by extrusion through a single spinneret. This filament is also called as self-bulking filament. The component polymers show different expansion and relaxation properties causing curls up during relaxed state like bimetallic strip and appears as three-dimensional spiral crimp [21, 27].

#### ***1.1.3 Eccentric core-sheath structure***

The core sheath structure in which the core is eccentric to the length axis of the filament is considered as eccentric core-sheath structure as shown in Figure 1(c). This type of

structure was developed to achieve combined properties of two different polymers as well as special effects in filaments. It is reported that Shima and co-workers developed an eccentric filament for the first time to achieve self-spiral crimp in the filament [27]. Later on, Chang *et. al.* also patented his work related to the development of self-crimped filament made from poly (trimethylene terephthalate) by doping small amount of polystyrene in one component [27].

#### *1.1.4 Coaxial core-sheath structure*

The composite filaments having the same central axis for all the layers is considered as coaxial composite filament as shown in Figure 1(d). Different coaxial structures have been developed and reported in literature for various applications. This sort of structure is particularly used for sensor and actuator, electrical conductivity, thermal conductivity and electromagnetic interference shielding applications.

#### *1.1.5 Islands in a sea structure*

The composite filament in which secondary polymer is spread in form of fibres in primary polymer matrix with longitudinal direction in parallel to principle axis of the filament is called as islands in sea structure as shown in Figure 1(e). This composite filament manufacturing technique was explored in 1970's in Japan using polyester fibrils dispersed in polymer matrix [27]. The polyester fibrils produced in this method have the diameter of 1  $\mu\text{m}$  and considered as microfibers. This technique was later on successfully used for the production of microfibers. In another study, steel fibres were blended with polyester fibres to develop a conductive composite yarn structure [28]. The composite filament exhibited good dielectric, magnetic and electrical properties.

#### *1.1.6 Pie structure*

The composite filament composes of different polymeric components arrange in wedge shape in filament cross-sectional structure is called a pie structure filament as shown in Figure 1 (f & g). This composite filament structure was also developed in view of getting microfibers by dividing the fibre into multiple parts by the action of mechanical stress [29]. The polymers used for manufacturing microfibers are incompatible, which adhere poorly with each other in composite filament structure. The individual polymer parts get separated to form bundles of microfibers with wedge cross-sectional shape from composite filament due to low level of adhesion between them. The suitable incompatible

polymer combination pairs are polyester-nylon-6 or polypropylene-polyester. These microfibers find their application in filter materials, polishing cloths for optical instruments and cleaning cloths for micro-cleaning components [27].

#### *1.1.7 Coated structure*

The composite structure developed by coating normal filament with some coating material is classified as coated composite structure as shown in Figure 1(h). The coating may be done by silver [13, 16, 22, 30], copper/nickel or copper sputtering [11, 31-33], graphene [34] and carbon nanotubes [35, 36] to induce specific properties including antimicrobial [37], UV resistance, electrical and thermal conduction [38, 39] etc. The coatings can be made by ion exchange mechanism [30], absorption and reduction processes [13], electroless plating [11, 32, 33], magnetron sputter [31], chemical vapour deposition [34], ionic deposition technique [39]. Coating effect the mechanical properties and have poor washing fastness for repeated cycles [11].

#### *1.1.8 Conjugated structure*

The combination of any two or more mentioned structures in single composite filament is considered as conjugated composite structure. The typical structure illustrations are shown in Figure 1 (i, j & k). A number of conjugated composite structures are reported in literature for obtaining some specific properties in the filament [13, 40-44]. The reported strain sensors [40, 41] developed by twisting technique did not exhibit required sensitivity due to slippage between the yarns.

#### *1.1.9 Hollow fibre*

The composite filament which have core composed of air is called as hollow composite filament as shown in Figure 1 (m & n). These filaments are cut into staple fibres after introduction of crimps and used mainly for thermal insulation purposes. The main volume of their production is used as staple fibrefill for quilts, thermal outwear, duvets and pillows. The presence of inside air brings this filament in the category of thermally insulated fibres. Multi layered hollow fibres were also fabricated with complex processes [45]. Hollow filaments find their applications in medical devices, sensor and actuators [45]. Hollow fibres have been developed by triblock co-polymer of poly[styrene-b-(ethylene-co-butylene)-b-styrene] [46] and PVDF-TrFE [45].

## 1.2 Homogeneous structure

### 1.2.1 Doped structure

The composite filaments developed by doping foreign nanoparticles are considered as doped composite structures as illustrated in Figure 1 (l). To produce such structures, the materials must be compatible and each material should exhibit its desired property. These nanoparticles are too small and dispersed homogeneously throughout the filament, which bring this filament in class of homogeneous composite filaments. The fillers embedded in the polymer matrix have volume packing fraction range from 52.3-74.1 vol% [6]. The materials described in literature for development of conductive composite fibres are different polymer such as polyaniline [47]; metal particles such as, Cu, Ag [6, 48-50], Pt and Au [12, 51, 52]; and/or non-metal particles such as carbon black [14, 42, 53-58], carbon nanotubes [6, 59-63], carbon fibre [64, 65] and graphite [66] are embedded in polymer substrate for fibre formation. It is reported that carbon nanotubes act as efficient nucleation agent for crystallization during elongation process which cause increase in mechanical properties of the structure [6]. On contrary, metal suppresses the crystallization in polymer and leads to low viscosity of the polymer [6]. The interruption of crystallization may lead to destruction of polymer chains by micro-sized Ag particles which weakens the elongation properties. This phenomenon is called “brittle fracture” which was observed at interfaces within polymer embedded Ag particles during stretching [67, 68]. The introduction of nanoparticles in polymer matrix induce special properties in the filament including antimicrobial, UV resistance, electrical and thermal conductance [69] etc. These fibres find their application in wearable electronic connectors, electromagnetic shielding and strain sensors [54, 59, 70]. The strain sensors developed with this configuration have non-linear electromechanical behaviour and lower working range which limited their applications in smart textiles [54, 59].

## 2 ***Electrical Conductivity***

### 2.1 Conductive composite filament

The filaments which can conduct electric energy through them are considered as conductive composite filaments. Conductivity through the filament may be due to inherent conductive polymer or additives in filament structure. Inherent conductive polymers (ICPs) have electrical conductivity similar to inorganic semiconductors, therefore can be used for antistatic applications [71]. These conductive polymers can be used for antistatic,

electromagnetic impedance shielding and corrosion resistance coating applications [72]. These polymers are prepared from inexpensive substrates and are highly cross-linkable having high solubility and process ability. The polypyrrole and polyaniline (PANI) are also used as conductive polymers [9, 10].

The transition of insulator to conductor phases in doped composites structures is explained frequently on percolation theory [14]. According to this theory, the filler particles are distributed throughout the insulated material and do not have the ability to contact with adjacent particles at low filler loadings. In such condition, the increase of filler loading do not increase the electrical conductivity of the composite structure sharply. On contrary, the composites having high filler loading develop three dimensional conductive network within insulated polymer material by linking of additives, wherein any increase in filler loading observe steep increase in electrical conductivity in such materials. The critical value of occupational probability in the composite matrix embedded with conductive fillers for the formation of long range connectivity is called percolation threshold [13]. The percolation threshold value decreases by increasing the length of the filler particles [73].

A large number of proportions of composite filament fall in this category because of its importance in intelligent textiles. The conductive filaments are further subdivided into two classes based on their conductivity level.

### 2.1.1 *Good conductors*

These filaments consist of such composite structures which have continuous metal or inherent conductive polymer. There are some inherent conductive polymers such as, poly (pyrrole) [74], poly (3, 4-ethylene dioxythiophene) and poly (aniline), which show high electrical conductivity of over  $10^2$  S/cm [75-78]. A carbon nano tubes-carbon fibre hybrid was developed by Saba *et. al.* [79] from carbon fibres coated with carbon nano tubes in dispersion of polypyrrole layers.

The use of metal as conductor was made in 1734 by Gray [80] which replaces the natural fibrous materials. The use of continuous metals such as Cu [5, 22], Ag [23], metal alloys [46] and stainless steel [81] in the filaments made them conductive for multiple applications. The liquid metal alloy (EGaIn) core composite fibre had the resistivity of about  $3 \times 10^{-5}$   $\Omega$  cm [46]. According to Pouillet's law, the resistance of wire depends upon



its cross-sectional area, length and resistivity. The reported resistance normalized by the length was 0.24  $\Omega/\text{cm}$ .

The conductive fibres can be manufactured by melt spinning [82], electrospinning [83], solution spinning [84], bubbfil spinning [85] and metal coating [30] techniques and their electrical conductivity is reported in the range of over  $10^3$  to  $10^4$  S/cm using polymer/Ag substrates. These filaments find their applications in strain sensors [81], electromagnetic shielding [22] and electrical and thermal conductors [86].

### 2.1.2 *Semiconductors*

In this class of conductive filaments, those filaments are concerned which have low level of conductivity. The conductivity is developed due to introduction of foreign particles. These filaments are used for resistive heating [87, 88], textile base electrodes [34], electrical signal transmission and strain sensors in smart applications. The foreign particles include metals such as Ag [6] and inorganic materials such as carbon nanotubes (CNT) [35, 36, 62, 63, 70, 87, 88], carbon black, graphene [34], carbon fibres [79]. CNT's are of great importance due to their extraordinary mechanical, thermal and electrical properties. The combination of these properties and its special morphology (nano sized diameter and high aspect ratio) makes it a potential candidate for use in textile structures and composites with improved electrical conductivity, mechanical properties and multi-functionality [53, 63, 69, 70, 89-91]. Some other polymeric fillers like polyaniline commonly called as PANI are also used for obtaining conductive filaments [47]. The cellulosic insulator matrix can be converted into semi-conductor by adding 2 wt.% of PANI to attain resistivity of  $10^6 \Omega \text{ cm}$ , which is the percolation threshold. At higher loading, resistivity decreases significantly.

The electrical resistivity obtained from carbon black doped polybutylene terephthalate sheath on polyethylene terephthalate core fibre was  $7 \times 10^5 \Omega/\text{cm}$  [14]. The percolation effect of carbon nano tubes was explained by Biron [72] with respect of weight percentage. According to which at filler content of above 2 wt% of carbon nano tube, the resistance decreases drastically. The optimization study of electrical conductivity with regard to stabilization conditions of the carbon nano fibres was done by Wu *et. al.* [92]. The electrical conductivity obtained at optimized conditions was approximately  $20.2 \pm 1.2 \text{ S cm}^{-1}$ , which was highly depended on stabilized conditions. The electrical conductivity obtained for a Ag doped polypropylene fibre of less than 100  $\mu\text{m}$  diameter

was in the range of  $4.1-7.2 \times 10^{-2} \text{ S cm}^{-1}$  for the concentration of 46 wt% and 4 wt% of Ag and single wall carbon nanotubes respectively [6].

The resistance observed for copper coated Kevlar composite fibre reduced by increase in coating deposition time,  $0.053 \text{ } \Omega \text{ cm}^{-1}$  which reduced to  $0.008 \text{ } \Omega \text{ cm}^{-1}$  after shift from 5 to 30 minutes deposition time [11]. In another study, a conductive fibre was fabricated with AgNP coated on doped matrix of AgNW-SBS structure. The composite fibre exhibited electrical conductivity of value  $2450 \text{ S/cm}$  [13]. In a study, monolayer graphene was coated on polypropylene fibre providing sheet resistance of  $1 \text{ k}\Omega/\text{sq.}$  to  $12 \text{ k}\Omega/\text{sq.}$  [34].

## 2.2 Non-conductive composite filament

A non-conductive coaxial composite filament was reported by El-Salmawy *et. al.* [93, 94]. The filament was developed with aromatic and aliphatic polyesters as coaxial composite filament. The core was developed with poly (butylene terephthalate) polymer having a sheath of poly (butylene succinate-co-L-lactate) polymer. In another study, poly (3-hydroxybutyrate-co-3 hydroxyvalerate) as core was produced with a sheath of poly (lactic acid) to develop coaxial composite filament [95]. Polytri-methylene terephthalate blended with polyethylene terephthalate bi-component composite fibre is also commercially available in market [96]. A polyethylene/polyethylene terephthalate sheath/core structure was also reported [97].

### **B Coaxial composite fibre**

These structures are developed to attain particular properties of participating polymer substrates which may or may not be feasible for spinning alone. The enhancement of multifunctional properties in these filaments do not cause to decrease in mechanical characteristics [98]. The main strength of the coaxial composite filament is derived from core while sheath is used to cover the core and to provide other functional characteristics to the coaxial filament [93]. Usually the particular properties which are taken into consideration for the development of coaxial composite filaments are conductivity or strength of the core with the sheath to provide the aesthetic, adhesive, textile or other properties to the filament. A number of patents were filled for developing these composite filaments [99-101].

Coaxial composite filaments and its conjugated structure filaments are developed with different constituent materials including fibres, polymer resins, metals and inorganic

particles. There are some polymers such as poly (3-hydroxybutyrate-co-3 hydroxyvalerate), which are not strong enough to be processed as fibre alone; therefore, coaxial composite filament technique can be used to blend them with other polymers for future applications [95]. In another study, polypropylene core was sheathed with polyethylene polymer to develop core sheath structure [102]. Poly (butylene terephthalate) polymer was used as core with poly (butylene succinate-co-L-lactate) polymer as sheath in manufacturing of coaxial filament [93]. In another study, poly (ethylene terephthalate) polymer was used as core with sheath of poly (butylene terephthalate) and poly (butylene succinate-co-L-lactate) were investigated [94].

Sancak *et. al.* [103] used copper and stainless steel wire to fabricate cotton coated composite yarns for electromagnetic shielding applications. Bedeloglu *et. al.* [104] investigated the mechanical and electrical properties of composite metallic core cotton yarn. The effect of various material ratios, wire diameters and types were reported in terms of yarn hairiness, count, bending rigidity and tensile properties. It was explained that bending rigidity of the yarn increased by increasing metallic content in the yarn. It was also reported that the change in metallic wire structure lead to change in yarn properties. The images of the composite yarn are shown in Figure 2 where C have no wire, C1 and C2 have stainless steel wire, C3 and C4 have copper wire in their core.

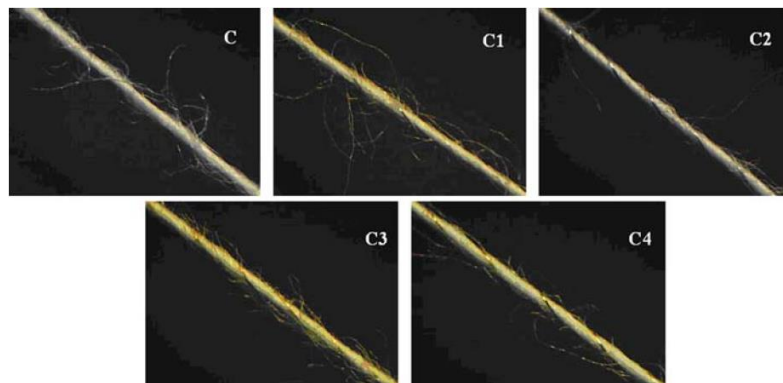


Figure 2. Images of composite metallic core cotton yarns

Rajendrakumar and Thilagavathi [22] also used core sheath yarn of copper cotton composite for electromagnetic shielding purpose. The composite yarn was produced on ring spinning frame. Same like, Liu and Wang [105] used stainless steel cotton blend with different linear densities to develop blended electromagnetic shielding fabric. In another study, Ortlek *et. al.* [106] manufactured a composite yarn made of stainless steel core with cotton as sheath. They used SIROCORE spun technique to produce the hybrid yarn for

electromagnetic shielding applications. The use of metal wire rigid the formed structure, therefore a future research can be made by formation of hybrid yarn with conductive polymer core may prove more useful.

Antistatic and antisoil properties were achieved by developing coaxial composite filament using polyester as core and polyester-polyethylene glycol block copolymer as sheath. The composite filaments which have lower heat of fusion for sheath than core are widely used for the development of randomly laid nonwoven webs. The web is heated to a temperature of softening point of sheath which is less than heat of fusion of core to adhere to the other fibres where they are crossed [27]. Core sheath structure was also reported using polyethylene as sheath and polyethylene terephthalate as core [97]. Bi-component core/sheath coaxial filament was developed using poly (butylene terephthalate)/poly (butylene succinate-co-L-lactate) polymer substrates [93]. The developed filament showed good adhesion between the core and sheath layer. These filaments were flexible as well as showed good tensile strength even after drawing of the filament. The filaments of diameter in the range of 50-70  $\mu\text{m}$  were obtained by changing the melt drawing ratio in range of 54:1 - 20:1 followed by cold drawing at 5:1 ratio. The filaments developed with poly (ethylene terephthalate) core with sheath of poly (butylene terephthalate) and poly (butylene succinate-co-L-lactate) were also reported [94]. The tensile strength obtained from the later filaments were higher than the former reported filament.

Green [107] described different method to construct an electrically conductive composite yarn which is durable and can be dyed and used in clothing. He employed different techniques for constructing these yarns by using conductive and non-conductive nylon fibres with cotton. He also proposed a core/sheath structure having conductive core by incorporating carbon black particles in the core with sheath of cotton fibres.

Alexis *et. al.* [87, 88] used different weight % of carbon nanotubes incorporated into polypropylene substrate to develop three layered structure. The developed coaxial structures include two conductive layers having insulating layer between to work as data transfer coaxial cable and single conductive core layer having external layer doped with thermos-chromic microcapsules for electro-thermic and colour-change properties. In another study, Lund and Hagstrom [108] fabricated a composite sheath/core fibre using melt spinning technique as shown in Figure 3. The developed fibre was used as sensor due to inner conductive core filament formation. The core of the fibre was produced using

electrically conductive carbon black in a polymer compound and sheath was produced using PVDF polymer. The outer electrode was developed using various ways. It was reported that the outer electrode can be developed using elastomer/carbon black film. The fibre was heat pressed between the two films of the compound, which develops conductive outer layer on the composite yarn structure [109]. The same coaxial composite filament construction was made by Benjamin *et. al.* [110], who used carbon nano tubes doped polypropylene as core material for piezoelectric applications. Hull [111] constructed an electrically conductive core/sheath filament with synthetic polymers. The core was doped with carbon black to increase the conductivity of the core. The core filament used had higher melting point than sheath polymer filament. Different core and sheath polymers were used to construct different yarn. Polyethylene core was used with sheath of polyester/polyamide and for Nylon 6 core, the sheath used was Nylon 6, 6.

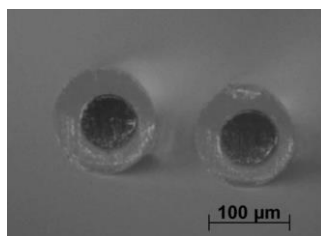


Figure 3. Cross sectional view of bicomponent fiber

A carbon nano tubes-carbon fibre hybrid was developed by Saba *et. al.* [79] from carbon fibres coated with carbon nano tubes in dispersion of polypyrrole layers. It was reported that the electrical conductivity of the carbon nano tube-carbon fibre hybrid has higher than the pristine carbon fibre. This biocompatible and conductive layer was deposited electrochemically on carbon fibre. Electrochemical process had the advantage to control the deposited layer thickness according to the requirement. It was reported that the thickness of the polypyrrole layer negatively influence the electrical conductivity of the treated fibre. The major role of polypyrrole deposition relates with the carbon nano tube dispersion and fixation. A new method was developed by Deng *et. al.* [53] for the production of high performance conductive composite polymer fibre in which bicomponent fibres/tapes comprising two layers of conductive polymer composites (CPCs) filled with carbon black or multiwall carbon nano tubes based on lower melting temperature polymer and an unfilled polymer as core having higher melting temperature were manufactured by melt base method. The morphological control of the conductive network formed by nano fillers were obtained by solid state drawing followed by

annealing process. The mechanical properties of the core were remained almost intact with only reduction in the resistivity of the tape during annealing. A very high draw ratio polymer tapes or fibre were achieved by this method having unique mechanical and electrical properties. The conductivity obtained from these polypropylene fibres were  $275 \text{ S m}^{-1}$  having tensile strength of around 500 MPa. These fibres have potential usage in smart textiles which include vapour, temperature and strain sensing; EMI shielding; electrodes for flexible solar cells and self-reinforced polymers. In another study, a coaxial composite filament with sheath of polyamide or polypropylene was used with a core of polypropylene doped with carbon black and polyethylene doped with carbon nanotubes [112].

Schwarz *et. al.* [113] developed polypyrrole-copper-gold coated para aramid yarn by electroless deposition method as intended application as electrode material (Figure 4). It was found that the mechanical properties of the polypyrrole-copper coated para-aramid yarn were not significantly decreased by gold coating. The coated yarn conductivity was found good which was retained conductive even after 25 washing cycles. A silver coated polyamide yarn in single as well as in plied structure was reported by Alagirusamy *et. al.* [114] for different electro-conductive applications. For electrical insulation of conductive yarn in presence of water, polypropylene fibres were coated by friction spun method followed by melting in hot oven for uniform and homogenized coating.

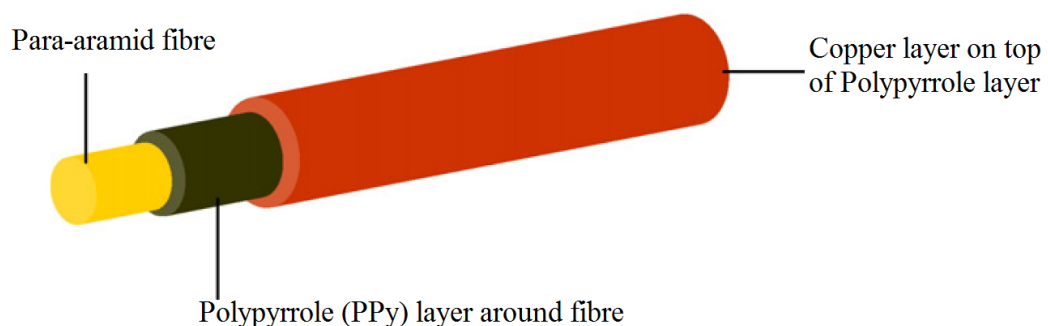


Figure 4. Schematic image of copper and polypyrrole coated para-aramid fiber

Sato *et. al.* [115] developed a composite sheath/core fibre having metal in the core with sheath of lead zirconate titrate (PZT). They used this fibre as sensor for the detection of resonance vibrations. The outer electrode was developed using carbon fibres in an epoxy resin. The developed fibres were embedded in the resin matrix to formulate external electrode and could be used as sensor.

A very particular type of core sheath fibre was manufactured using hollow fibre by injecting liquid metal inside the hollow fibre core composed of triblock copolymer, poly[styrene-*b*-(ethylene-co-butylene)-*b*-styrene] resin, after fibre production [46]. The liquid metal alloy used in core was eutectic gallium indium (EGaIn, 75% Ga, 25% In by weight) having a melting point of 15.7 °C. This low viscosity metal allows made it possible to overcome the shear forces by the application of pressure to easily inject inside the hollow core of the fibre. The reported results claimed the highest electrical conductivity obtained so far in composite fibres at a level of magnitude of 30. The limitation of this sort of composite fibre was displacement flow of metal at concentrated pressure or collapse of liquid core during application of stress which increases the overall resistance in the fibre.

A coaxial filament developed for bio scaffold application was developed using a specialized extrusion design [116]. The independent melt reservoirs pumped the polymer through the die to develop filaments of  $0.7 \pm 0.1$  mm diameter whilst maintaining the core/sheath structure. The core position offset was reduced by increasing the feed rate to achieve very good coaxial composite filament.

Kechiche *et. al.* [5] developed a coaxial composite fibre using poly (vinylidene fluoride-trifluoroethylene) and copper filament as shown in Figure 5. He characterized the developed composite fibre as well as analysed the mechanical properties. The developed fibre can be used as sensor and can be incorporated in textile material for online data acquisition. In this structure, the outer electrode of the sensor was developed using gold coating on the fibre surface while inner electrode function was performed by core copper filament. The sandwiched piezoelectric material (PVDF-TrFE) between the two electrodes generates a voltage difference between them on application of force.

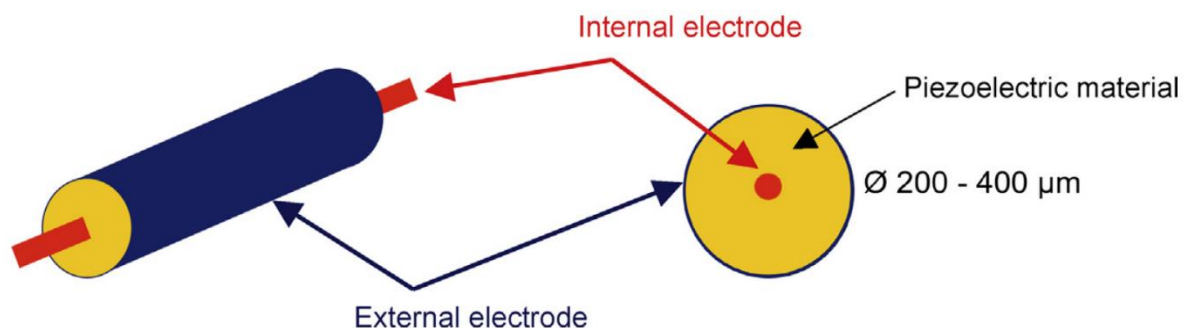


Figure 5. Cross sectional view of the composite fiber

In another study, Khoffi *et. al.* [82, 117, 118] developed a composite fibre having core of copper filament with sheath of polyester using melt spinning technique. They reported that mechanical and frictional properties of the composite filament were superior to pure polyester filament.

In recent work, three layered coaxial composite filament structure was reported using wet extrusion technique [7]. The developed filament has carbon nanotubes doped conductive polypropylene inner and outer layer to sandwich the poly (vinylidene fluoride) polymer layer. The filament is potentially used for piezoelectric strain sensor applications. The layer thickness obtained was non-uniform across the filament diameter.

## ***1 Materials used for coaxial composite fibre***

### ***1.1 Fibres***

#### ***1.1.1 Conventional fibres***

The conventional fibre used in literature for the development of coaxial composite filament is cotton [104].

#### ***1.1.2 High performance fibres***

The high performance fibre reported for fabrication of composite fibre includes para-aramid fibre (Kevlar) [113].

### ***1.2 Metals***

Different metals are used for the manufacturing of coaxial composite filament which includes copper [5], stainless steel [103] and metal alloys [46].

### ***1.3 Foreign particles***

The foreign nano particles used for fabrication of coaxial composite filaments includes copper [113], gold [5], silver [114], carbon nanotube [53], carbon black [107], carbon fibre [79] and lead zirconate titrate [115].

### ***1.4 Polymers***

#### ***1.4.1 Conventional polymers***

Polymer is a lightweight and the only material which can recover after wrinkling, stretching and bending, therefore it is widely used as base material for wearable technology [6]. The polymers used for fabrication of coaxial composite fibres includes



polypropylene [87, 88], polyamide [111], polyethylene terephthalate [14, 27], poly (butylene terephthalate) [94], polyester-polyethylene glycol block copolymer [27], poly (butylene terephthalate) [93], polypyrrole [79], epoxy [115] and poly[styrene-b-(ethylene-co-butylene)-b-styrene] [46]. The detailed explanation of polyester manufacturing and its properties is available in Annexure 1.

#### *1.4.2 Piezoelectric polymers*

The coaxial composite fibres developed with piezoelectric polymers includes polyvinylidene fluoride (PVDF) [108, 119] and poly (vinylidene fluoride-trifluoroethylene) [5]. The detailed literature for piezoelectric polymer properties is stated in Annexure 2.

### **2 Application areas of coaxial composite filament**

Coaxial composite filaments can be used to fabricate biomaterials [93], antistatic applications [14], antisoil applications [27], vapour sensor [53], strain sensor [5], vibration sensor [115], temperature sensor [53], electrodes for flexible solar cells [53], electromagnetic shielding [22], marine filament [94] and self-reinforced polymers [53]. These filaments also find its applications in technical textiles and handicraft items [120].

### **3 Manufacturing techniques of coaxial composite filament**

#### *3.1 Fibre spinning*

Coaxial composite filaments can be developed using conventional fibre spinning techniques including ring spinning [22], SIRO core spinning [106] and friction spinning [114].

#### *3.2 Extrusion*

##### *3.2.1 Wet extrusion*

In this method, the polymer need to be dissolved in some solvent before extruded in coagulation bath for solidification in required filament shape. The suitable solvents and coagulation liquids for wet spinning of particular polymer material can be found by examining their Hildebrand and Hansen solubility parameters, which represent their solubility in each other [13, 121]. When the values of these parameters are similar, the materials can be miscible. This extrusion technique has been used for the manufacturing of three layered coaxial composite filament using special spinneret type [7].

### 3.2.2 Melt extrusion

The polymer processing in which the polymer shape is modified just by the use of thermal energy is called as melt extrusion. A number of studies presented in literature were carried out using this technique for coaxial composite fibre development [108]. In this technique, the polymer is melted in a machine called spin line, where the temperature above to polymer melting temperature and extruded through the nozzle to develop the required shape and structure of the product. The systematic illustration of the melt extrusion process is shown in Figure 6 [27].

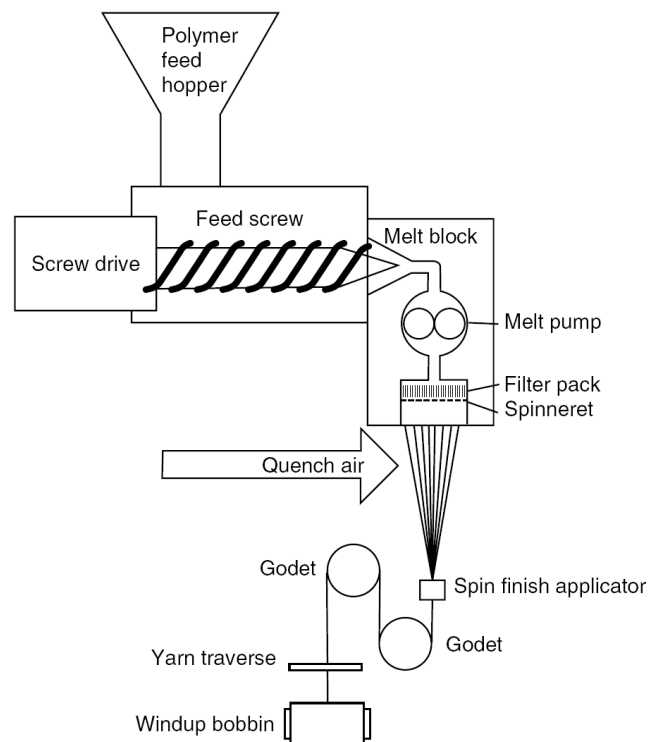


Figure 6. Systematic illustration of melt extrusion process

The polymer in form of dried chips are introduced in the feed hopper which transfer it to the temperature chamber where shear forces also applied. The processing temperature of feed stock is kept in range of 280-300 °C for polyester for uniform melting [27]. The shear stress applied during the feeding of molten polymer to the spinneret also increase the temperature as much as 10-15 °C of the molten polymer. The molten viscosity of the polymer lies in range of 200-2000 Pa.s depending upon the molecular weight of the polymer. A pressure of 10-20 MPa is required to force the polymer stream through the spinneret pack [122]. The polymer stream is fed to the spinneret pack through the metering pump to ensure uniform feeding of polymer. The spinneret pack is comprised of filters

and spinneret for clean polymer feeding and extrusion respectively. The spinneret may have one or hundreds of thousand holes for filament extrusion process. The typical diameter of the spinneret hole is in the range of 180-400  $\mu\text{m}$  in diameter.

The pack and spinneret designs are the subject of specialized expertise on which a number of patents and open literature is available. The complex rheological environment faced during the passage of polymer through the spinneret cause local increase in molecular orientation and distribution of molecular orientation between the spinneret wall and centre line. The polymer gets swell on exiting the spinneret due to the combined effect of relaxation of molecular orientation and surface tension, this is also called as die swell (increase in filament diameter on exiting the spinneret hole).

The molecular chains in the melt polymer are randomly oriented and characterized by their entanglement density, molecular weight distribution, average chain length between entanglement and molecular weight of polymer. The diagrammatic representation of molecular orientation is illustrated in Figure 7 [27]. The polymer chains start orienting themselves under the applied stress after the exit from the spinneret hole up till the first take up roller and converted from fluid network to highly interconnected solid state semi-crystalline morphology. The filament is wound and stored on winding unit attached at the end of spin line for further processing.



Figure 7. Diagrammatic representation of molecular chain arrangement in molten polymer

Melt spinning is considered advantageous over other spinning techniques because of scaling up to production, which is fast and economical process. In addition, the fibre produced by melt spinning exhibit high mechanical strength as compared to the fibre produced with other spinning techniques. The limitation of melt extrusion is regarding the processing of high volume packing fractions of doped polymer melts. These limits are different for different doping materials as well as also dependent upon the polymer matrix.

i                    Screw method

A spinning machine of two screw extruders was utilized for the manufacturing of bicomponent filaments [93, 94]. Each extruder was used for particular polymer. After melting the polymer pellets in each extruder, the melt polymers combined in the extrusion die for the manufacturing of coaxial composite filament. In another study, single screw method was employed to developed coaxial composite filament with doped sheath layer [14].

ii                    Piston method

In this method, polymer is pressurized by means of a piston to extrude through the extrusion die. The coaxial composite filaments developed through this method are available in literature [5, 82, 123].

3.3                 Drawing

3.3.1             *Hot drawing*

It is the drawing process which is carried out on the semi-molten phase of polymer just after extrusion from the spinneret. This process is very crucial with regard of polymer crystallization and chain orientation, and also influence on the physical and mechanical properties of the product. The detailed explanation is provided in Annexure 3.

3.3.2             *Cold drawing*

It is reported that the tenacity and modulus increased by increasing the draw ratio with lower extension at break for the filaments, and vice versa [27]. Irrespective of the orientation achieved in the hot drawn filament, the molecular chains are still arranged in irregular orientation which do not provide higher mechanical properties. Additional increase in molecular order is necessary to be carried out for achieving required properties in polymer filaments through a separate drawing process called as cold drawing. Keeping in view that the molecular weight is sufficient enough to prevent the premature chain breakage, the filaments are drawn with formation of “neck” which localizes the draw point where the crystallization and deformation occurs and can be easily distinguishable by the change in opacity of the filament due to its optical anisotropy.

The polymer chain crystallites and molecular entanglements consolidated the molecular arrangements during heat drawing which affects the mechanical properties of the filament. The crystallization and molecular orientation in the filament improved by drawing

process. The draw ratio is the ratio of filament feed velocity to draw roller haul-off speed which is in the range of 1.5 to 6. The optimal mechanical properties are achieved when the filament is drawn close to its maximum drawn ratio for the drawing to be effective.

The drawing was done previously by passing the filament around a metallic snubber pin which was heated at 10 °C above the glass transition temperature of the polymer to allow the polymer chains to move. This alone was considered insufficient as it also causes unacceptable degree of heat shrinkage. The later effect was controlled by passing the filament over the heated metal plate having temperature of 55-65 °C above the glass transition temperature for heat setting of the filament. With the increase in draw speeds, the previously developed system was unable to do the job hence new system was designed having separate feed and draw rollers. The heated rollers are allowed to have longer yarn contact times for efficient thermal transfer by wrapping of filament several time around the rollers. The load supporting molecular chains in the filament moves to crystalline from non-crystalline regions of fibre morphology during high speed spinning process [27].

#### ***IV Process design and development***

##### **A Extrusion dies**

The dies used for extrusion of liquid polymer to develop required shape and structure are called as extrusion dies. These dies can be used to develop filaments, sheets and profiles of different shapes and sizes. The only aspect under discussion in this book is for filament extrusion dies. All dies have some common attributes which can be generalized.

##### ***1 Die designs***

The co-extrusion spinneret designs are modified combination of conventional mono-extrusion die designs with circular and annular exit cross-sections joined with specialized combination methods. Therefore, the basic design concepts of both types of extrusion designs should keep under consideration for the development of co-extrusion die design.

##### ***1.1 Mono-extrusion dies***

The conventional die for filament manufacturing with circular cross-section is commonly called as spinnerets. These spinnerets are extensively used for the manufacturing of varied types of polymeric filaments with different diameters and shapes. Spinnerets are placed in horizontal position to draw the filaments in downward direction. The polymers having low

viscosity are facilitated with a gear pump installed between the extruder and spinneret to ensure uniform melt stream.

### 1.1.1 Dies with circular exit cross-section

Circular cross-sectional dies can be used for different applications including filaments and rods. The particular name of the die for filament manufacturing is spinneret. The spinnerets can be of circular shape with diameters and thickness ranging from 40 to 80 mm and 10 to 45 mm respectively containing 10 to 1000 individual holes. There are some rectangular spinneret shapes having dimensions from 60 mm × 60 mm to 150 mm × 450 mm, with plate thickness between 20-30 mm having up to 10,000 number of holes [124]. The individual number of holes can be arranged in circular or linear fashion in plate with distance between them range between 6 to 10 mm. The individual holes have inlet diameter, exit diameter, borehole cylinder length to exit diameter ratio ( $L/D$ ) and transition angle between 2-3 mm, 0.2-0.6 mm, 1-4 and 60-90 degrees respectively. On contrary, for other applications the  $L/D$  ratio of cylindrical part and opening angle are under 10 and between 30-90 degrees respectively as shown in Figure 8 [124]. It is reported that smaller transition angle produces better surfaced fibres. Studies suggested that good quality fibres can be produced from smooth surface boreholes with sharp outlet edge without burrs [124]. Triangular, Y shaped and T shaped cross-sectional geometries are also used in these dies. During production conditions, spinnerets encounter with severe conditions including temperature and pressure up to 300 °C and 30 MPa respectively with high mechanical stresses, which may cause strong corrosive attack. Therefore, all factors are required to be under consideration while selecting the material for spinneret manufacturing.

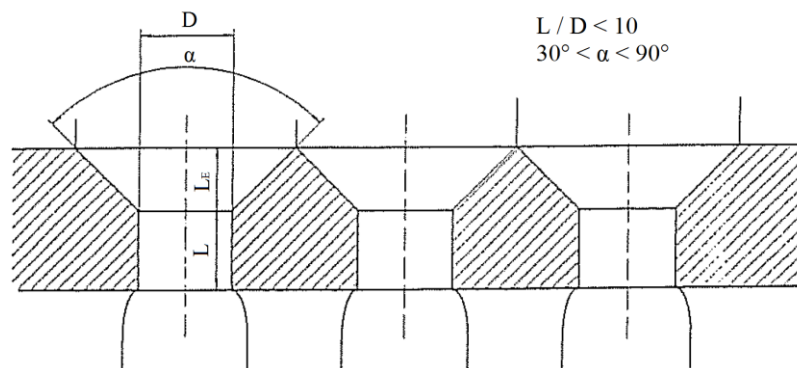


Figure 8. Geometrical design measurements of circular exit die

The basic performance requirements of spinneret design are:

- Low pressure loss
- Uniform

The extrusion of doped polymer with different particles was extruded through circular spinneret as reported in literature [6].

### 1.1.2 Dies with annular exit cross-section

These dies are designed to produce pipes, tubes and blow moulded products. These dies have parallel land zone at the exit point of the die to facilitate the melt to relax and reduce the deformation imposed by stresses during the process. The exit point is called as outer die ring and it can be separately temperature controlled for surface quality finish of the extrudate. These dies can be classified into different types which are as under:

#### i Centre fed mandrel support dies

The melt flow supplied through circular flow channel by the extruder is converted into annular flow by the mandrel in these dies. The spider legs further divide the annular stream into several melt streams in mandrel support zone. The melt streams are connected and converged together at angle of 10-15 degrees after flowing around the spider legs followed by die ring with parallel channel walls as shown in Figure 9 [124], where 1 is the mandrel tip, 2 is the mandrel support, 3 is the spider leg, 4 is the centring screw, 5 is the die ring and 6 is the relaxation zone. Outer die ring and mandrel housing are the essential parts of the die which are also exchangeable, therefore, a number of different extrudate geometries can be possible to produce through these dies.

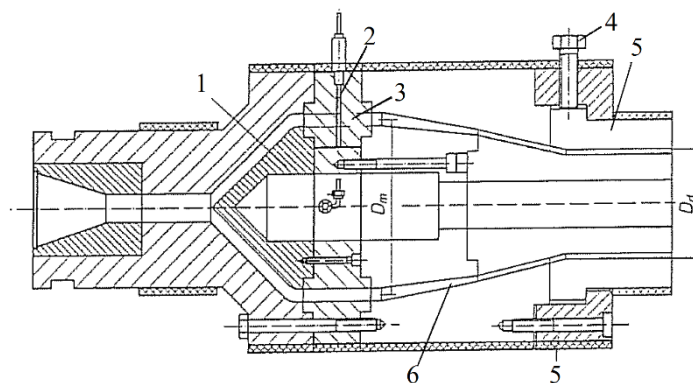


Figure 9. Schematic illustration of centre fed mandrel support die structure

These dies are most widely used due to uniform distribution of melt by centre-fed principle and melt distribution is also independent of operating conditioning. The main

disadvantage of these dies is that they produce weld lines generated by spider legs. These weld lines are not always visible as local thin sections but always present in structure and lead to mechanically weak sections. The high degree of melt orientation in region of spider legs is one of the reasons for flow marks. The high velocity gradient in vicinity of spider legs zone facilitates orientation when melt adheres to the channel walls and predominately due to the large extension of the melt particles near the spider legs. It is also reported in literature that temperature gradient of melt and spider, enhances the differences in melt density which also play role in orientation [124]. The flow marks can be reduced by increasing the temperature or resident time of melt in die, uniform melt distribution using smearing device along the circumference and orienting the molecules longitudinally over the entire circumference and also between the spider legs to produce uniform structure as shown in Annexure 4 [124]. The die designs in literature recommended the spider legs specifications for length, width and run out angle of not more than 30-80 mm, 9-12 mm and 8 degrees respectively. The recommended passage gap heights are 10-25 mm and square of diameter defines the approximate increase in number of spider legs. In addition, the roots of the spider legs should also be designed in a way to avoid stagnation of melt which ultimately cause material degradation.

## ii Screen pack dies

Melt polymer stream is fed axially from the extruder to this die where cone shaped mandrel diverted it to radial direction flow. The melt passes through a screen pack, which is a tubular body with numerous boreholes as shown in Figure 10 [124]. The material is directed to another mandrel attached with screen pack after passing through it. The melt is diverted into axial flow after passing screen pack and flows through the parallel die land with an exchangeable die ring, similar as in centre fed mandrel support dies. The area of the screen pack is large to avoid pressure losses through it. The advantage obtained from this die is that it is compact as compared to centre fed mandrel support die, therefore it is considerably light in weight and much easier to handle. These dies are particularly used for extrusion of large diameter pipes.



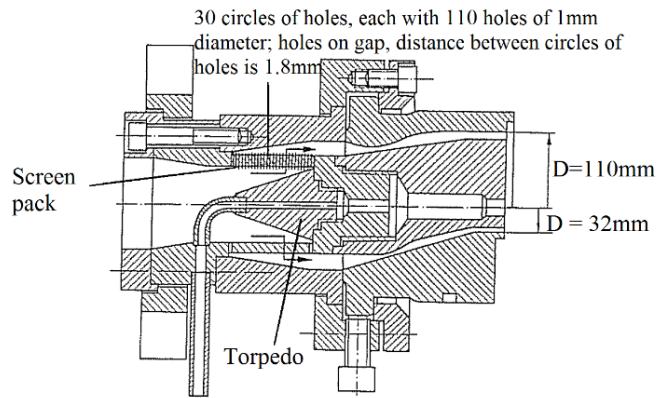


Figure 10. Schematic design illustration of screen pack die

iii Side fed mandrel dies

The melt stream is usually fed at an angle of 90 degrees to the die. This die is particularly used when something need to pass through the mandrel to be jacketed, for example cooling air or semi-finished product. The melt stream passed around the mandrel by way of manifold which is mounted on the outer body of the die and/or the mandrel as shown in Figure 11 [124]. The manifold helps to divert the radial directional flow to axial flow direction.

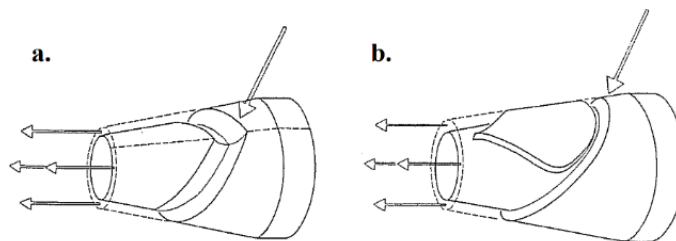


Figure 11. Mandrel of side fed die with, (a. coathanger manifold, b. heart shape manifold)

The problem faced in these dies are regarding the designing of manifold where the material is required to exit uniformly around the entire circumference through the annular opening. Melt lines are also observed in these dies, which are reduced by using heart shape manifold which separate melt streams and guided them on flow paths around half of mandrel followed by joining them again at their maximum pathway length. The characteristic difference between side fed and mandrel support dies is that the melt flows around the torpedo and not over it as the case of mandrel support die.

In these dies the melt stream supplied by the extruder is primarily distributed in several various streams by using a star shaped or ring shaped distributor systems as shown in Figure 12 [124]. Ring shaped distribution system is preferable where large centre boreholes are required in mandrels. These melt streams are discharged in spiralling flow channels which are machined in the mandrel in helical shape as multiple threads. The depth of the channel decreases gradually with increasing gap between the mandrel and the die housing in the extrusion direction. In such way, the stream flowing through one spiral is assumed to be divided itself into two partial streams. One stream flows in the grooved flow channel in helical direction while the other flows axially over the land formed between two spirals. The final flow stream is in axial flow direction at exit of die. This final stream is formed by the superposition of both partial streams from all of the spiral channels. In such arrangement, no weld lines are developed along with uniform melt temperature and required mechanical homogeneity are also achieved. The greatest advantage of these dies are the elimination of flow marks and weld lines in extrudate obtained from them.

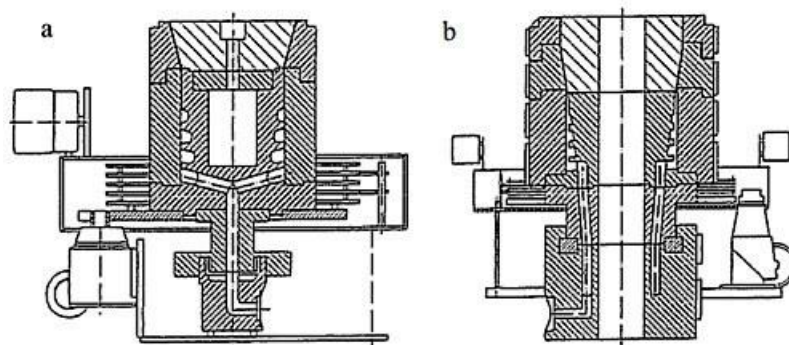


Figure 12. Spiral extrusion dies, (a. star shaped melt distribution with radial bore holes, b. ring shaped melt distribution with axial boreholes)

### 1.2 Co-extrusion dies

These dies are designed to extrude two different materials through same die structure. These dies have different designs based upon individual stream configurations up to extrusion point which are, completely separate, first separate then together, or together.

### 1.2.1 Externally combining dies

In this die design, the melt polymers flow through fully separate channels and combined after emerging from orifice. These dies are frequently made with two die slits because more slits make the manufacturing and design more complicated. The melt layers are combined by a pressure roller which is particularly used when a third layer is need to be attached or at high speed extrusion process, as shown in Figure 13 [125]. The air encapsulation between the layers may cause defects in the product during adhesion process. The flow rate of both streams can be controlled separately. The thermal insulation between the flow channels can be done by air gap as shown (1) in Figure 13, pressure roller is shown as (2). This formation allows the processing of different materials at different temperatures.

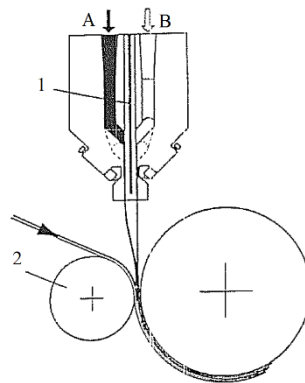


Figure 13. Flat-slit dual-slot co-extrusion die

The disadvantage of these dies are that the two orifices must be adjusted, the minimum difference should be maintained in the neck-in of both layers, adhesion problem caused by rapid cooling of thin layer and organoleptic problem is produced due to the generation of fumes between the layers.

### 1.2.2 Adaptor dies

These die designs are produced by using the conventional extrusion dies with inclusion of an adaptor which allow the individual melt streams to flow through the conventional die inlet. The melt streams flow together through the conventional die and leave it as multi-layer co-extrudate. This design is also called as feed block dies.

A number of individual layers can be combined through this procedure. The disadvantage is that the polymer melts should have almost identical flow and processing temperatures.

This system is most adaptable because of less change in the extrusion process setup which make it widely acceptable. The adaptors are classified in two different types, based on:

i Feed control mechanism

- Fixed adaptor

The individual layer thickness in extrudate depends upon the mass flow rate of melt polymer and the cross-section of the flow channels. The individual melt streams should have almost the same melt velocities when meet in the die.

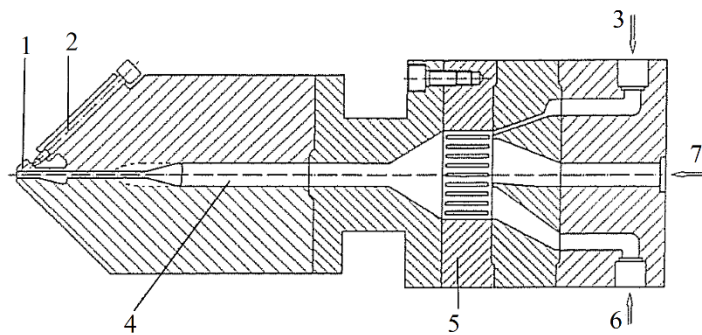


Figure 14. Fixed adaptor feed block die for flat sheets extrusion

This design is also called as Dow design as shown in Figure 14, where (1) is the flex lip, (2) is the flow controller, (3) is the top layer material inlet, (4) is the melt channel with flow restrictor, (5) is the adaptor, (6) and (7) are the base layer and main layer material inlet respectively [125].

- Slide adaptor

It is also called as Reifenhäuser system in which the flow velocity is controlled by a slide for individual streams to meet at equal velocity. This slide also serves as choker bar to regulate the flow distribution across the dimensions. The design is made in profile or in sections of the side of the melt. These slides are inserted and removed from the side as a cassette without having any connection between die and extruder as shown in Figure 15 [125].

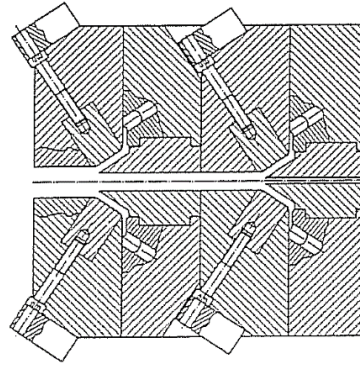


Figure 15. Flat slit feed block die with sliding adaptor

- Vane adaptor

It is also called as Cloren system which differs from the Reifenhäuser system in the element which controls the process of the joining of the streams are in shape of vanes. These vanes can be turned to control individual stream separately. The vanes also have profiles to control the flow distribution. This system is shown in Figure 16, where (1) is the flex lip, (2) is the pressure screw, (3) is the cover layer material inlet, (4) is the inlet for other materials, (5) inlet for main layer material, (6) is the vane adaptor, (7) is the inlet for base layer material, (8) is the vane adaptor for base and cover materials and (9) is the flow restriction zone [125].

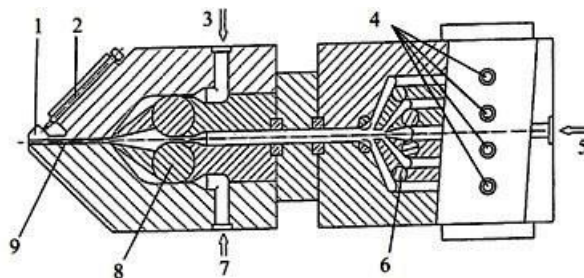


Figure 16. Flat slit feed block die with vane adaptor

ii Layer configuration mechanism

These adaptors are connected in series and joined to obtain the required number of layer configuration.

- Outer layer adaptor

This type of adaptor is used to apply a new layer onto other layers from outside. It is shown in Figure 17 (a) for flat slit die with three-layer configuration.

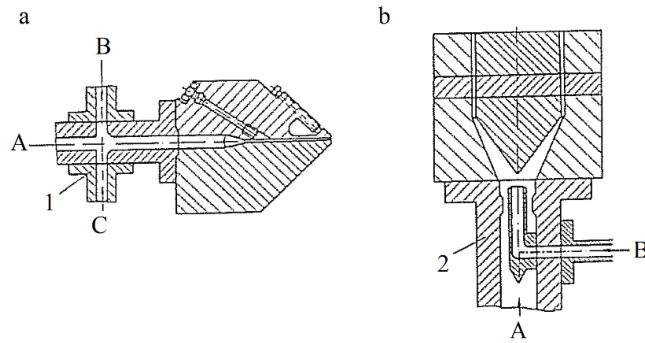


Figure 17. Feed block dies with, (1) outside layer adaptor and (2) inside layer adaptor

A single step coaxial composite filament having three layers was developed using specially designed melt extrusion die with screw mechanism [87, 88]. The design of the die was not reported in literature. The process comprised of three different melt extruders with screw mechanism joined with three cross-head modules. Each module was responsible for development of each layer of coaxial composite filament as shown in Figure 18 [88]. The extruder ‘A’ was for the core layer, extruder ‘B’ was used for intermediate layer, extruder ‘C’ was used for the sheath layer, ‘D’ was the cross-head module for the intermediate layer, ‘E’ was the cross-head module for the sheath layer and the arrow indicates the exit point of the spinneret. The developed coaxial filaments were not uniform in layer thickness at radial positions as shown in Figure 19 [88], where  $\lambda$  is the stretching ratio.



Figure 18. Melt extrusion used for the development of three layered coaxial composite filament

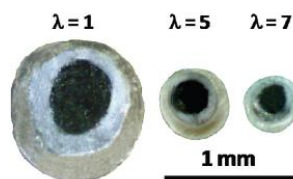


Figure 19. Cross-sectional view of three layered coaxial composite filament

- Inner layer adaptor

In this type, one melt is extruded into the other. This type of adaptor is used for extruding very thin central layer imbedded between thick layers. It is also employed where the internal layer should have minimum contact with the walls. This adaptor type for blown film made with two layers having mandrel support is shown in Figure 17 (b).

A composite fibre was developed by filling hollow fibre with liquid metal alloy paste [46]. The hollow fibre was fabricated on lab scale Fuji Filter melt extrusion machine with screw mechanism for polymer feeding at 230 °C and 400 psi through extrusion die. The extrusion die consists of circular slit divided into three equal regions. The slits were 3 mm deep and sections were separated by 0.2 mm. The triangular shaped hollow fibre was manufactured after quenching the melt extrudate in the water bath at room temperature by collection roller.

- Revolving adaptor

This type of adaptor is used to manufacture variable arrangement of layers in extrudate products. The sequence of the layers is changed by the rotation of the adaptor as shown in Figure 20 [125]. Installation of exchangeable feed block is another method to manufacture such products. The extruder is stopped during the change in arrangement of layers and hence one or more layers are eliminated. Check valves are required to install to prevent the return flow of melt into the idle extruder during change.

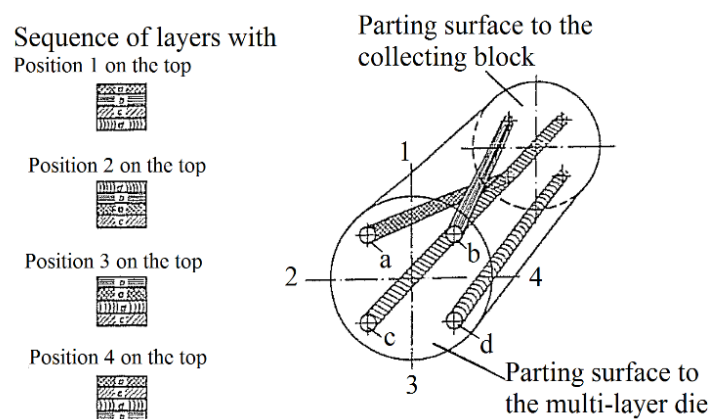


Figure 20. Revolving adaptor for changing order of layers

### 1.2.3 Multi-manifold dies

In this die design, the melt streams are fed and distributed individually into desired form followed by combined just before the die exit as shown in Figure 21 (a. flat slit die for two



layers, b. blown film die for two layers with spiral distributor). The streams are controlled individually with feed controllers. The overall gauge of the co-extrudate is controlled with adjustment of the die orifice or lip. Mutual adhesion also improves by combining the melt streams under pressure inside the die.

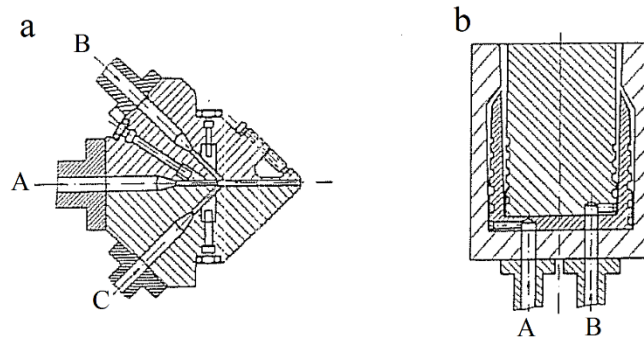


Figure 21. Multi-manifold dies for co-extrusion

Materials with enormous different melt temperatures and flow behaviours can be processed in these dies. The disadvantage of these dies are the complex design and thermal insulation of individual channels. Combination of more than four layers die design become very complex and costly to manufacture.

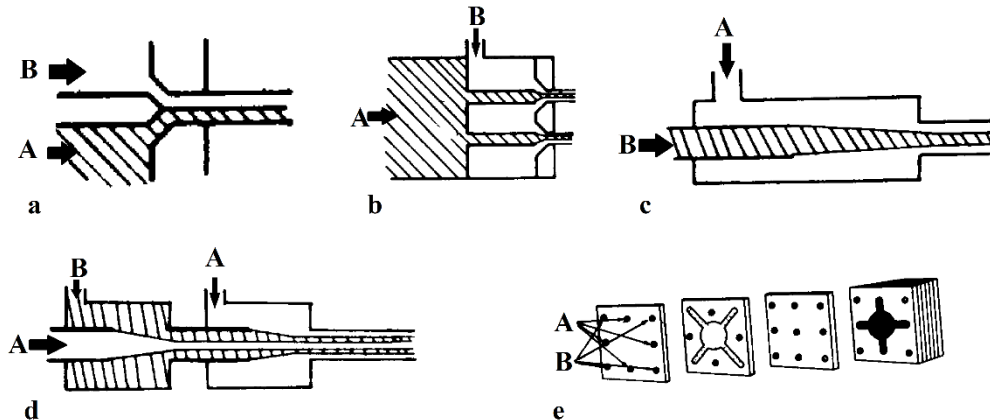


Figure 22. Schematic illustration of co-extrusion spinning die designs (a. side-side design, b. coaxial design, c. hollow fibre design, d. multi-layered design, e. circular stream plate mixer design)

A number of co-extrusion designs were reported in literature for the manufacturing of different shaped composite structures as shown in Figure 22 [126]. These designs can be used for almost all shapes of the composite filament production. These designs are more or less modified to form current extrusion designs used in industry after optimization for



bulk production. These designs only use melt streams for composite structure development.

A spinneret design used to manufacture coaxial composite filament using screw based melt extruders was reported by El-Salmawy *et. al.* [93, 94]. The core of the filament was extruded through a nozzle having diameter of 0.5 mm while the sheath was developed by the nozzle of 1.0 mm diameter. The schematic illustration of the used extrusion die is shown in Figure 23 [93, 94]. A sheath core composite filament was developed by Cho *et. al.* using extrusion die shown in Figure 24 [97].

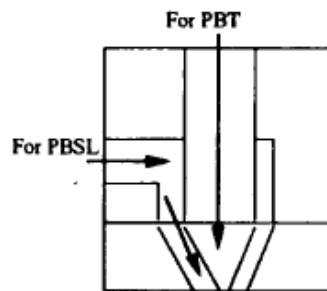


Figure 23. Schematic illustration of extrusion die for monofilament coaxial spinning process

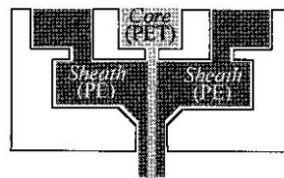


Figure 24. Schematic illustration of core sheath spinneret die

In another study, a conjugate spinning process was used to manufacture core sheath composite structure using screw based melt extrusion process [14]. The die geometry was not discussed properly, but as per understanding, the die was almost the same like as shown in Figure 23.

Cornock *et. al.* [116] developed a co-extrusion die for melt extrusion of poly (caprolactone) polymer. The die is able to develop coaxial filaments of very fine diameters. The die was fabricated using laser melting system using stainless steel power. The schematic illustration of the die is shown in Figure 25.

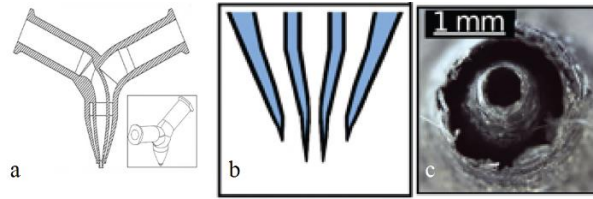


Figure 25. Schematic illustration of extrusion die, (a. section and isometric die design, b. coaxial die exit shape, c. die exit diameter with electro-polishing effect)

## 2 *Design methods*

### 2.1 Traditional method

The extrusion dies were traditionally designed by experts which rely completely on their expertise and involved extensive trials and die modifications. In general, about 10 or more trials were needed to attain the desired results. During the trials and die modifications, the production line remains stopped which cause production as well as monetary losses. The cost of material, die design and modification are also counted in the total loss during the whole process. It is estimated that about 1000 new dies are designed each year in Europe [127], with the final cost for each die reaches about 15,000-20,000 Euros [128].

### 2.2 Computer added method

The time consumed during the designing of new die along with reduction of trials are achieved by using simulation based die design method. In this method, computer simulation is used to investigate the flow behaviour through the die in virtual extrusion trials. These trials play as first design which replaces the physical extrusion trails, while the interpretation and changes made in the die design solely based on designer's expertise. The optimization of die design is done by enclosing the simulation in an optimization shell which automatically optimize the design measurements based on the mathematical definition of optimization problem to achieve required performance characteristics. The mathematical equations for sensitivity analysis are also introduced in the finite element model for optimized design [129]. This whole designing and optimization process not only reduce the total design cost but also helpful in time estimation to the market. The final refine tuning of the optimized design still based on the experimental process and rely solely on the expertise of the developer. The design which can perform well under perturbed conditions is called as robust design, and non-robust designs have limited practical usage.

### 3 Construction types of extrusion die designs

#### 3.1 Plate dies

The simplest type of extrusion die is the plate die. These dies can be developed by single or multiple plates joined together. The multiple plate die is called as stepped die in which plates are placed behind the first and may be bevelled to smooth the flow transitions. An abrupt contraction of  $90^\circ$  is observed before plate die which cause stagnant zones or corner vortices for the material to degrade [128]. To obtain correct dimensions of the extrudate, the mass flowrate should be ensured uniform from all regions of the die. To facilitate the mass flow rate in narrow regions, lead-in chamfer is machined at the back side of the plate to enhance the flowrate leading to required dimensions at face of the extrusion die. This approach is called as face relief strategy which was successfully designed for tyre sidewall die [130]. This construction type was used by Martins *et. al.* [7] to design a co-extrusion die for wet extrusion mechanism. A configuration of seven plates were used to construct the die. A number of seven plates were used to develop the complete spinneret design as shown in Figure 26.

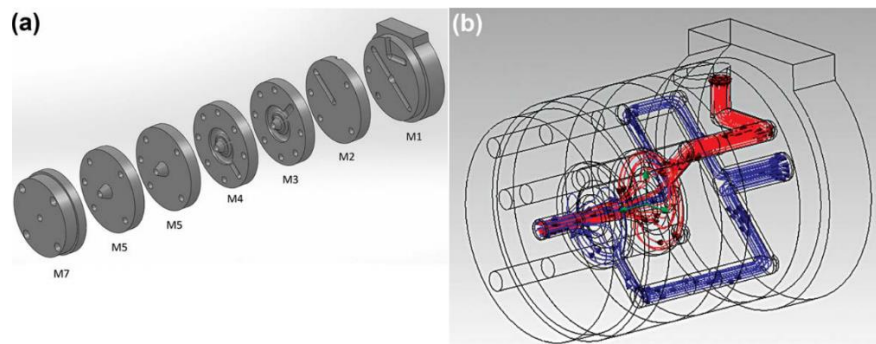


Figure 26. Schematic representation of co-extrusion die, (a. exploded view, b. material streamlines view)

#### 3.2 Streamlined dies

The complex designs including internal segments or hollow chambers in the extrudate are developed with streamlined dies. These dies can be successfully used for high scale production processes and usually have four basic regions including die inlet, pre-forming, adapter and parallel zone as shown in Figure 27 [131], where  $2H$  is one of the land gap and  $L$  is the land length. The extrudate shape and structure is refined smoothly in different regions between the die inlet and exit. These dies are constructed with stack of plates

arranged on pins. More details of the extrudate shape are introduced in successive plates starting from extruder outlet.

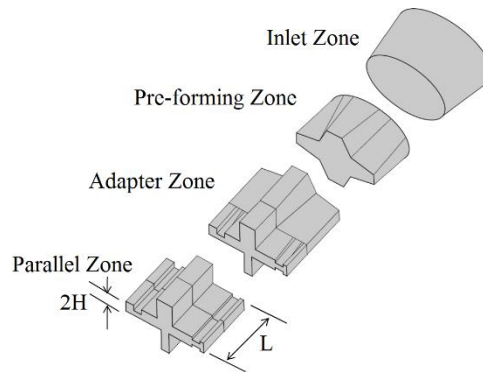


Figure 27. Schematic illustration of die cavity regions in streamline die

Mandrels are supported on streamlined spider arms to introduce internal chambers in the extrudate. Air is blown through the mandrel to provide an internal pressure to avoid the collapse of extrudate walls for hollow shaped extrusion process. The final exit has parallel land zone which helps to reduce the stresses, caused during extensional deformations in converging flow, in the die to relax and to provide a better controlled mass flow at the exit.

Uniform flowrate is the basic key parameter for the designing of every die. The regions with varied thickness in extrudate flow geometry may have different flow velocities. To reduce this effect, different flow adjustment tools are used at particular wide channels to keep constant the flow distribution across the whole extrudate. The wire electric discharge machining (wEDM) is used to develop flow channel geometry which is characterized by contours on contiguous faces of die plates [128]. A skewed surface geometry in the plate is obtained by developing different contours on both sides of the plate which changes the channel cross-sections. The contours are joined together by ruled surfaces to finally develop the 3D flow channel geometry in extrusion die.

#### **4 Types of die construction methods**

##### **4.1 Core-plate technique**

This construction technique uses the wire electrical discharge machining (wEDM) method to develop both inner and outer cavities in the plate. Each plate has a number of cavities separated by spider arms to define the structure of the extrudate. The spider arms or flow separators are introduced to support the inner parts. The advantage of wEDM cutting

method is that it provides high precision in flow channel dimensions but large amount of required machining is potential disadvantage of this type of technique.

#### 4.2 Torpedo technique

A torpedo (mandrel) that extends over a number of plates and provides inner voids in the extrude geometry is employed in this technique. The outer boundary of the channel is still machined with wEDM, but only a single cavity is required to develop on each plate which reduces the amount of machining by wEDM method. The torpedo is suspended between the plates by spider arms which is mounted with one of the plate. The torpedo is usually mounted in the middle of the die. A balance is made between mounting the torpedo close to the exit, which improves precision of land channel gaps, and allowing sufficient gap downstream of the spider arms, to avoid weld lines in the extrudate, when the torpedo extends over the land.

A combined construction is also possible in which both plate and torpedo techniques are used. In this design the torpedo provides the inner voids at the extruder outlet. The plates installed ahead of the torpedo furnishes the final geometry of the extrudate. A schematic illustration of this type of design is shown in Figure 28 [128].

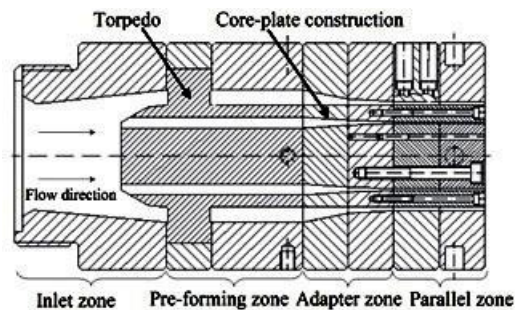


Figure 28. Schematic illustration of combined plate-torpedo construction of extrusion die

## 5 *Phenomenon affecting die designs*

### 5.1 Rheology and kinematics of flow

The normal flow properties are described by first and second normal stress coefficients and non-Newtonian viscosity when the shear flow is in steady state [132]. This condition applies when constant shear rate is experienced by the material element of fluid long enough for the transient stresses to die out, and is approximated in a long channel in which the geometry is constant or change very slowly along the direction of flow, and also the temperature field changes very slowly. The kinematics is derived from Newtonian flow

model with viscosity depended upon shear rate when compressibility is neglected [128]. The generalized Newtonian model is commonly used for non-isothermal and not strictly shearing flows. A number of models are available with increasing number of parameters which are able to include shear thinning effects, limiting high shear rate viscosity and low shear rate Newtonian region [128]. The shear viscosity ( $\mu$ ) can be calculated by using Power law which is based on two parameters model as given in Equation 1.

$$\mu = \mu_0 \dot{\gamma}^{n-1} \quad (1)$$

Where  $\mu_0$  is the consistency coefficient dependent upon rate of deformation tensor (and temperature, when applicable), and  $\dot{\gamma}$  is the shear rate and  $n$  is the Power Law index. Generalized Newtonian model do not explain the differences between normal stresses, which play their role in extrudate swell after die exit. Furthermore, generalized Newtonian model is used when flow simulation within die is the primary concern. This model need less computation demand for flow simulation as compared with viscoelastic constitutive models. The flow modelling can be simplified as a result of high melt viscosity, while neglecting the effects of gravity and inertia.

The generalized modelling does not explain the pressure drop in converging flow caused because of extension thickening and melt elasticity. These effects cause reduction of flowrate in narrow channels in die. Viscoelastic computational modelling can estimate these effects; however, the viscoelastic properties are determined by fitting the shear properties, hence the extensional behaviour may not be accurately modelled [133]. Extensional viscosity, function of local instantaneous viscosity, is introduced for estimation at first instant. In steady shear extension rate, the polymer melt may or may not exhibit constant extensional viscosity. In converging dies, this property will not achieve and hence engineering extensional viscosity is used under the same approximated conditions of the die flow. The method of incorporating extensional viscosity in flow simulations are proposed and their effect on converging flow are demonstrated in literature [134, 135].

## 5.2 Wall slip

Fluids have the tendency to adhere to the channel walls. It was observed that the highly entangled polymers have apparent slip with channel walls [136, 137]. In consideration of sparse of data and generally non-significant effects, it is usually ignored in die flow

modelling of these materials. Additives are added in the polymers to promote wall slip which is essential for extrusion process of some materials. The wall slip is considered to be caused by adhesion of low viscosity thin lubricating layer to the wall which promote apparent slip of the polymeric materials. According to this concept, slip should be the function of viscosity and thickness of the lubricating layer rather than dependent upon local pressure. A relation between slip velocity of the bulk material ( $v_w$ ) to wall shear stress ( $\tau_w$ ) is associated in non-linear Navier Law as given in Equation 2 [128].

$$\tau_w = C v_w^m \quad (2)$$

Where C and m are coefficient and index in Navier slip law respectively. As C decreases, the slip effect increases, and when C increases and approaches to infinity the no-slip condition prevails. It was found that slip mechanisms vary according to the height of the asperities on the die surface. The value of C for smooth die ( $R_a$  0.6  $\mu\text{m}$ ) at 200 °C was found as  $1.3 \times 10^6 \text{ Pa(s/m)}^m$  and m as 0.5 [128]. Apart from the conventional procedures, capillary rheometer can be used to determine wall slip and shear thinning viscosity, by extracting the parameters from solution of system of non-linear equations, which is briefly explained in literature to reduce the number of experiments [128].

### 5.3 Extrusion instabilities

Extrusion velocity have significant influence on the surface morphology of the extrudate. Surface defects are produced on extrudate for some materials at higher flowrates resultantly leading to gross distortions [138, 139]. The first type of extrusion instability to appear is known as sharkskin. It is the development of regular periodic ridges on the surface of the extrudate. It is usually observed for highly entangled linear polymers. It is reported that this instability originates due to rapid tensile deformation that occurs at die lip when fluid adjacent to wall accelerates in free surface after exiting the die. It is reported that when the tensile stresses reach a critical level, the material in a region just upstream of the lip detaches from the wall to relieve applied stresses, followed by re-attaching of the material in self-oscillating method. The possible reason explained in literature is the time scale for deformation which is shorter than required for entangled polymer chains to slip over one another [128]. The material act as forced rubbery state in which flow is impossible and it deform as an elastic solid or fracture.

A substantial experimental evidences are reported in literature relating occurrence of small scale surface defects to shear stresses at wall of the die [128]. The critical values correspond to most of the polymer melts, in region of 0.1-0.3 MPa, having Weissenberg number in the range of 3-10 [138]. Weissenberg number is defined as the product of shear rate and material relaxation time, which explains the importance of elastic effects.

The enhancement of wall slip phenomenon, either by introduction of lubricants in the melt or by surface treatment of the die, has been proven to prevent the sharkskin instability by reducing the influence of singularity at die lip. By increasing the material flowrate, the sharkskin instability increases due to large scale deformations caused by periodic stick-slip in the die.

Another large scale instability known as melt fracture may occur due to rapid extensional deformation which convert the material into forced rubbery state at regions of converging flow in the die. The rate of deformation at which this may occur can be estimated from the frequency in oscillatory rheometry, where constant value of storage modulus is obtained. In this instability, the surface of the extrudate becomes rough and non-uniform as shown in Figure 29 [124]. It is caused predominantly by partial loss of the wall adhesion in the flow channel. Another type of extrusion instability is known as corkscrew extrudate which is caused by unstable flow in inlet region. It can be reduced by introducing conical inlet zone and long cylindrical land region in the flow channel. The introduction of flow instabilities depends upon rate of deformation causing limitation in the productivity of the equipment. It also depends upon the material being processed and the level of instability caused in inlet and/or outlet zone. A uniform volume flow through all the holes can be achieved by such a geometrical arrangement in which all holes have equal flow path from the melt entrance to each hole [124]. It is also reported in literature that uniformity of the individual streams can be improved by higher pressure loss of individual holes.

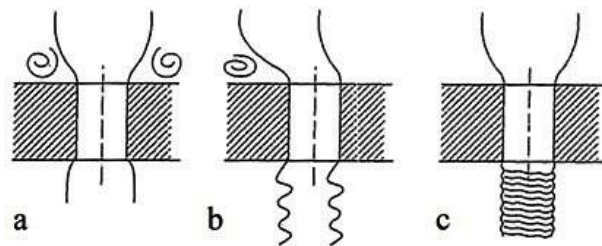


Figure 29. Flow through circular cross-section, (a. stable flow; b. unstable inlet zone; c. melt fracture)



There are some other extrusion instabilities, other than typical for single layer which are explained above, in multilayer flow such as encapsulation and interfacial instability. Both of these phenomena have their separate cause, mechanism and consequences. In a study, two melt streams having equal melt flow rate were allowed to flow through a round capillary side by side [140]. The co-extrusion results were analysed by determining the location of the interface on cross-sectional plane of two-layer strand. It was observed that the polymer having low melt viscosity always tries to encapsulate the other polymer having relatively higher melt viscosity. It was observed that if the relative viscosity reverses between them during the progress of apparent shear rate, the tendency to encapsulate can also reverse keeping the same rule after the crossing of their viscosity curve as shown in Figure 30 [125]. This encapsulation phenomenon is the result of flow behaviour of materials. It occurs in accordance with principle of minimizing of energy. The self-arrangement of both melts themselves suggest to keep the pressure loss of the flow at minimum. To achieve this, the melt having relatively less viscosity flow in contact with the channel wall and resultantly forms a slip film to facilitate the flow of relatively higher viscosity material in the middle of flow channel.

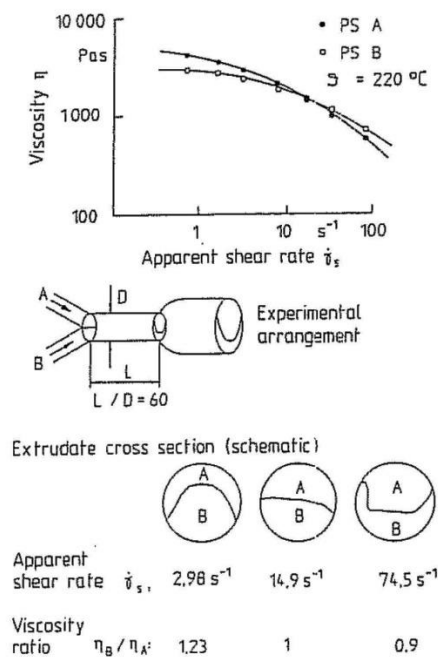


Figure 30. Rearrangement of interface in melt co-extrusion of polystyrene

In another study using two different grades of polyethylene polymer [140], it was observed that the interface formed between them was very rough and irregular in nature as shown in Figure 31 [125]. This sort of instability is not directly related to encapsulation. This sort

of interfacial instability was also observed in co-extrusion of films as shown in Figure 32 [141]. This interfacial instability has following characteristics:

- Interfacial instability may occur in thin middle layers as well as thin outer layers depending on the combination of materials
- The instability in interface vary in amplitude and frequency
- Interfacial instabilities occur even in identical material co-extrusion
- These disturbances occur directly after merging zone, and also remain after a longer, parallel stable flow

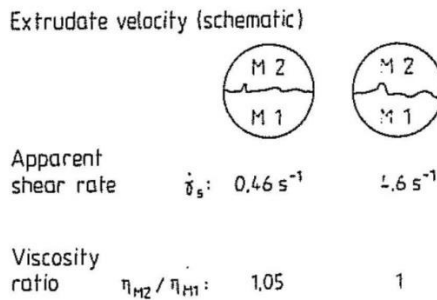
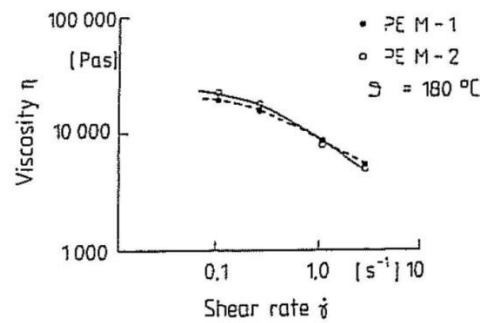


Figure 31. Rearrangement of interface in co-extrusion of two different grades of PE

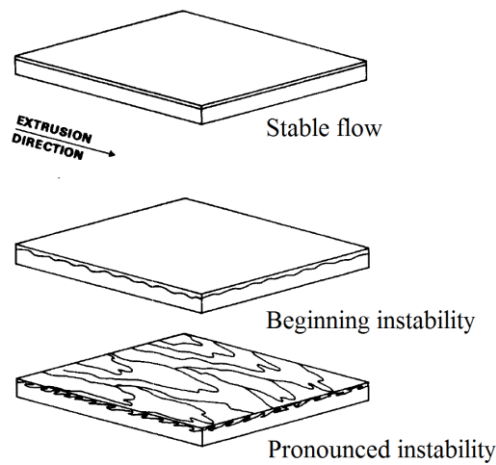


Figure 32. Instability build-up in interface of coextruded films

A model for explaining the interfacial instabilities must have to explain all the above stated characteristics. Two models were reported in literature for the explanation of interfacial instabilities with different approaches.

In another study based on mathematical stability analysis of multilayer flow, it was found that viscosity ratio has significant effect on the delineation in the region of interface between stable and unstable flows [142]. A number of experiments had verified this model. The approach based on considering viscosity ratio as criteria responsible for instability in boundary layer cannot explain the interfacial instabilities produced in co-extrusion of identical materials.

The alternate approach to model the interfacial instability is based on forces of flow acting on interface. It is considered that the interface is the weak spot in the bond between two adjacent melts. The molecular arrangement of polymer melts at interface in co-extrusion is shown in Figure 33 [125]. During the extrusion, the polymer macromolecular chains adhere to the flow channel walls due to macro-roughness on the walls (Stokean condition for adhesion), which make them align parallel to the flow direction as shown in Figure 33 (I). The macromolecular chains in the middle remain disoriented and entangled. When both polymeric melts joined together (Figure 33 (II)), the oriented chains make the interface between them which remain preserved over the duration of orientation relaxation. According to the statistical studies on segmental motions [143], longer time is required to develop entanglements. The last region (III) shows the entangled region across the boundary dimensions after completely disappearing of the oriented chains in the interface region. This region is not obtained during the usual resident times in die.

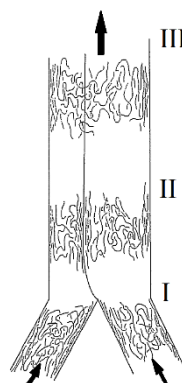


Figure 33. Schematic illustration of model for explanation of adhesion at interface

The interface has oriented chains which can slide past each other more easily because of weak spot in interface than individual layers in the material. Experimental studies also

confirmed this hypothesis, and it also explains the interfacial instabilities observed during the co-extrusion of identical materials. It was also reported that the flow marks observed for flow around the spider arms in mandrel support die represent the same effect to co-extrusion of identical materials [125]. The interface links are instable weak spots which explains the theory of failure of the material at interface links when stresses are applied. The shear stress is applied on the interface in one dimensional flow. It is deduced from it that a critical shear stress in the interface can be calculated for each combination of material, beyond which an instability in the interface appears. Shear stress in the interface is evaluated only when the instabilities are present in one dimensional flow region. Critical shear stress depends on the surface forces of melts acting along the interface. The critical shear stresses found in one dimensional flow cannot transfer to two dimensional flow because of the fact that normal stresses also acting on the interface, along with shear stress, which result from elongational flows. It was reported that divergent flow channels have strong destabilizing effect while convergent flow channels have stabilizing effect on the flow [125, 141].

#### 5.4 Material degradation and residence time

Material degradation is avoided by reducing the residence time and high temperatures in the die. Stagnant zones and recirculating vortices developed because of sharp contractions in flow channels are unacceptable and should be avoided. Abrupt contractions in flow are present behind the plate in simple plate dies, where problems are avoided only by particular flow properties of the material. The residence time field ( $t_{res}$ ) can be obtained through integration of its convected derivative on velocity field ( $v$ ) obtained in post processing operation from flow simulation as shown in Equation 3 [144].

$$\frac{Dt_{res}}{Dt} = \frac{\partial t_{res}}{\partial t} + v \cdot \nabla t_{res} = 1 \quad (3)$$

Where  $t_{res}$  approaches to infinity at recirculating and stagnant regions of the die, same like for the material adhere to the walls unless wall slip is present. Resident time spectrum is obtained in the absence of such regions from the residence time distribution over the exit cross-section of the die. The material change over is faster during the extrusion, when narrow resident time spectrum is observed.

A more detailed study of the degradation is possible using the kinetics of the process. The material degradation measure  $\theta$  is a function of temperature and exposure time in the

extrusion process. The degradation map can be obtained by integrating the convective derivative.

### 5.5 Extrusion swell

It is the increase in thickness or diameter of the extrudate that occur soon after exiting the die. The ratio of equilibrium free surface jet diameter to capillary diameter is called as swell ratio. The extrudate swell is caused by rearrangement of the velocity profile in an isothermal Newtonian liquid at die exit. The swell ratio obtained for isothermal Newtonian liquid at low Reynolds number as it leaves circular die is approximately 1.13 [128]. Elastic materials have high swell ratio due to elastic recoil, values up to 4 are also observed for highly elastic materials. This effect changes the cross-section of the extrudate from that of the die exit. It is also reported as well-known example that for obtaining square cross-sectional extrudate, a star shaped cross-sectional die exit is used [124]. The relation between capillary diameter and swell ratio is given in Equation 4 [128].

$$\frac{D_{swell}}{D} = \left( 1 + \frac{1}{2} \left( \frac{N_1}{2\tau_w} \right)^2 \right)^{\frac{1}{6}} \quad (4)$$

Where  $D$  is the capillary diameter,  $D_{swell}$  is the equilibrium diameter of the cylindrical extrudate after unconstrained swelling,  $N_1$  is the first normal stress difference,  $\tau$  is shear stress and  $w$  is the symbol of capillary wall. The ratio of first normal stress difference to twice of shear stress is calculated at capillary wall. The swelling of low Reynolds number Newtonian fluids may be adjusted by adding value of 0.13. Swell, shear rate dependent viscosity and wall shear stress can be measured from capillary rheometry. The first normal stress difference is not easy to measure, therefore, semi-empirical relationships with viscosity were proposed in literature [128].

It is found that swell increases by increasing extrusion rate. It is also reported that swell decreases by increase in the parallel land length, as stresses are able to relax in the upstream region caused due to extensional deformation. In addition, the swell also found decreasing by decrease in the convergence angle of upstream flow. Swell may also increase by annealing the extrudate. Swelling can be controlled by rapid cooling or curing the extrudate, so that extent of swelling will depend upon the rate of these applied processes. It is also reported in literature that draw down ratio and temperature variation within the melt can influence the swelling, high draw down ratio decreases the

swelling [145]. In simulation study, it was found that swelling at higher Weissenberg number (equal to 1.2) significantly increases by viscous heat generation [128]. The product of characteristic shear rate with relaxation time is defined as Weissenberg number, where shear flow varies from recoverable shear only by a constant factor dependent upon the definition of the characteristics shear rate [128]. The inclusion of carbon black and lubricating oil significantly reduces the swell.

#### 5.6 Draw down

The process in which extrusion velocity is less than haul-off or conveyor belt speed causing extension of extrudate, resulting in reduction of thickness of the extrudate is called as draw down. It occurs downstream after die exit. It is reported that by the variation of velocities across the die exit will cause differential draw-down of material across the extrudate wall thickness. Tensile stresses are produced during draw-down process which may be frozen in the extrudate and later on became the reason of distortion of the product as stresses recoil as a result of unequal draw-down. The development and design of the die is optimal which can provide uniform exit velocities across the whole die exit. The applied tensile stress at the die exit cause negative pressure, resultantly increases the flowrate from die. As the outer periphery of the extrudate is constrained by rapid cooling restrict the chain movement, the internal partitions in the cross-sectional plane set up to bear the tensile stresses. These frozen stresses result in distortion of the shapes having unequal balance across cross-sectional plane [128].

#### 5.7 Thermal effects

At low Reynolds numbers in dies rapid kinematic development is achieved, which suppresses the thermal development by increasing the Graetz number value. It is reported that single point temperature measurement does not represent the actual temperature of melt because of the fact that temperature of the melt polymer entering from extruder is seldom uniform. It is reported in a study that the temperature differences may reach at about 25 °C with in the melt. It was also observed that the viscous energy dissipation also causes non-uniformity of temperature in the melt within the die. The melt layer along the flow channel walls have also non-uniform temperature and not equal to the temperature of the die. The change in temperature cause change in viscosity, which could be deliberately used to manage the flow velocities within narrow channels in the die [128].

The variation in temperature across the extrudate may cause bending or distortion of the shape after cooling.

## 6 *Strategies and approaches for die design*

### 6.1 *Flow balancing*

The basic aspect of the internal design of the die is to deliver the correct mass flowrate to all parts of the extrudate at the die exit so that the required cross-sectional shape and dimensions of the extrudate can be obtained in finished product. In flow balancing, all the points around the cross-sectional plane at the exit of the die have the flow rate equal to the product of haul-off velocity and required extrudate thickness at corresponding position in finished product (with the adjustment of change in density of the product on cooling). The flowrates can be measured by dividing the extrudate shape in number of segments at cross-sectional plane of the flow at obvious features. The introduction of these separator lines onto the die exit divide the extrudate in different segments followed by the measurement of flowrates at each particular position [146]. The change in flow velocities at different regions of die can change the shape of the extrude profile. Evenly distributed polymeric melt along the flow channel made it possible for uniform velocity of melt at die exit. The evaluation of the die exit section can be done by dividing it in different zones and their objective function is evaluated. The objective function is the representation of flow balance based on difference in flow velocities in different zones. The objective function used is given in Equation 5 [146].

$$\varphi = \frac{\sum_{i=1}^n (v_i - v_{ave})^2}{n(n-1)v_{ave}^2} \quad (5)$$

Where  $n$ ,  $v_i$  and  $v_{ave}$  are the number of divisions, average velocity of  $i$ th zone and total average velocity of profile respectively. The experimental average velocity of each zone can be calculated using Equation 6.

$$v_i = \frac{m_i}{\rho \cdot A_i \cdot t} \quad (6)$$

Where  $A_i$ ,  $\rho$ ,  $t$  and  $m_i$  are area of  $i$ th zone, melt density, extrusion time and average mass of sample during extrusion obtained respectively. The melt density was calculated by Archimedes method. Flow balancing in a die design can be achieved by keeping some considerations in mind. The excessive difference in flowrate at different segments over

the cross-section of the extrudate develop waviness in the extrudate product. It is recommended that the pressure drop should be minimized through the die which reduces the energy consumption and also promotes to enhance the temperature by viscous energy dissipation. Degradation can be avoided by limiting residence time, avoiding excessive temperature and excluding dead zones. The temperature of the flow channels should be controlled to maintain at uniform temperature. The die design should be constrained to avoid extension rates or wall shear stress exceeding critical values and flow instabilities must also be avoided.

### 6.2 Land dimension for streamline dies

Land dimensions are one of the important parameters for obtaining flow balancing in streamline dies. The adjustment of dimensions in parallel lands also influence the pressure drop through the die and local flowrates. Analytical results for developed flow in wide slit is applied when the length of the lands is at least several folds the gap-wise dimension, while assuming the flow as iso-thermal flow. The volumetric flowrate per unit width (Q) can be measured using Equation 7 through a wide slit of gap height 2H [128].

$$Q = \left( \frac{-dP}{dz} \right)^{\frac{1}{m}} \frac{2}{C^{\frac{1}{m}}} H^{\frac{m+1}{m}} + \left( \frac{-dP}{dz} \right)^{\frac{1}{n}} \frac{2n}{2n+1} \frac{1}{\mu_0^{\frac{1}{n}}} H^{\frac{2n+1}{n}} \quad (7)$$

Where C, P, m, n, z and  $\mu_0$  are coefficient in Navier slip law, pressure, index in Navier slip law, index in Power Law, extrusion direction coordinate and consistency coefficient in Power law respectively. The above equation can be used to identify issues in die designs, approximate design methods and optimize the die design.

### 6.3 Avoid-cross-flow strategy

Avoid cross flow strategy is the extension of gap adjustment technique back along the die into the adaptor and pre-forming zone of streamline dies. This strategy creates partitions in the melt flow in the upstream of the die and mapped onto the cross-section at die exit. The adaptor and pre-forming zones carries less details of the extrudate cross-sectional structure, leading to merging of partitions in some die designs. Partitions are the boundaries of stream tubes which are responsible for correct flow to all parts of die exit. Cross-flow defines the flow component in the plane of cross-section. The percentage of total flow required to pass through each partition is adjusted according to the actual cross-



sectional area percentage of each partition of finished extrudate, hence cross-flow is avoided between the partitions. The section observed uniform pressure in absence of cross-flow which is an essential feature of developed flow.

#### 6.4 Flow separators

The physical barriers which divide the flow in the dies to avoid cross-flow and end just before the exit of the die to allow the stream to merge are called as flow separators. These flow separators develop flow channel to feed a certain length of land. It may also introduce the possibility of weld line defects in the extrudate for which the land length should be enough to avoid this defect, but should not be long enough for cross-flow to develop which would spoil the effect of feeder channels in controlling flow distribution. Flow separators are used in different type of dies including streamline dies. The previously defined flowrate pressure drop relationship is extended to include the wall slip and given in Equation 8 [128].

$$Q_{total} = \frac{1}{C^{\frac{1}{m}}} \left( \frac{-dP}{dz} \right)^{\frac{1}{m}} \frac{a_c^{\frac{m+1}{m}}}{p_c^{\frac{1}{m}}} + \frac{1}{\mu_0^{\frac{1}{n}}} \left( \frac{-dP}{dz} \right)^{\frac{1}{n}} \frac{32n}{3n+1} \frac{a_c^{\frac{2n+1}{n}}}{p_c^{\frac{n+1}{n}}} \frac{1}{\lambda} \quad (8)$$

Where  $a_c$  is the cross-sectional area of the channel,  $Q_{total}$  is the total volumetric flowrate through the channel,  $p_c$  is the perimeter and  $\lambda$  is the shape factor which was tabulated for different shapes [147]; for cylindrical channel its value is 16. Dies with flow separators can be designed by adjusting the length of separate flow channels or by adjusting the cross-section of the flow channels with equal length.

#### 6.5 Neutralization of extrudate swell

In direct extrusion problem, the die geometry is specified through which the free surface is specified by the simulation to define the final geometry of the extrudate after swell. A number of adjustments and simulations are needed to be done to obtain the required design of the die. The problem can be solved by inverse extrusion analysis, in which the extrudate after swell geometry is specified and the solution provide the final geometry of the die [128]. The cross-section of the inlet surface of the die is fixed, transition to the die exit is achieved by specified rules, so that by changing the exit, the transition region of the die adapted automatically. The applied stress field and developed velocity can be defined

using 2D solutions. The cross-section of the extrudate is defined by the co-ordinates of boundary nodes on number of planes perpendicular to extrusion direction.

## **7        *General die design rules***

The basic principles required to be considered for designing of industrial extrusion dies are summarized and listed as under [148]:

1. The die should compose of minimum number of parts, which are easy to clean and accurately adjusted in required assembly relative to each other. It should also be considered that the die should be manufactured with close fits.
2. The number of joints should always be kept as minimum as possible. The joints are possible leakage points due to inadequate sealing, and also became the potential zones for material degradation in flow channel.
3. The sealing surfaces should be as flat and small as possible to bear the uniform distribution of sealing forces over the entire sealing surface.
4. Soft and temperature resistant materials can be used as gaskets for sealing purposes, for example aluminium or PTFE.
5. The die should have few large bolts rather than many small bolts to hold the die parts together.
6. A quick connect seal or hinged flange should be provided for the die.
7. The dimensions of the die body should be adequate, to bear the forces applied on it during extrusion process, for keeping deformations within justifiable limits. The machining of boreholes and channels weakens the die body which should be taken into consideration.
8. In a condition that the die parts have different temperatures, will also thermally expand in different dimensions, which should also be taken into consideration.

The configuration of the flow channels in the die should be established under these basic rules [148]:

1. Polymer melt should be centrally fed to the die.
2. Melt stagnation should be avoided by avoiding dead spots or corners, and sharp and sudden transitions in cross-sections and flow directions.
3. Materials have more resident time in zones with large cross-sections and low flow velocity, which may lead to material degradation for thermally sensitive materials. Principle of minimum flow channel volume should be followed for such materials.

4. Flow channels should be designed in such a way to avoid and reduce flow lines and weld lines in the extrudate product.
5. Parallel die land should be provided depending on material processed and produced semi-finished product so that reversible deformations can decay at the end of flow channel.
6. The surface roughness of the flow channel should be less than 0.2  $\mu\text{m}$ . It can be controlled by chrome plating, polishing or even honed. The surface roughness reduces the material tendency to adhere to the flow channel walls and promote better flow through it which ultimately reduces the residence time in the die and also facilitates die cleaning. Polyamides and polyesters exert high tension on cooling onto the die wall which may detach chromium layer. Corrosion resistant steel is a good option to be used in such extrusion dies. Flow channels are polished and hardened only in such dies.

Selection of material for extrusion dies should be made under following requirements [148]:

1. It should be easy to machine.
2. It should be resistant to wear, temperature and pressure.
3. It should have required sufficient toughness and strength.
4. It should have sufficient surface hardness.
5. It can be easy to polish to obtain required surface roughness value.
6. It responds adequately to simple heat treatment.
7. It should have minimum thermal expansion and distortion.
8. It should be resistant to chemical attack.
9. It can be polished in various surface treatments.
10. It should have good thermal conductivity.
11. It should be stress free.

These requirements are not possibly achievable completely in a single material. Therefore, a compromise need to be taken based on the material processed, conditions observed during the process and the key requirements considered for particular extrusion setup.

## **B Process modification**

It is related to the modification in the process design to introduce some material or to obtain some particular properties in the extrudate. These modifications include introduction of some metal or cooling and heat treatment processes.

## ***V Characterization of polymer***

### **A Thermal characterization of polymer**

#### ***1 Diffraction scanning calorimetry analysis***

The presence of aromatic benzyl group substituted at 1, 4 (para) positions significantly affect the thermal properties of the polyester by inducing stiffness in the polymer repeating unit [149]. Relatively high thermal stability can be obtained by these substitutions in polyester. The chain scission or thermal degradation produced in polyester at elevated temperature without oxygen. Degradation is prominent above glass transition temperature and usually tested in range of 270-370 °C in order to simulate the processing conditions of polyester [149].

The amorphous polyester freezes like a clear, glassy solid. The molecular chains have van der Waal forces between them which overcome by thermal energy followed by induction of bond rotation and molecular vibrations. Amorphous polymer is not stable structure in a state of molecular alignment and considered as metastable structure. It tries to align the molecular chains to more perfect crystalline structure or completely amorphous structure. Free energy is liberated in any case and structure become more stable in form. The molecular chains align themselves at low temperature and converted into more regular microstructure pack in a repetitive structure with orientation and become crystalline. This characteristic temperature is called as glass transition temperature ( $T_g$ ). At higher temperatures, the chains movement becomes easier which allow plastic deformation in the polymer. The binding forces in crystalline region are stronger and need more energy to break down, this characteristic temperature is called as melting temperature ( $T_m$ ). The melting temperature depends upon the size of crystallites which make this phase transition not sharp in real polymers. Small crystallites melt easily than large ones. The standard melting heat for polyester is 32.5 cal/g [150].

In an attempt to analyse the thermal properties of composite filament manufactured with core/sheath structure of poly (butylene terephthalate)/poly (butylene succinate-co-L-

lactate) polymer, a heating rate of 10 °C/minute under nitrogen atmosphere was used [93]. It was reported that the crystallization in Poly (butylene terephthalate) core experienced more crystal orientation as compared with poly (butylene succinate-co-L-lactate) polymer sheath which was explained on the basis that Poly (butylene terephthalate) core solidifies at higher temperature which interrupts the elongation of sheath polymer during melt drawing. They reported that crystallization increased by increase in melt draw ratio during extrusion process. In another report, it was confirmed that the crystallization of polyester core remarkably enhanced during drawing under the same conditions as compared to single polyester filament [94], particularly after thermal annealing process. This increase in crystallinity and crystal orientation in the core structure is responsible for the increase in mechanical properties of the coaxial composite filaments, while sheath polymer retains an amorphous state. The driving force for this improvement in crystallinity is the interfacial shear which arose between the two layers [94]. This effect increases the crystal orientation in the core filament while suppressing it in the sheath layer at the same time.

## **B Rheological characterization of polymer**

The degree of polymerization is the number of repeating units in a molecular chain of polymer. It is achieved according to the desired properties required in polymer including filament strength and molten viscosity. In general, approximately 100 repeating units per molecule is required for textile grade polyester polymer which extends the chain length up to 100 nm (repeat distance 1.075 nm along major axis [122]) constituting the molecular weight of about 20,000 [21]. Higher strength will be achieved by obtaining higher molecular weight polymer which also become more vulnerable to chain break down by moisture during melting. The molecular weight of the polymer can be measured by determining the dilute viscosity in appropriate solvent or by molten viscosity through a specified orifice. Polymer molecular weight in above stated method is calculated using intrinsic viscosity ( $\eta$ ) of the polymer using Mark-Houwink equation. The most common method to measure intrinsic viscosity of polyester is by using o-chlorophenol (OCP) as solvent which provide intrinsic viscosity value of 0.62 for textile grade. Different solvents provide different values, therefore the method employed for the measurement need to be mentioned. Mark-Houwink equation can be employed to measure molecular weight of the polymer using intrinsic viscosity as [21]:

$$\eta_{OCP} = k (M_n)^\alpha \quad (9)$$

Where  $M_n$  is molecular weight,  $k$  and  $\alpha$  are constants for a given polymer solvent temperature system. These constants are determined by evaluating a plot of  $\log [\eta]$  versus  $\log [M_n]$ . When the value of  $\alpha \geq 0.8$ , it represents semi-flexible polymers. For polyester polymer using OCP method values of  $k$  and  $\alpha$  are  $1.7 \times 10^{-4}$  and 0.83 respectively [21]. The relationship between low shear melt viscosity of polyester and intrinsic viscosity (OCP) is stated in Equation 10 [21].

$$\eta_0 = 0.0129 (\eta_{OCP})^{5.35} \exp\left(\frac{6800}{T}\right) \quad (10)$$

Where  $\eta_0$  is the Newtonian melt viscosity (Pa.s) and  $T$  is the temperature (K).

### **1 Melt flow rate analysis**

It is the estimation of polymer flow through a standard orifice under specified pressure at provided temperature in 10 minutes. The polymer viscosity varies with temperature; therefore, temperature should need to be considered as per standard test procedure.

### **2 Shear rate analysis**

#### **2.1 Constant shear rate**

It is the study of observed change in viscosity of the polymer under constant shear rate at different temperatures. It explains the temperature effect on the apparent change in the viscosity parameter.

#### **2.2 Variable shear rate**

It explains the study of change in viscosity of the polymer under different shear stress at constant temperature. It is studied to consider the effects observed during polymer processing at various stages.

## **VI Morphological characterization of coaxial composite filament**

### **A Cross-sectional cutting technique**

The cross-sectional cutting of the coaxial composite filament was done by different means including binding or no binding of fibre before cutting. The fibre binding is usually done in some resin such as epoxy or methyl methacrylate to secure the fibre peripheral structure followed by cutting with standard razor [7] or ultra-microtome [151]. Polishing is done after cutting the resin to clarify the image followed by metal coating in case of non-

conductive material analysis. As an alternative method, the fibre is immersed in water at room temperature followed by immersion in liquid nitrogen and breaking [93, 94]. The cross-sectional shape obtained in the later is not sharp and smooth.

## **B Surface morphology**

The surface morphological analysis of fibre is mostly done with scanning electron microscopy. This technique provides high resolution images of fibre rough surfaces which high depth of field [152]. SEM is capable to provide high resolution images from fibre network to fibre surface at near molecular level. SEM technique was compared with other techniques such as polarised light microscopy in some studies keeping the same specimen for both of them. It was found that SEM is especially useful for studying compression failures and kinks in fibres [152]. In fibre composite studies, SEM can identify inorganic phases in composites by using atomic number contrast which is the characteristic of backscattered electrons [152].

The morphology of the filament is characterized by the orientation of spatial distribution of non-crystalline regions and the net orientation, size, shape and amount of crystalline units. All these units are interconnected by molecular chains which traverse to more than one region and is responsible for load bearing element in the filament structure [27].

The coaxial composite filaments were melt drawn at higher ratios followed by analysed for surface morphology [93, 94]. It was observed that mutual diffusion of the polymer layers was limited during the extrusion process irrespective of their tight adhesion in interface of poly (butylene terephthalate)/poly (butylene succinate-co-L-lactate) core/sheath filament. On contrary, poly (ethylene terephthalate) as core with poly (butylene terephthalate) or poly (butylene succinate-co-L-lactate) polymer sheath exhibit stronger and tight adhesion between the layers. There was no clear distinction between the layers at cross-sectional analysis of the filament. The reason reported for it is that the ester-interchange reaction probably occurs between the polymer layers during melt extrusion which developed a copolymer between them. This copolymer not only reduces the interfacial distinction between the layers but also have profound impact on enhancing the mechanical and physical properties of the core filament.

Another method used for analysing surface morphology is Atomic Force Microscope (AFM). In this analysis, very small area of specimen is under observation and molecular level images are obtained to determine surface roughness and crystal orientation.

## VII Mechanical characterization of coaxial composite filament

### A Tensile test

The mechanical analysis of the textile material is done by stress-strain behaviour. The influence of drawing ratio and polymer structure are significant factors for the mechanical behaviour of the material. The filament which are drawn at high levels attain more chain orientation and hence achieve more strength and modulus, while the filament which are drawn at low levels have less orientation with little stiffness and more dye penetration. The stress-strain curves for polyester filaments manufactured from same spun process with different drawn ratio are presented in **Error! Reference source not found.** [21]. The stress and elongation are presented in terms of initial fibre area in the curve. The circles represent the true stress values which the fibre have at breaking stress with correction of decreased area after extension in tensile test. It was observed that at higher elongation values, the breaking stress increases significantly. Furthermore, the extension also decreases by increase in draw ratio.

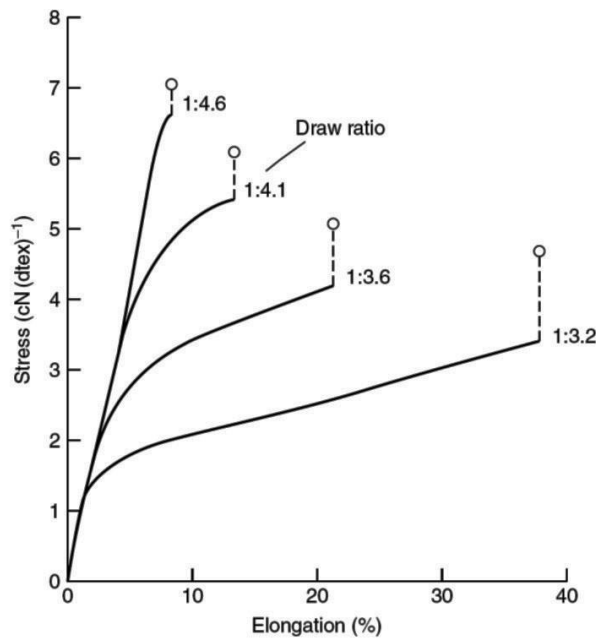


Figure 34. Stress-strain curve for PET fibre at different draw ratios

An inverse relationship is found between tenacity and elongation at break as shown in Equation 11.

$$t = \frac{K}{e_b^\alpha} \quad (11)$$



Where  $\alpha$  and  $K$  are constants,  $t$  is engineering tenacity. According to literature,  $\alpha$  has value of approximately 0.3, and  $K$  is the inherent fibre strength and depends upon molecular weight of the polymer [21].

The tensile strength and modulus of the composite filament significantly increased by increase in melt draw ratio of coaxial composite filament [93]. This increase in the properties is attributed to the increase in crystallinity as well as crystal orientation in the structure. The influence of thermal annealing on the mechanical properties was also found positive in nature [94]. It was reported that the tensile strength and elastic limits of the composite coaxial filament increased from the individual strength of the polymer filament drawn under the same conditions [94], which indicated that the load was uniformly applied over the core of composite filament. The reason for this increase in the mechanical behaviour was probably because of reduction of stress concentration by the elastic nature of the sheath.

The skin-core structure formation is the term used for non-uniform cooling process of the filament. The filaments developed with high speed spinning have oriented chains at the surface than at the inner region of the filament which is caused due to non-uniform solidification. The oriented skin molecular chains supports spinning stress while the interior chains are disoriented and relaxed due to higher temperatures [122]. During mechanical stress, the skin is prone to more stress and breaks first, hence the filament rupture occurs before the inner molecular chains contribute much resistance. The overall tenacity and fibre strength is lost as a result.

The mechanical characterisation of hollow fibre with and without conductive liquid metal alloy was reported by Zhu *et. al.* [46]. The sheath was composed of ultra-stretchable triblock polymer resin and the core was filled with liquid metal having low viscosity. It was observed that the liquid metal had negligible effects on the mechanical properties of the composite fibre.

### ***VIII Tribology characterization***

It is tribology analysis of the specimen. The friction coefficient of the sample is calculated and wear profile is observed caused due to frictional effect.

## ***IX Piezoelectric sensors***

The piezoelectric sensor is developed by incorporating the piezoelectric matrix in between two electrodes. These both electrodes can be developed during the extrusion [7], or one during the extrusion followed by post-extrusion process [5].

Piezoelectric polymers may have more than one morphological form. The morphological form of polymer which have larger dipole moment in its polymer chain and which can be aligned to form a polar crystal can exhibit piezoelectricity [153]. Considering the PVDF polymer, there are three morphological forms existed in which only beta form has such a structure which have piezoelectric character. The PVDF-TrFE is more adaptable due to the reason that it can be crystallizes in its beta form spontaneously on extrusion [154, 155]. While PVDF requires different processes like stretching, rolling followed by polling of polymer for obtaining piezoelectric phenomenon [156].

## ***X Conclusion***

Coaxial composite filament is a particular type of composite filaments having core at central axial position surrounded by sheath. These filaments can be produced in different textile configurations with conductive or non-conductive nature. This work focuses on development of coaxial composite fibres for intended application as sensors, actuators and electrical signal transmission yarns. The principle requirement for being used as sensor in SMART material lies is excellent conductivity of core. Excellent sensitivity of sensor can only be achieved by using excellent conductive core. This excellent conductivity can only be achieved using pure metallic wire as core. Different configurations of coaxial composite filament reported in literature don't provide high electrical conductivity except usage of copper wire as core by Kechiche [5].

A number of spinneret types with different flow configurations are reported in literature. All these spinnerets used number of melt polymers to develop composite fibre. The spinneret used for introducing metallic filament in melt extrusion is only reported by Kechiche. The required spinneret should have low cost and easily workable and machine able as per requirements of industrial extrusion dies. The desired die design would be a mixed design developed with circular and annular exit cross-sectional dies. Different die design configurations and their design methods are reported in literature. These dies are constructed with different types including plate and streamlined dies using core-plate or

torpedo construction methods. A number of strategies and approaches used for die design are also discussed. The general die design rules used for designing of industrial extrusion dies are also discussed.

The polymer characterization techniques, morphological characterization methods for coaxial composite filaments, mechanical characterization methods of coaxial composite filaments are also explained which are reported in literature. In the end, piezoelectric sensors development and characterization methods are explained as potential application of this study.

## CHAPTER 3

### EXPERIMENTAL

#### *I Introduction*

This chapter introduces the materials required for machine modifications, manufacturing of new machine parts and constituent materials required for fabrication of coaxial composite materials. The equipment required in the whole study and methods used for machining, developing and characterization of composite filaments were also introduced. The polymer characterization methods were also reported.

#### *II Materials*

##### **A Conductive filament**

The selection of core was based on electrical conductivity value. The core with fillers proved not to be feasible for highly conductive core. The ultimate application of the desired fibre is to perform well in sensors and actuators for which electrical conductivity value has far most importance for highly sensitive applications. Metals proved to be excellent conductors, among which copper has highest electrical conductivity after silver. Silver is costly as well as have high risk of oxidation at required processing temperature. In consideration of all these factors in mind, copper monofilament produced by Goodfellow with 99.9 % purity having diameter of  $50\pm 5 \mu\text{m}$  was used as core filament for the development of composite filament structure. The technical data of the copper monofilament is shown in Table 1.

Table 1. Technical specifications of copper monofilament

<b>Attribute</b>	<b>Value</b>
Temper Form	As drawn
Diameter	$50\pm 5 \mu\text{m}$
Purity	99.9 %
Density at 20 °C	$8.96 \text{ g cm}^{-3}$
Melting point	1083 °C
Boiling point	2567 °C

Attribute	Value
Tensile strength	224 MPa
Thermal conductivity from 0 °C to 100 °C	401 W K <sup>-1</sup> m <sup>-1</sup>
Specific heat at 25 °C	385 J K <sup>-1</sup> Kg <sup>-1</sup>
Electrical Resistivity at 20 °C	1.69 μ Ohm cm

## B Spinneret material

Special Brass rod was used for the machining of extrusion die and piston lower end part. The main advantage of this metal to be considered for machining parts is because of its high mechanical properties, good resistance to wear under heavy loads and atmospheric agents. The chemical composition and mechanical characterization of the metal obtained from manufacturer are shown in Table 2 and Table 3.

Table 2. Chemical composition (%) of elements used to form brass

Standard	Cu	Zn	Al	Fe	Mn	Ni	Si	Sn	Pb	Others
EN12163	58/60	Rest	0.3/1.3	<0.5	105/2.5	2/3	<0.1	<0.5	0.2/0.8	<0.3

Table 3. Mechanical characterization of brass

Attribute	Value
Tensile Strength (MPa)	≥640
Conventional elastic limit at 0.2% (MPa)	≈400
Elongation (%)	≥5
Hardness (Brinell)	≈180

## C Tubing material

The tubing used for the passage of copper monofilament through the oven was made of stainless steel 316 grade obtained from Sigma Aldrich and ceramic obtained from Sceram Ceramics. The selection of stainless steel (S.S) material is based upon the facts that it is excellent resistant to environmental, chemical and corrosive impacts and good wear

resistance. While ceramics are very hard, excellent abrasion and corrosive resistant materials, particularly used for thermal applications.

The outer diameter of the S.S tube was 1.59 mm, while different inner diameters (178  $\mu\text{m}$ , 254  $\mu\text{m}$ , 508  $\mu\text{m}$  and 762  $\mu\text{m}$ ) were selected to analyse their influence on composite filament. The ceramic tube was primarily made of alumina oxide (99.7 %), having Inner and outer diameter of 0.8 mm and 1.5 mm respectively. The material specifications are given in Table 4.

Table 4. Specifications of stainless steel and ceramic tubes

Attribute	Stainless steel	Ceramic (Alumina)
Density ( $\text{g/cm}^3$ )	7.97	3.8
Compressive strength (MPa)	270	3200
Endurance limit (MPa)	285	300
Hardness (MPa)	739	20050
Poisson's ratio	0.27	0.30
Latent heat of fusion ( $\text{kJ/kg}$ )	280	1160
Maximum service temperature (K)	925	1850
Melting point ( $^{\circ}\text{C}$ )	1391	2050
Specific heat ( $\text{J/kg.K}$ )	510	825
Thermal conductivity ( $\text{W/m.K}$ )	15	12.1
Thermal expansion ( $10^{-6}/\text{K}$ )	16	8.6

## D Polymers

The polymer materials used for the study were polyethylene terephthalate (PET), Nylon 6,6, low and high molecular weight of polyvinylidene fluoride trifluoroethylene copolymers (PVDF-TrFE) in shape of pellets. PET is a cheap polymer having thermal characteristics near to ferroelectric copolymers. The selection of this polymer is based on the fact that the developed process could be easily useable for ferroelectric copolymer processing considering their extrusion temperature range in mind. In addition, it is a

conventional and easily available polymer which can be used for wide application areas in composite structures as well.

Polyvinylidene fluoride trifluoroethylene copolymer (PVDF-TrFE) produced by Piezotech having 70:30 ratio of monomers was used. PVDF-TrFE exhibit strong ferroelectric, piezoelectric and pyroelectric effects. The copolymer obtained after cooling from melt is in ferroelectric phase, which transformed to piezoelectric after application of high electric field for polarization. The appealing structural characteristic is that TrFE monomer compel the polymer into all-trans configuration which has a polar crystalline phase due to which mechanical stretching is eliminated for achieving polar phase. The degree of crystallinity is much higher for P(VDF-TrFE) than PVDF providing a good remanent polarization, much sharper hysteresis loop and lower coercive field. The maximum usage temperature is close to 100°C. In consideration of the fact that piezoelectric constant for the copolymer is not as much as that of homopolymer, the advantage obtained of P(VDF-TrFE) with higher usage temperature, enhanced crystallinity and process ability makes it encouraging for different applications. The characteristic data in shape of 100 µm thin film of this copolymer is give in Table 5. The properties of polyester and PVDF(TrFE) polymers are briefly provided in Annexure 1 & 2 respectively. The properties of Nylon 6,6 are given in Annexure 7.

Table 5. Characteristics data of 100 µm thin film of PVDF-TrFE copolymer

Attribute	Value
Piezoelectric properties	
d33 (pC/N)	-20 ± 10%
d31 (pC/N)	6 ± 10%
d32 (pC/N)	6 ± 10%
g33 (V m/N) at 1 kHz	0.2 ± 10%
Dielectric properties	
$\epsilon_r$ of 10 at 1 kHz	8 ± 10%
tan $\delta$ at 1 kHz	0.010 ± 10%
Mechanical properties	
E (MPa)	1000 ± 20%

Attribute	Value
Elongation (%)	$60 \pm 30\%$
Breaking stress (MPa)	$60 \pm 15\%$
Thermal properties	
Melting temperature (°C)	$156 \pm 5$
Glass transition Temperature (°C)	$112 \pm 5\%$

### *III Equipment and methods*

#### **A Polymer sample preparation equipment**

The polymer samples need to be moisture free to avoid oxidation and degradation in the oven. The conditioning of the polymer samples was done in desiccator Prolabo DV-29 (Figure 35) manufactured by Drivac Limited, USA having heated plate floor in a glass vacuum chamber in accordance with ASTM D618-13 standard test method [157]. The polymer was conditioned by placing the sample in the desiccator whose temperature was set at  $50 \pm 2$  °C with a pressure of -93.33 MPa for 48 hours in the chamber to evaporate the moisture from the polymer. The completely dried sample was later used for the experimental purposes.



Figure 35. Desiccator for conditioning



## B Characterization of polymer

### 1 Thermal characterization

The thermal behaviour of the polymer was analysed using differential scanning calorimetry (DSC) Q200 marketed by TA Instruments, shown in Figure 36. It is capable to analyse the thermal behaviour of the polymers up to the temperature range of 300 °C. The sample weight used was 10 mg. The temperature range lies from 25 °C to 280 °C at a rate of 10 °C/min under nitrogen atmosphere. The results obtained were recorded in the thermal analysis control station attached with calorimeter. The DSC analysis provide information regarding glass transition temperature ( $T_g$ ), cold crystallization temperature ( $T_{cc}$ ), melting temperature ( $T_m$ ), enthalpy of crystallization ( $\Delta H_c$ ), enthalpy of cold crystallization ( $\Delta H_{cc}$ ) and enthalpy of melting ( $\Delta H_m$ ). The crystallinity percent ( $\chi$ ) of the polymer was calculated using the Equation 12 [159].

$$\chi (\%) = \frac{\Delta H_m - \Delta H_{cc}}{\Delta H_m^\circ} \times 100 \quad (12)$$

where  $\Delta H_m$  is the enthalpy of melting,  $\Delta H_{cc}$  is the enthalpy of cold crystallization and  $\Delta H_m^\circ$  is the heat of fusion of 100% crystalline polyester which is 136.07 J/g [160].

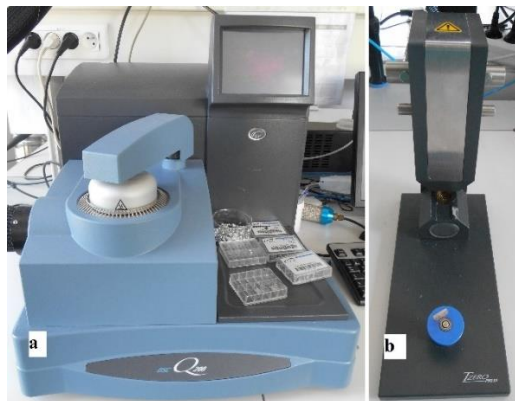


Figure 36. Differential scanning calorimeter (a. operating chamber, b. sample preparation fixture)

### 2 Rheological characterization

The extrusion plastometer MVI-3350 developed by Matériau Ingénierie Limited, France was used for determination of melt flow index of the thermoplastic polymer. It is based on piston extrusion mechanism as shown in Figure 37 **Error! Reference source not found.** The melt polymer at specified temperature is forced under load to flow through a capillary hole in 10 minutes and considered as indirect measure of molecular weight of

the polymer. The melt flow rate test was carried out in accordance with ASTM D1238-13 [158] standard test method to determine the melt flow rate of thermoplastics. The standard die having the smooth straight bore diameter of  $2.095 \pm 0.005$  mm having a length of  $8.000 \pm 0.025$  mm was used. The sample was conditioned at  $65\text{ }^{\circ}\text{C}$  for 24 hours before melt flow test. The temperature of  $285 \pm 0.2\text{ }^{\circ}\text{C}$  with a load of 2.16 kg was used as per standard operating conditions for Polyester. The preheat period lasted for  $5.0 \pm 0.5$  minutes before initialization of test. The time of test had been set at 1 minute as per actual standard conditions.



Figure 37. Extrusion plastometer

Modular compact rheometer MCR500 manufactured by Physica was used to investigate the steady shear rheological property of the polymer (Figure 38). The plate-plate 25/50 configuration was employed for the said test. The electrically heated measuring system temperature ranges from  $-40$  to  $+350\text{ }^{\circ}\text{C}$ . The sample was subjected to shear rate in the range of  $0.1$ - $300\text{ 1/s}$  after pre-shear time and resident time between them of 1 min and 5 minutes respectively. The test was carried out at the stabilized temperature of  $280\text{ }^{\circ}\text{C}$ .



Figure 38. Physica MCR modular rheometer

### 3 *Analytical characterization*

The crystalline structure analysis of the polymer was carried out using X-Ray diffractometer X'Pert Pro marketed by PANalytical B. V as shown in Figure 39. This analytical instrument was equipped with copper anode having wavelength of 0.154 nm with lone fine focus ceramic tube. It can be used for high resolution diffraction analysis, phase identification and quantitative phase analysis, crystallite size and strain determination analysis.



Figure 39. XRD used for analytical analysis of polymers

### **C Modification of melt extrusion process**

The lab scale conventional melt extrusion machine marketed by FilaTech GmbH was used for the development of composite filaments. The operating principle is based on piston mechanism which make it possible to use very less quantity of polymer material. It comprises of spinneret head, winding section and control section, which controls the whole process. The spinning head includes attachments for metal filament, piston drive and heated oven with spinneret (extrusion device). The winding sections comprises of stretching and cooling chamber, winding spool and winding drive. The piston extrusion mechanism makes it possible to use hollow piston for the passage and delivery of core filament through it. The machine is designed for the manufacturing of monofilaments with various controlling parameters including the feed-rate speed in range from 0.1 mm/min to 20 mm/min, oven temperature selected up to 350 °C and winding speed can be varied up to 52 m/min.

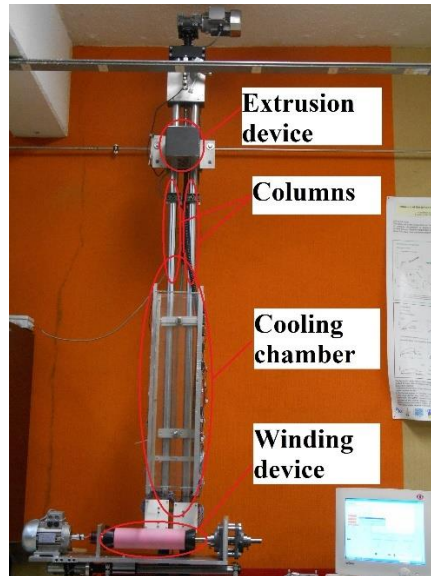


Figure 40. Melt extrusion machine

## ***1 Development of new designs***

### ***1.1 Spinneret design***

An economical, efficient and reliable process for the development of the composite filament were the key points for the researchers. In this regard, the previous work done particularly in this laboratory has added a key knowledge in the field of science for the development of composite filaments [5]. The economical and easy to manufacture technological characteristics were not taken into account in the previous work. The current work includes the machine modification by introduction of new parts and especially a new spinneret design for the manufacturing of coaxial composite filament. The spinneret need to be designed in light of set rules explained in literature for extrusion dies which are also outlined in previous chapter. This modification was made using the following equipment.

#### ***1.1.1 Lathe machine***

It is considered as mother of machines. The machine used was manufactured by N.V. Mondiale 81, model M-165, Belgium. It rotates the workpiece on its axis to perform various operations such as drilling, cutting, facing, knurling, sanding and turning, with tools that are applied to the workpiece to develop an object in symmetry about the central axis. This machine can be used for variety of materials such as metal, wood and glass etc. It primarily consists of bed, headstock, carriage and tailstock as shown in Figure 41. The bed holds the headstock, carriage and tailstock. Headstock comprised of horizontal axle called spindle which is placed in a high speed bearing. Workpiece is mounted in the dogs

(chuck) of spindle which is driven by a motor through train of gears. Carriage can slide horizontally on outer ways of the bed and capable to hold tools for drilling and cutting etc. Tailstock rests on an assembly which make it possible to slide it on the inner ways of the bed to the required position and contains a barrel parallel to axis of bed which is a horizontal assembly to grip different tools.

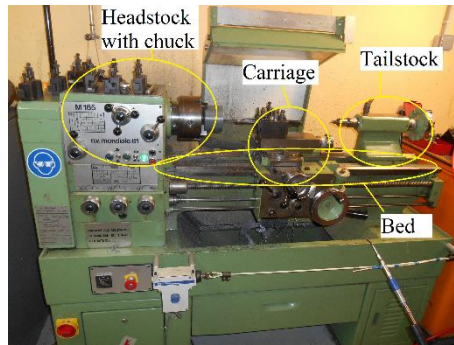


Figure 41. Lathe machine with parts

This machine has been used to develop different spinneret prototypes and piston bore designs by cutting, drilling and polishing in the metal piece. This machine only perform operation in 2D mode.

### 1.1.2 *Drilling and tapping machines*

Separate drilling and tapping machines were used for extra operations in 3D mode on spinneret workpiece. The geared head drill press model TL-25 manufactured by Ibarria, Spain was employed for the said operation. The operation in radial direction was not possible on lathe machine due to 2D working limitations.

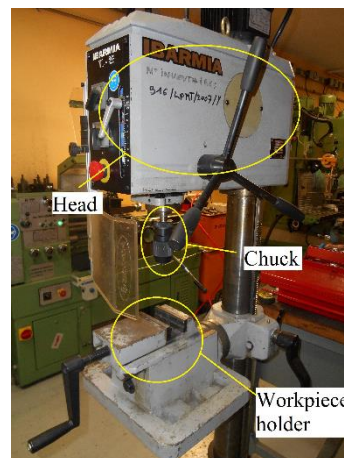


Figure 42. Geared head drill press with parts

It consists of a bit which is gripped by a chuck being rotated by the motor while pressed against the material (Figure 42). It was used to make small holes for screw in the spinneret workpiece. Drill bit is used to machine a bore while tap bit is used to generate spirals inside the bore for screw installation purposes.

## *1.2 Core filament passage*

A number of earlier experiments revealed that core filament finds high resistance during its way through the viscous melt polymer in the oven. Move over, the development of bends and kinks during polymer charging increases the resistance and also broke the filaments. To address all these problems, a tube was inserted in the oven for the passage of filament core through it. Different tubes were selected having different materials and specifications.

### *1.2.1 Selection of tube material*

The material selection should cover two basic aspects which a tube face during the extrusion process which include high temperature resistance and high strength. The materials which can provide these aspects includes stainless steel and ceramics. Both tubes were used to analyse their performance during the extrusion process.

### *1.2.2 Optimization of tube inner diameter*

The tube provides passage up to the middle of the designed spinneret. The role of inner diameter increases for positioning of core in the centre of the filament. Five different inner diameter tubes were selected to analyse their influence on the positioning of core which include 178  $\mu\text{m}$ , 254  $\mu\text{m}$ , 508  $\mu\text{m}$  and 762  $\mu\text{m}$ . This factor was studied and optimized for better coaxial filament development.

## **2 Modification of process design**

The conventional melt extrusion machine was further modified through the followings:

### *2.1 Piston bore modification*

The bore in the piston for the passage of copper filament developed in previous study [5] also allow the melt polymer to rise in the piston. Temperature gradient across the oven diameter give the opportunity to the melt to solidify inside the piston, restricting the copper monofilament to pass through it along with chocking the piston for further process. The bore size was limited by using aluminium foil without using tube in the oven [161]. Later

on, modification and optimization of design with inclusion of tube were done on lathe machine to optimize the extrusion process.

## 2.2 Modification of cooling process

### 2.2.1 *Forced cooling arrangement*

Cooling of the melt polymer plays important role in determining its properties. The temperature difference between the spinneret exit region and the cooling arrangement encountered just after the extrusion had proved to play vital role in mechanical and morphological properties of the filament. In this regard, forced cooling arrangement was designed using air media for filament cooling. Eight arrays of small electrical DC fans were installed using drilling machine in sheet of plastic on opposite sides of chamber to form a tower.

### 2.2.2 *Cooling chamber height*

The overall distance from the spinneret to the winding station was increased to investigate the effect of cooling length on the peripheral shape and structure of the filament. the length was increased by replacing the main columns on which all the system was attached. The columns were made of stainless steel rod having diameter of 50 cm. to ensure vertical position of the oven and all the arrangements attached on the column, the column was mounted with the wall at the top level to reduce vibrational effect during extrusion.

## 3 *Optimization of extrusion parameters*

The machine parameters were optimised through a number of experimental runs for the development of coaxial composite filament having diameter in range of 250  $\mu\text{m}$  to 350  $\mu\text{m}$ . The selection of this diameter range is based on the fact that the optimized extrusion process can be used for the development of piezoelectric sensors which need to be in this diameter range for better operating conditions, while maintaining almost constant value of remnant polarization [5]. Fibres having higher diameter proved to be difficult for polarization. The variables considered for centralization of core and process optimization were flow rate speed (2-5 mm/min), bobbin winding speed in range of 100 – 140 rpm (25.6 - 35.85 m/minute) [86], snail guide position (0 – 1.61°) [162] and spinneret hole diameter (1 – 2 mm) [163]. The response parameter was regularization of structure and positioning of core in composite filament. The design of experiments will be elaborated in next chapter.

## **D Development of coaxial composite filament**

The copper wire was drawn through the hollow piston, tube and composite spinneret followed by charging of oven with dried polymer chips. The temperature of the extrusion oven was set at 280 °C [82] and resident time for polymer in oven was 5 minutes. The spinning parameters including piston speed and winding speed were set at 5mm/min and 35.85m/min respectively as per optimization results.

The drawing was done with homogeneous temperature field drawing technique which provide constant drawing rate with necking. The drawing of filament was done at temperature ( $T_{dr}$ ) of 25 °C, which was 55 °C less than the glass transition temperature ( $T_g$ ) to reduce the crystallization in composite filament from virgin polymer. The drawing below or equivalent to glass transition ( $T_{dr} \leq T_g$ ) is specified as cold drawing which resultantly generate neck formation and propagation of neck along the specimen [164]. The coaxial filament was wound on package with winding system. The coaxial filaments obtained have the diameter in the range of 250  $\mu\text{m}$  to 350  $\mu\text{m}$ .

## **E Characterization of coaxial composite filament**

### ***1 Physical characterization***

The filament linear density was determined using the ASTM D1059 standard test method [165]. A very sensitive weighing balance which can provide results up to 4 decimal figures was used for the said test as shown in Figure 43.



Figure 43. High precision weighing balance



## 2 *Morphological characterization*

### 2.1 *Cross-sectional surface morphology*

The coaxial composite filaments are widely used in smart textiles for applications including sensors and actuators where the shape and structural periphery has high importance for their working. The integrity of cross-sectional shape during cutting of the composite filament is the crucial factor for successful development of coaxial composite filament in required structure and integration in textile materials. A small change in cross-sectional shape leads to unavoidable noise in sensor hence reducing the credibility of the filament. There were a number of ways used by different researchers including conventional as well as hi-tech cutting methods. Different techniques used for fibre cutting includes laser cutting, cold breaking with nitrogen gas and standard or ultra-microtome methods [7, 93, 94, 151]. The operation time for these techniques are long and complicated to perform the job. All techniques provide very good cross-sectional cutting surface except nitrogen gas technique. There is no study being focused on the evaluation of different cutting methods for composite filaments. Considering a number of tests to be performed, these methods can't be feasible to use. A new method was developed and optimized for obtaining sharp and smooth surface without damaging the position of core and integrity of the fibre shape.

To facilitate the process, different cutting methods were analysed [123]. Different tools including scissors, sharp edge cutting blades and surgical blades were studied for cutting. The sharp edge cutting blade is the paper cutting blade having flat saber grind blade type. This blade has flat bevels that extends up to the cutting edge from centreline of the blade as shown in Figure 44 (a). This blade maintains full thickness across the blade length for increasing strength.

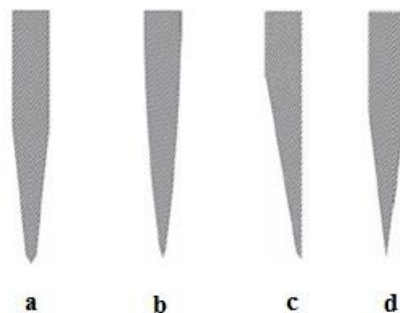


Figure 44. Blade types used in the study

The surgical blades are shown in Figure 44, which include hamaguri grind blade (b), single bevel grind blade (c) and zero ground saber blade (d). Hamaguri grind blade is a convex shaped ground bevels. It is also called as convex and Appleseed grind blade. Single bevel grind blade is ground at one side to form the bevel. This type of blade is also called chisel grind. The zero ground saber blade is a sharp blade which is grounded on both sides. It does not have secondary bevel as in the case of flat saber grind blade. The smoothness of the bevel plane makes it smoother to cut the samples.

Conductive coating is required for clear and better image of non-conductive samples in scanning electron microscope for dissipation of electron charges. High resolution of polyester region can't be obtained without conductive coating. The coating of the filaments was done with gold under argon gas environment in Metalizer E5100 developed by Polaron Equipment Limited, shown in Figure 45. The coating was made at pressure of  $0.1 \pm 0.05$  torr with a current supply of  $20 \pm 1.0$  mA at resident time of  $2.0 \pm 0.1$  minutes.



Figure 45. Gold coating metalizer

Scanning electron microscope S-2360N model manufactured by Hitachi Limited, Japan was used to investigate the cross-sectional shape and dimensions of the filament (Figure 46). The shape and peripheral structure of the composite filament was analysed at 20 kV voltage.

The images obtained from scanning electron microscope were further investigated by measuring the dimensions at various positions. The dimension measurements were made using the ImageJ software [166].



Figure 46. Scanning electron microscope

## 2.2 Linear surface morphology

The filament linear surface was characterized with an Atomic Force Microscope to study the surface roughness and grain size evaluation. Atomic Force Microscope (AFM) works on the principle of cantilever having a very small molecular tip which touches and moves on the surface under observation. A laser beam is pointed on the head of cantilever and reflected back to the detector. Any change in surface height, changes the position of cantilever and ultimately the laser beam which is recorded on the control station. The AFM used was based on solid contact cantilever type, in which cantilever tip continuously touches the surface during movement. AFM provides real 3D image of the surface in which each pixel has respective x, y and z coordinates; which is not possible in SEM analysis. In addition, AFM is a slow and sensitive analysis as compared to SEM, which provide more detailed results regarding the very small area surface under observation. The AFM used was NanoScope IIIa, model EX-1, manufactured by Digital Instruments, USA as shown in Figure 47.



Figure 47. Atomic force microscope

### 3 *Mechanical characterization*

The developed filaments faced large amount of stress during integration in textile structure. To analyse their resistance ability without compromising on their performance parameter, tensile strength need to be studied. The mechanical testing of the samples was done on MTS 20/M tensile strength tester as shown in Figure 48. The ASTM D2256/D2256M-10 standard test method was used for the investigation [167]. The modified gauge length of 25 mm was used while keeping all the other parameters as per standard test procedure. The high sensitive captor of 100 N was used for the measurement of mechanical test. The breakage of the copper monofilament inside the composite filament was considered as maximum acceptable strength. Filament tenacity, elongation at break and work of rupture were analysed. The strength of copper monofilament with and without heat treatment was also studied for comparison purposes. A number of 10 replicates for each sample were analysed and mean values were calculated for each parameter.



Figure 48. MTS tensile strength tester

### 4 *Tribology characterization*

Filament tribology characterization explains the friction and wear analysis which a filament observed during integration in textile structures as well as during intended end use. Yarn to yarn friction was studied by wrapping two filaments together of 2 rounds and placed between different pulleys as shown in Figure 49 [168]. This assembly was designed to determine comparative results of friction coefficient values. The standard filament taken was also the same to determine friction between same types of filaments. The sample length of specimen and standard filament was 200 mm each. The lower standard sample length was attached with weights on both ends. The other specimen length was grabbed

by the upper clamp of friction tester. Upper sample end was given vertical displacement of 0.03 m at rate of 0.0127 m/min. The tension applied was 0.5 N. The displacement between two samples with respect to each other requires a variable force (F) which was recorded by the device.

The equation used to determine the friction coefficient is given in Equation 13, where  $\mu$ , n and  $\beta$ , F,  $T_o$  are friction coefficient, number of wrapping rounds, angle between warped filaments, recorded tension and initial tension respectively. The displacement length used was 10 mm.

$$\mu = \frac{\log(F/T_o)}{n\pi\beta} \quad (13)$$

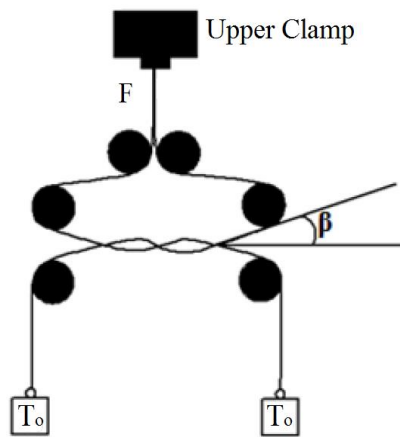


Figure 49. Device arrangement used to measure friction coefficient by twist method

## 5 *Bending characterization*

Stiffness is the main parameter for the handle and bending assessment of textile structures. It is one of the distinguishing factor as well between the wearable and non-wearable textile structures. The developed composite filament intended application is based on textile instrumentation for electronic wearable technology for which their stiffness analysis is also important to study. The bending stiffness was analysed on Kawabata Evaluation System (KES) module for single hair bending tester as shown in Figure 50. It is comprised of two jaws, one moveable around the other as a circular arc by a constant rate of 0.5 cm/s till a specific curvature of  $\pm 2 \text{ cm}^{-1}$ . The sample length was 10 mm. The fixed jaw is lined with sensitive load cell whose torque sensitivity value can be changeable from 0.08 to 1 gf cm. The slope was obtained between the curvature (K) value of 0.5-1.5  $\text{cm}^{-1}$ .

Bending moment per unit width ( $M$ ) is called as bending rigidity,  $B$  ( $\text{gf cm}^2$ ). The apparent bending modulus,  $E_B$  (GPa), is the ratio between normalized bending rigidity,  $B$  ( $\text{mN mm}^2/\text{tex}^2$ ), to geometrical moment of inertia,  $I$  [169]. This formula is defined for bending characteristic of circular cross-sectional materials.



Figure 50. KES - Single hair stiffness tester

## **F Conclusion**

The materials, equipment and methods used in the study were reported. The main objective of the study was to introduce a conductive metallic filament which was selected as copper monofilament. The polymers include polyester, polyamide (Nylon 6,6) and ferroelectric (PVDF<sub>70</sub>-TrFE<sub>30</sub>) polymer. The spinneret parts and machine parts were machined with brass and stainless steel respectively. The melt extrusion machine based on hollow piston mechanism was employed for the study. The machining equipment used were lathe machine, drilling machine and tapping machine. The characterization of polymer was done using XRD, extrusion plastometer, DSC and rheometer. The characterization of filaments was done using Scanning Electron Microscope, Atomic Force Microscope, tensile strength machine, friction tester and Kawabata Evaluation System.



## CHAPTER 4

### RESULTS AND DISCUSSION

#### *I Introduction*

This chapter explains the development of spinneret designs and their optimization of parameters. The spinneret designs and extrusion parameters were optimized using polyester as polymer matrix. The characterization of polymers was explained in detail. The modification of machine process and design were also introduced in it. The physical, mechanical, morphological, tribology and objective characterization of developed coaxial composite filaments were also reported. The finalized spinneret design and process were employed to develop composite filaments using polyamide and ferroelectric polymers. The developed composite filaments were also characterized and reported in this chapter.

#### *II Modification of melt extrusion process*

##### **A Development of spinneret design**

An economical, efficient and reliable process were the key points considered for the development of the composite filament. In this regard, the previous work done particularly in this laboratory has added a key knowledge in the field of science for the development of composite filaments [5]. The economical and easy to manufacture technological characteristics were still lacking in the previous work done. This work includes the machine modification by introduction of special spinneret design for the manufacturing of composite filament.

##### *1 Evaluation of flow stability*

The melt polymer flow stability is a crucial factor in extrusion process. The turbulent flow deteriorates the properties required in the output structure. The evaluation of flow stability in a duct is done by calculation of Reynolds number, which is a dimensionless quantity. The Reynolds number is calculated using the Equation 14, where R,  $\rho$ , V, D and  $\eta$  are Reynolds number, polymer density ( $\text{kg/cm}^3$ ), velocity of melt polymer in oven (cm/s), diameter of oven (cm) and dynamic viscosity of melt polymer ( $\text{kg/cm.s}$ ) respectively.

$$R = \frac{\rho V D}{\eta} \quad (14)$$



Reynolds number was calculated in the oven and at exit hole of spinneret. The velocity of the melt polymer in the oven was estimated with velocity of piston. The polyester has standard density of 0.00133 kg/cm<sup>3</sup>, velocity of melt is equivalent to velocity of piston (5 mm/min = 0.00833 cm/s), inside diameter of oven was 0.96 cm and dynamic viscosity of polyester chips was obtained from rheometer analysis (872 Pa.s = 8.72 kg/cm.s). The calculation for oven was as below:

$$R = \frac{0.00133 \times 0.00833 \times 0.96}{8.72} = 1.22 \times 10^{-6}$$

The value obtained for Reynolds number was very less, which expressed that the polymer melt flow in oven was laminar in nature. The Reynolds number for spinneret having 1 mm exit diameter was also calculated. The velocity of melt in spinneret was calculated using continuity equation as given in Equation 15.

$$A_1V_1 = A_2V_2 \quad (15)$$

$$V_2 = \frac{0.96 \times 0.00833}{0.1} = 0.08 \text{ cm/s}$$

The Reynolds number was calculated using velocity in spinneret and diameter of spinneret using Equation 14.

$$R = \frac{0.00133 \times 0.08 \times 0.1}{8.72} = 1.22 \times 10^{-6}$$

The value obtained of Reynolds number in spinneret was almost same as obtained earlier, which expressed that the flow was in laminar state.

## **2 Material performance calculation**

The material for spinneret was selected based on its performance at high pressure and temperature conditions. The spinneret temperature required in current process set up should be maximum at about 350 °C considering the temperature field required for polymers used. The load applied during the extrusion process was calculated using a load cell on piston which was 0.055 MPa during normal extrusion process and maximum load was observed at the end of extrusion at 4.572 MPa. In addition to the above mentioned parameters, the material should also comply with requirements explained in General die design rules [148]. Keeping all these facts under consideration, special brass rod was selected. The selected material provided higher tensile strength (>640 MPa) than the

maximum load applied during the whole extrusion process. In addition, the elastic limit at 0.2 % is still quite high at value of >400 MPa. Considering the performance characteristics, brass was selected as good material for selected application.

### **3 *Spinneret Prototypes***

In the design process, a number of spinneret designs were developed, tested and analysed based upon the requirements for the manufacturing of composite core sheath filament. The spinnerets were designed according to the hollow cylinder dimensions where spinneret will be fixed in extrusion machine. Some of the spinneret designs gone through the development stage and tested for composite filament manufacturing, while others were declined due to limitations in manufacturing and or manufacturing cost issues.

#### **3.1 *Full length spinneret design***

In this spinneret design, the spinneret set was composed of two parts, outer part and inner part. The outer part was designed having full length of required spinneret dimension for manufacturing of composite filament. The outer part was designed as a cylindrical geometry with a hollow conical shape at its central axis. The inner part was shaped as trilobal conical structure. The central region of inner part had hollow central passage for core filament. The conical shape made it possible to land inner part in the outer spinneret part and the space generated between the trilobes allowed the molten polymer to pass through. The passage designed for the core filament in the centre of the spinneret separates the core from the molten polymer and helps in better positioning of the core in the centre of the composite filament.

Keeping in view of the above explained basic design, a number of different variables were considered in inner and outer part designs which made it possible to develop a number of different spinneret designs having the same basic design theme. These designs were only traced in black and white. These designs were declined based on following points:

- a. Complex to manufacture conical regions
- b. Difficult to drill bore of small diameter for large lengths
- c. Very high chances of flow instability problems like weld lines etc.

These designs are reported as follows.

### 3.1.1 Prototype 1

The outer part was designed in a cylindrical shape having hollow conical shape at central axial position from top to near bottom. A hollow disc shape ring was developed at central axial position of bottom end of inner part joining the hollow conical shape to the end of outer part. The schematic illustration of outer part is shown in Figure 51. The inner part was designed as hollow conical tube with trilobes (wings) around it. The conical tube had hollow conical shape at central axial position for the passage of core filament as shown in Figure 52.

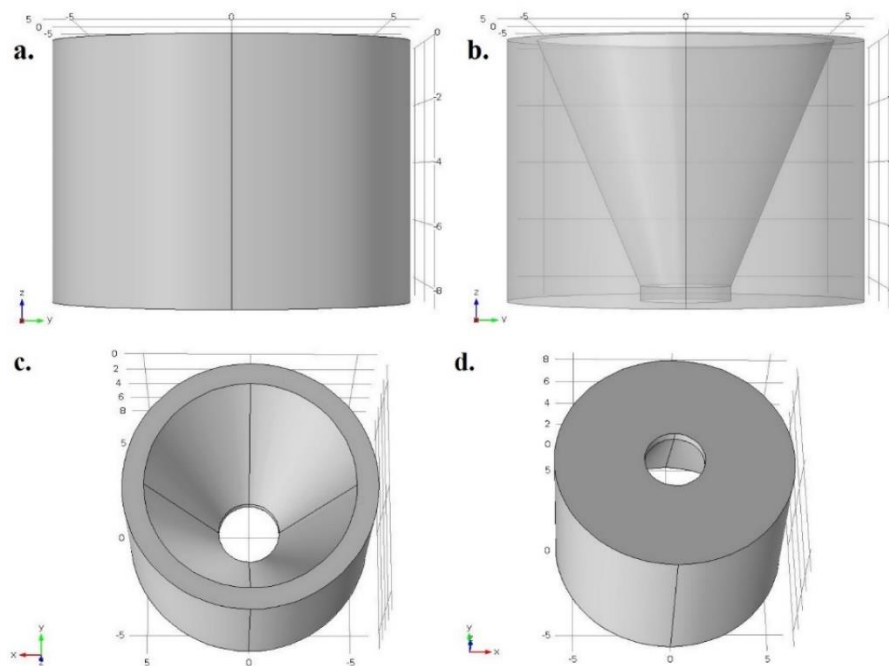


Figure 51. Schematic illustration of outer part of full length spinneret design prototype 1, (a. solid front view, b. transparent front view, c. inclined top view, d. inclined bottom view)

The thickness of the tube remained same at both ends of inner part. The lobe structure diameter reduces from higher diameter of tube to lower end of tube with same slope as designed inside of outer part. The lobe structure had the same angle of curvature on its surface as developed inside of inner part for proper fitting. The inner part was adjusted inside the outer part with complete fitting along conical walls of outer part without leaving any gap between them. The space created between the lobes was considered as flow channels for the melt polymer as shown in Figure 53 (c).

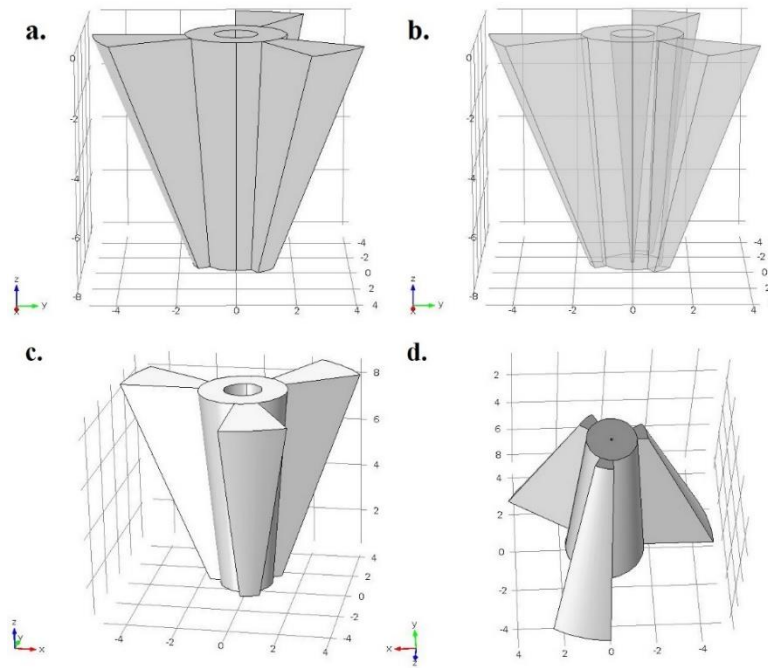


Figure 52. Schematic illustration of inner part of full length spinneret design prototype 1 inclined views, (a. solid view, b. transparent view, c. top view, d. bottom view)

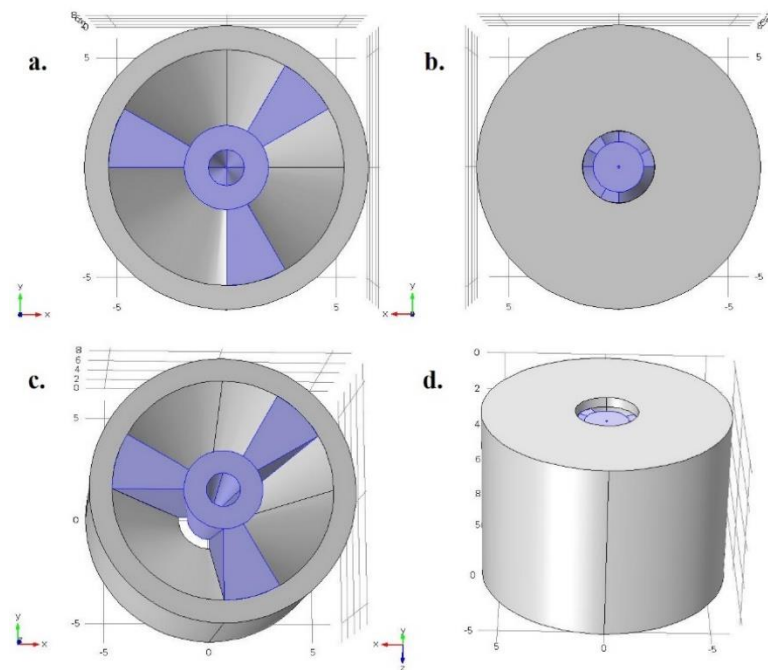


Figure 53. Schematic illustration of full length spinneret design prototype 1 solid views, (a. top view, b. bottom view, c. inclined top view, d. inclined bottom view)

The particular key points in this prototype design were the conical shape tube surrounded with trilobes having hollow conical passage at central axial position in inner part for core

filament (Figure 54), trilobal structure to support the conical tube as well as act as flow separators and ring type design at exit section of outer part (Figure 53).

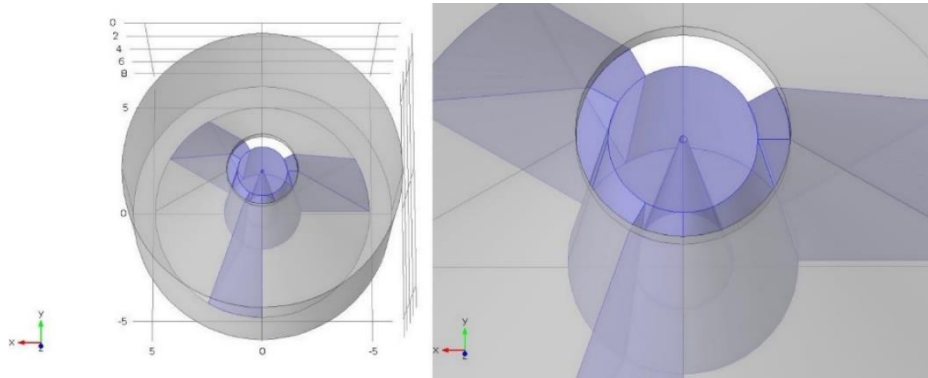


Figure 54. schematic illustration of transparent bottom view of full length spinneret prototype 1, (a. inclined view, b. magnified inclined view)

The basic reason considered for the conical shape geometry in inner part was ease of passage with minimal frictional contact between the die walls and core filament. The ring shape was considered to provide parallel land region for compensation of stresses, incurred during convergence of melt flow at upstream region resulting in extensional deformation, were able to relax. The controlling of melt swelling will produce regular and smooth surface of filament.

### 3.1.2 *Prototype 2*

The prototype 1 was modified to produce prototype 2. The ring structure was removed from outer part and complete conical design at central axial position from top to bottom was developed as shown in Figure 55.

The conical tube was extended up to the bottom level of spinneret while length of trilobal structure was unchanged as shown in Figure 56. The flow channels were straight and convergent at diagonal position between the inside walls of outer part and outside walls of inner part. The ring structure was removed to allow the melt stream to get coherent with adjacent streams under applied stresses. The conical tube was extended to facilitate and guide the flow stream at exit. The concept for this modification lies in the fact of converging and joining the melt streams at end of separators (trilobes) to reduce the weld line instability in the filament as reported in literature [125, 141].

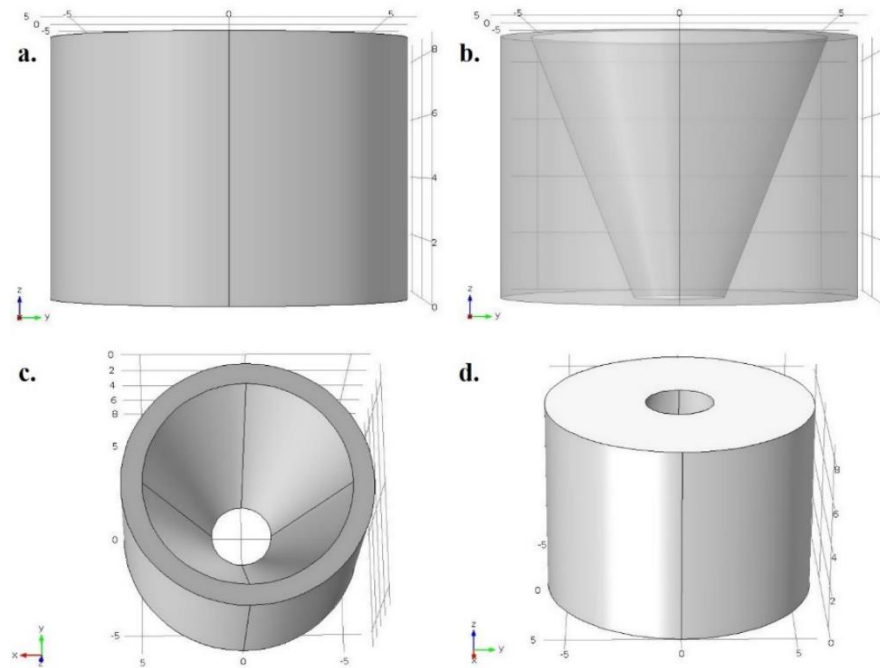


Figure 55. Schematic illustration of outer part of full length spinneret prototype 2, (a. solid front view, b. transparent front view, c. inclined top view, d. inclined bottom view)

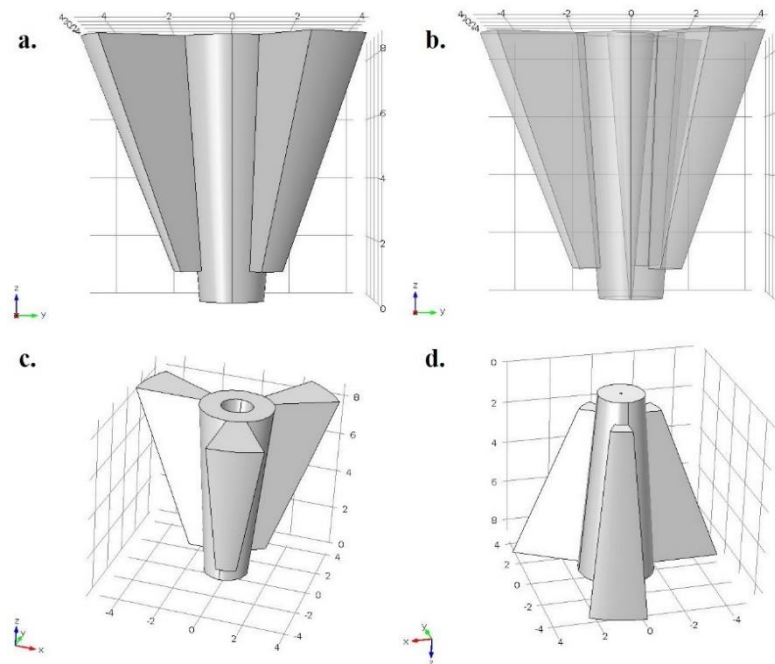


Figure 56. Schematic illustration of inner part of full length spinneret prototype 2, (a. solid front view, b. transparent front view, c. inclined top view, d. inclined bottom view)

The top and bottom views of the complete spinneret with their inclined views are shown in Figure 57. The transparent top view with magnification is shown in Figure 58. The two

parts were joined to develop the complete geometry of the whole spinneret. The flow channels were created between the free space created between the two parts.

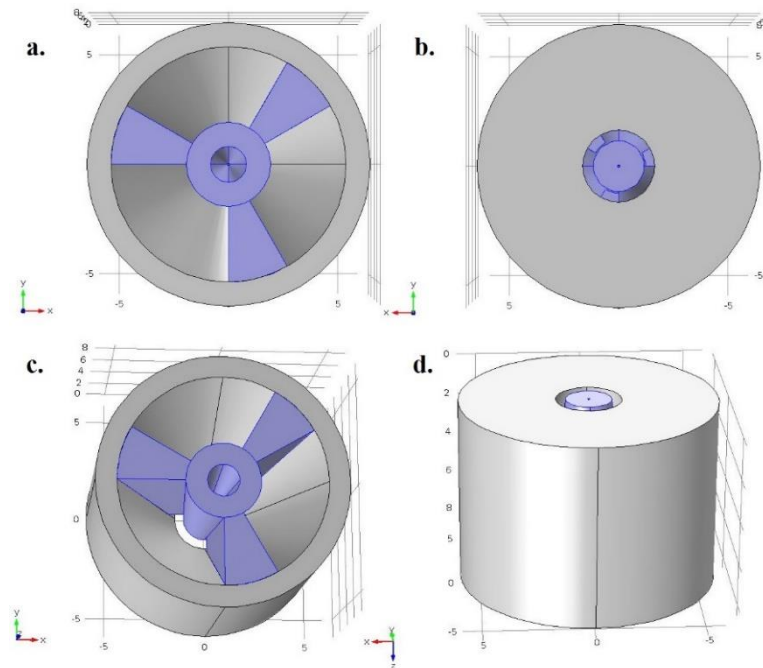


Figure 57. Schematic illustration of full length spinneret prototype 2 solid view, (a. top view, b. bottom view, c. inclined top view, d. inclined bottom view)

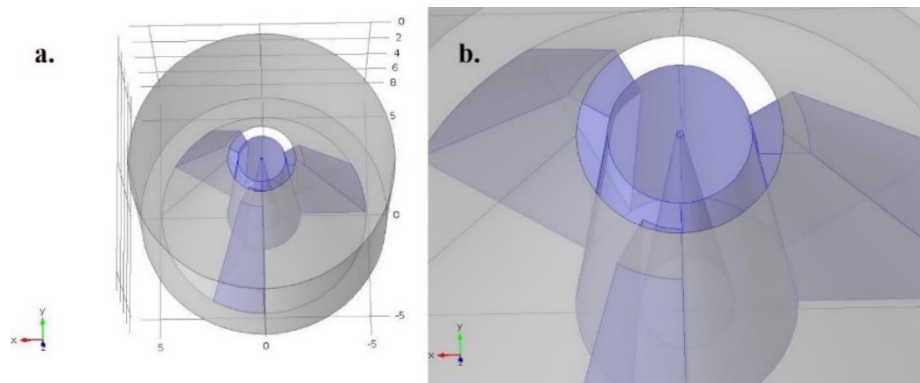


Figure 58. Schematic illustration of full length spinneret prototype 2 transparent view, (a. full inclined view, b. magnified inclined view)

The walls of flow channels facilitate the convergent flow due to their conical geometrical shapes. The development of conical tube having hollow conical shape at central axial position with conical shaped trilobes around it required high expertise and precise machining equipment. In consideration of cost effective design criteria, the developed spinneret designs were not explored further. Therefore, prototypes 1 and 2 were only remained at designed stage and were not machined for experimentation.

### 3.1.3 Prototype 3

The non-realization of previously developed designs brought new modifications with consideration of economical manufacturing methods. The outer part geometry remained intact as described in prototype 2 design (Figure 55). The inner part of prototype 2 was modified by replacing the conical tube with straight tube structure as shown in Figure 59.

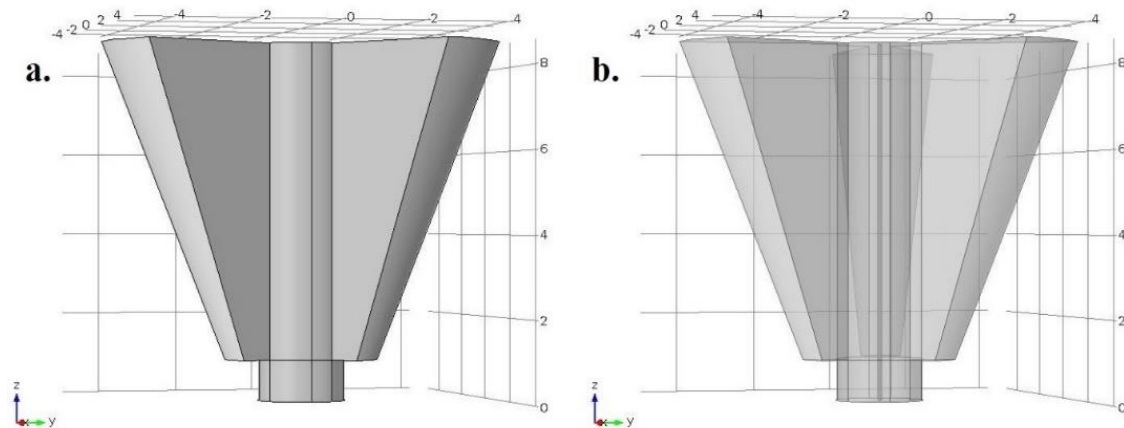


Figure 59. Schematic illustration of inner view of full length spinneret prototype 3, (a. solid view, b. transparent view)

The modified spinneret design also followed the convergent flow rule for stabilization of melt streams. The change of conical tube to straight tube in inner part changed the impact on applied stresses. The overall impact will remain favourable for melt stabilization due to steep slope in outer part wall as shown in Figure 60. The introduction of hollow tube design at central axial position for core filament will introduce frictional effect between the core filament and spinneret material (Figure 61). This contact was unavoidable and friction would only can be reduced using plating technique.

It was observed that the melt polymer stream had no contact area with core filament, which may lead non-attachment or weak bonding between them. In addition, large gap caused due to thickness of tip of tube at bottom end would also cause in creation of gap between the core and sheath material.



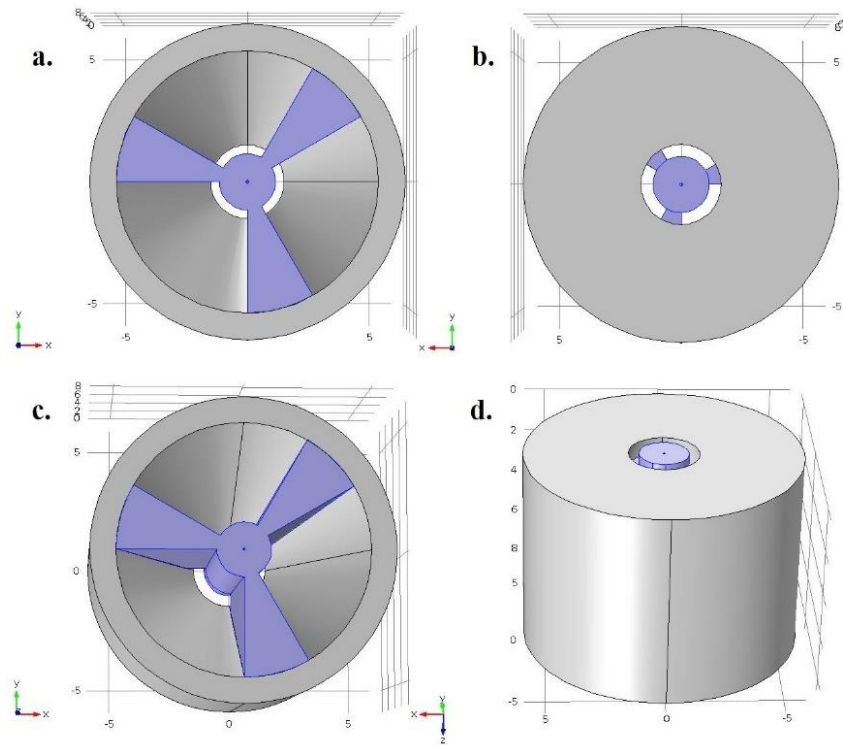


Figure 60. Schematic illustrations of full length spinneret prototype 3 solid views, (a. top view, b. bottom view, c. inclined top view, d. inclined bottom view)

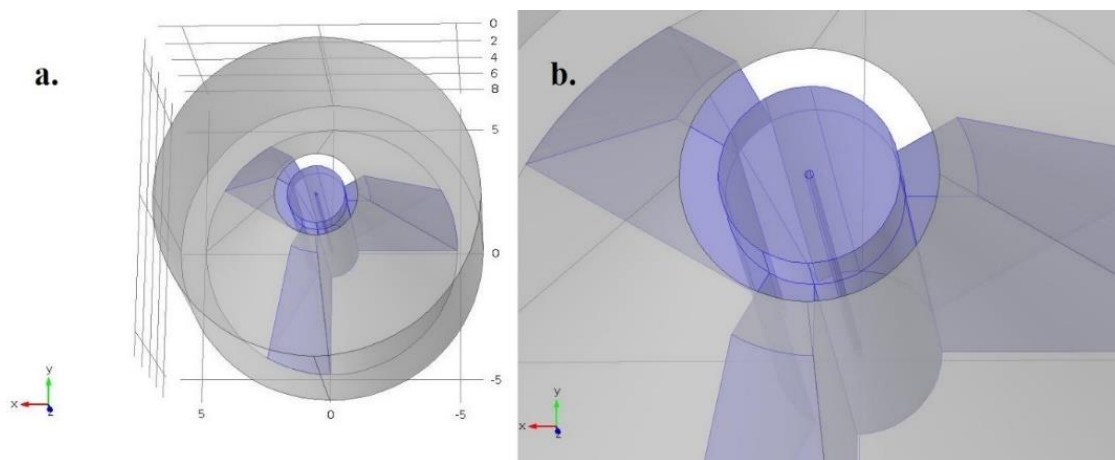


Figure 61. Schematic illustrations of full length spinneret design prototype 3 transparent views, (a. full view, b. magnified view)

### 3.1.4 Prototype 4

In order to address the design faults observed in prototype 3, a modified spinneret design was developed. The outer part remained unchanged as presented in prototype 3 (Figure 55). The inner part was modified by decreasing the length of tube. The extended part of tube after trilobal structure was removed to have the same length of tube and trilobal

structure as shown in Figure 62. The fixing of this inner design in outer part provided space at the exit region of the spinneret as shown in Figure 63 (d).

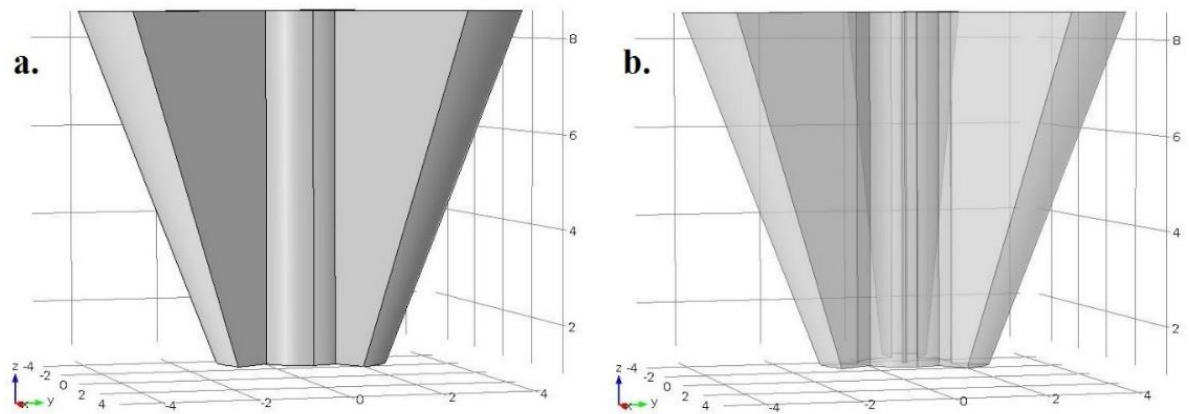


Figure 62. Schematic illustration of inner view of full length spinneret prototype 4, (a. solid view, b. transparent view)

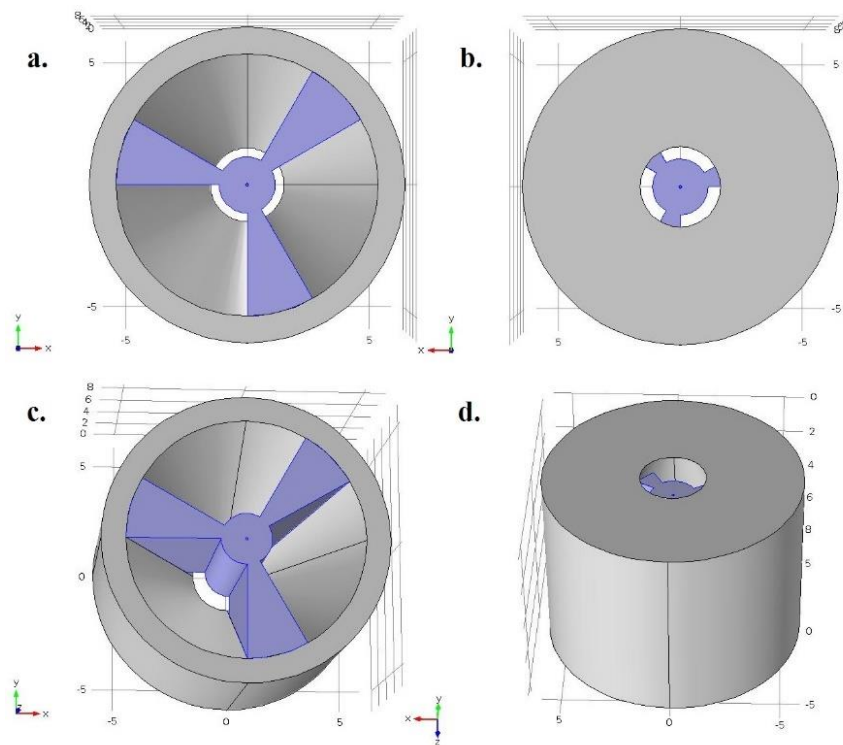


Figure 63. Schematic illustrations of full length spinneret prototype 4 solid view, (a. top view, b. bottom view, c. inclined top view, d. inclined bottom view)

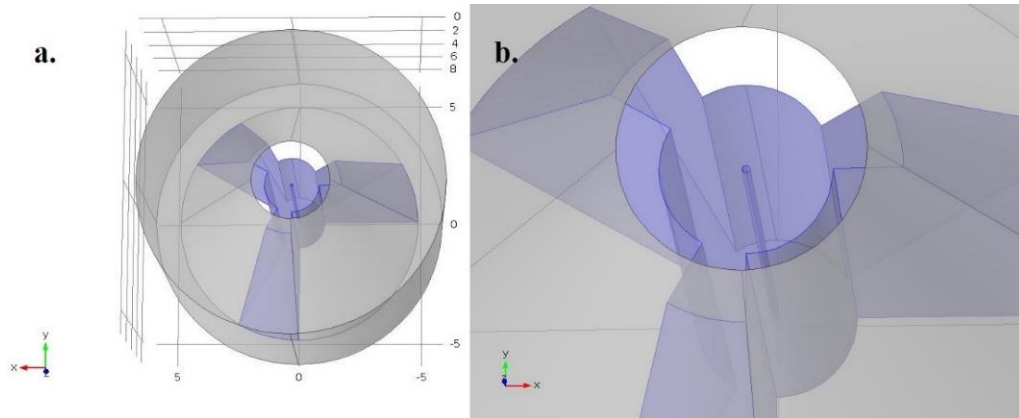


Figure 64. Schematic illustrations of full length spinneret prototype 4 transparent view, (a. inclined full view, b. inclined magnified view)

The developed design provides contact area between the core filament and melt polymer at melting temperature just before the exit from spinneret as shown in Figure 64. The conical flow channel design with trilobal structure which end shortly before the exit of spinneret facilitated the controlled cross-flow between the adjacent flow streams to prevent weld lines. The design provided high frictional contact between the core filament and the spinneret material. Furthermore, the cleaning of very small diameter inner part tube required reconsideration.

### 3.2 Fragmented spinneret design

#### 3.2.1 Prototype 5

The short coming identified in previous design were resolved in next developed prototype design. The cleaning of the spinneret can be done more easily as the total length of the spinneret was divided into two parts. The manufacturing, maintenance and cleaning of short length is also easier than long length parts. The centralization of core is considered to be depended upon the position of its delivery at exit of spinneret. If the core is very precisely and accurately delivered at central axial position, very good centralization may be achieved. Under the light of this hypothesis, very small diameter was required to deliver the core filament at very precise position in the composite filament. This very small boring in metal with high precision can only be done using wire electrical discharge machining technology. The stated technology is costly which ultimately increase the cost of the spinneret. Furthermore, the chocking of small hole with polymer will directly influence on the adaptability of such costly process.

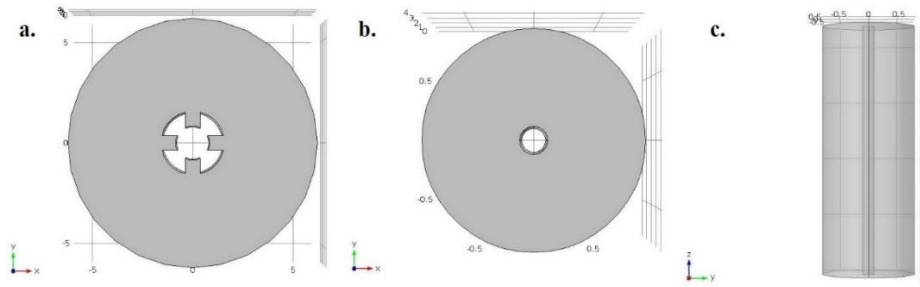


Figure 65. Schematic illustration of upper part of prototype 5, (a. top view of main body, b. magnified top view of tube, c. magnified front view of tube)

To address above stated problems and reduce the cost of the spinneret, a commercially stainless steel tube was used. The inner diameter of the tube was available in different gauges. Owing to usage of metal as core, the frictional influence should also be considered in mind and required tolerance should be provided to reduce the frictional drag. The upper part was composed of a cylinder having hollow X shape at central axial position and small diameter tube as shown in Figure 65. The tube was fixed in the arms developed by X shape and the passage of polymer was around the tube between the arms as shown in Figure 66. The arc shaped flow channels allowed the polymer to surround the core at the exit from upper spinneret part.

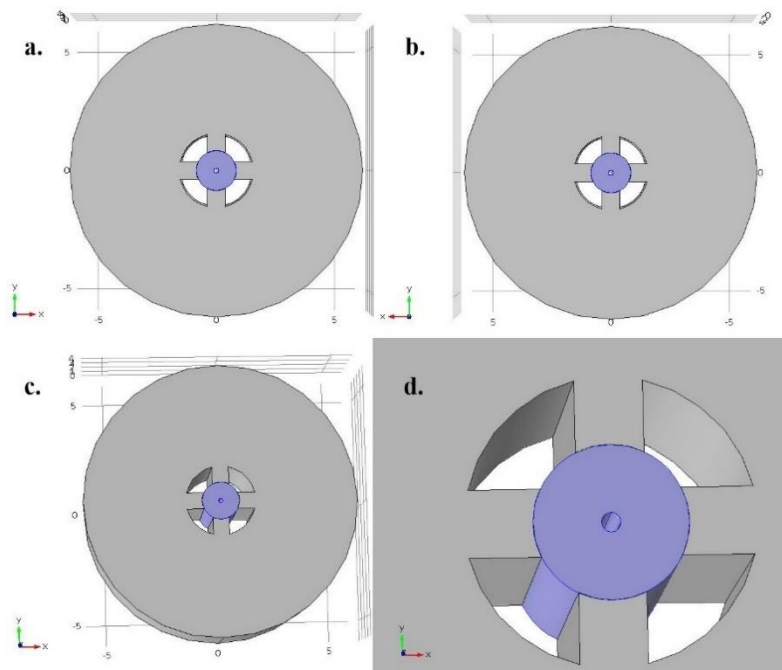


Figure 66. Schematic illustrations of solid view of upper part prototype 5, (a. top view, b. bottom view, c. inclined top view, d. magnified top view)

The upper part was joined with lower part to develop complete spinneret. The lower part had funnel shape geometry at central axial position for the collection of polymer through different flow channels in the central exit bore as shown in Figure 67. The Y shape or funnel shape helped to reduce the weld lines by allowing controlled interflow between the flow streams from adjacent flow channels. In addition, the convergent design helped in flow stabilization. The large land length to diameter ratio was considered in this design to accommodate die swell as described in literature [128].

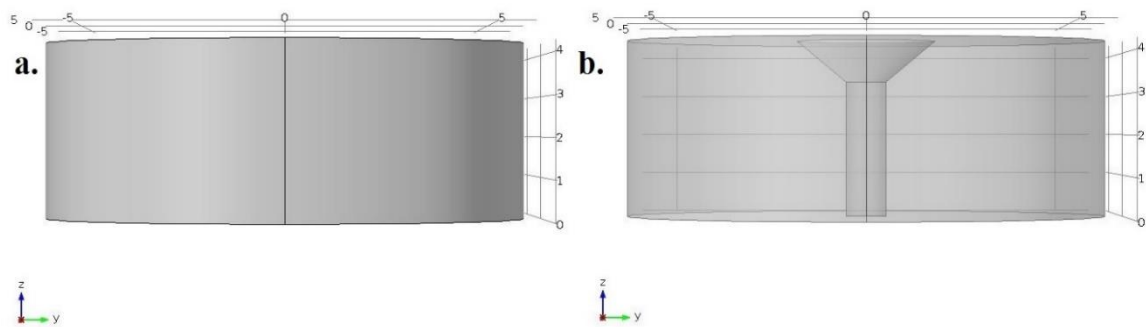


Figure 67. Schematic illustration of front view of lower part of prototype 5, (a. solid view, b. transparent view)

The cutting of tube in required very small length was not feasible using standard cutting tools. The chocking of the tube hole with polymer after extrusion process was also one of the biggest issues found in this design. These manufacturing and processing disadvantages lead to the development of new design having better process ability.

### 3.2.2 *Prototype 6*

This design was inspired by prototype 5 design. The small length tube previously used was extended to full length of oven to provide a separate passage for the core filament. The introduction of tube has completely modified the complete path of the core filament for extrusion process (Figure 68). The tube lower position was rested on the upper spinneret part in U shaped geometry at central axial position having small hole at lower position for core filament to pass through as shown in Figure 69.

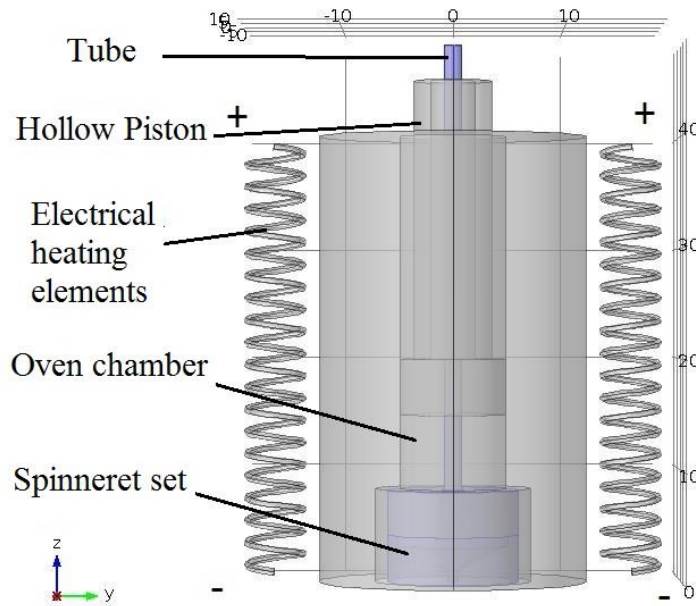


Figure 68. Schematic illustration of extrusion process design

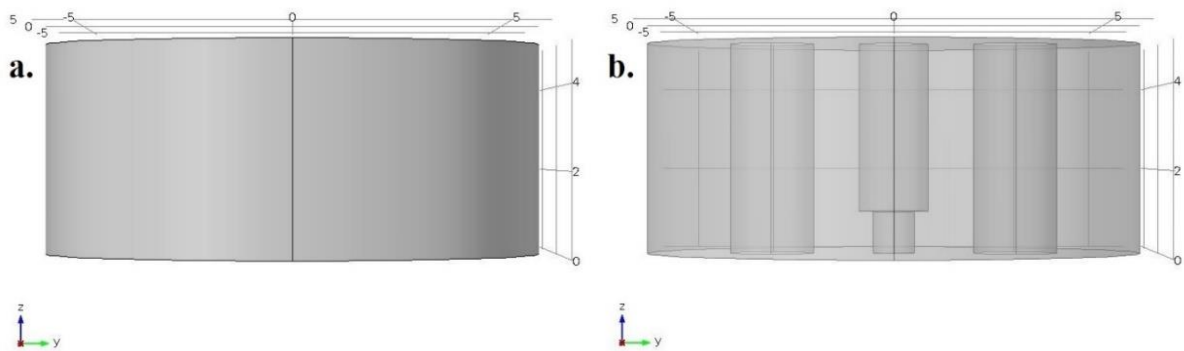


Figure 69. Schematic illustration of front view of upper part of prototype 6, (a. solid view, b. transparent view)

The fixation of tube in U shaped upper part helped to retain the tube at its position during the extrusion process. The tolerance between the tube and spinneret part was low to restrict the penetration of polymer between them. The two hollow cylindrical flow channels were designed at 180-degree angle in upper part for the polymer melt as shown in Figure 70. The bore size was enough to control high turbulent flow as already expressed in Reynolds number calculation.

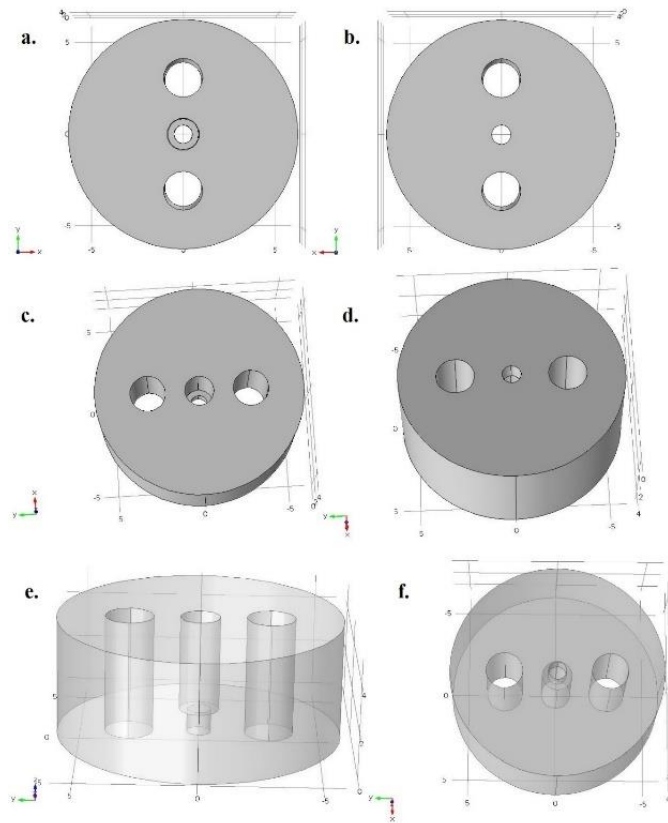


Figure 70. Schematic illustrations of top and bottom views of prototype 6, (a. top view, b. bottom view, c. inclined top view, d. inclined bottom view, e. inclined top transparent view, f. inclined bottom transparent view)

The lower part was developed having hollow conical shape at central axial position as shown in Figure 71. The hollow conical shape helped to divert both melt flows to central axial point for exit. The length of conical shape was increased by increasing the inside angle to achieve stabilization of polymer stream. The land length (horizontal width of exit geometry) to diameter ratio was also considered equal to unity to control melt swell instability.

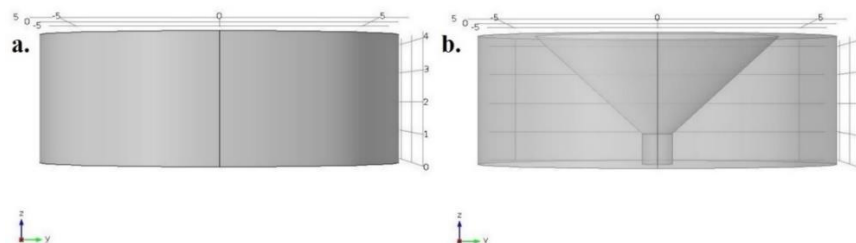


Figure 71. Schematic illustration of front view of prototype 6, (a. solid view, b. transparent view)

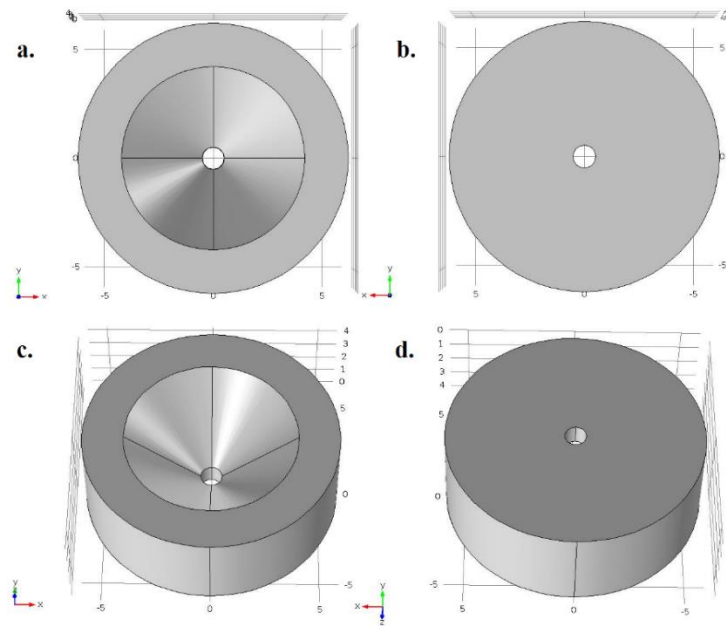


Figure 72. Schematic illustrations of top and bottom views of lower part of prototype 6, (a. top view, b. bottom view, c. inclined top view, d. inclined bottom view)

The top and bottom views of lower part are shown in Figure 72. The conical shaped developed had low roughness for smooth flow over it. The upper and lower parts were joined to develop complete spinneret as shown in Figure 73. The tube will be fixed in the top position of upper part in U shape design. The flow channels are also visible in inclined top view in Figure 73 (d).

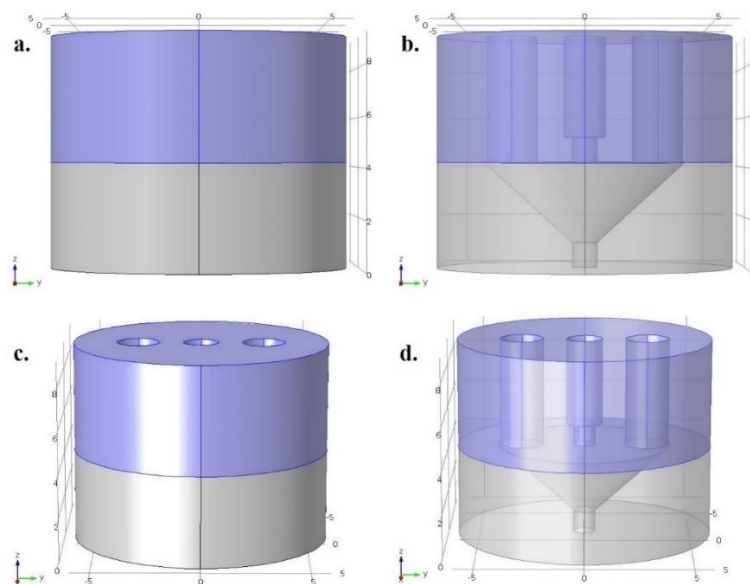


Figure 73. Schematic illustrations of complete spinneret set of prototype 6, (a. solid front view, b. transparent front view, c. top inclined solid view, d. top inclined transparent view)



The top and bottom view of complete spinneret set are shown in Figure 74. Three bores are visible at the top view, two for the polymer melt flow and one for the tube for passage of core filament through it. The bottom view shows only single bore as exit for composite filament.

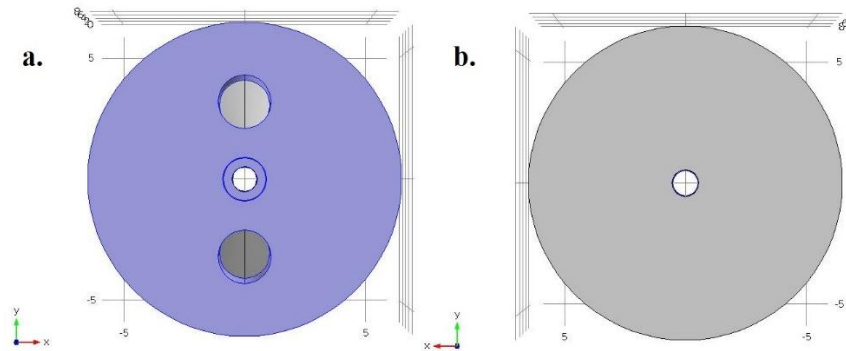


Figure 74. Schematic illustrations of top and bottom view of prototype 6 spinneret set, (a. top view, b. bottom view)

After an extrusion process, the piston need to be retreated back at initial position. During retreating, the tube gets stuck with the hollow piston due to adherence of viscous melt polymer between them. This shortfall was addressed in the next design.

### 3.2.3 Prototype 7

It was a modified version of prototype 6 design with inclusion of a screw in upper part to firmly grip the tube as shown in Figure 75. The rest of the design was kept same. The stainless steel hexagonal socket screw with flat tip was used. This modification allowed the piston to retreat to its initial position without changing the position of the tube.

The little lateral shift of any part with respect to other is enough to change the whole geometry of the spinneret. As there was no any locking mechanism to keep the parts at their desired respective position, the geometry of the spinneret may change during installation of the spinneret. In addition, according to the previous hypothesis regarding the delivery of core at central axial position for better positioning, the closeness of delivery media would also support for better positioning. Therefore, the second hypothesis is that closer the core delivery device (tube) provide better positioning. In light of second hypothesis, the position of the tube need to be lowered from its current position. Therefore, this U shaped geometry need to be replaced with hollow cylindrical shape. These modifications were introduced in the further refined spinneret design.

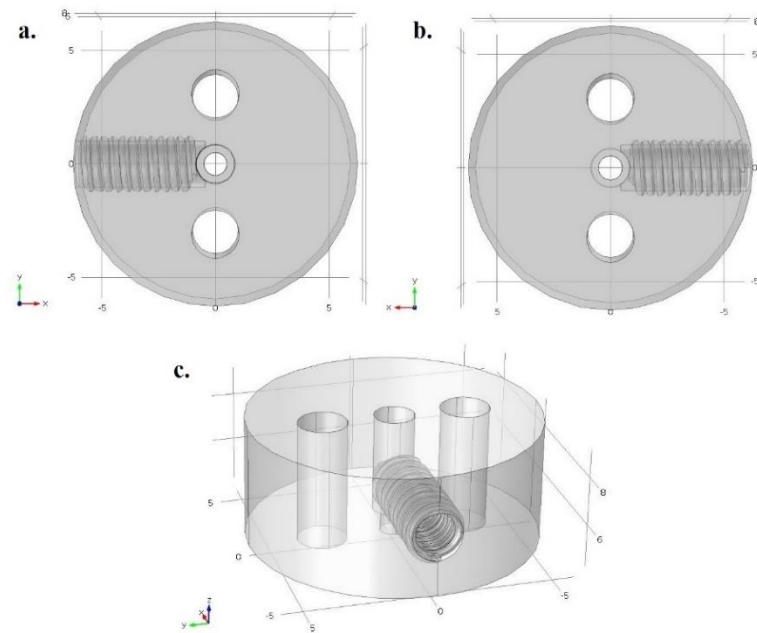


Figure 75. Schematic illustrations of top and bottom view of upper part of prototype 7, (a. top view, b. bottom view, c. top inclined transparent view)

### 3.2.4 Prototype 8

It was the design used for most of the experimental work. It was designed based upon the previously designed prototypes with respect to their structure and performance. It was based on two spinneret parts, upper and lower part [170]. Each part had half of the length of total spinneret and hence actual total length with complete spinneret geometry would be obtained by joining both parts at their respective position. Each part had specified geometrical details in it. The front view of the upper part is shown in Figure 76. The upper part had a central axial passage for the tube to pass through it along with hollow cylindrical flow channels around it at same angular and radial positions from the centre as shown in Figure 77.

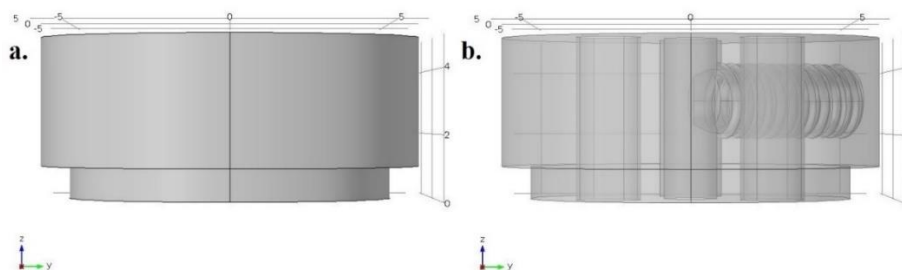


Figure 76. Schematic illustration of front view of upper part of prototype 8, (a. solid view, b. transparent view)

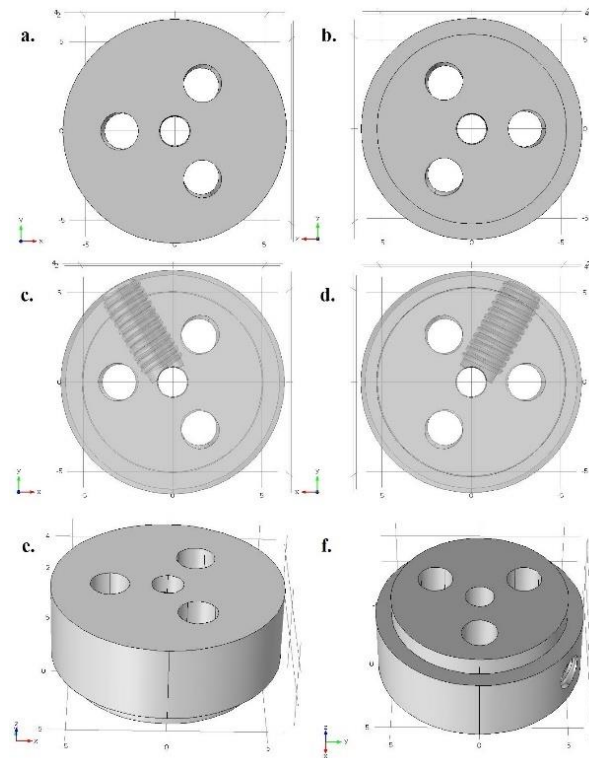


Figure 77. Schematic illustrations of top and bottom view of upper part of prototype 8, (a. top solid view, b. bottom solid view, c. top transparent view, d. bottom transparent view, e. top inclined solid view, f. bottom inclined solid view)

The tube was fixed in the central hole by a horizontal screw machined at vertical centre of the upper part. The flow channels were used for the passage of melt flow through them. To ensure the positioning of the parts, flange type rigid coupling was used. The upper part was machined with male flange while the lower part was machined with female flange type. The joining of both parts made these flanges to fix in each other providing firm geometrical structure.

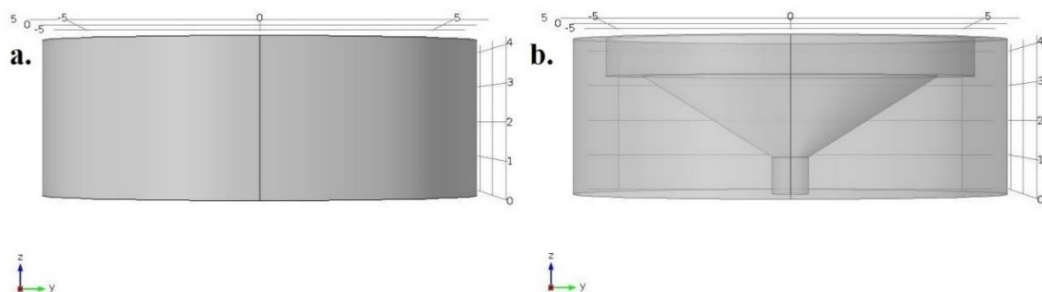


Figure 78. Schematic illustrations of front view of lower spinneret part of prototype 8, (a. solid view, b. transparent view)

The lower part was designed as cylinder having hollow conical shape at central axial position as shown in Figure 78. The inside angle of the cone was increased for better flow stabilization and controlled interflow of adjacent flow streams to reduce weld lines. In addition, the difference between the collection land length of melt polymer for a single stream from spinneret central position made it possible to reduce the effect of weld lines in the final filament. The melt material flowing through far point from spinneret central axial position need to travel more than the material flowing near to it. This arrangement also promotes good adherence between core and polymer before extrusion from the exit.

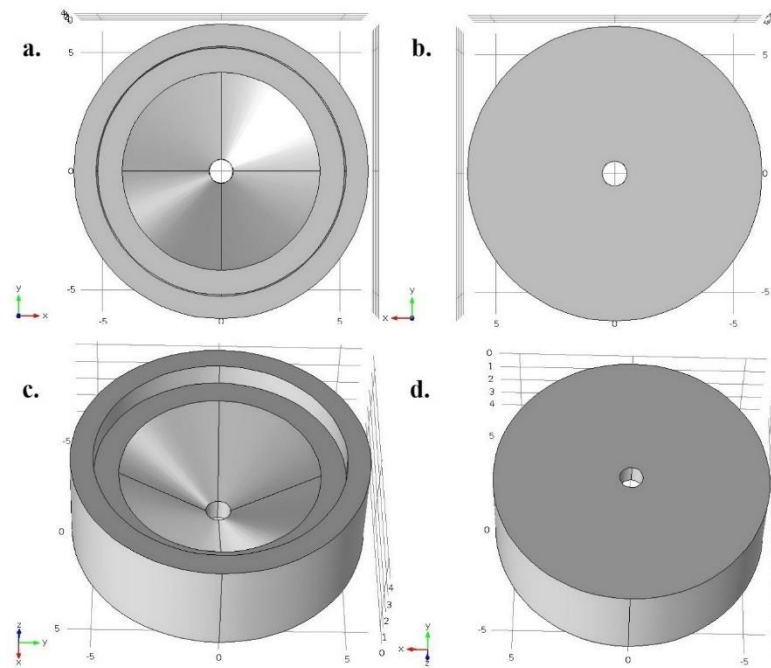


Figure 79. Schematic illustrations of top and bottom view of lower part of prototype 8, (a. top view, b. bottom view, c. inclined top view, d. inclined bottom view)

The geometrical shape of top and bottom views of lower part are shown in Figure 79. The both parts were joined through flange type assembly to achieve required geometry and dimensions of the spinneret as shown in Figure 80.

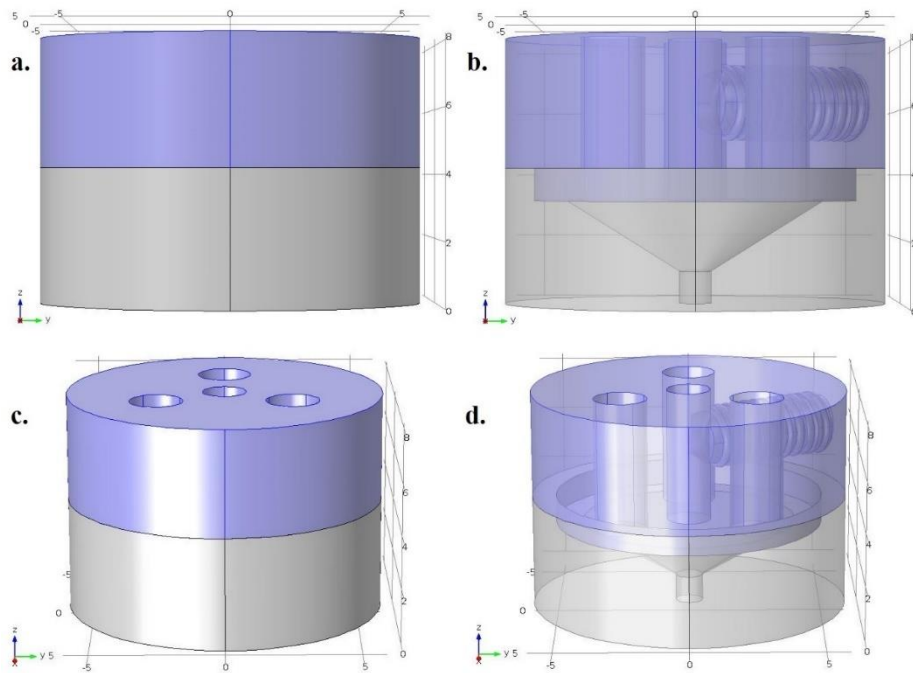


Figure 80. Schematic illustrations of front and inclined view of prototype 8 complete spinneret set, (a. front solid view, b. front transparent view, c. top inclined solid view, d. top inclined transparent view)

The flow channels for the polymer are designed in a way that they open completely within the diameter of lower part. The boring may reduce the strength of the material, therefore, spinneret was designed in such way to retain enough strength in the part to sustain the load applied during its service life. The top and bottom views of the complete spinneret are shown in Figure 81.

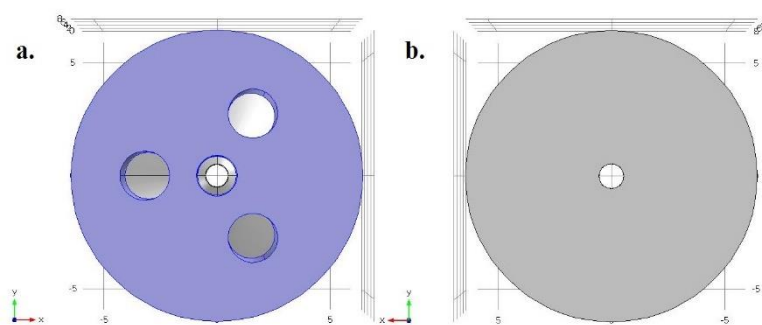


Figure 81. Schematic illustrations of top and bottom view of prototype 8 complete spinneret set

### 3.2.5 Prototype 9

This design was developed after optimization of the parameters and variables in prototype 8 design including number of holes, tube diameter, tube type, tube position and

spinneret exit diameter. The contours and edges of bores were smoothed using large diameter drill in the whole geometry to minimize turbulence created during the extrusion process. The sharp edges of bores cause turbulence in flow which can be reduced by smoothing of edges. The screw was removed and the tube fixation was carried out using thermal expansion technique as shown in Figure 82. The upper part having less diameter than the diameter of tube was machined and then thermally heated to obtain thermal expansion. When the diameter of the hole expanded due to heat, tube was inserted and then cooled to fix the tube at required position.

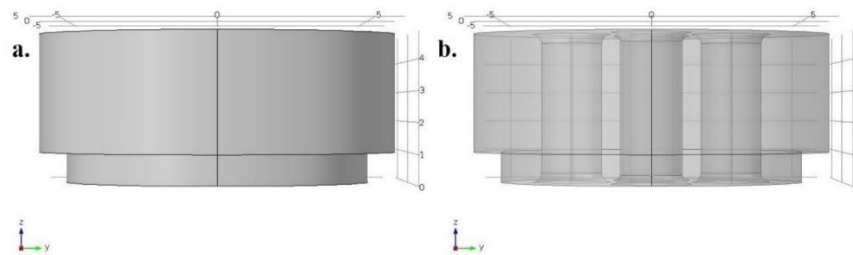


Figure 82. Schematic illustrations of upper part of prototype 9, (a. solid view, b. transparent view)

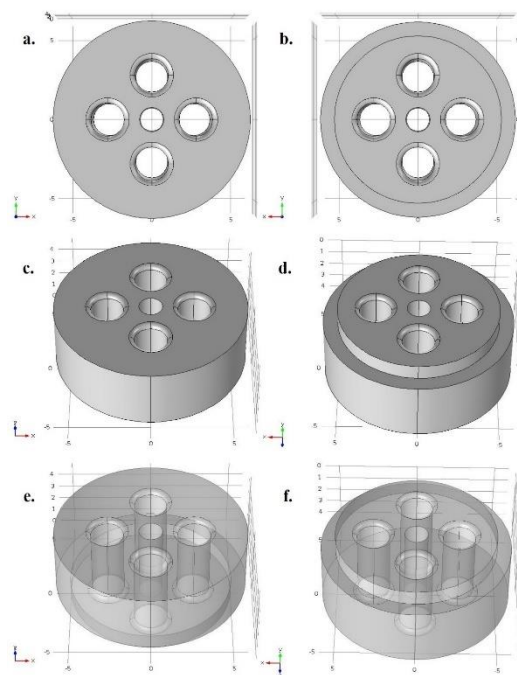


Figure 83. Schematic illustration of top and bottom views of upper part of prototype 9, (a. top solid view, b. bottom solid view, c. top inclined view, d. bottom inclined view, e. top inclined transparent view, f. bottom inclined transparent view)

The four number of holes were considered in upper part as per optimization for required shape of composite filament as shown in Figure 83. The lower part geometry was almost the same with only smoothing of edges as shown in Figure 84. The optimized spinneret exit diameter configuration was used in this design. The top and bottom views of this optimized design are shown in Figure 85.

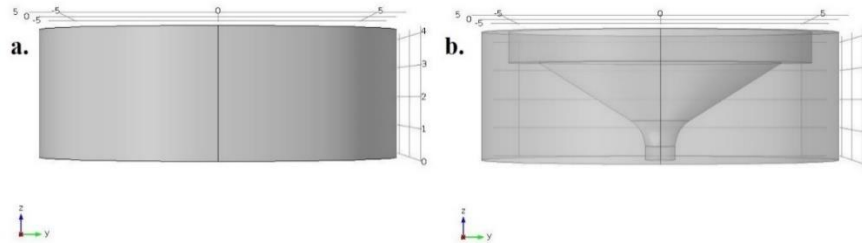


Figure 84. Schematic illustration of front view of lower part of prototype 9, (a. solid view, b. transparent view)

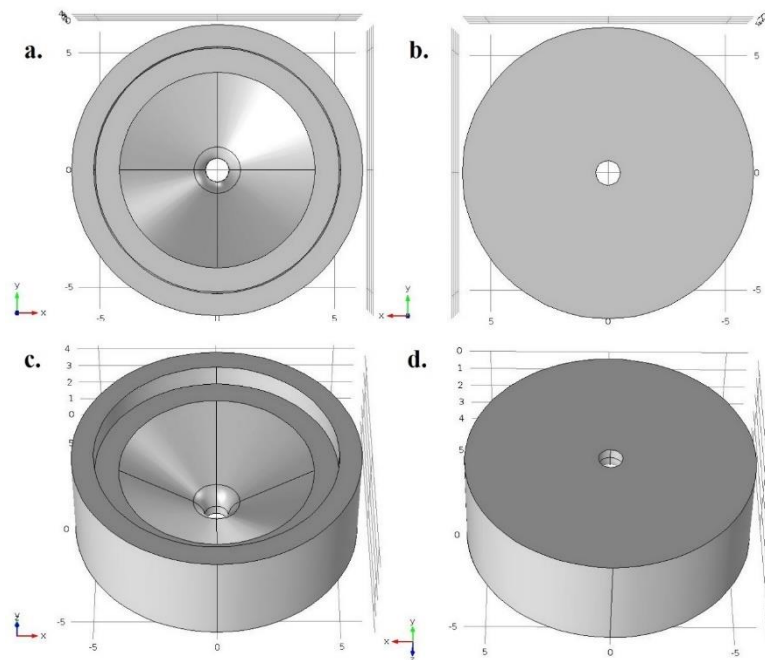


Figure 85. Schematic illustrations of top and bottom view of lower part of prototype 9, (a. top view, b. bottom view, c. top inclined view, d. bottom inclined view)

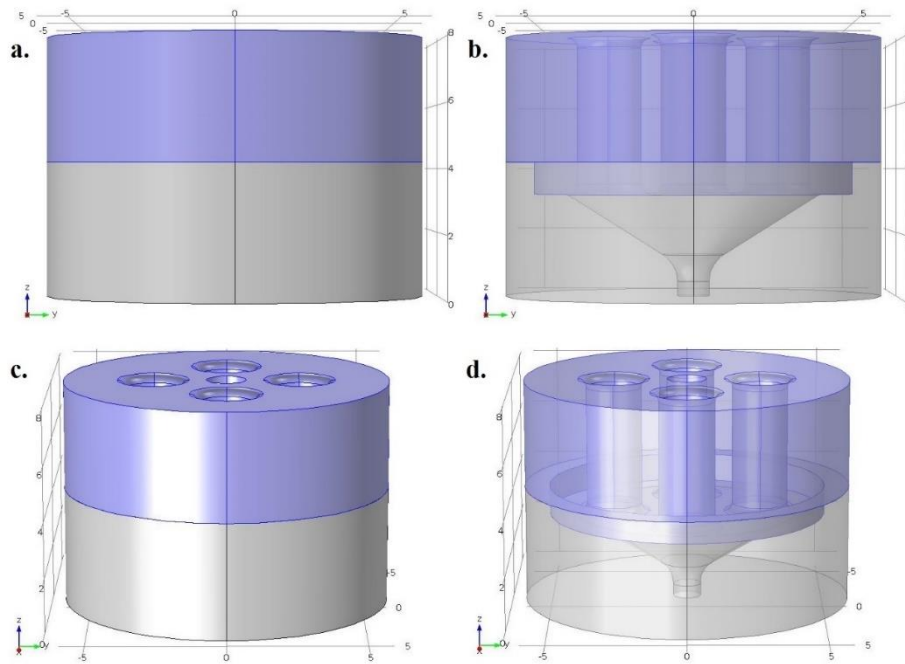


Figure 86. Schematic illustrations of complete set of prototype 9, (a. front solid view, b. front transparent view, c. top inclined solid view, d. top inclined transparent view)

The connection of both parts were fixed using flange type rigid coupling method. The upper part was developed with male flange while lower part was designed with female flange type. Each part had partial design of spinneret geometry which completed by joining both parts as shown in Figure 86.

### 3.2.6 *Prototype 10*

This prototype was developed under consideration of results for better design of composite filament. It was a part of series to made design less complex, more economical and easily cleanable. This design has less surface contact of polymer with spinneret surface, hence weld lines will be reduced in the filament. The only change considered in this design from prototype 9 was the in upper part while lower part remained unchanged.



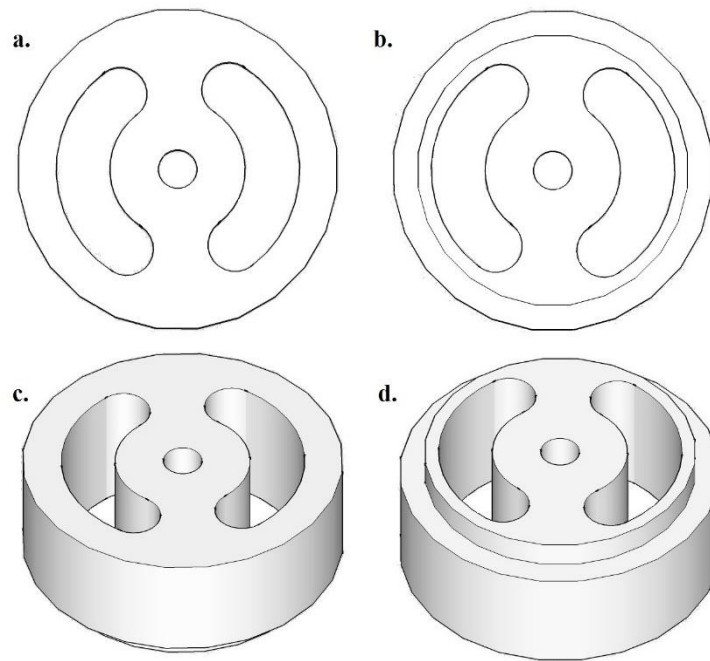


Figure 87. Schematic illustrations of top and bottom views of upper part of prototype 10, (a. top view, b. bottom view, c. top inclined view, d. bottom inclined view)

The flow channel circular holes were replaced with bean or kidney shaped design in upper part. Two bean or kidney shaped designs were used at same angular and radial positions at opposite to each other as shown in Figure 87. The rest of the design of the spinneret was kept same. It is proposed that this design will provide good results with circular filament shape and good positioning of the core in centre.

## **B Modification of machine design**

### ***1 Introduction of tube***

The conventional lab scale melt extrusion machine was modified for the development of composite filament. The hollow piston was used to pass the core filament through it for core sheath composite filament manufacturing. During the melt extrusion process, the core filament passed through the molten polymer having high viscosity. The viscosity introduced frictional drag and resisted to pass the core through it. In addition, the piston mechanism made kinks and bends of core in the oven which enhanced the frictional drag forces on the core filament. The core filament broke during the extrusion process due to high impact of these frictional forces on it. To address this problem, a separate path for core filament was suggested using tube. Two different tubes were analysed and checked for their performance in the prevailing environmental conditions. The high temperature,

compressional and elongational forces and impact forces were the conditions which a tube faced during extrusion process. The compressional forces are observed during descending of piston in oven, elongational forces are observed due to viscous attachments and frictional contact of piston during retreating step from oven. The impact forces can be observed during cleaning steps after extrusion. Considering these factors, ceramic and stainless steel tubes were selected for designing of separate path for core filament.

The ceramic tube had good thermal resistance and compression resistance, but poor impact resistance. The spinneret prototype 6 was used for the said experimentation. The tube was fixed in the U shape of upper spinneret part and the other end of the tube was free to move inside the hollow piston. The core filament was threaded through the hollow piston, tube and spinneret before start of extrusion process as shown in Figure 88. The experimental results obtained using the ceramic tube were acceptable for single run of the process. The breakage percentage of the core was reduced with smooth extrusion process. The ceramic tube was found difficult to clean as it didn't tolerate impact forces. Its brittle nature made it non user friendly for the current experimental runs. In addition, the lower end got choked with polymer. The melt polymer under load found it easy to move inside due to higher inside diameter of tube.

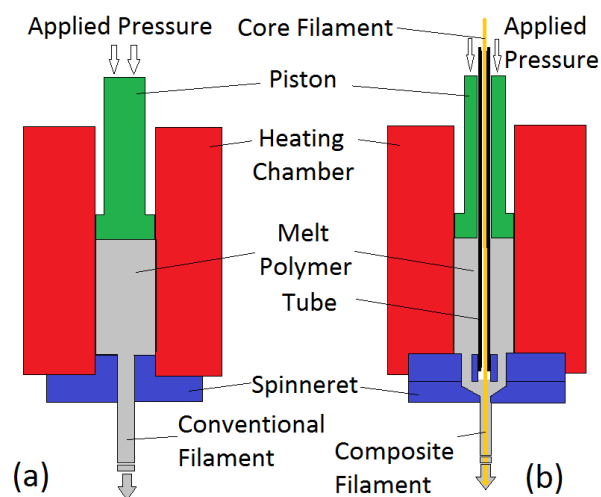


Figure 88. Schematic illustration of the melt extrusion process comparison, (a, conventional process, b. modified process)

Considering the drawbacks in ceramic tube, stainless steel tube was introduced in the centre of the oven for the passage of the core filament through it. The spinneret prototypes 6-10 were used for experimentation with this tube. The lower end of the tube was fixed in the composite spinneret while the upper end was free to move in the hollow piston though

a very close gauge hole at piston lower end as shown in Figure 88 and Figure 89. This modification made it possible to draw the core filament through the oven for development of core sheath structure. The core got in contact with the melt polymer in spinneret region just above the exit point.

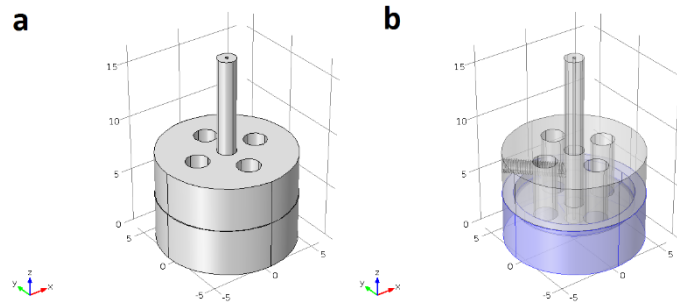


Figure 89. Schematic illustration of fixation of tube in the spinneret set prototype 8, (a. solid inclined view, b. transparent inclined view)

## 2 *Piston modification*

A hollow piston was designed in this lab for the development of composite filament. The developed design was not feasible for extrusion due to flowing of polymer melt inside the piston through its lower end large diameter. The temperature gradient present across the oven walls particularly in hollow piston converted the polymer melt into solid or semi solid state which ultimately cause breakage of the core filament. To recover this problem, the lower end of the piston was modified through number of different designs.

### 2.1 *Type 1*

It was the first design used for experiments without tube in oven. The spinneret prototypes 1 to 5 were used in connection with this piston lower end type. The first top narrow cylindrical region was fixed inside the hollow piston while the lower wider cylindrical region was the bottom end of the piston. In this type, the bottom diameter of the lower end was reduced to very small bore so that it only allowed the core filament to pass through while restricting the polymer melt to flow inside the piston. The conversion from high to lower diameter had smooth surface to reduce the frictional effect on the core filament as shown in Figure 90.

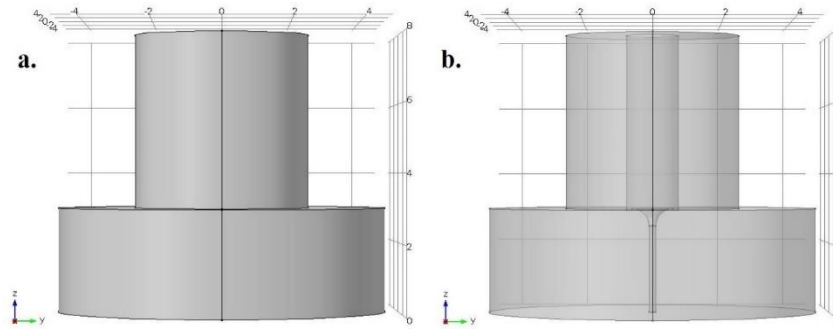


Figure 90. Schematic illustration of front view of piston lower part type 1, (a. solid view, b. transparent view)

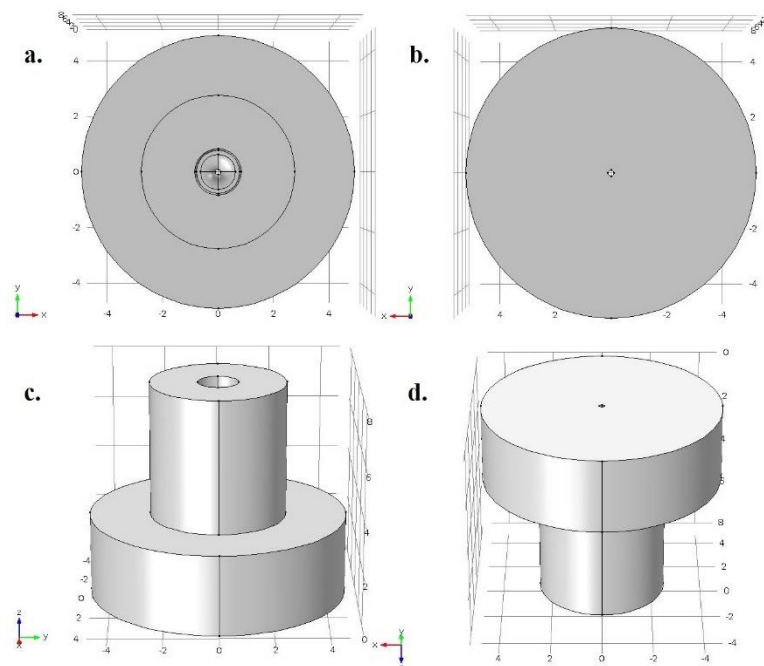


Figure 91. Schematic illustrations of top and bottom view of piston lower end type 1, (a. top view, b. bottom view, c. top inclined view, d. bottom inclined view)

Owing to very small outlet diameter at bottom end of part 1, the flow of polymer was restricted. The high viscosity made it easy to also resist to flow through small holes. The small diameter hole was difficult to clean after extrusion process. Therefore, this design was not found to be a user friendly.

## 2.2 Type 2

This structure was designed in view of easy cleaning. It was comprised of two parts which include central horizontal discs and outer shell. The central horizontal discs had gradual decrease in central axial hollow passage as shown in Figure 92. These discs were two in

number, the upper disc had wider diameter as compared to lower disc. The sharp edges may enhance abrasion of core filament surface due to friction. The top edge of upper disc central hole was grounded to reduce the frictional effects, same like the edges of both sides of lower disc hole were also grounded as shown in Figure 92.

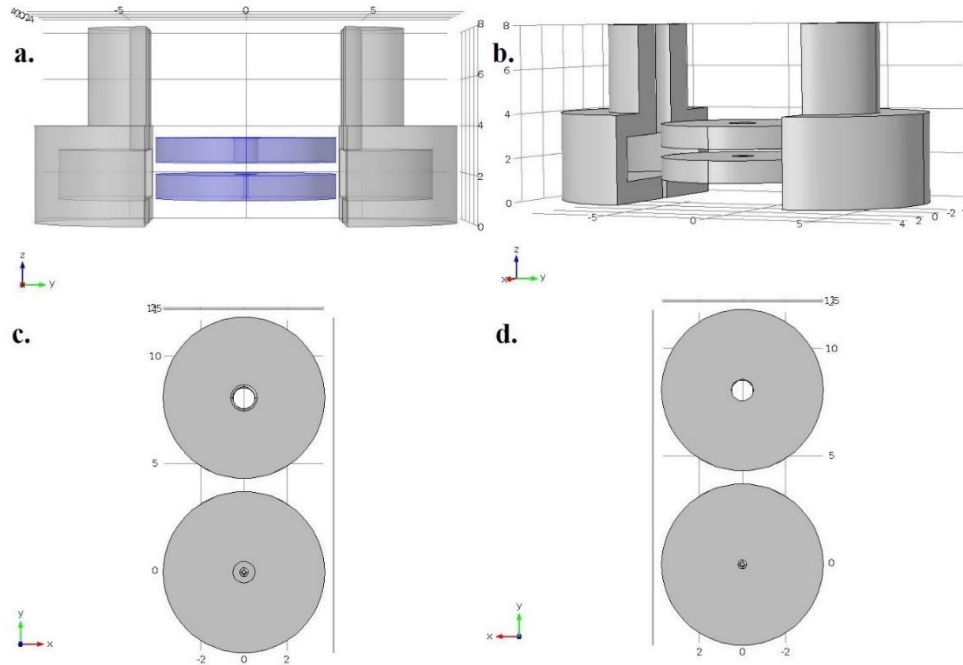


Figure 92. Schematic illustration of parts of piston lower end type 2, (a. front opened view, b. side opened view, c. top view of discs, d. bottom view of discs)

The shell case was made in two semi-circular parts, each having hollow passage for the discs and wide passage above and below to the discs at central axial position as shown in Figure 93. The discs need to be placed in the central hollow position within the shell case part and closed it with the other shell case part to form the complete geometry. The hollow passage above the discs in shell case had wider diameter than upper disc hole, while the hollow passage below the disc in shell case was wider than the lower disc hole to facilitate graduation reduction and easy fixation of shell cases respectively (Figure 94). This design was quite complex as compared to the previous design. Owing to a number of parts, cleaning time increases which was biggest drawback.

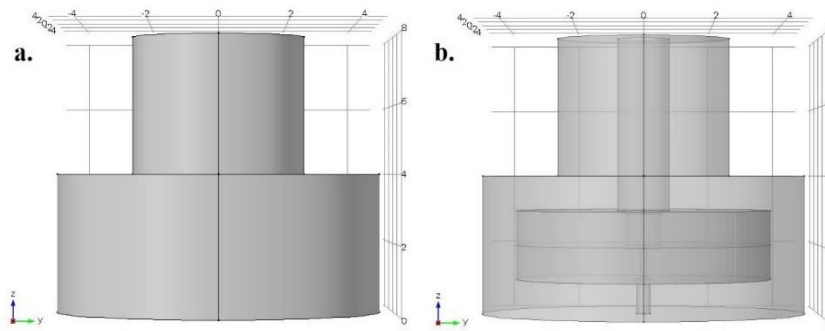


Figure 93. Schematic illustrations of front view of piston lower end type 2, (a. solid view, b. transparent view)

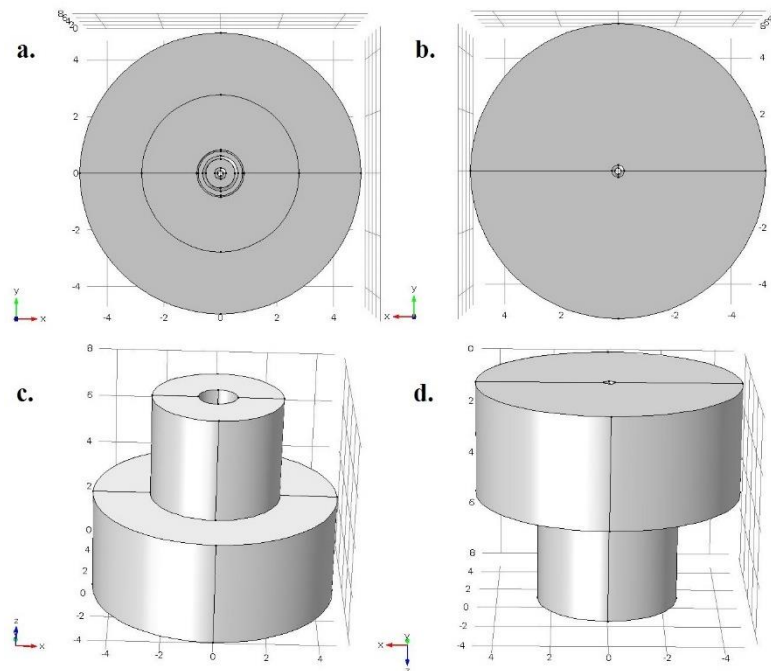


Figure 94. Schematic illustrations of top and bottom views of piston lower end type 2, (a. top view, b. bottom view, c. top inclined view, d. bottom inclined view)

### 2.3 Type 3

This structure was designed for tube movement within the hollow piston. The spinneret prototype 6-9 were tested using this lower piston end type. The design was quite easy to manufacture and easy to clean. a notch was developed at side edge of upper cylindrical part for proper fixation of the design in the piston end. The hollow cylindrical passage designed at the central axial position for tube had small tolerance gap between the hole and the tube. Owing to very small gap, the polymer didn't flow through this small gap around the tube. The front geometry of the design is shown in Figure 95.

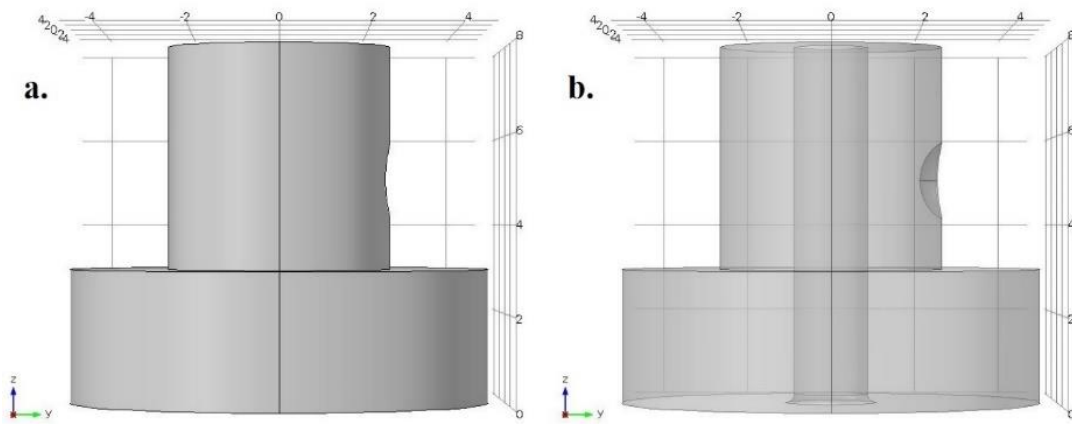


Figure 95. Schematic illustration of front view of piston lower end type 3, (a. solid view, b. transparent view)

The bottom edge of the hole was grounded to made it plain for tube to enter inside the piston easily as shown in Figure 96. The simplest design made it easy to install and clean.

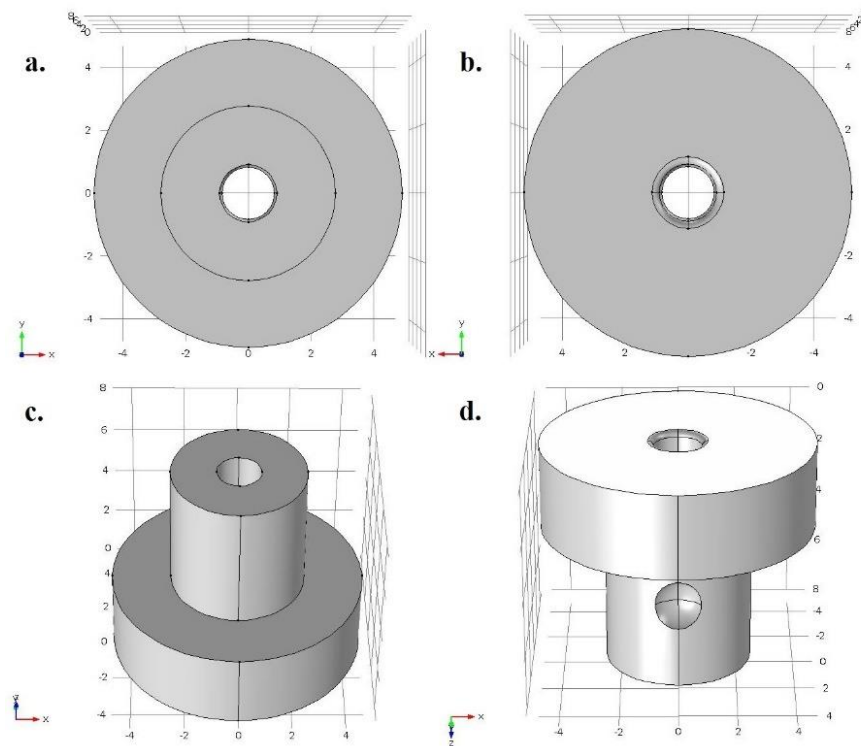


Figure 96. Schematic illustrations of top and bottom views of piston lower end type 3, (a. top view, b. bottom view, c. top inclined view, d. bottom inclined view)

### 3 Cooling chamber

The cooling chamber environmental conditions influence morphological, thermal and performance properties of the filament. These conditions include cooling chamber

temperature, temperature gradient along the length of the chamber and cooling media type used. The dry cooling of the filaments in air was employed in the current study. The change in cooling chamber temperature just after the spinneret and temperature gradient along the length of chamber were studied.

### 3.1 Forced counter airflow

The cooling temperature just after the spinneret was changed by installation of fans. A filament cooling system composed of a number of fans was used to cool down and solidify the polymer extruded out from the spinneret. The cooling system was attached just below the spinneret having height and width of 86 cm and 21 cm respectively. The two arrays of eight fans on opposite sides of the chamber directed the air across the boundaries for efficient cooling process. The one array of fans at one side direct the air from outside to inside of the chamber while the array of fans on the opposite side direct the air out from the chamber to ensure uniform and streamline flow of air as shown in Figure 97.

The spontaneous reduction of temperature of the extrudate exiting the spinneret hole below its glass transition temperature by the help of this arrangement influence on degree of crystallinity obtained in the filament. The change in molecular arrangements ultimately influenced mechanical properties of the developed filament.



Figure 97. Arrangement of fan arrays in cooling chamber

### 3.2 Increase in length

The cooling temperature gradient along the length of the chamber can be changed by changing length of the chamber. The length of the cooling chamber was changed by



increasing the distance between the oven and winding device as shown in Figure 98. A distance was created between the spinneret exit hole and cooling chamber having forced counter airflow to provide temperature gradient from normal cooling at room temperature up to forced cooling level. The change in length of about 60 cm was made to estimate the influence on structural morphology of the composite filament.

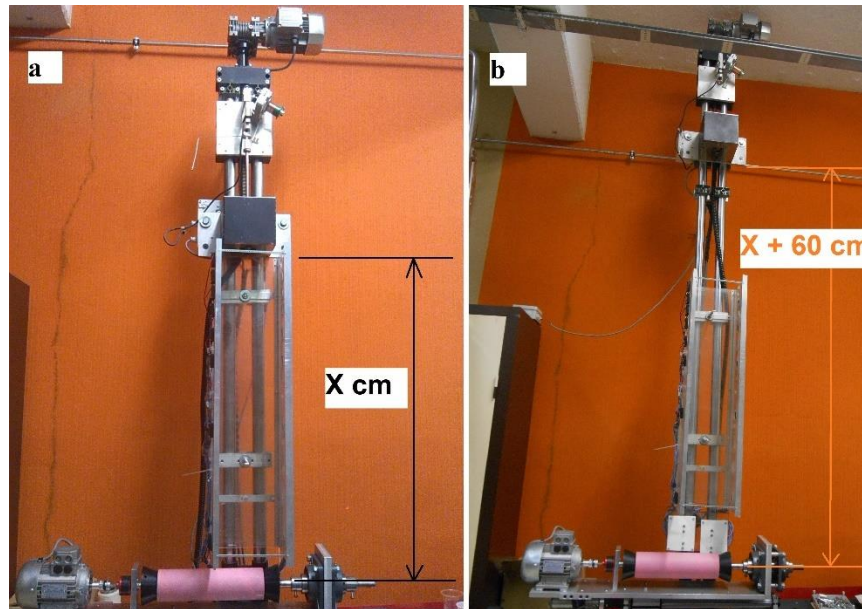


Figure 98. Change in column length of melt extrusion machine, (a. small column length, b. large column length)

### ***III Characterization of polymers***

#### **A Thermal characterization**

##### ***1 Differential scanning calorimetry***

The thermal properties of polyester obtained from diffraction scanning calorimetry analysis are shown in Table 6. It was observed that the polyester in chips form did not exhibit cold crystallization peak (Figure 99), which expressed that the polymer was fairly crystalline in nature. The glass transition temperature and melting peak maxima obtained for polyester chips were 76.96 °C and 237.24 °C respectively. The glass transition, cold crystallization peak maxima and melting peak maxima were obtained at 74.8 °C, 127.93 °C and 250.27 °C respectively for composite filament (Figure 100). It was observed that the composite filament had sharp narrow exothermal peak of crystallization during heating run of sample as shown in Figure 101. This peak was developed because of polymer drawing in a homogeneous temperature field below the polymer glass

transition temperature. The difference between drawing temperature and glass transition temperature was about  $50 \pm 2$  °C. A total draft ratio of 747 was achieved for the melt polymer between spinneret exit and winding package. The polymer chains didn't find the appropriate time to align themselves resultantly crystallinity reduced in the final structure. The uniaxial cold drawing technique converted the fairly crystalline polymer to nearly isotropic glassy structure which is in accordance with previously reported results [164]. It was also observed that the spread of the cold crystallization peak was narrow in width, which explained the fact that the polymer did not faced high stress during the extrusion process. The reason behind is that during extrusion and winding, the stress was faced mainly by the copper filament while the melt polymer just coated the filament during its way through the spinneret. In addition, the rate of elongation of polymer chains was very low due to low level of stress on melt polymer. The low values of stress, drawing temperature and rate of drawing made it possible to reduce crystallization which is also in agreement with literature[171-173]. The line falls after the cold crystallization to almost the same level of virgin polyester which explains that the composite filament polymer attained the same crystallization as virgin polyester during heating run (Figure 101).

Table 6. Thermal properties of polyester in chips and composite filament form

<b>Attribute</b>	<b>PET chips</b>	<b>Composite PET Filament</b>
Glass transition temperature (°C)	76.96	74.8
Cold crystallization temperature (°C)	--	127.93
Melting temperature (°C)	237.24	250.27
Enthalpy of cold crystallization (J/g)	--	27.89
Enthalpy of fusion (J/g)	59.64	40.47
Crystallinity (%)	43.83	9.24

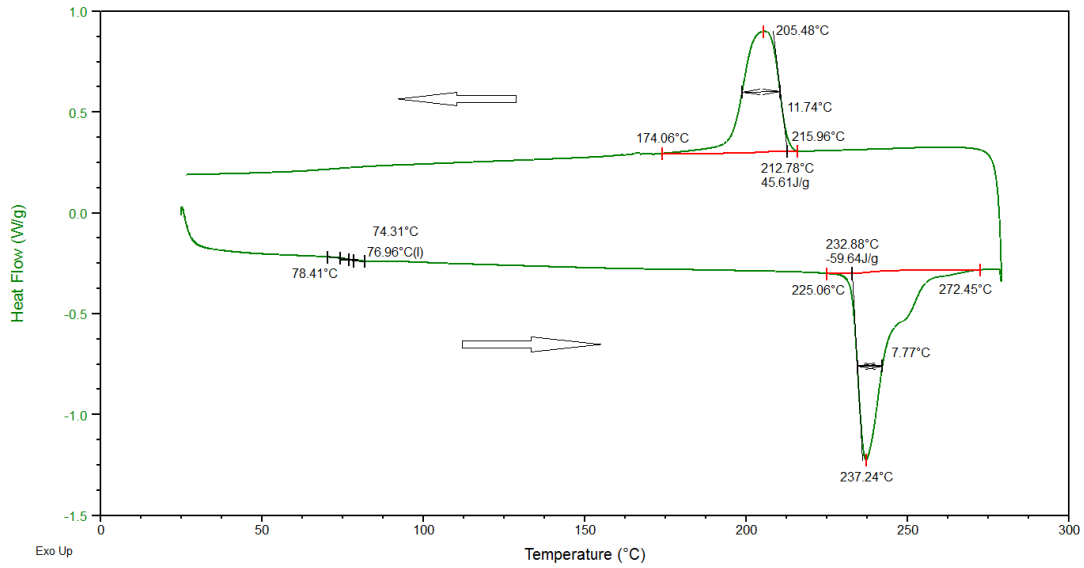


Figure 99. DSC thermogram of PET in chips form

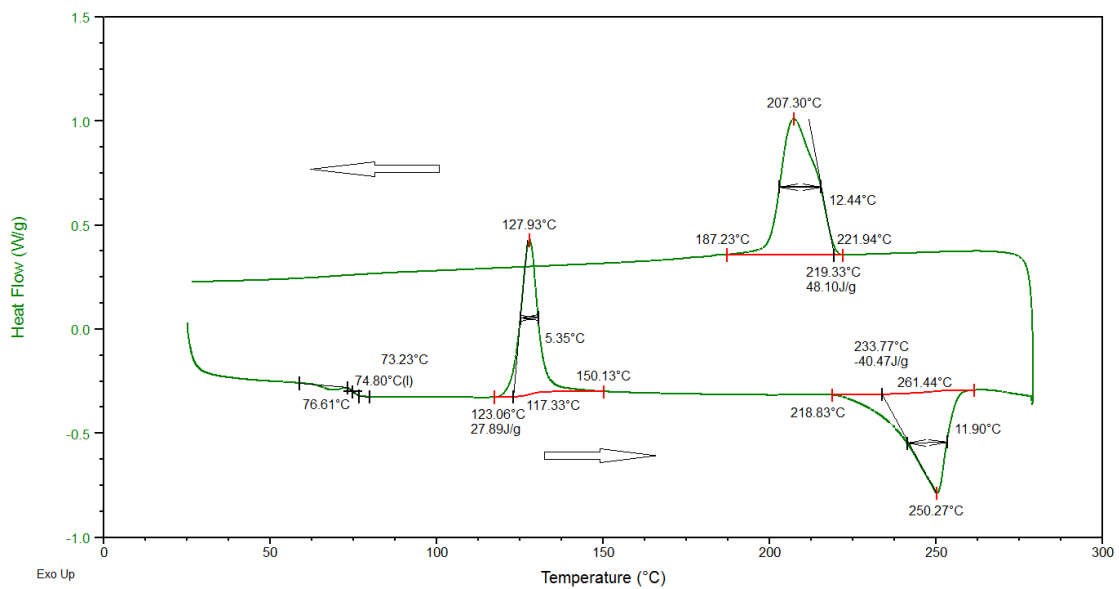


Figure 100. DSC thermogram of PET in composite filament

It was also observed that the melting maxima peak shifted to higher temperature level with more spread for PET composite filament. This is because of the change in the crystallinity of the polymer. The PET polymer in chips form was more crystalline, therefore, it showed narrow heighted peak, while the composite filament polymer become more amorphous in structure and melting peak became wider as shown in Figure 101.

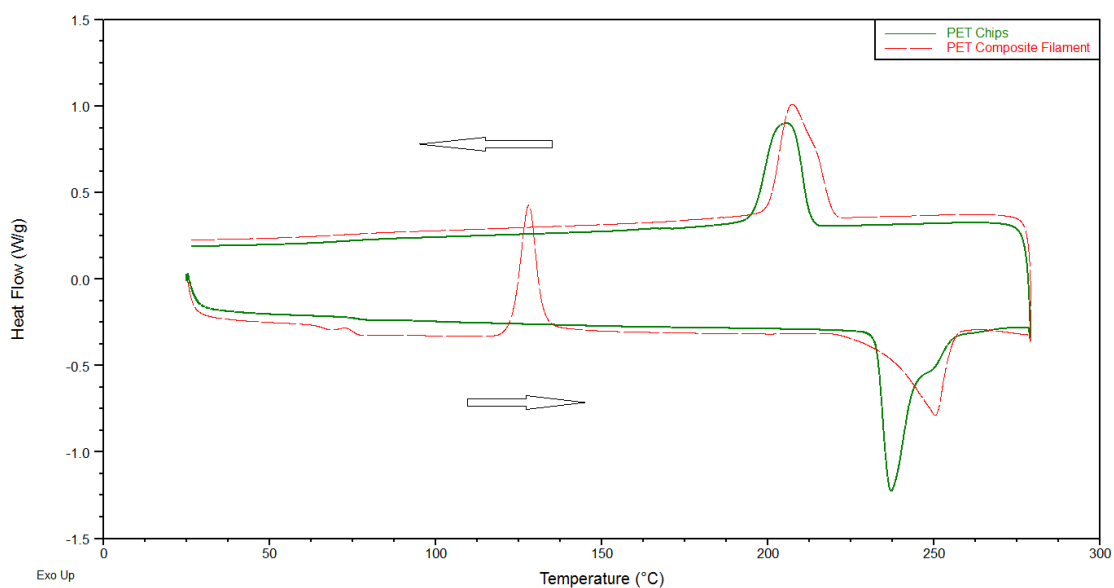


Figure 101. DSC thermogram comparison of PET in chips and composite filament

The degree of crystallinity (%) was low because of the reason that constant temperature field applied was set at temperature of 20 °C which is about 55 °C less than the glass transition temperature. When the polymer gets out of the oven, quenching was done which did not provided enough time to the polymer chains to align themselves. In addition, winding stress applied during the winding process tried to stretch the polymer chains as long as they got in contact with the core filament. The stretching region was too less in length that required stretching didn't be attained for polymer chain alignment. In consideration of all these circumstances, the crystallization percentage decreases from the PET polymer chips.

The ferroelectric copolymer was also analysed for their thermal properties and recorded in Table 7. Two different molecular weight copolymers were used. The thermogram of low molecular weight copolymer in chips form is shown in Figure 102. The temperature observed around 100 °C for ferroelectric copolymers is called as Curie transition which was obtained at 95.5 °C during the heating run of the sample. The melting maxima peak was obtained at 152.75 °C with enthalpy of fusion of 25.78 J/g.

Table 7. Thermal properties of PVDF-TrFE copolymer in chips and composite filament form

Attribute	PVDF-TrFE chips		Composite PVDF-TrFE Filament	
	Low MW	High MW	Low MW	High MW
Curie temperature (°C)	95.5	108.36	103.72	119.45
Melting temperature (°C)	152.75	155.01	151.77	151.28
Enthalpy of fusion (J/g)	25.78	29.17	22.02	23.57
Crystallinity (%)	28	32	24	25

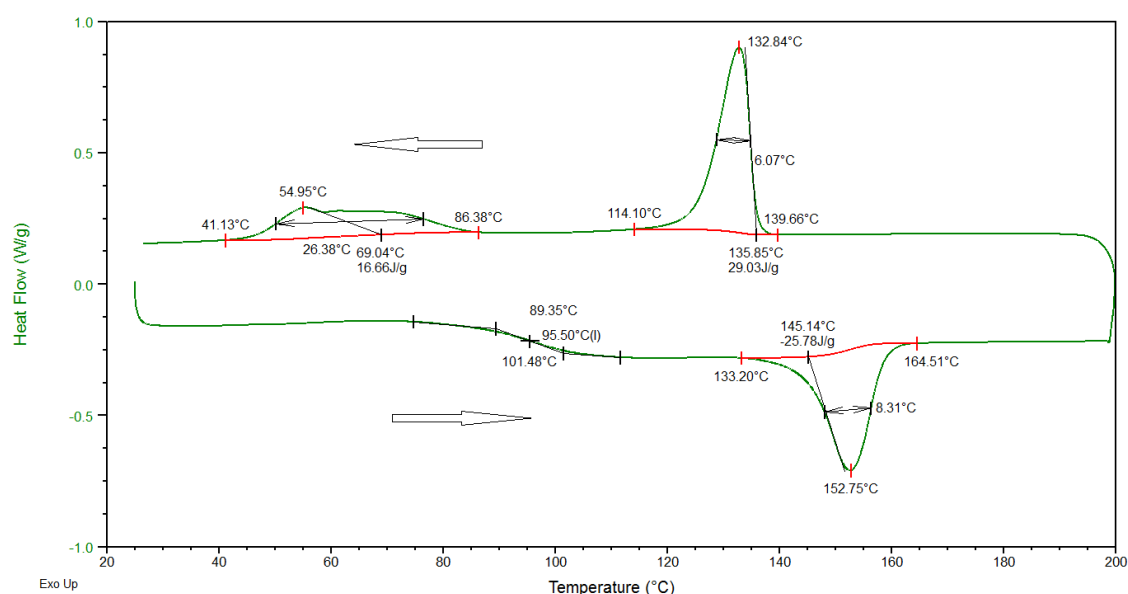


Figure 102. DSC thermogram of low molecular weight PVDF-TrFE copolymer in chips form

It was observed that the curie temperature of the copolymer was raised in composite filament to 103.75 °C as shown in Figure 103. The melting maxima peak shifted to lower value of 151 °C with decrease of enthalpy of fusion to a value of 22 J/g. The crystallinity percentage was also reduced from 28 % to 24 % for chips form to composite form respectively. The reason for the reduction of crystallinity is the same as described before. A very small amount of drawing and stretching of polymer chains along with temperature reduction at fast rate did not provide time to crystallites to align themselves, resultantly crystallinity percentage reduces. The possible reason behind the shift of peak, decrease of

fusion enthalpy and fall of line of composite filament with respect to chips form (Figure 104) was due to transformation of some  $\beta$ -phase crystallize structure to  $\alpha$ -phase. This transformation may be caused due to quenching of polymer without providing enough time along with almost zero stretching of polymer chains during extrusion.

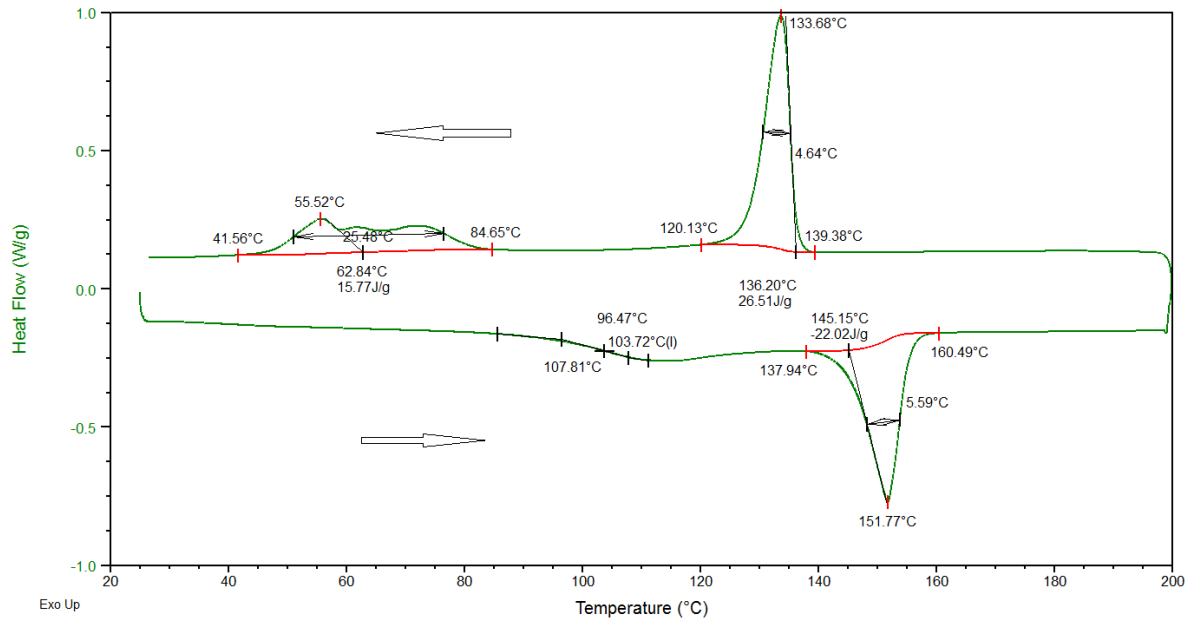


Figure 103. DSC thermogram of low molecular weight PVDF-TrFE copolymer in composite filament

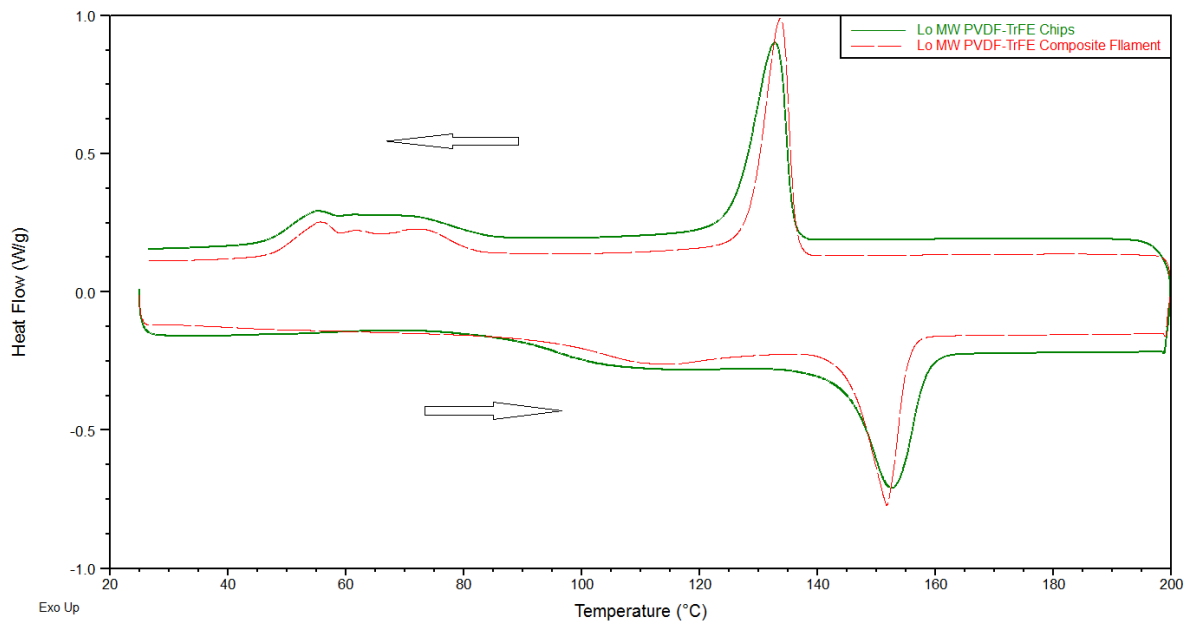


Figure 104. DSC thermogram comparison of low molecular weight PVDF-TrFE in chips and composite filament

The thermograms of high molecular weight ferroelectric copolymer chips and composite filament are provided in Annexure 5. The degree of crystallinity reduces from 32 % to 25 % caused due to above stated reasons. A comparison thermogram of high and low molecular weight copolymer chips and composite filaments were also shown in Annexure 5.

## **B Rheological characterization**

### **1 Melt flow index**

The obtained results of melt flow rate of the thermoplastic polymers are shown in Table 8. The results obtained for polyester were at 2.16 kg mass (21.18 N weight) and 285 °C temperature. The PVDF-TrFE copolymer was tested at 2.16 kg mass and 230 °C temperature.

The obtained results showed that polyethylene terephthalate polymer have very low viscosity resulting which high melt flow rate was obtained at specified temperature. The PVDF-TrFE copolymer exhibit very low melt flow rate resulting high polymer viscosity. The high viscosity may interrupt the melt extrusion process; therefore, high temperature will be required to reduce the viscosity of the polymer for extrusion.

Table 8. Melt flow rate of polymers

<b>Polymer</b>	<b>Melt flow rate (g/10minutes)</b>
Polyethylene terephthalate	27.77
Polyvinyledene fluoride-co-Trifluoroethylene (High Molecular weight) (Hi MW)	0.5
Polyvinyledene fluoride-co-Trifluoroethylene (Low Molecular weight) (Lo MW)	1.5

### **2 Shear rate analysis**

The rheological behaviour of the polymer can be analysed by determining its viscosity at different temperatures and shear rates. The graphical representation of results obtained of viscosity of polyester polymer chips at different shear rates are shown in Figure 105. It was confirmed as per understanding that viscosity decreases by increase in temperature.

The zero shear viscosity obtained for polyester chips at 275 °C, 280 °C and 285 °C were 891 Pa.s, 835 Pa.s and 722 Pa.s respectively. For smooth and efficient process, the viscosity of the polymer should be low within a particular range for ease of flow. At higher temperature, polymer chains became more vibrant and apart from each other, resultantly viscosity decreases.

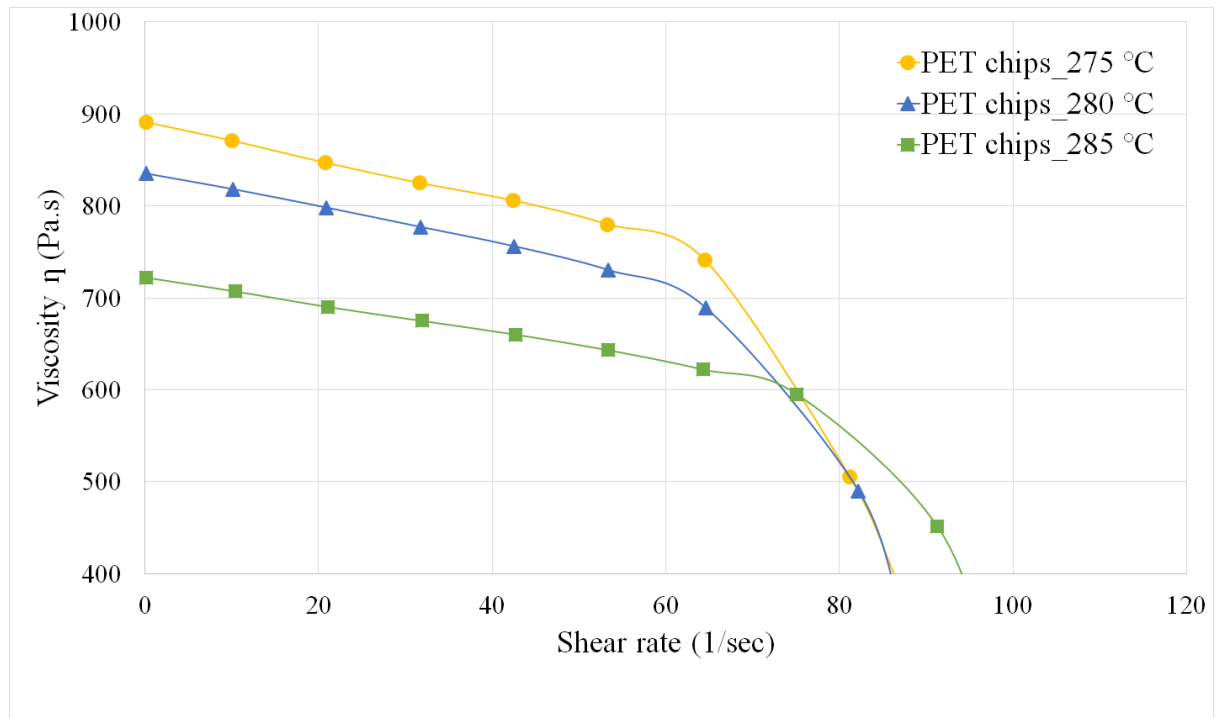


Figure 105. Viscosity Vs shear rate for polyester at different temperatures

The viscosity is plotted vs shear rate obtained at 280 °C showed a significant difference between the viscosity of polymer chips and polyester filament which was developed with the same parameters designed for composite filament development as shown in Figure 106. The Newtonian plateau region for polyester filament was more stable as compared to virgin polyester which explains the change in macromolecular structure during the application of shear forces. The shear thinning region of virgin polyester was found steeper than filament polyester which was caused by higher shearing speed. The zero shear viscosity observed for virgin polyester and filament polyester was 872 Pa.s and 400 Pa.s respectively. The decrease of the zero shear viscosity of PET filament was due to the change in the crystalline structure and chain alignment within the polymer.



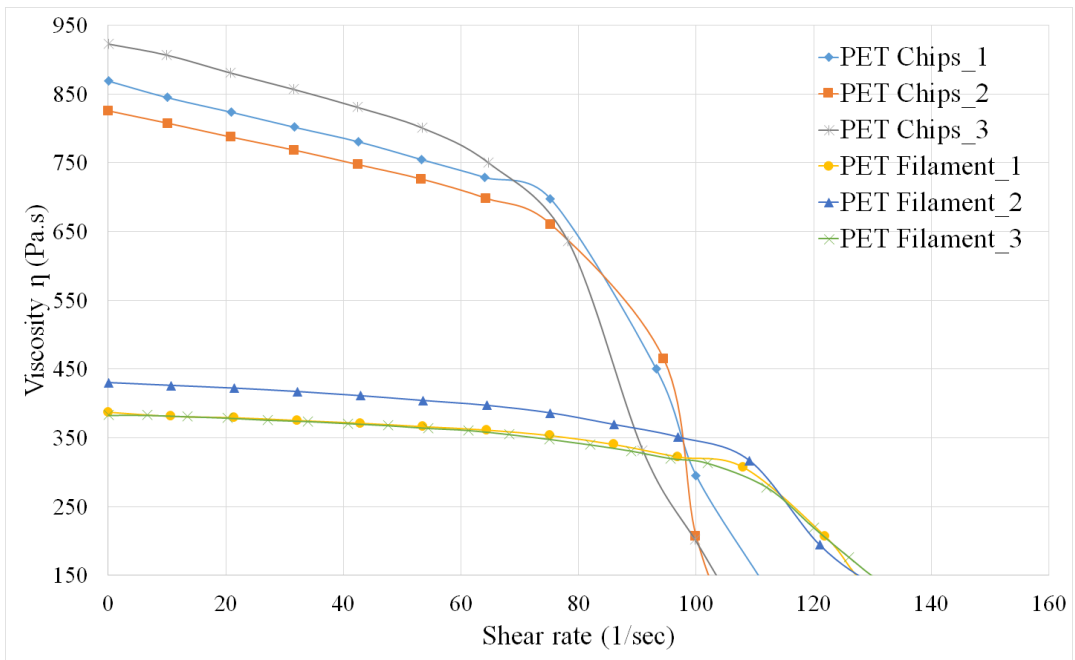


Figure 106. Viscosity vs shear rate of polyester chips and filament at 280 °C

The viscosity versus shear rate analysis was done at different temperatures for PVDF-TrFE copolymer to find out good extrusion temperature as shown in Figure 107. Two different copolymers having high molecular weight (Hi MW) and low molecular weight (Lo MW) were used in this study. The temperature range used for analysis was 250 to 320 °C.

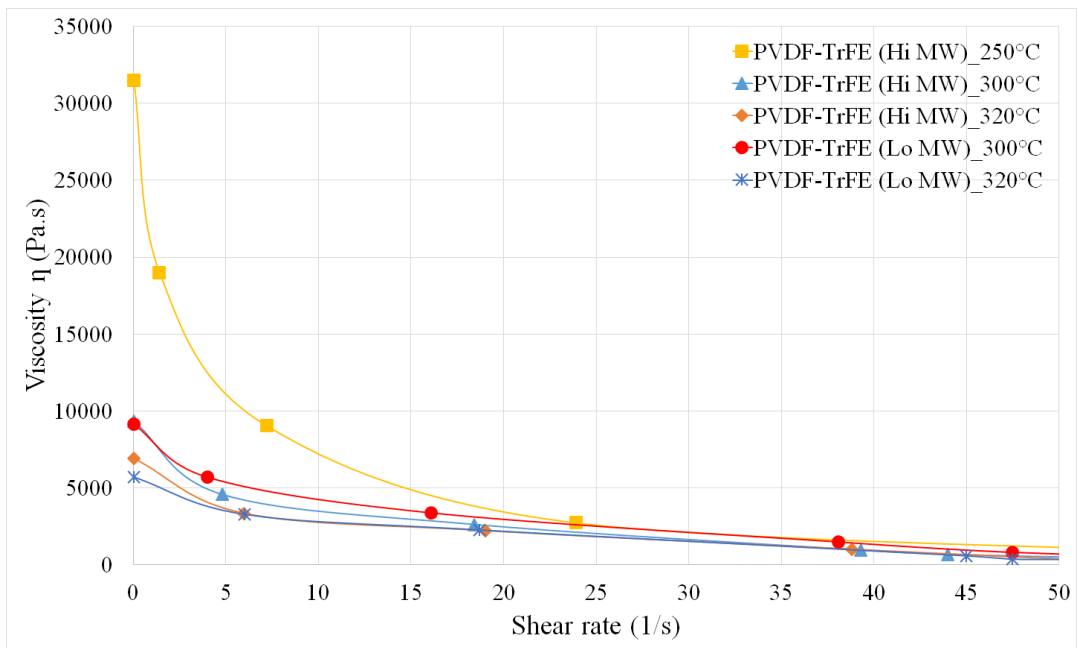


Figure 107. Viscosity vs shear rate of PVDF-TrFE copolymer of different molecular weights at different temperatures

It was observed that the zero shear viscosity for high molecular weight copolymer obtained at 250 °C, 300 °C and 320 °C were 31500 Pa.s, 9350 Pa.s and 6900 Pa.s respectively. Likewise, for low molecular weight copolymer, the zero shear viscosity obtained at 300 °C and 320 °C were 9150 Pa.s and 5700 Pa.s respectively. It was also observed that by the increase of shear rate, the viscosity drops steeply until it came within range of 5000 Pa.s. Afterwards, the change in viscosity was slow and steady. In addition, at high temperatures, the zero shear viscosity observed was quite less as compared to low temperature.

### C Analytical characterization

The structural analysis was done using X-ray diffraction method for polymer chips and composite filaments. In this method, x-ray of linear monochromatic copper-K $\alpha$  1 beam having a wavelength of 1.5405 Å generated from sealed tube generator of 600 Watt equipped with bent quartz monochromator was used. The X-ray patterns were recorded with a curved Inel CPS 120 counter gas filled detector.

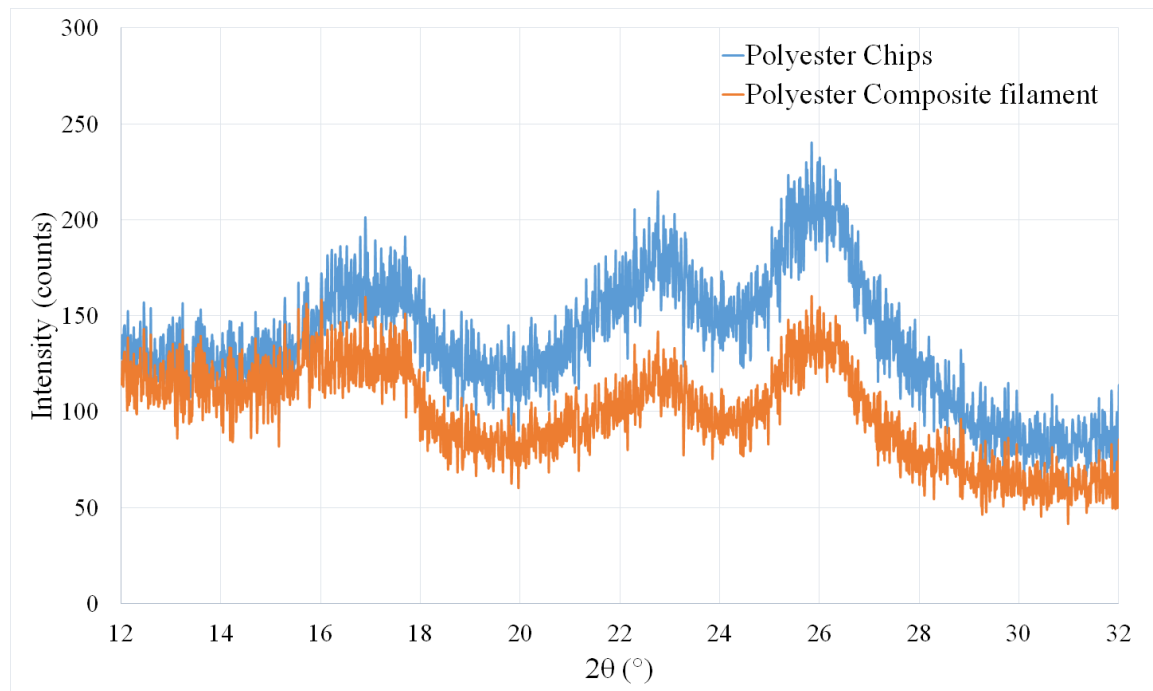


Figure 108. X-ray diffraction patterns for polyester in chips and composite filament form

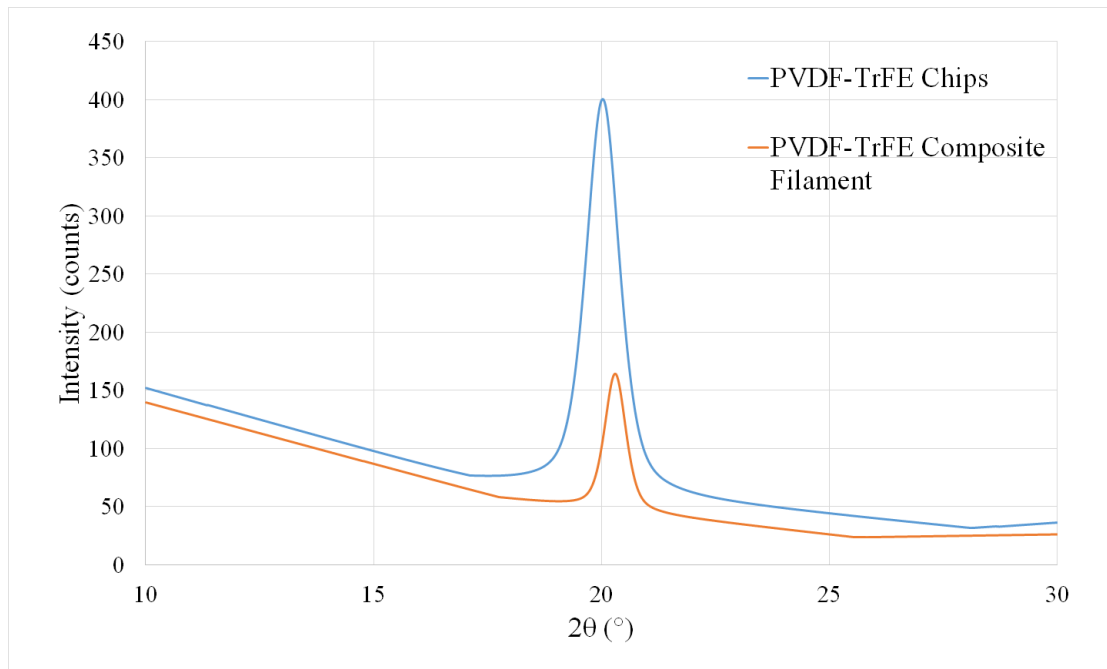


Figure 109. X-ray curves obtained for PVDF-TrFE copolymer in chips and composite filament form

The X-ray diffraction curve obtained for polyester polymer is shown in Figure 108. It was observed that the patterns obtained for polyester chips were having high intensity as compared to the composite filaments. It confirms the DSC results of reduction of crystallinity of polyester in composite filament.

The X-ray curves obtained for PVDF-TrFE copolymer in chips and composite filament form are shown in Figure 109. It was observed that copolymer in chips form had higher intensity as compared to composite filament. this increase in intensity confirms the higher crystallinity obtained in chips form than composite filament which comply with the results obtained in DSC measurements.

#### ***IV Optimization of melt extrusion process***

##### **A Optimization of spinning parameters**

A design of experiment (DOE) was developed for optimization of spinning parameters including piston speed and winding speed as given in Table 9. The spinneret prototype 8 having 3 holes in upper part, position of tube at 2 mm down position with respect to bottom level of upper spinneret part, tube inner diameter of 254  $\mu\text{m}$  and 1 mm spinneret diameter was used.

Table 9. Design of experiments for optimization of spinning parameters

Serial No.	Piston speed (mm/min)	Winding speed (rpm)
1	3	120
2	5	
3	7	
4	5	100
5		120
6		140

The winding package used had diameter of 81.5 mm. The temperature of the oven is capable to be set at different temperatures at upper and lower regions which were set at 280 °C and 290 °C at upper region and lower region respectively.

The results obtained showed that by increasing piston speed, the input material flow increases and ultimately cross-sectional geometry got effect as shown in Figure 110. At lower input, the polymer was dragged out of the spinneret which made the formation of a coating assembly; when input increases, the material flow rate effected the cross-sectional shape of the filament.

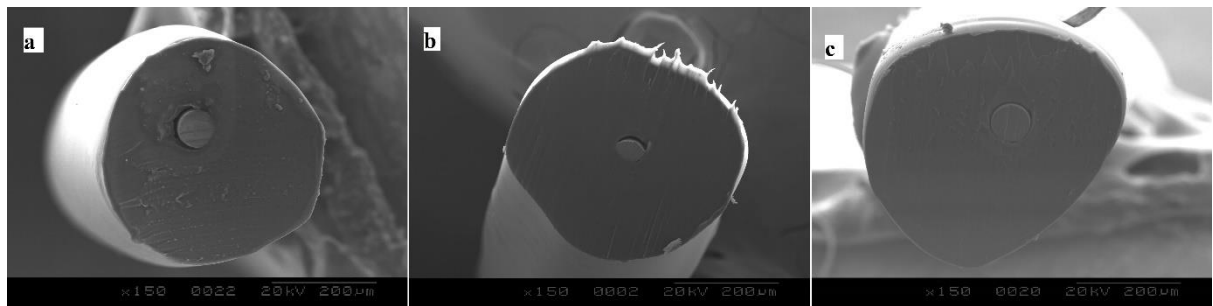


Figure 110. SEM cross-sectional images of composite filament developed at different piston speeds, (a. 3 mm/min, b. 5 mm/min, c. 7 mm/min)

On contrary, when the winding speed increases, the filament became more regular in shape as shown in Figure 111. It was observed that by increasing speed, the cross-sectional shape of the filament changed. At slow speed, a triangular shaped filament was obtained keeping all the parameters same. As the speed increases, the triangular started to change to regular shape and surface. The reason lies in the fact that at slow speed, the flow velocity act upon the shape, as the conical region of lower spinneret part was already filled up so upcoming

flow induces pressure on the material already present in that region which bring change in shape. When the speed increases, the material in conical region of lower spinneret part started consuming as long as it enters in it. The incoming flow didn't find more time to start pushing the material already present in the region and hence a very smooth coating started to develop on the core filament. the walls of the exit hole also play its role to regularize and smoothen the surface of the filament.

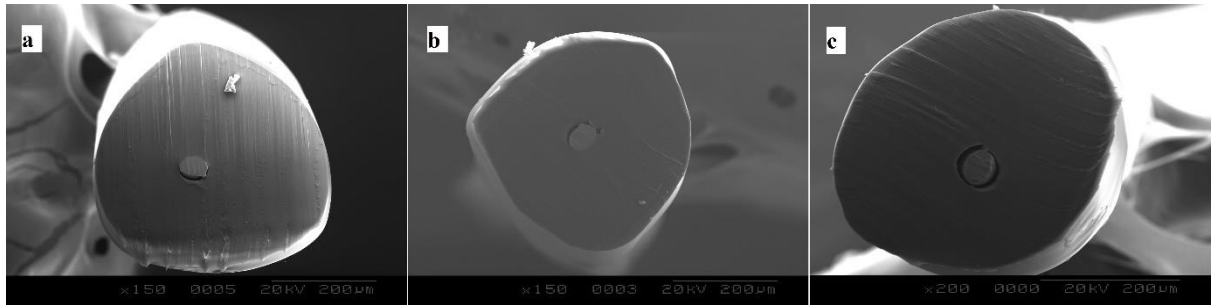


Figure 111. SEM cross-sectional images of composite filament at different winding speeds, (a. 100 rpm, b. 120 rpm, c. 140 rpm)

The drawing ratio was calculated for the developed filament using the Equation 16.

$$D.R = \frac{V_2}{V_1} = \frac{\pi DN}{V_1} \quad (16)$$

Where, D.R is the draw ratio,  $V_2$  is the linear speed of package, D is the diameter of package (8.15 cm), N is the revolutions of package (rev./sec) and  $V_1$  is the linear speed of melt polymer through spinneret (cm/s). The linear speed of melt polymer through spinneret was used as calculated by Equation 15 which was 0.08 cm/s.

$$D.R = \frac{\pi \times 8.15 \times (140/60)}{0.08} = 746.78$$

The draw ratio obtained for the extrusion process was too high at value of 747, which did not provided time for the polymer chains to align themselves. The melt polymer started dragging along with the surface of copper filament and a coating type mechanism was achieved.

## B Optimization of filament cutting method

The composite filament samples were developed by cutting at cross sectional direction by different tools including scissors, sharp edge cutting blades and surgical blades at different

temperature conditions including room temperature and at  $-10 \pm 3$  °Celsius temperature. The results of different cutting methods are shown in Figure 112.

The obtained results revealed that the shape of the composite filament deteriorates with non-proper method of cutting. It was evident from the obtained results that the core of the filament changes its position due to non-proper cutting tool which impart a large noise variable in product characteristics. Furthermore, it was also observed that the impact of pressure and temperature during cutting also influence significantly on the cross-sectional shape deterioration. The results shown in Figure 112 explain the clear view of cross-sectional deterioration by different methods.

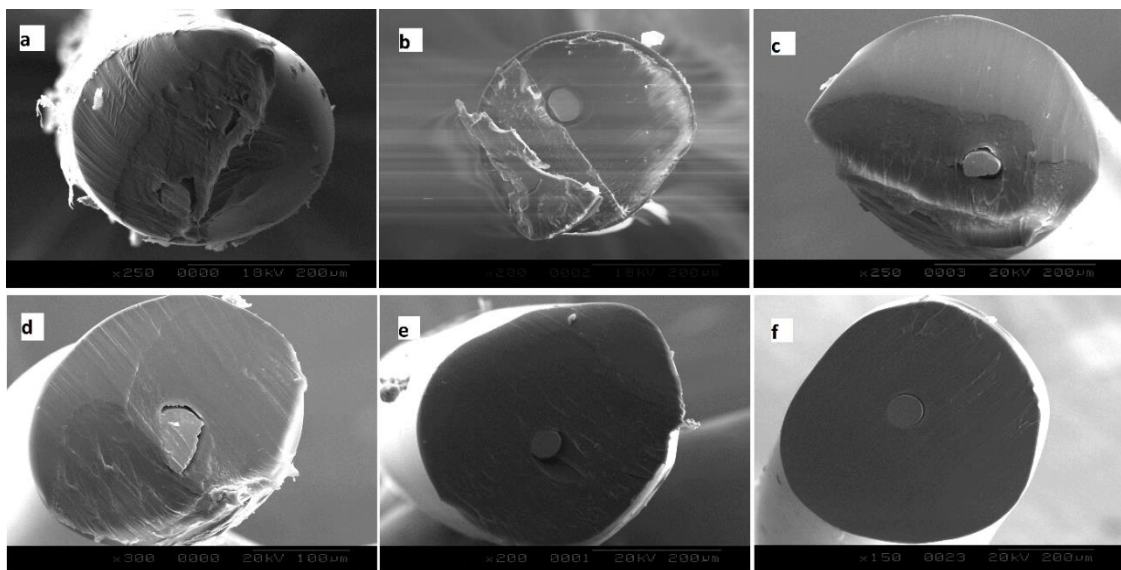


Figure 112. SEM cross-sectional images of polyester coaxial composite filaments cut by different techniques, cutting at room temperature (a) scissor, (b) paper cutting blade, (c) Hamaguri grind blade, (d) single bevel grind blade, (e) Zero ground saber blade; cutting at  $-10 \pm 3$  °C (f) zero ground saber blade

At temperature higher from  $0^{\circ}\text{C}$  (room temperature), the polymer starts behaving like a soft material and caused sliding during cutting. At lower temperature, the brittle nature of the polymer became prominent which cause breakage of the polymer due to applied stress at cut point. Both of the stated causes made the cut irregular and also caused the dislocation of the core filament from actual position.

The clean and fine cut of the composite filament was achieved using zero ground saber grind blade below zero Celsius ( $-10 \pm 3$  °C). The increase in polymer hardness made it possible to have a clean cut along with minimal core movement during the cutting process.

## **C Optimization of spinneret design**

### ***1 Conventional simple spinneret***

The conventional simple round spinneret was used to produce coaxial composite filament. The results were non-reliable and non-reproducible. The core was found at edges due to improper supply of core at central position as shown in Figure 113. The core passed through the melt polymer and observed high frictional drag during the whole extrusion process.

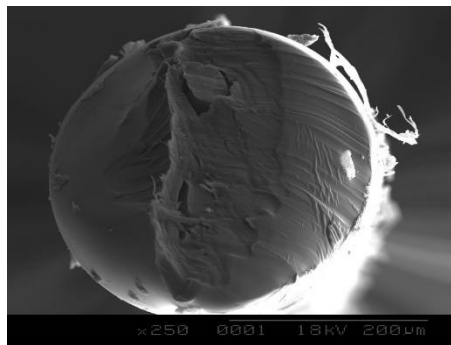


Figure 113. SEM cross-sectional image of composite filament through conventional spinneret

### ***2 Prototype 1-4***

The spinneret design prototypes 1-4 were not manufactured physically for experimentation due to their complex and sophisticated contours and design. The large length drilling was not possible in small diameters and conical shapes using conventional mechanical methods. These designs need precise machining equipment with good expertise to manufacture.

### ***3 Prototype 5***

This design had the feature to supply core at central axial position of the spinneret through a very small hole in a tube. The small length of tube having diameter of 127  $\mu\text{m}$  was cut to install in the developed design. The inner diameter was so small that during cutting it got blocked with conventional tube cutter. Owing to complexities of development, this design was not functional to be used for experimentation.

### ***4 Prototype 6***

The prototype 6 was developed and tested for its performance. Polyester virgin polymer was used as resin matrix. The ceramic Alumina tube was used for passage of copper

filament having inner diameter is 0.8 mm. the experiment was carried out at temperature of 295 °C, resident time of polymer in the oven of 5 minutes, piston speed of 4.5 mm/minute and winding speed of 60 rpm. The ceramic tube has low bending and impact resistance. The ceramic tube broke during extrusion due to bending caused by the solid polymer chips. The results obtained using this prototype design is shown in Figure 114. It was observed that the core of the filament was not at central coaxial position. It was explained by the inner diameter of the ceramic tube where the core found large space to move across the inner diameter. The results were not reproducible nor reliable.

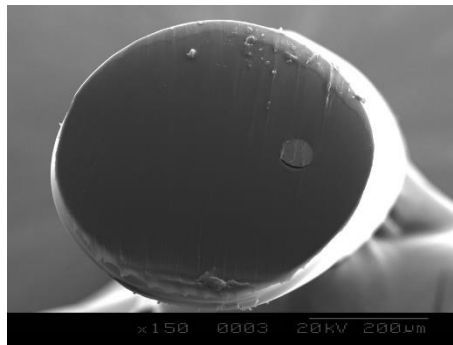


Figure 114. SEM cross-sectional image of composite filament through prototype 6

### 5 *Prototype 7*

A screw was installed in the upper part to hold the tube placed inside the U shaped geometry. Considering the brittle property of ceramic, stainless steel tube was introduced in this structure. The tube having diameter of 762 µm was used. The extrusion was carried out at 295 °C with resident time of 5 minutes, piston speed of 5 mm/min and winding speed of 60 rpm. It was observed that core was not at coaxial position. The reason lied in the fact that the tube inner diameter was wider as well as the end point of the tube was also at higher position from spinneret exit hole.

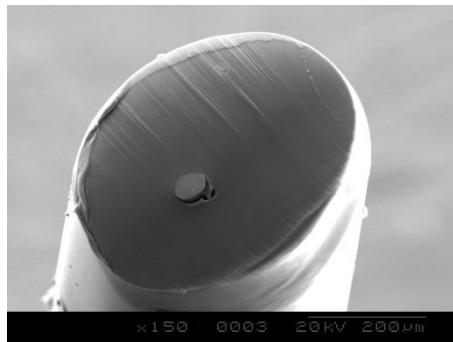


Figure 115. SEM cross-sectional image of composite filament with prototype 7



## 6 *Prototype 8*

In the whole process of improvement of spinneret design, prototype 8 was the first design which was considered to be the real potential design in economical, manufacturing as well as performance point of view. The first trial run was carried out using tube of 254  $\mu\text{m}$  inner diameter at temperature of 290  $^{\circ}\text{C}$ , resident time of 5 minutes of polymer in oven, using piston speed of 5 mm/min and winding speed of 60 rpm. The position of the tube was at 2 mm below the level of upper spinneret part. The number of holes in the upper part were 2 in number. The cross-sectional image of the filament developed is shown in Figure 116.

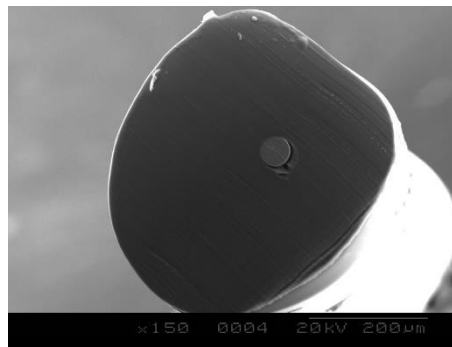


Figure 116. SEM cross-sectional image of composite filament using prototype 8

It was observed that the obtained filament had core at quite near to the central coaxial position. The shape of the filament obtained was not circular in geometry. Optimization was performed to find the best level of parameters to obtain required morphology of composite filament.

A number of variables were considered to analyse their influence on the performance and quality of the developed composite filament structure. The optimization results were later on used for modification in design in prototype 9. These variables include number of holes, tube position with respect to upper spinneret part, lower part exit diameter and tube internal diameter. Different number of holes were analysed including 2 holes, 3 holes and 4 holes in upper spinneret part as shown in Figure 117. All the holes were drilled at same angular and radial position from central axis. The position of the tube would impact on the positioning of core as per our second hypothesis. Therefore, two tube positions were selected which was measured with reference of bottom level of upper spinneret part. The tube end at same level with bottom of upper spinneret part was considered as 0 mm while the tube whose end was below 2 mm from bottom of upper spinneret part was considered

as 2 mm position as shown in Figure 118. The spinneret exit diameter was also studied having different diameters of 1 mm and 2 mm as shown in Figure 119. Five different inner diameter stainless steel tubes were selected for this study having diameters of 127  $\mu\text{m}$ , 178  $\mu\text{m}$ , 254  $\mu\text{m}$ , 508  $\mu\text{m}$  and 762  $\mu\text{m}$  as shown in Figure 120. At first, the core filament was tried to pass through tube having inner diameter of 127  $\mu\text{m}$  and 178  $\mu\text{m}$ , which was not possible due to large tube length and higher frictional contact between them. Therefore, these diameter tubes were excluded from the design of experiments. The design of experiments developed is given in Table 10. Starting from smallest inner diameter tube, the results were optimized and applied the best results on larger inner diameter tubes.

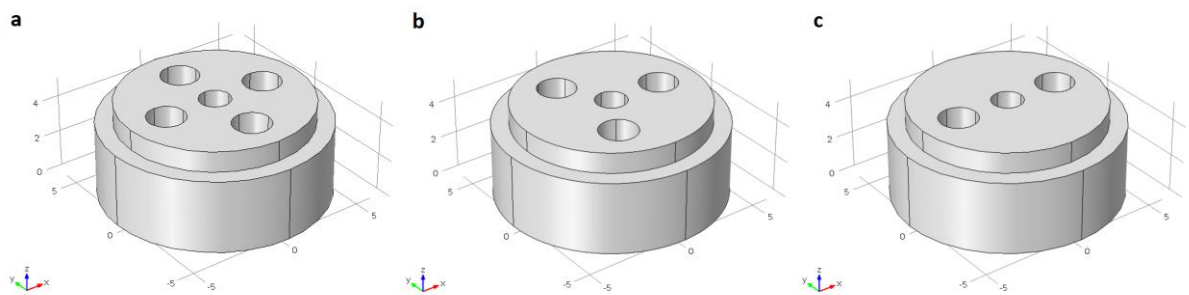


Figure 117. Schematic illustration of different number of holes in upper part for characterization, (a. 4 holes, b. 3 holes, c. 2 holes)

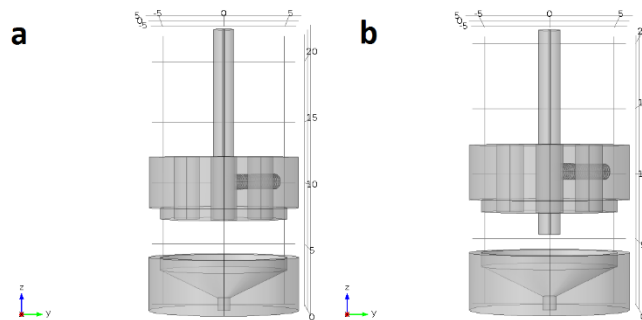


Figure 118. Schematic illustration of tube position with respect to upper part bottom level for characterization, (a. position 0 mm, b. position 2 mm)

The copper wire was drawn through the hollow piston, tube and composite spinneret followed by charging of oven with dried polymer chips. The temperature of the extrusion oven was set at 280  $^{\circ}\text{C}$  and 290  $^{\circ}\text{C}$  at upper and lower region of oven respectively and resident time for polymer in oven was 5 minutes. The spinning parameters including piston speed and winding speed were set at 5 mm/min and 35.85 m/min (140 rpm) respectively. The drawing was done with homogeneous temperature field drawing technique which

provide constant drawing rate with necking. The drawing of filament was done at temperature ( $T_{dr}$ ) of 25 °C, which was 55 °C less than the glass transition temperature ( $T_g$ ) to reduce the crystallization in composite filament from virgin polymer. The drawing below or equivalent to glass transition ( $T_{dr} \leq T_g$ ) is specified as cold drawing which resultantly generate neck formation and propagation of neck along the specimen [164]. The coaxial filament was wound on package with winding system. The coaxial filaments obtained have the diameter in the range of 350  $\mu\text{m}$  to 500  $\mu\text{m}$ .

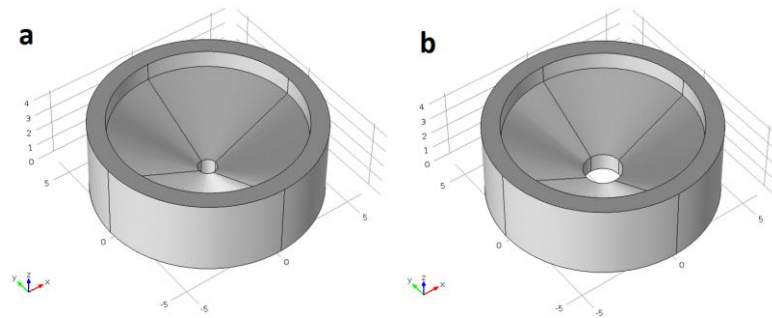


Figure 119. Schematic illustrations of different spinneret exit diameters in lower part for characterization, (a. diameter 1 mm, b. diameter 2 mm)

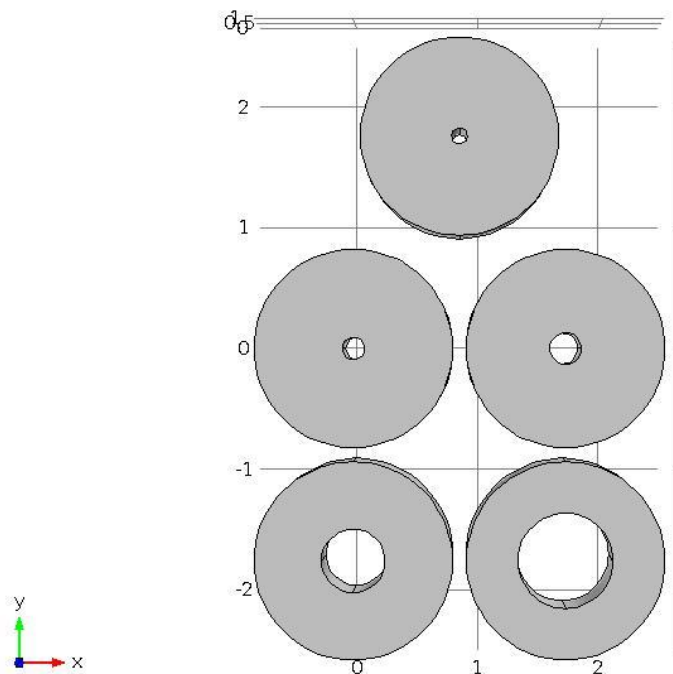


Figure 120. Schematic illustration of different tube internal diameters for characterization

Table 10. Design of experiments for characterization of spinneret design

Sample code	Tube internal diameter ( $\mu\text{m}$ )	Number of holes	Tube position (mm)	Spinneret exit diameter (mm)
1	254	2	0	1
2				2
3			2	1
4				2
5		3	0	1
6				2
7			2	1
8				2
9		4	0	1
10				2
11			2	1
12				2
13	508	3	2	2
14		4	2	1
15	762	3	2	1
16		3	2	2

A total number of 208 experimental runs, comprising of 16 individual samples with 13 replicates each, were analysed for characterization of spinneret design. The cross-sectional cutting of developed coaxial filaments was done in cold environment with sharp blade [123]. The SEM analysis was used to obtain the cross-sectional images for further geometrical analysis of the coaxial filaments.

#### 6.1 *Effect of number of holes on geometrical structure of composite filament*

The samples were developed and cut vertically to analyse their cross-section on SEM. It was observed that the number of holes had significant influence on cross-sectional shape

of the filament. The filaments were developed in shape of elliptical, triangular, rectangular and circular shapes by changing number of holes in upper spinneret part as shown in Figure 121. The spinneret having 2 holes produced filament in elliptical shape, spinneret having 3 holes produced triangular shaped filament and spinneret having 4 holes produced rectangular shaped filament. The reason lies in the fact that holes were the source of input material in the conical section of lower spinneret part. The flow velocity influenced on the filament shape and structure. This effect was more pronounced when the exit hole diameter increases and effect of flow directly control the filament shape which was reduced in small diameter exit hole. Circular cross-sectional filaments were obtained both by 3 holes and 4 holes' spinneret design using smaller diameter spinneret exit hole.

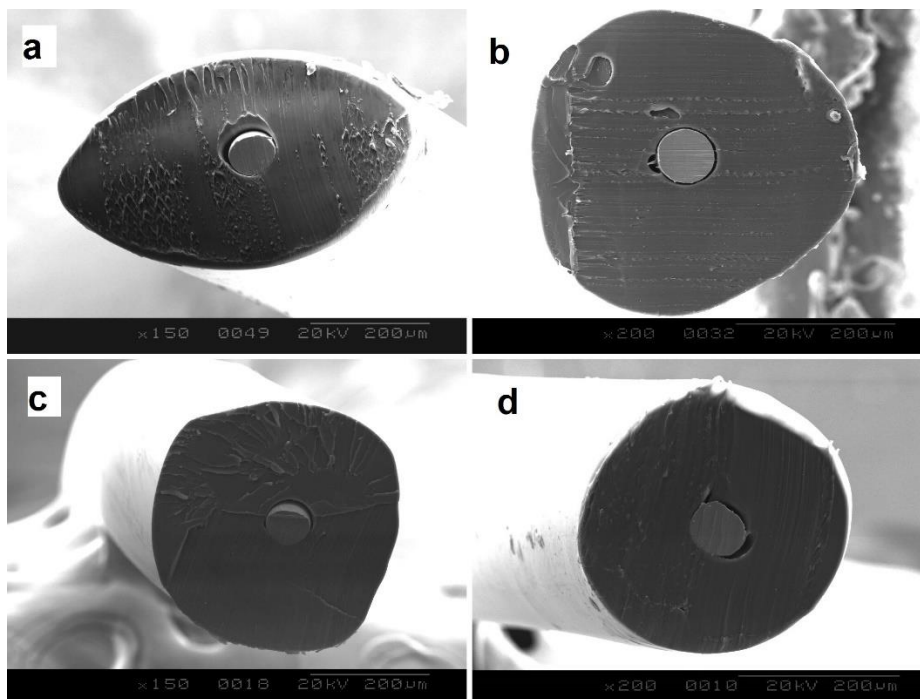


Figure 121. SEM cross-sectional images of composite filaments developed by different number of holes in prototype 8, (a. 2 holes, b. 3 holes, c. 4 holes, d. 4 holes)

## 6.2 Effect of tube position on geometrical structure of composite filament

It was also observed that tube position significantly influenced the position of the core in composite filament structure as shown in Figure 122. A good coaxial composite filament was obtained when the position of the tube was closer to the exit hole of the spinneret. The reason was that core filament was introduced in control manner at central position when tube position was near to exit point of spinneret (2 mm). As the tube was raised, the probability of the core to be at the central position started reducing. At higher position more forces started acting on the core filament which drag it from central position to other

paths, any small drag will change the central axial position of the core in the composite filament. When the core filament exits from the tube, the control over the core filament reduced and its path may be changed due to flow velocity or applied stresses in extrusion process.

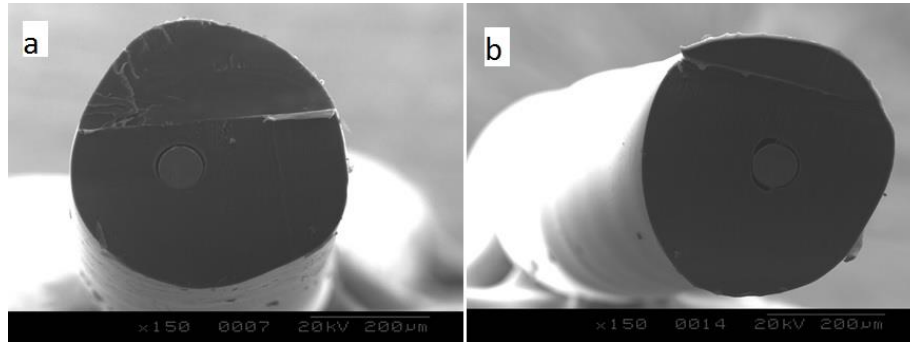


Figure 122. SEM cross-sectional image of composite filament developed with different position of tube in spinneret, (a. 0 mm, b. 2 mm)

### 6.3 Effect of spinneret exit diameter on geometrical structure of composite filament

The cross-sectional shape of the filament also changed by change in spinneret exit diameter as shown in Figure 123. The flow velocity in the conical region was partially neutralized by the conical shape of the lower spinneret part, while the rest was neutralized by the spinneret exit diameter. When the spinneret exit diameter was smaller, it restricted the over flow as well as induced effect of flow velocity from different directions. This limiting effect of flow velocities from different directions changed the shape of the filament as the shape of the exit hole of the spinneret. As the hole was circular in shape, therefore exit hole of smaller diameter provided more regular and circular cross-sectional shaped filament as compared to large diameter exit hole as shown in Figure 123.

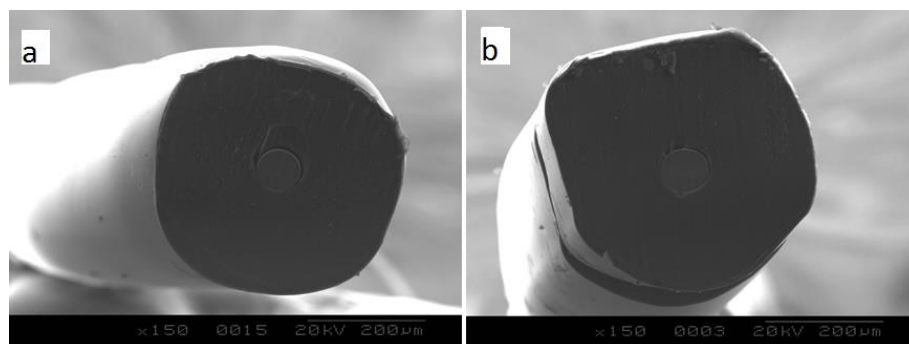


Figure 123. SEM cross-sectional images of composite filament developed with different spinneret exit diameters, (a. 1 mm, b. 2 mm)

#### 6.4 Effect of tube inner diameter on geometrical structure of composite filament

It was observed that the tube inner diameter influenced the position of the core in the composite filament. The tube having larger inner diameter provide more space to the core to move across the inside boundaries of the tube. This high tolerance reduces the control over the core to introduce it at exact central position for the development of coaxial composite filament. Therefore, a tube having smaller inner diameter provide the required control on the core filament to be introduced at central axial position of the spinneret for coaxial filament development. These effects were also observed in the experiments performed using three different inner diameter tubes. The tube having smallest inner diameter provided the best results of positioning of core at coaxial position as compared to larger inner diameter tubes as shown in Figure 124.

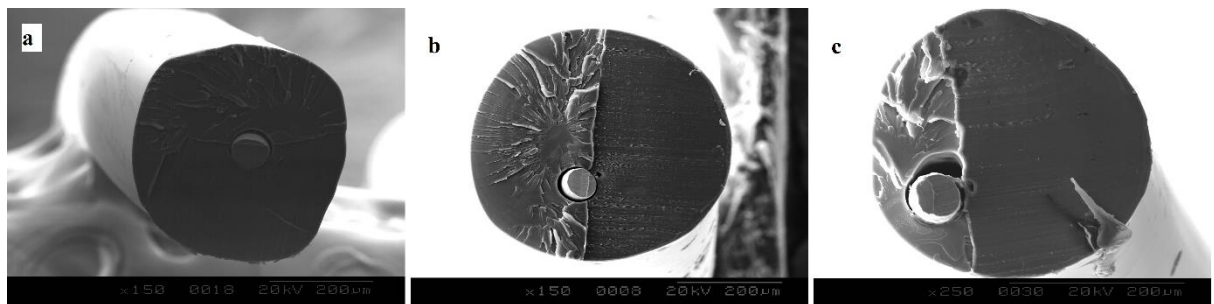


Figure 124. SEM cross-sectional images of composite filament developed with different tube inner diameters, (a. 254  $\mu\text{m}$ , b. 508  $\mu\text{m}$ , c. 762  $\mu\text{m}$ )

Considering all these results, it was concluded that for the development of regular and circular coaxial composite filament, the variables in spinneret design should be 4 holes in upper part, 2 mm position of tube with respect to upper spinneret, 254  $\mu\text{m}$  inner diameter tube and 1 mm of spinneret exit diameter.

#### 7 **Prototype 9**

This design was obtained after optimization of a number of parameters in prototype 8. The contours and edges were grounded to facilitate streamline flow in lower part. The results showed that the filament surface became more regular and smooth as compared to previous results as shown in Figure 125. The core was obtained at central axial position to form perfect coaxial composite filament.

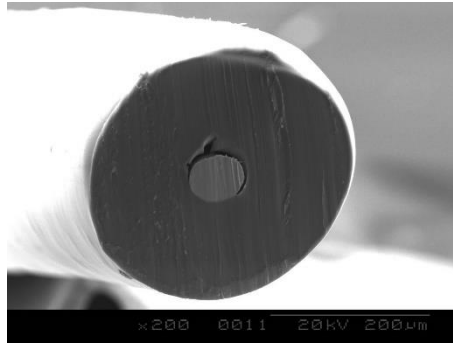


Figure 125. SEM cross-sectional image of composite filament by spinneret prototype 9

## **8** *Prototype 10*

This prototype was not experimentally tested. As per experience and extrapolation of results obtained from previous designs, it was assumed that this design will prove to provide more regular coaxial filament. The reason lies in the fact that only two weld instabilities will be present in this filament due to joining of two flow streams. While in previous designs four flow streams joined to form four weld lines in the same filament cross-section. Although those weld lines were prominent visually due to stabilization of flow in lower spinneret part, but they still exit in some extent. These weld lines may become semi-apparent at higher spinning speed.

## **D Optimization of modifications in machine design**

### **1** *Selection of tube*

The tube material didn't influence the quality of the filament developed keeping the same inner diameter of the tube. The reason lies in the fact that the speed of the extrusion process was too low in which the frictional effect was not prominent. In general idea, ceramics provide lower resistance than stainless steel. As a matter of fact, ceramics should prove to be more acceptable for the passage of core filament in terms of lower frictional value and operate able at higher temperature values. In these experimental runs, gripping was required with lower inner diameters; therefore, stainless steel tubes were selected as they are available in very small inner diameter tubes and can bear applied force to grip by screw. The extrusion speed was also less in experimental stage, so stainless steel tube performed the operation. For industrial upscaling, the ceramic tube will prove to be the best solution for passage of core filament. The inner diameter of the tube was already optimized as variable in spinneret optimization prototype 8.



## 2 *Piston lower end*

### 2.1 Conventional design

The previously developed conventional lower end [5] having large inner diameter for passage of core through the hollow piston was not suitable to be a good design. The melt polymer flow inside the hollow piston on application of applied load and choked the hollow piston on cooling of polymer caused due to temperature gradient present inside the hollow piston. To reduce this issue, higher temperature was required in the oven to keep the polymer in melt form at temperature gradient across the oven boundaries. It was the reason of using higher temperature in the oven for earlier experimentations.

### 2.2 Type 1

This design was used based on the earlier experiments done using tri layers of aluminium foil having a hole of 200  $\mu\text{m}$  at its centre and placed it at the bottom of conventional lower end. The small hole allowed the passage of the core while restricted a large quantity of melt polymer to flow inside. This design solved the problem of choking inside the hollow piston. On other hand, the very small hole diameter was not easy to clean. The experiments performed with conventional spinneret were made using this design.

### 2.3 Type 2

This design was developed keeping in view of cleaning the end easily. The end was divided into number of parts to reduce the length of cleaning holes. Furthermore, the diameter of the holes was gradually decreased which made it possible to clean the parts easily. Large diameter holes are more easily to clean as compared to small hole diameter. As the small hole diameter reduced to very small length, therefore the cleaning of the end became easier. On contrary, the parts need to clean were increased. Owing to complexity of design, this type was not used.

### 2.4 Type 3

This design was developed to use after introduction of tube inside the oven. The small gap generated between the tube and inside walls of the design didn't allowed the polymer to flow inside due to higher viscosity. This design was developed with inner diameter very close to tube outer diameter to generate very small gap between them. This design was used in conjunction with spinneret prototypes 6-9. The inner diameter of the design was

optimized to reduce the frictional contact with the tube as well as to restrict the polymer flow inside the piston through a number of experimentation.

### 3 *Cooling chamber*

A clear difference between the surface smoothness and regularity was observed by change in temperature gradient in cooling chamber. It was observed that the filament developed with large length of cooling chamber had more regular surface than the other as shown in Figure 126. It was developed using prototype 8. These filaments were developed by four holes in upper spinneret, 2 mm down position of tube with respect to upper spinneret part, 1 mm exit diameter in lower part and 254  $\mu\text{m}$  inner diameter of tube. The extrusion parameters were 5 minutes of resident time, 5 mm/ min piston speed, 35.85 m/min of winding speed and temperature at lower and upper end of oven of 290 °C and 280 °C respectively.

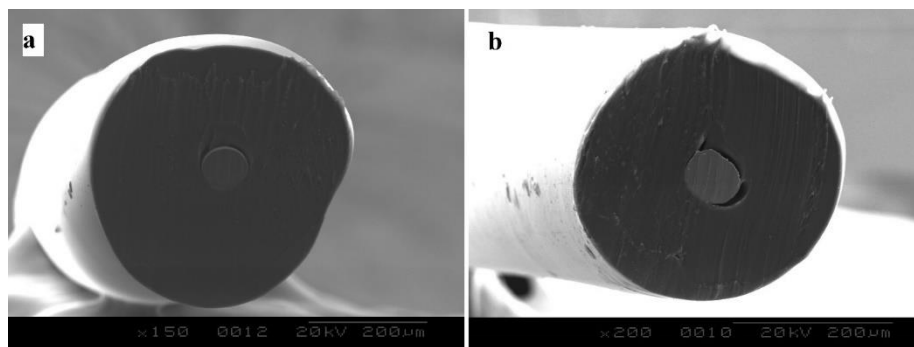


Figure 126. SEM cross-sectional view of composite filament developed at different cooling chamber length, (a. short length, b. large length)

The regularity in cross-sectional shape and smoothness in longitudinal surface obtained was due to gradual cooling of the filament. gradual cooling provided time to the melt polymer to rearrange itself after exiting the spinneret. In addition, the processing temperature was quite higher than melting point, which reduces the viscosity of the polymer and hence influence of surface tension may act upon it.

## V Characterization of coaxial composite filament

### A Physical characterization

#### 1 Linear density

The linear density of the composite filament was calculated using the ASTM D 1059 standard test method using short test specimens. A number of 10 specimens were considered for each sample code to determine mean linear density.

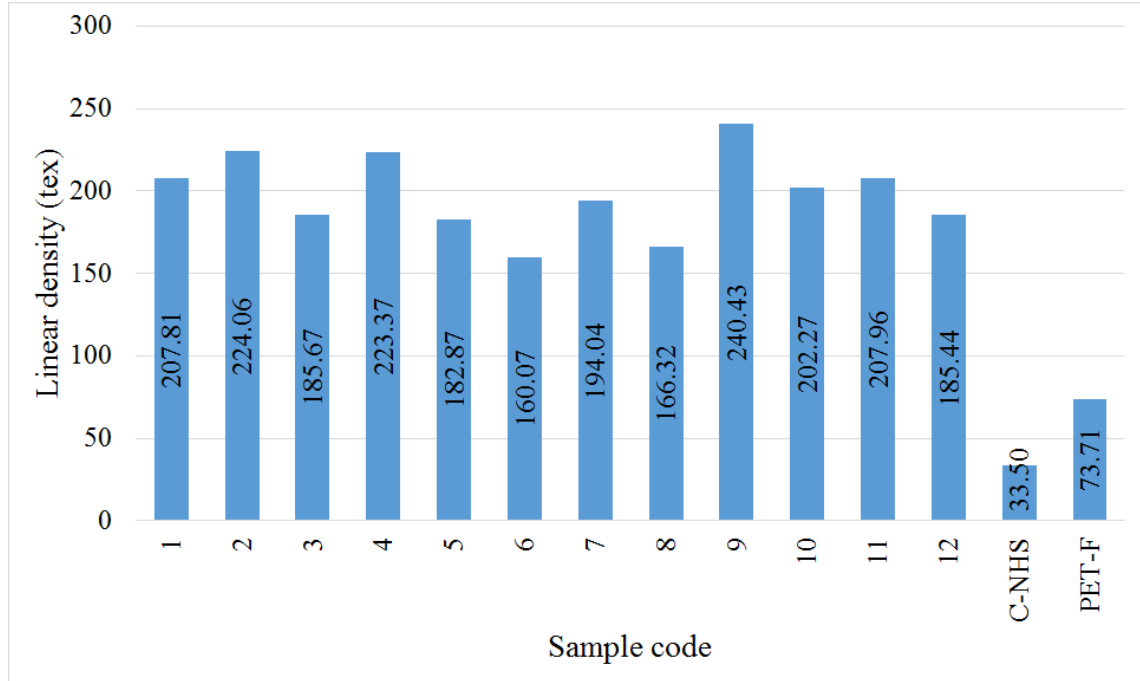


Figure 127. Graphical representation of filament linear density of different sample codes

The graphical representation of linear density vs sample codes is shown in Figure 127. The copper core filament without any heat treatment (C-NHS) and polyester filament (PET-F) are also given for reference.

Linear density can also be calculated using the basic equation as follows:

$$T_t = 1000 \frac{M}{L} \quad (17)$$

This equation can also be written as:

$$T_t = 100000 \times \rho \times S = 100000 \times \rho \times \pi \times r^2 \quad (18)$$

Where M is the mass (g), L is the length (m),  $T_t$  is linear density (tex),  $\rho$  is the material density ( $\text{g/cm}^3$ ), S is the filament cross-sectional area ( $\text{cm}^2$ ) and r is the radius of filament (cm). Using the mean diameter obtained from SEM image analysis for each sample, the surface area can be calculated. The density of the composite filament can be calculated by considering 100 g ( $w_c$ ) of composite material and finding the volume of each component by dividing the weight (w/w) percent of each component with its density. The weight of each component through volume percent was calculated using Equation 19.

$$w_i = V\%_i \times \rho_i \quad (19)$$

Where,  $w_i$  is the weight of individual component in whole (g),  $V\%_i$  is the volume percent of individual component in composite material ( $\text{cm}^3/\text{cm}^3$  %) and  $\rho_i$  is the density of individual component ( $\text{g/cm}^3$ ). The weight percent ( $W\%_i$ ) of individual component was calculated using Equation 20.

$$W\%_i = \frac{w_i}{\sum_1^n w_i} \quad (20)$$

To find volume of individual component:

$$V_i = \frac{W\%_i}{\rho_i} \quad (21)$$

Where,  $V_i$  is the volume of a component ( $\text{cm}^3$ ),  $W\%_i$  is the weight percent of individual component ( $\text{g/g}$  %) and  $\rho_i$  is the density of a component ( $\text{g/cm}^3$ ). The density of the composite material can be calculated using the Equation 22 [174].

$$\rho_c = \frac{w_c}{\sum_1^n V_i} \quad (22)$$

Where,  $\rho_c$  is the composite density ( $\text{g/cm}^3$ ) and  $w_c$  is the weight of composite initially taken (g). The average V% of copper and polyester in all samples were 3.28 % and 96.72 % respectively. The calculated W% of copper and polyester became 18.5 and 81.5 % respectively. Calculating the volume of each component using Equation 21.

$$V_{Cu} = \frac{18.5}{8.93} = 2.07 \text{ cm}^3$$

$$V_{PET} = \frac{81.5}{1.33} = 61.27 \text{ cm}^3$$

The composite density is calculated using Equation 22.

$$\rho_c = \frac{100}{2.07 + 61.27} = 1.58 \text{ g/cm}^3$$

Using the method stated above, the composite density and surface area were calculated individually for each sample. The linear density ( $Tt_c$ ) of samples was calculated using Equation 17. The error percentage was calculated using the Equation 23.

$$\text{Error (\%)} = \frac{\text{Abs}(Tt_c - Tt_a)}{Tt_a} \times 100 \quad (23)$$

Table 11. Calculated linear density for different samples

Sample code	Mean diameter (D') [ $\mu\text{m}$ ]	Area ( $\times 10^3$ ) [ $\text{cm}^2$ ]	Cu (V%)	PET (V%)	Composite density ( $\rho_c$ ) [ $\text{g/cm}^3$ ]	Calculated linear density ( $Tt_c$ ) [tex]	Actual linear density ( $Tt_a$ ) [tex]	Error (%)
1	464.81	1.70	0.02	0.98	1.50	254.03	207.81	22.24
2	379.75	1.13	0.02	0.98	1.50	169.56	224.06	24.32
3	396.42	1.23	0.02	0.98	1.50	184.77	185.67	0.48
4	442.40	1.54	0.02	0.98	1.50	230.12	223.37	3.03
5	438.52	1.51	0.03	0.97	1.58	238.57	182.87	30.46
6	389.16	1.19	0.03	0.97	1.58	187.88	160.07	17.37
7	414.88	1.35	0.03	0.97	1.58	213.54	194.04	10.05
8	348.71	0.96	0.03	0.97	1.58	150.86	166.32	9.30
9	493.79	1.92	0.02	0.98	1.50	286.41	240.43	19.12
10	480.81	1.82	0.02	0.98	1.50	271.55	202.27	34.25
11	439.16	1.51	0.03	0.97	1.58	239.26	207.96	15.05
12	386.09	1.17	0.03	0.97	1.58	184.94	185.44	0.27
Average Error (%)								15.49

It was observed that the calculated linear density was quite near to the experimental linear density ( $Tt_a$ ). The average error obtained was 15.5 % which depicts that composite linear density can also be calculated theoretically with significant percent of accuracy. The graphical representation of actual and theoretical linear density is shown in Figure 128.

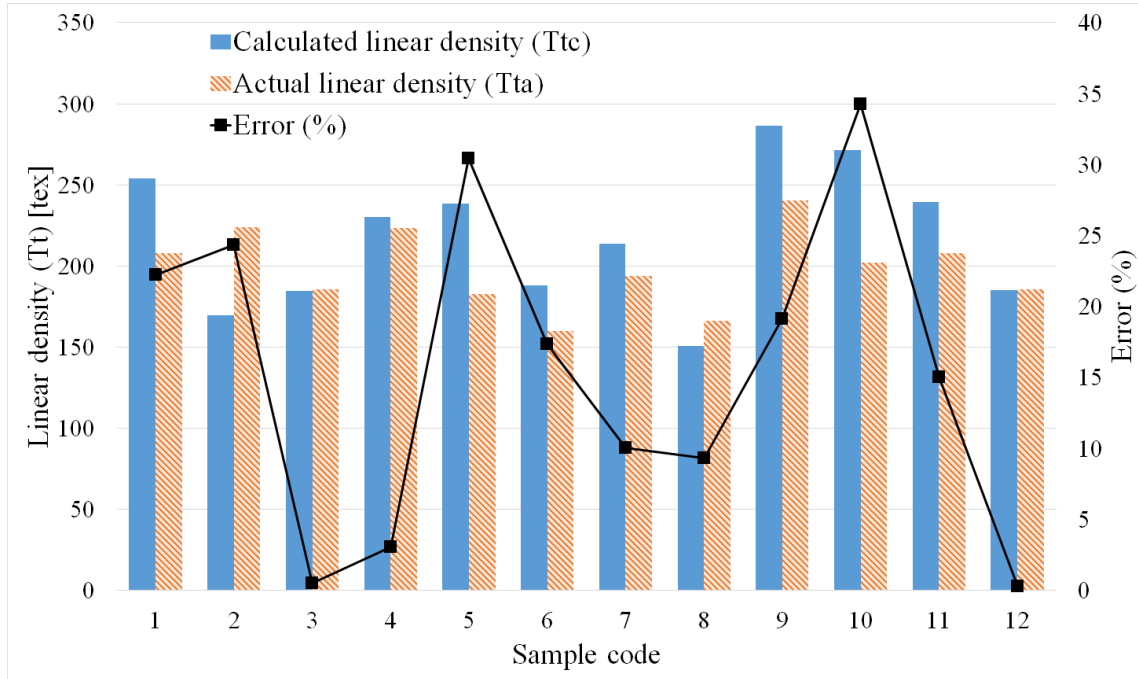


Figure 128. Actual and theoretical linear density with error percentage of polyester composite filament

## 2 Diameter of composite filaments

The diameter of the developed composite filaments was measured using SEM images in different directions. The arithmetic mean diameter was calculated for each sample code and graphically shown in Figure 129. The obtained results for irregular cross-sectional filaments had less importance for mean diameter due to variant diameters in different directions. The circular and regular cross-sectional filaments are well described by this measurement method. It was observed that filaments were developed having mean diameter in range of 350 – 500  $\mu\text{m}$ . The error bar at top of each sample bar expressed 95 % confidence interval of obtained data values of respective sample code.

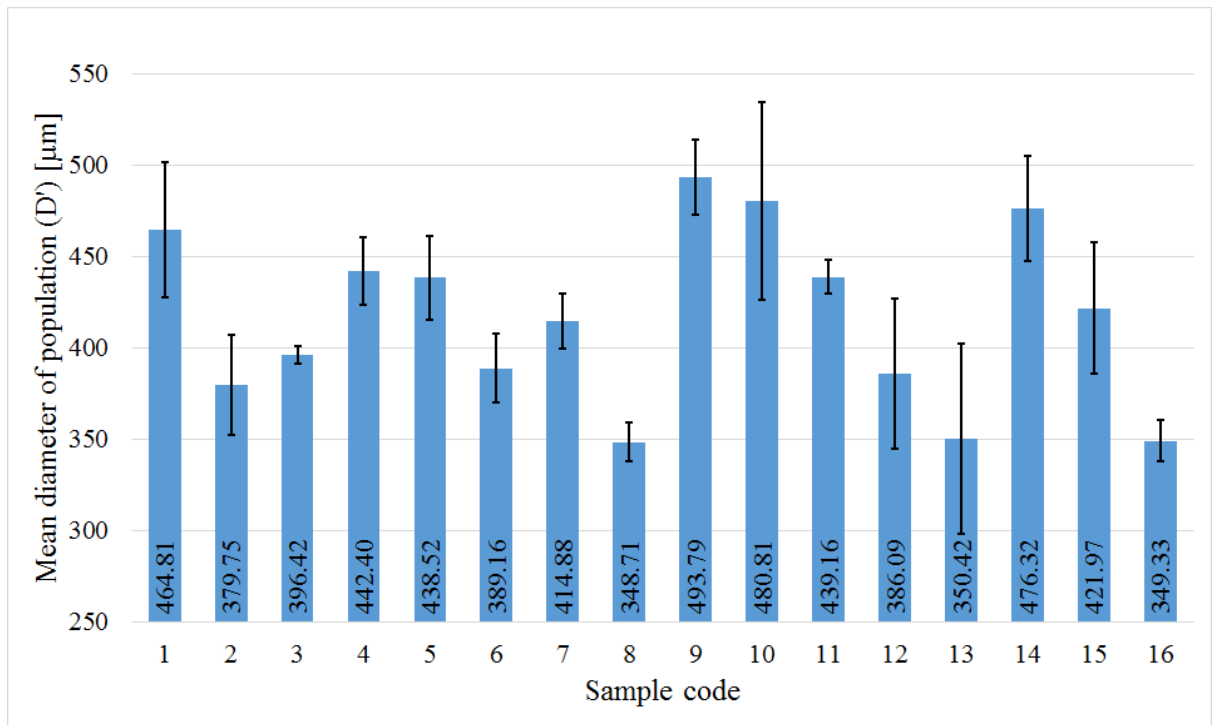


Figure 129. Graphical representation of mean diameter of samples vs sample codes

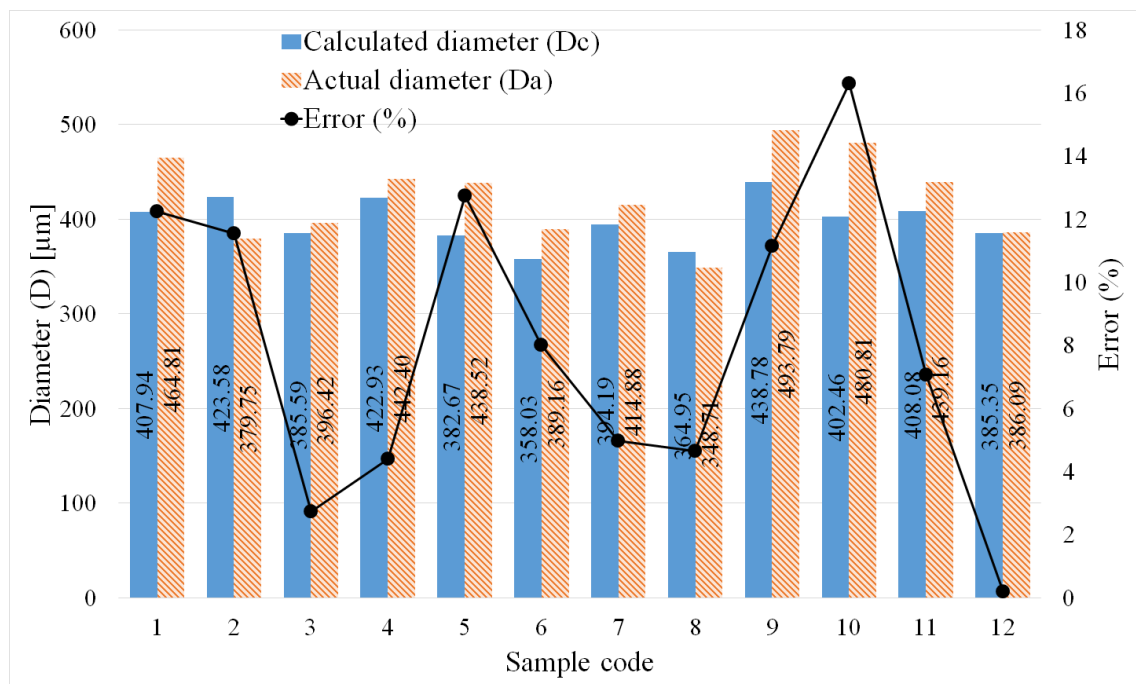


Figure 130. Theoretical and experimental diameter comparison with error percentage of Polyester composite filament

The diameter of the composite filament can be calculated using the Equation 18. The experimental linear density of filament was used to calculate the theoretical diameter of

the filament. The graphical representation of the data is shown in Figure 130. The average error obtained for all the samples was 8 %. The results depict that linear density can be used to determine the diameter of the composite filament with adequate accuracy.

## **B Morphological characterization**

### ***1 Cross-sectional surface morphology***

The cross-sectional shape of filament was traced in rectangle. The diagonal lines were drawn to locate the proposed centre of the filament. Two further lines between both of diagonal lines were developed at 90 ° with each other. These four lines were used as reference to measure the diameter of the coaxial filament at different angular positions with accuracy. The centre of the core filament was also located with the same method. The distance between the centre of coaxial filament and centre of core filament was considered as eccentricity of the core filament. The filament was characterized mathematically by taking four diameter parameters as shown in Figure 131, which later on used for the calculation of diameter uniformity ratio of the coaxial filament using the Equation 24.

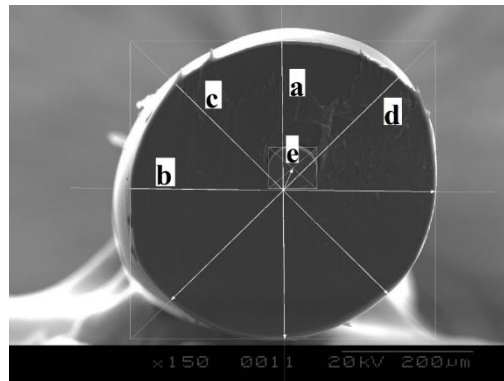


Figure 131. Geometrical characterization codes for composite filament

$$X = \frac{X'}{X''} \quad (24)$$

Where  $X'$  and  $X''$  were the corresponding diameter uniformity constant 1 and diameter uniformity constant 2 respectively. These constants were calculated using the following Equations 25 and 26 with their respective rule.

$$X' = a/b \text{ (Where numerator } > \text{ denominator)} \quad (25)$$

$$X'' = c/d \text{ (Where numerator } > \text{ denominator)} \quad (26)$$



The mean diameter uniformity ratio of population was calculated using arithmetic mean rule as shown in Equation 27.

$$X_{mean} = \frac{\sum_1^n X_i}{n} \text{ (where n is the number of experimental run)} \quad (27)$$

It was observed that the coaxial filaments obtained were in the range of 350-500  $\mu\text{m}$  diameter. The standard deviation between the mean diameter of samples ( $\sigma_D$ ) varied in the range of 10  $\mu\text{m}$  to 90  $\mu\text{m}$ .

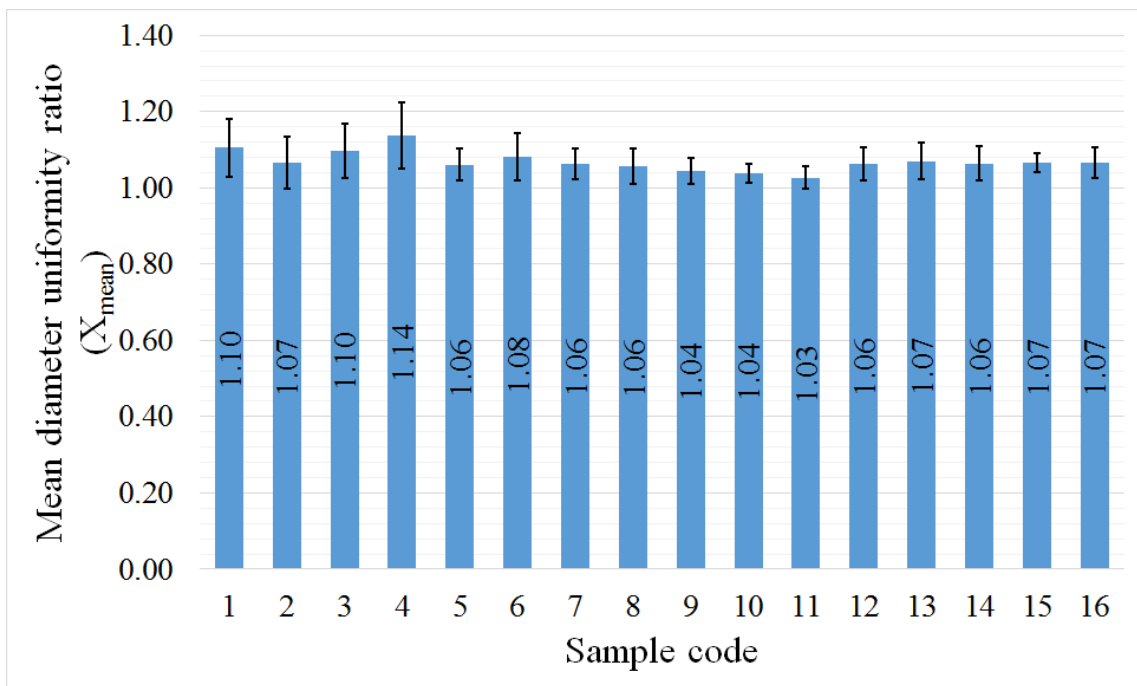


Figure 132. Graphical representation of mean diameter uniformity ratio vs sample code

The diameter uniformity ratio explains the uniformity between diameters at various angular positions. A perfect circle has diameter uniformity ratio of 1, therefore the filaments having values more than 1 are more irregular in cross-sectional shape. It was observed that sample code 11 showed the least value for mean diameter uniformity ratio which explained that it was most regular in cross-sectional shape. This result proved that the exit diameter had significant influence on cross-sectional geometry of the filament. The standard deviation of the samples was also reported as error bars for diameter uniformity ratio in Figure 132.

The deviation between diameters within the sample were recorded and arithmetic mean for the population was represented by standard deviation graph in Figure 133. It was

observed that the sample code 8 showed the least S.D followed by 11 and 10 respectively. This value explained the variation in diameter for particular sample type and hence also the estimate of the quality and reproducibility of the samples.

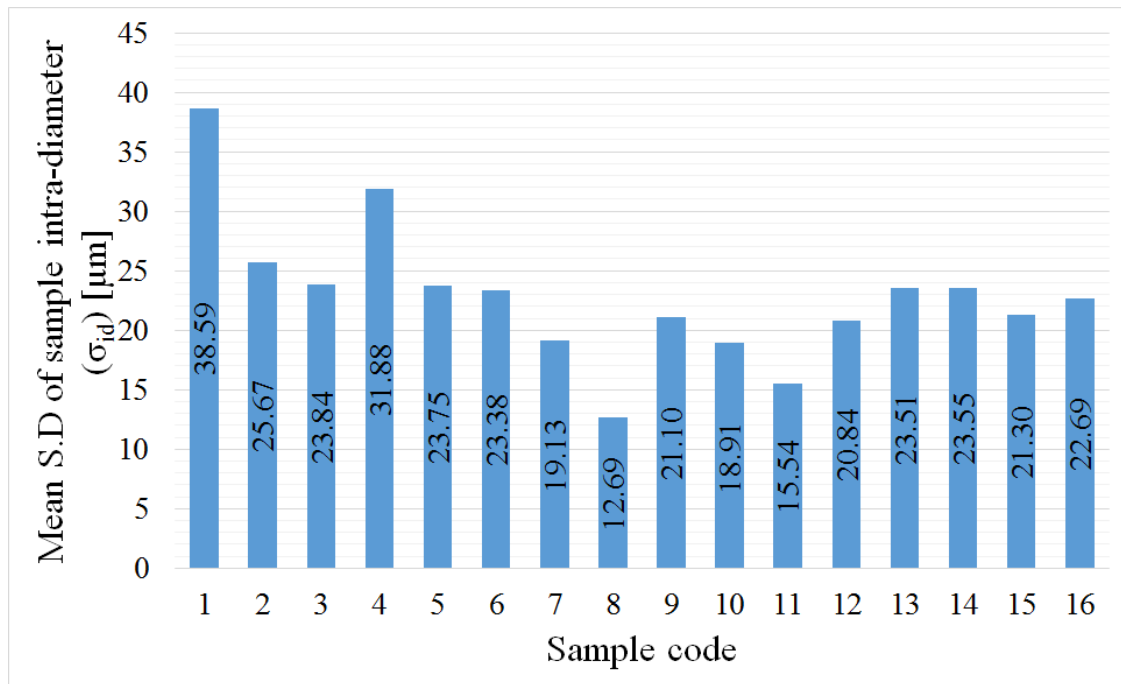


Figure 133. Graph between mean standard deviation of diameter within sample vs sample code

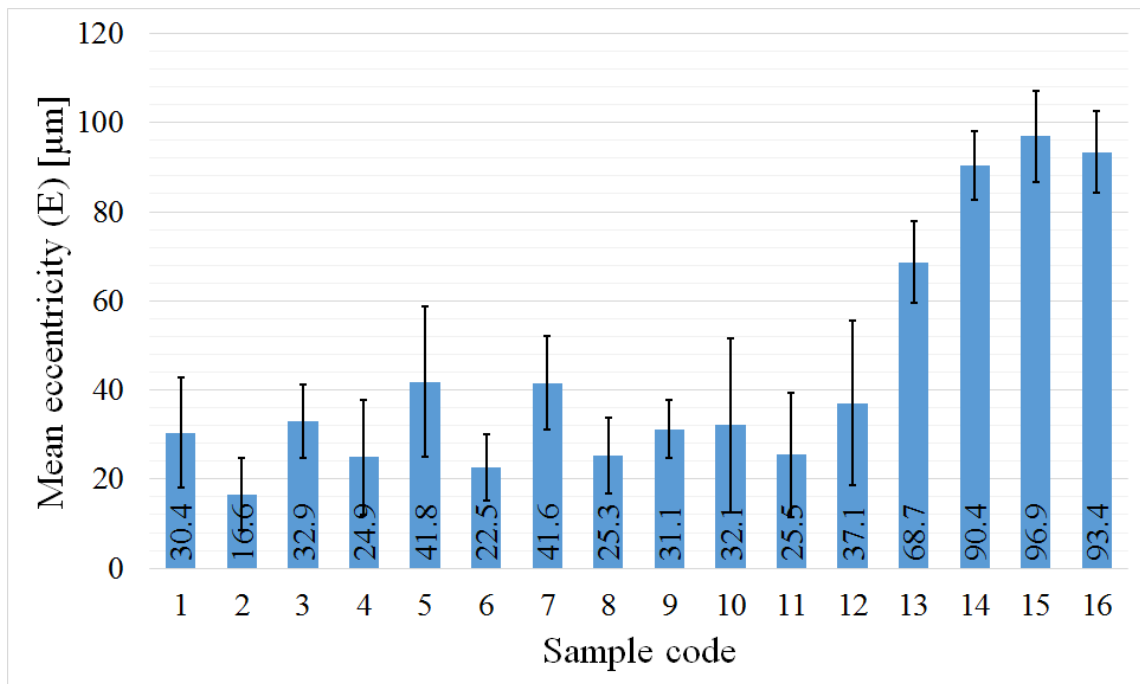


Figure 134. Eccentricity of core filament graph of samples

The deviation from the centre of the filament is called as eccentricity. The shift of core filament from proposed centre of the coaxial filament was calculated and reported in Figure 134. It was observed that the least eccentric value was obtained for sample code 2 followed by 6 and 4 respectively. The error bars expressed standard deviation for each respective sample code.

## 2 *Linear surface morphology*

The linear surface morphology was analysed using Atomic Force Microscope. The surface roughness was observed in the AFM for estimation of spinneret quality and melt instabilities. It was observed that filament surface was very smooth without any prominent melt instabilities as shown in Figure 135. The instabilities observed were caused due to imperfections in tip of probe and vibrations. The grain size of spherulites are also visible in the magnified view. It was observed that the spherulites were properly developed without any imperfection and no melt instability was found during extrusion operation on the filament surface.

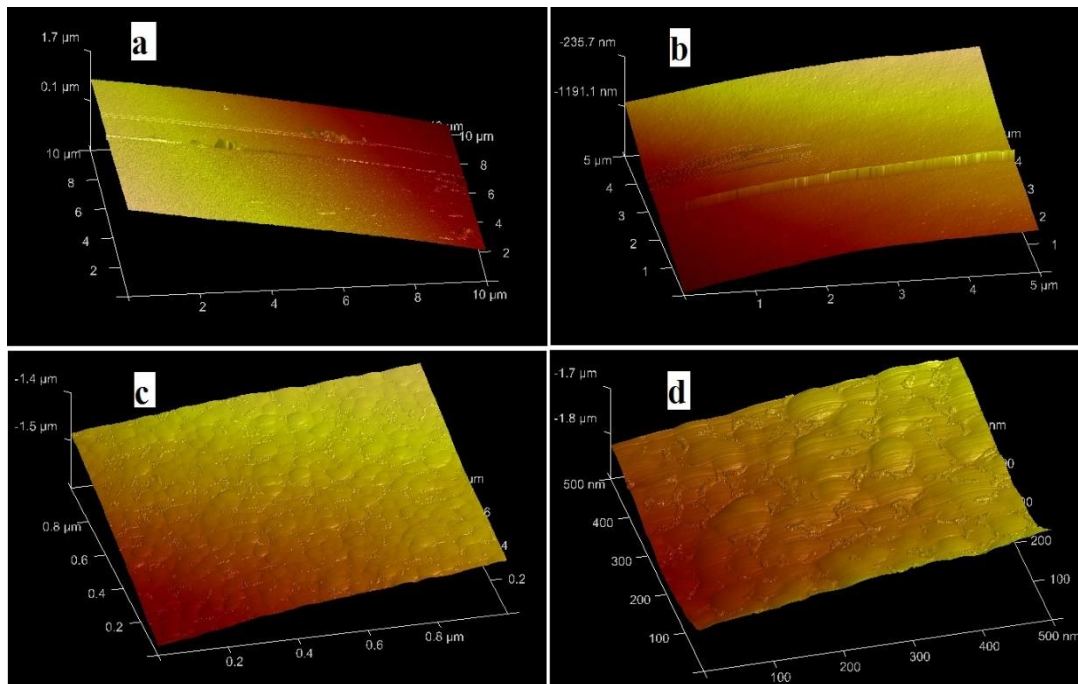


Figure 135. Longitudinal 3D surface morphology of composite filament at different magnification levels

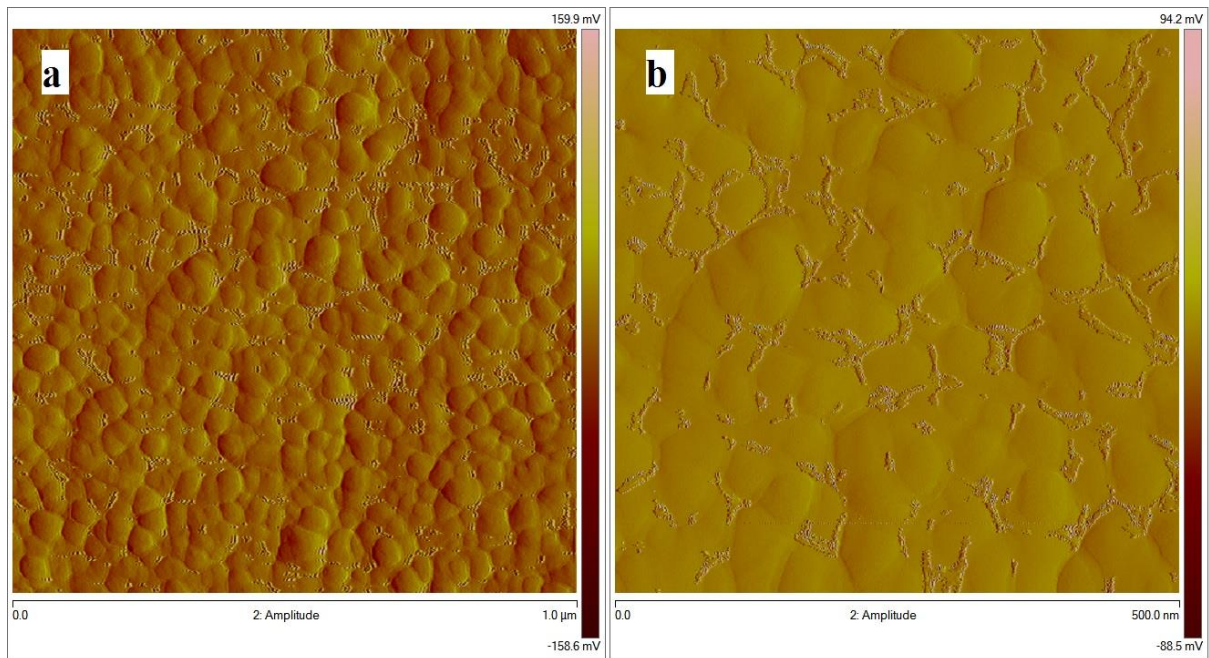


Figure 136. Surface roughness amplitude of composite filaments at different magnification levels

The surface roughness of the surface was measured using the area difference of projected with surface area of the captured image. The captured images at different magnification levels are shown in Figure 136. It was observed that the surface roughness measured for (a) and (b) of Figure 136 was 7.71 and 12.7 % respectively. The amplitude or height of profile parameters on surface are the primary parameters in characterizing surface topography [175]. The average roughness ( $R_a$ ) value for (a) and (b) were 6.54 nm and 6.86 nm respectively, while root mean square roughness ( $R_q$ ) value for (a) and (b) were 8.29 nm and 8.63 nm respectively. The obtained values of  $R_a$  suggested that the roughness of the samples was very less. The results at different magnification levels showed that the amplitude of roughness was too less. In such case, it is proved that the produced filaments are good in surface quality and smoothness, and designed spinneret geometry can be successfully used for the development of composite filaments.

### C Mechanical characterization

The filament was characterized by measuring tensile properties on MTS tensile strength tester. The samples developed by prototype 8 design were tested to analyse the effect of spinneret variables on tensile properties of the composite filament. A number of 150 specimens were tested comprising of 10 replicates of each sample. The specimen failure near the jaw were discarded and were not used in calculations. The failure of interfacial

bonding between core and sheath by macroscopic sliding or slip or breakage of composite filament were considered as the failure of the composite filament as shown in Figure 137. Necking formation started to build up after failure of interfacial bonding up till breaking point. In other cases, filament break wholly as complete failure of the composite filament structure as shown in Figure 138. Rubber pads were used in the jaws to avoid slippage and strong grip.

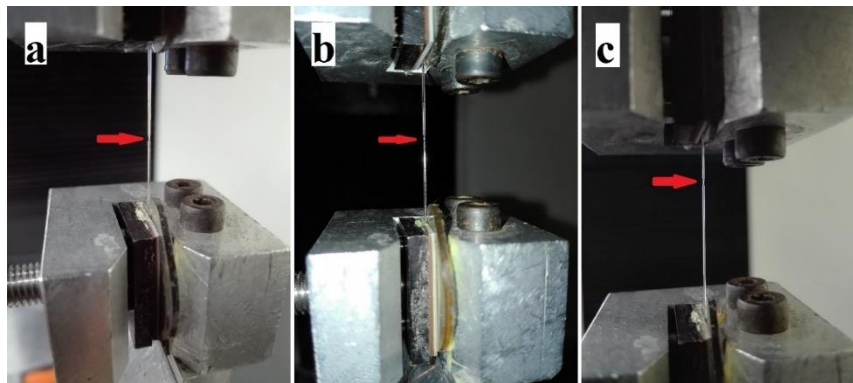


Figure 137. Failure of composite filaments as necking during tensile test

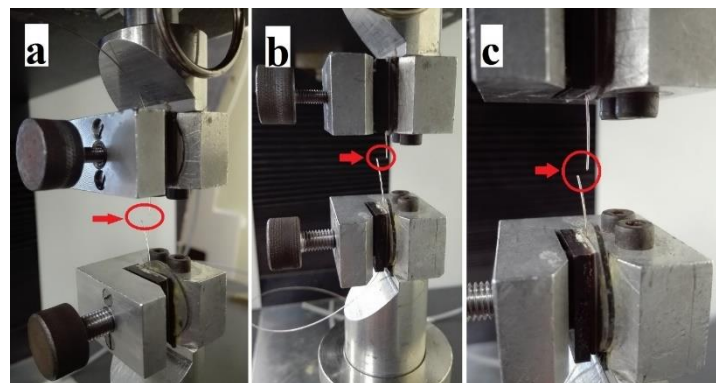


Figure 138. Failure of composite filaments as breakage during tensile test

The specific load-extension curve obtained for sample code 1 is shown in Figure 139. The initial straight line obtained showed the elastic region of the filament up till applied force of 1.8 N. After this elastic limit, plastic deformation started in the composite filament. This limit was defined by the copper wire inside the filament. The elastic range of the composite filament was governed by copper wire as shown in Figure 140. The specific load-extension graph of copper wire showed steep slope of elastic limit followed by moderate slope level for plastic deformation up till breaking point. Any deformation caused within the elastic limit can be retreated back to its original position. Once applied load increased above elastic limit, the deformation became permanent in the filament. The region from the elastic limit up to maximum load applied is considered as plastic region

and was dominantly govern by polyester polymer. The plastic range and necking region of the specific load-extension curve of composite filament were quite similar to the specific load-extension graph observed for polyester filament as shown in Figure 141.

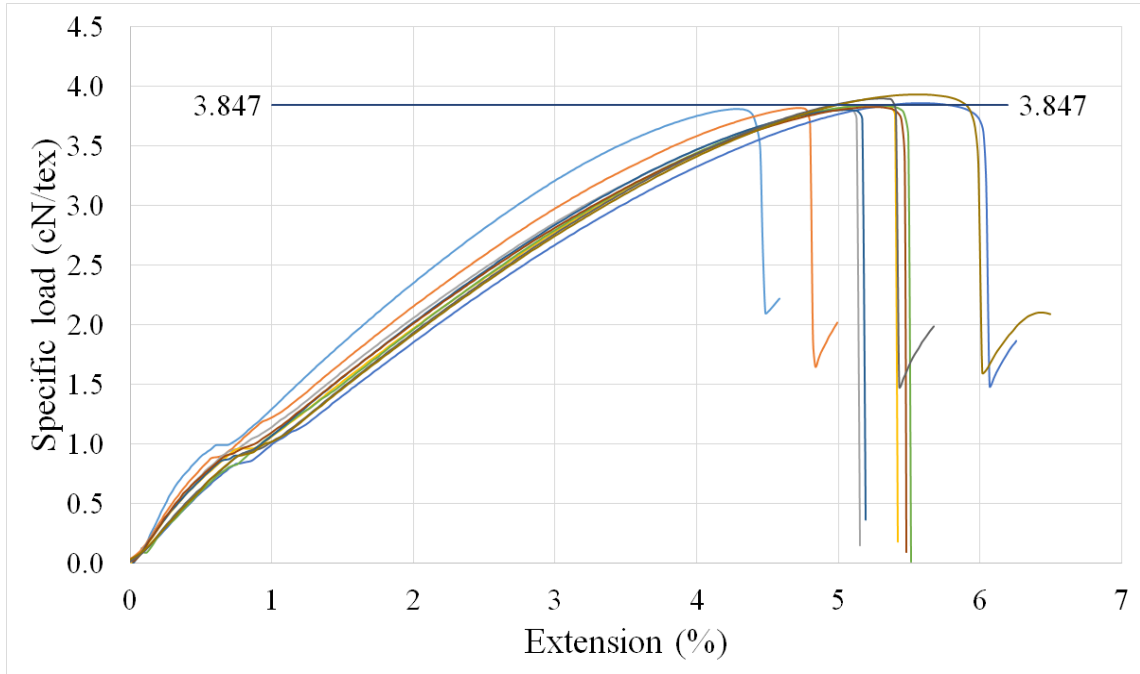


Figure 139. Specific load-extension curves obtained for sample code 1

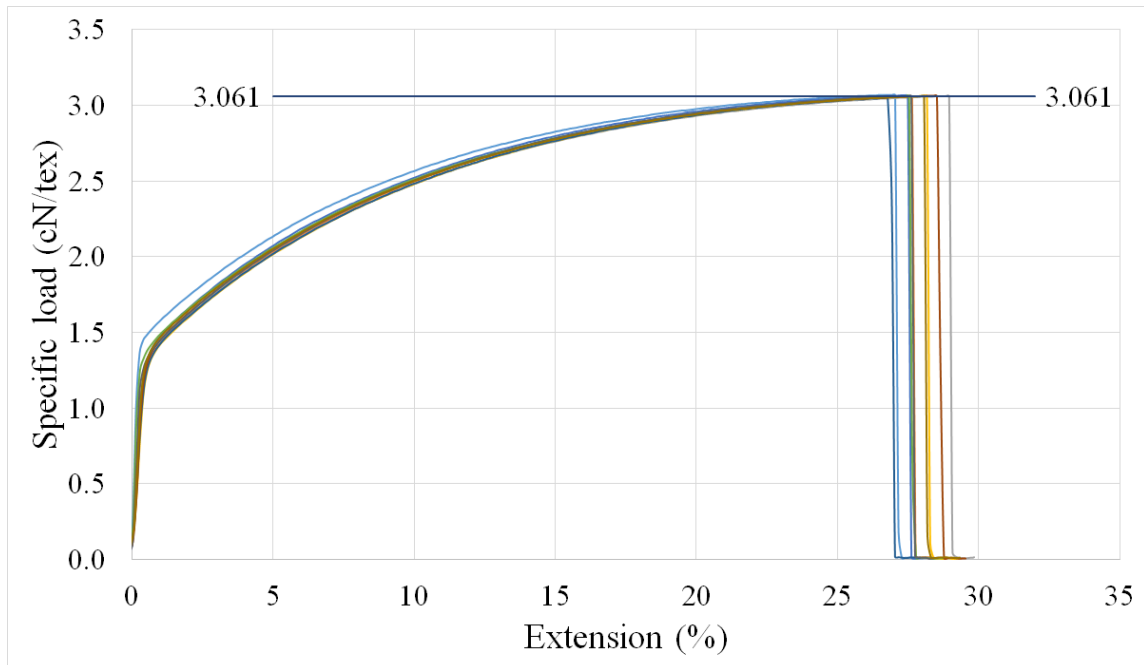


Figure 140. Specific load-extension curves of copper filament without thermal treatment



The polyester specific load-extension curve showed almost zero elastic curve and steep plastic curve up till formation of necking and breakage. The composite filament curve reduced from the maximum applied load to a lower value until the de-bonding of interface occurred between core and sheath with a sharp decrease in applied stress. The maximum load that the filament resist before failure is called as tenacity. The mean value of tenacities of all the specimens was also recorded and marked as straight horizontal line in the graph.

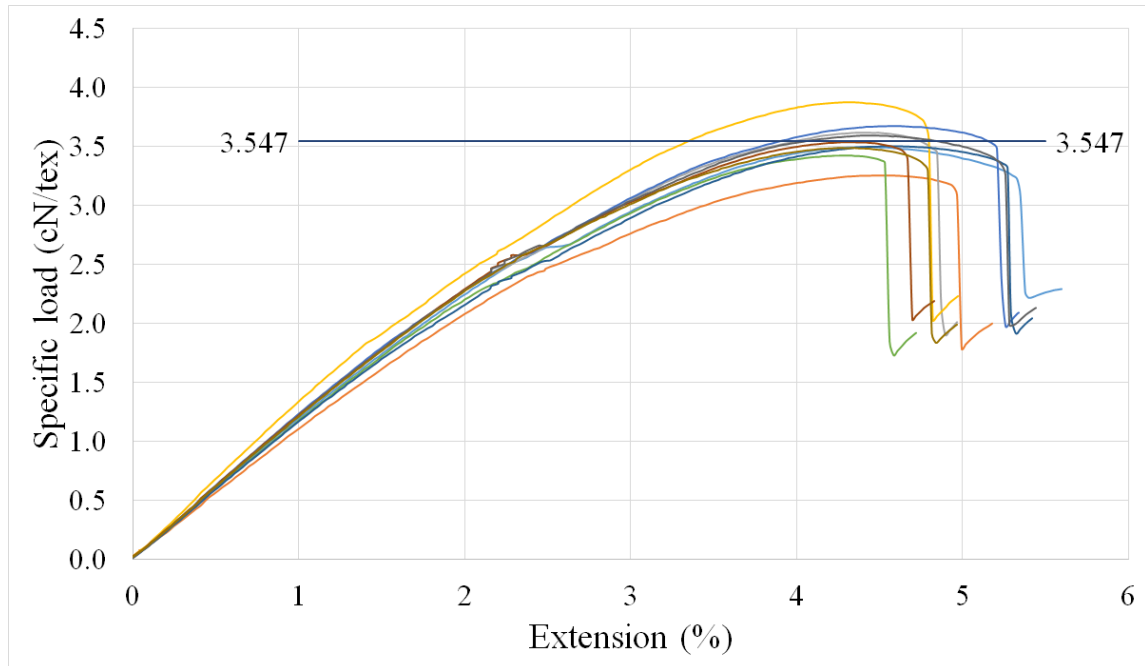


Figure 141. Specific load-extension curves of polyester filament

The arithmetic mean of each parameter obtained by testing 10 specimens of each sample were recorded in dataset as given in

Table 12. The specific breaking stress, breaking extension, elastic modulus and work of rupture were measured for each sample. The standard deviation and coefficient of variation observed between the population were also calculated. The modulus was calculated at 1% of extension value of specific load-extension curve. The pure polyester filament (PET-F) and virgin copper filament (C-NHS) without any heat treatment were also tested as reference. The specific load-extension curves for the rest of the samples are given in Annexure 6.

Table 12. Tensile properties of different samples

Sample code		Tenacity ( $\sigma_B$ ) [cN/tex]	Breaking Extension ( $\epsilon_f$ ) [%]	Modulus ( $E_y$ ) [cN/tex]	Specific work of rupture ( $W_{pl}$ ) [ $\mu$ J/tex]
1	Mean	3.85	5.13	80.36	31.76
	S.D	0.04	0.37	6.50	3.48
	C.V %	1.04	7.23	8.08	10.94
2	Mean	3.50	4.09	77.69	20.73
	S.D	0.22	0.18	7.10	2.05
	C.V %	6.16	4.30	9.14	9.89
3	Mean	3.56	5.47	74.93	32.74
	S.D	0.18	0.32	4.57	3.34
	C.V %	5.05	5.94	6.10	10.22
4	Mean	3.77	4.80	82.92	27.34
	S.D	0.25	0.31	4.78	3.6
	C.V %	6.70	6.41	5.76	13.17
5	Mean	4.06	5.17	87.35	33.73
	S.D	0.09	0.25	4.48	3.35
	C.V %	2.30	4.82	5.13	9.94
6	Mean	3.73	4.47	105.19	28.74
	S.D	0.07	0.28	4.41	2.44
	C.V %	1.92	6.35	4.19	8.49
7	Mean	4.16	5.45	85.49	38.53
	S.D	0.02	0.20	6.66	3.55
	C.V %	0.54	3.66	7.79	9.2
8	Mean	3.85	4.75	92.77	29.91
	S.D	0.17	0.31	6.16	3.45
	C.V %	4.37	6.54	6.64	11.55
9	Mean	3.91	5.08	87.46	31.3
	S.D	0.09	0.28	8.02	3.74
	C.V %	2.37	5.56	9.17	11.94
10	Mean	3.71	4.31	81.19	23.92
	S.D	0.11	0.23	9.22	2.36
	C.V %	2.96	5.43	11.36	9.87



Sample code		Tenacity ( $\sigma_B$ ) [cN/tex]	Breaking Extension ( $\epsilon_f$ ) [%]	Modulus ( $E_y$ ) [cN/tex]	Specific work of rupture ( $W_{pl}$ ) [ $\mu$ J/tex]
11	Mean	4.05	4.90	91.73	31.31
	S.D	0.10	0.25	7.95	3.67
	C.V %	2.39	5.12	8.66	11.72
12	Mean	3.96	4.33	90.59	26.37
	S.D	0.32	0.37	8.80	4.85
	C.V %	7.98	8.59	9.72	18.4
C-HS	Mean	3.08	24.65	88.93	168.57
	S.D	0.01	1.02	25.30	9.26
	C.V %	0.24	4.14	28.44	5.49
C-NHS	Mean	3.06	27.35	43.06	177.82
	S.D	0.01	0.62	11.68	4.49
	C.V %	0.16	2.27	27.12	2.53
PET-F	Mean	3.55	4.38	118.86	29.32
	S.D	0.16	0.10	5.53	2.61
	C.V %	4.37	2.24	4.65	8.91

### 1.1 Tenacity

The graphical representation of the arithmetic mean values of tenacity in column graph is shown in Figure 142. The dispersion of data in terms of standard deviation and coefficient of variation for each sample were also represented as error bars and line graph respectively in the same graph. The error bars express 95 % confidence interval of each sample. Higher bar explains high potential of variation from mean values. The coefficient of variation is the standardized measure of data dispersion in given dataset. Therefore, it is used to compare data dispersion having different mean values. Coefficient of variation for each sample was measured in percentage and represented as line graph on secondary axis.

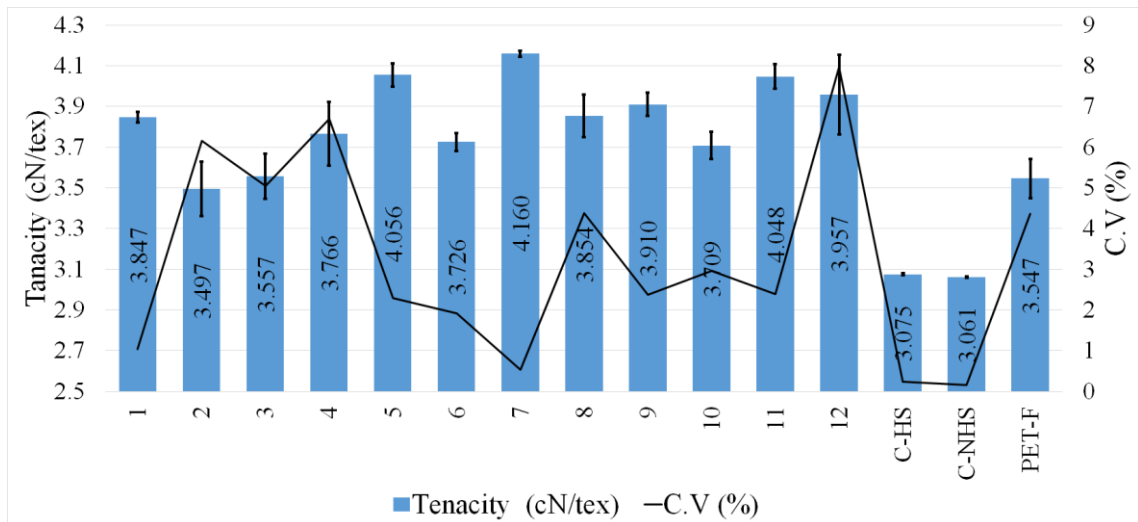


Figure 142. Graphical representation of tenacity of samples

The results showed that the sample codes 1-4 having 2 number of holes had generally lower tenacity values as compared to 3 and 4 holes' spinneret samples. In addition, samples from 4 holes have higher tenacity values comparatively to 3 holes' spinneret design samples. The reason for these differences in values can be explained on the basis of load bearing capacity of the filament. It is assumed that central circular region of the filament is mainly bearing the applied load. Composite filaments of different shapes have different cover percentage in circular ring shape. To estimate this variation, all the composite shapes were used to find the circular area around them as shown in Figure 143. The area outside circular ring is supposed to be not imparting their role for load bearing during stress application. The area calculations are given in Table 13. It was observed that the area percentage outside circular ring was highest for elliptical followed by triangular shaped filament. The circular shaped filament had area outside circular ring higher than rectangular, which might be caused due to angular position of the circular filament during image processing and may also cause due to imperfections in shape. On comparison basis, circular shaped filament will be considered as having zero area outside circular ring, therefore, the descending sequence of area outside circular ring will be elliptical, triangular, rectangular and circular shaped filaments. The area outside circular ring may have non-aligned molecular chains due to flow geometry in spinnerets, therefore considered as not playing their role in bearing applied forces on the composite filament.

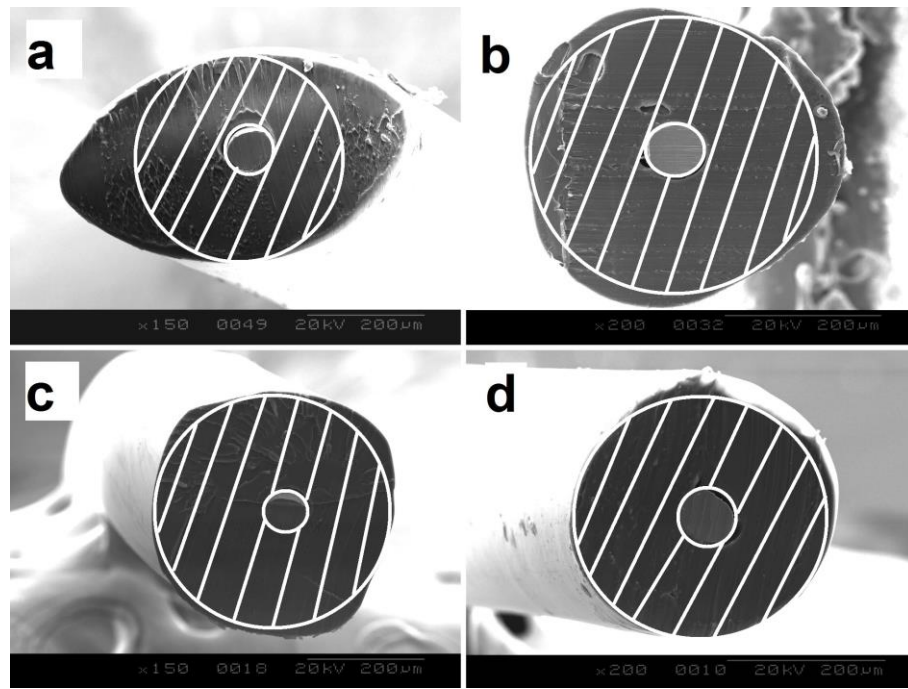


Figure 143. Estimation of area around core in different shaped composite filaments

Table 13. Area calculations of different shaped filaments

Position	Elliptical	Triangular	Rectangular	Circular
Core area ( $\mu\text{m}^2$ )	3364.21	3774.41	2489.59	3557.15
Circular ring with core area ( $\mu\text{m}^2$ )	102502.40	105418.85	73687.05	73170.48
Complete filament area ( $\mu\text{m}^2$ )	129576.70	123789.25	80393.65	81486.93
Circular ring without core (%)	76.51	82.11	88.56	85.43
Area outside circular ring (%)	20.89	14.84	8.34	10.21

This effect can also be explained on the terms of surface area of the filament. The circular shaped filaments have least value of surface area which increases in order of rectangular, triangular and elliptical shapes in turn. A compacted structure contributes higher in bearing applied load on it. A circular filament shape is most compacted having least surface area and hence can contribute precisely in bearing applied load. Therefore, elliptical cross-sectional shape bear least amounts of load while circular shaped filament can withstand high load values.

It was also observed that the spinnerets having 1 mm exit diameter hole have higher tenacity values as compared to 2 mm exit diameter hole. The reason was based on the shape of the filaments developed with 1 mm hole having more regular and approaching to circular shape as compared to 2 mm spinnerets. As a result, 1 mm spinneret samples had higher tenacity values.

In addition, the tenacity values for 3 holes and 4 holes' samples had higher trend of tenacity values due to regular cross-sectional shapes of these samples. It was also observed that composite filaments had higher tenacity values as compared to polyester (PET-F) and copper filaments alone. There was no difference in tenacity value observed between thermally treated (C-HS) and non-treated (C-NHS) samples of copper filament. The thermal treated samples were developed at same conditions in which composite filament samples were made. In such condition, it is evident that tenacity value of composite filaments synergistically increased from its constituent materials' attribute.

The experimental value of tenacity was verified with mixture law using associated values of copper and polyester filaments. The theoretical tenacity value was obtained using the Equation 28.

$$\sigma_{th} = \phi_{PET}\sigma_{PET} + \phi_{Cu}\sigma_{Cu} \quad (28)$$

Where  $\phi_{PET}$  and  $\phi_{Cu}$  are the volume fractions of polyester and copper in the composite filament respectively, while  $\sigma_{PET}$  and  $\sigma_{Cu}$  are the breaking stress of polyester and copper filaments respectively.

It was observed from Table 14 that the error percent obtained was less than 15 % which expresses that copper filament had good adherence with polyester sheath, so that much of the applied load on polyester sheath was transmitted to the core copper filament.

Table 14. Comparison of theoretical and experimental tenacity values of composite filaments

Shape	Serial No.	Area ( $\mu\text{m}^2$ )		Area fraction (%)		Theoretical tenacity ( $\sigma_{th}$ ) [cN/tex]	Mean theoretical tenacity ( $\sigma_B^{mean}$ ) [cN/tex]	Experimental tenacity ( $\sigma_B$ ) [cN/tex]	Error [%]
		Composite filament	Cu	Composite filament	Cu				
Elliptical	1	134559.25	3578.19	0.97	0.03	3.53	3.54	3.85	8.08
	2	145060.65	3333.62	0.98	0.02	3.54			
	3	149324.93	2443.38	0.98	0.02	3.54			
Triangular	1	139061.024	3740.13	0.97	0.03	3.53	3.53	4.06	12.94
	2	117634.43	4474.96	0.96	0.04	3.53			
	3	120961.167	4062.87	0.97	0.03	3.53			
Rectangular	1	193105.72	3525.414	0.98	0.02	3.54	3.54	3.91	9.55
	2	174663.69	3634.715	0.98	0.02	3.54			
	3	155425.85	4087.614	0.97	0.03	3.53			
Circular	1	105258.5	4398.2	0.96	0.04	3.53	3.54	4.05	12.89
	2	81486.93	3557.15	0.96	0.04	3.53			

### 1.2 Breaking extension

The percentage ratio of maximum extension before failure to initial length of sample is called as breaking extension. It explains the percentage of the extension which a sample can expand up to its failure point. It was observed that the copper filaments have very high breaking extension as compared to composite filaments and polyester filaments as shown in Figure 144. The composite filaments did not exhibit same level of extension due to limitation imposed by polyester. The composite filament had same level of extension which was exhibit by the polyester filaments. It is quite clear that composite filaments principally adopt the breaking extension limit from polyester sheath. The error bars express the standard deviation of data sets from mean value.

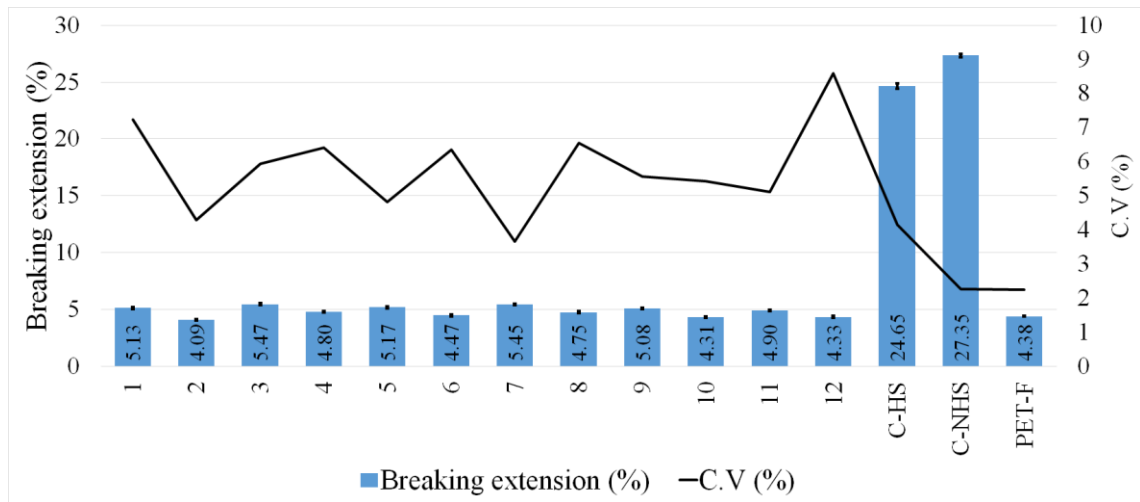


Figure 144. Graphical representation of breaking extension in percentage

### 1.3 Modulus

The modulus was calculated at 1 % of extension value because of lower value of elastic limit obtained for composite filaments. It is a measure of the stiffness of the filament which is explained as resistance to extension. It is observed that heat treatment changed the modulus of the copper filament (Figure 145). The non-thermal treated copper filament (C-NHS) has less modulus as compared to thermally treated copper filament (C-HS). The copper filament was thermally treated due to extrusion temperature before exiting from spinneret hole. As a result, the modulus of composite filaments was in close proximity to the value of modulus exhibit by copper filament. Furthermore, the polyester filament (PET-F) exhibit higher modulus as compared to composite filaments. Owing to inclusion of metal in the polyester filament, the changes in molecular arrangement occurs before cooling which reduces the modulus of the composite filament [6].

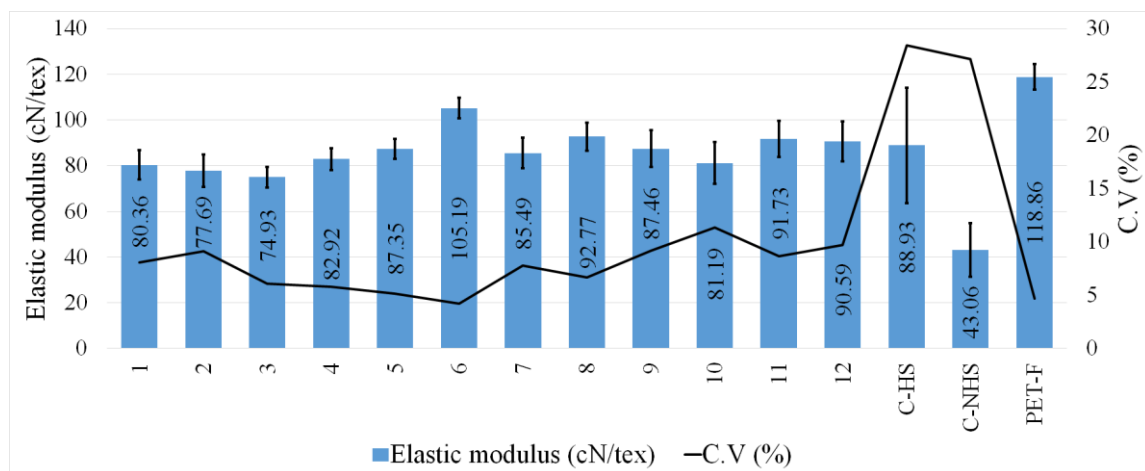


Figure 145. Graphical representation of elastic modulus of samples

#### 1.4 Work of rupture

It is a measure of toughness of the material. It explains the total energy required for failure of the composite filament. The area under the specific load-extension curve is a measure of the work done required to break specific sample. An automatic curve fitting software, Tablecurve 2D version 5.01 was utilized for determining area under the curve. The work of rupture for different samples is shown in Figure 146. The energy required to break polyester filament was quite low as compared with composite filaments. It is observed that the work of rupture increase by the inclusion of copper filament in the polyester polymer.

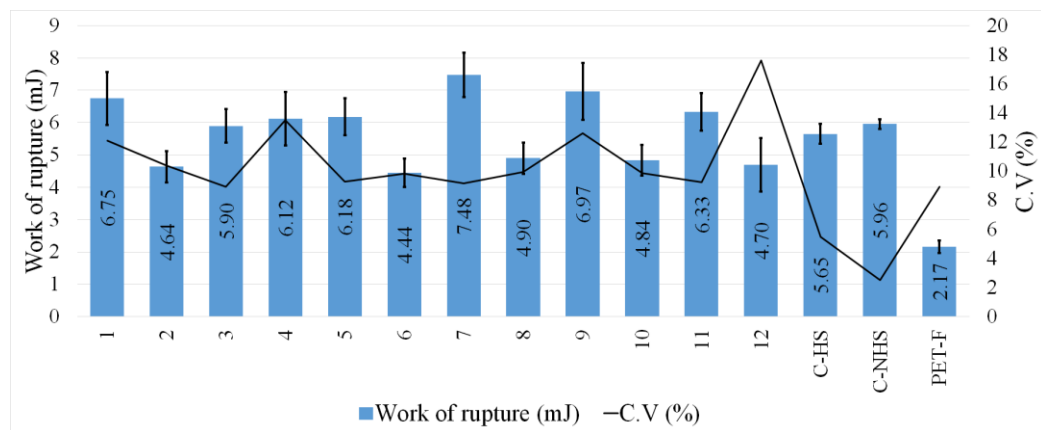


Figure 146. Graphical representation of work of rupture of different samples

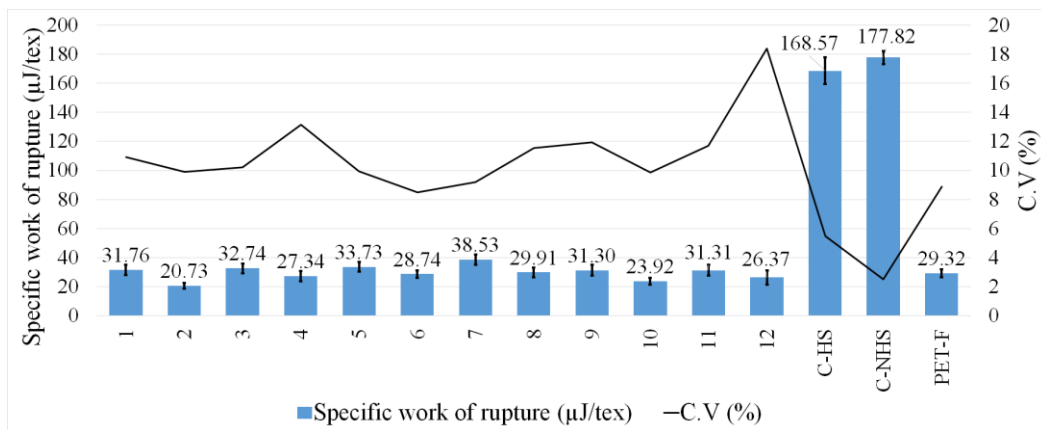


Figure 147. Graphical representation of specific work of rupture of samples

The specific work of rupture is a ratio of work of rupture to linear density of the material. It is used for comparison basis for materials having different linear densities. The specific work of rupture of the samples are shown in Figure 147. It was observed that copper filament had highest specific work of rupture, considered as stronger material in composite filament. The differences between copper and composite filament's specific work of rupture is because of high density and very small diameter of copper filament.

## D Tribology characterization

The coefficient of friction of samples were measured. The force versus displacement curve obtained for sample code 1 during testing is shown in Figure 148. The average frictional coefficient difference ( $\overline{\mu_s - \mu_k}$ ) between successive minimum ( $\mu_s$ ) and maximum ( $\mu_k$ ) coefficients corresponding to generated forces in slip ( $F_s$ ) and stick ( $F_k$ ) points of filament was used to compare different samples.

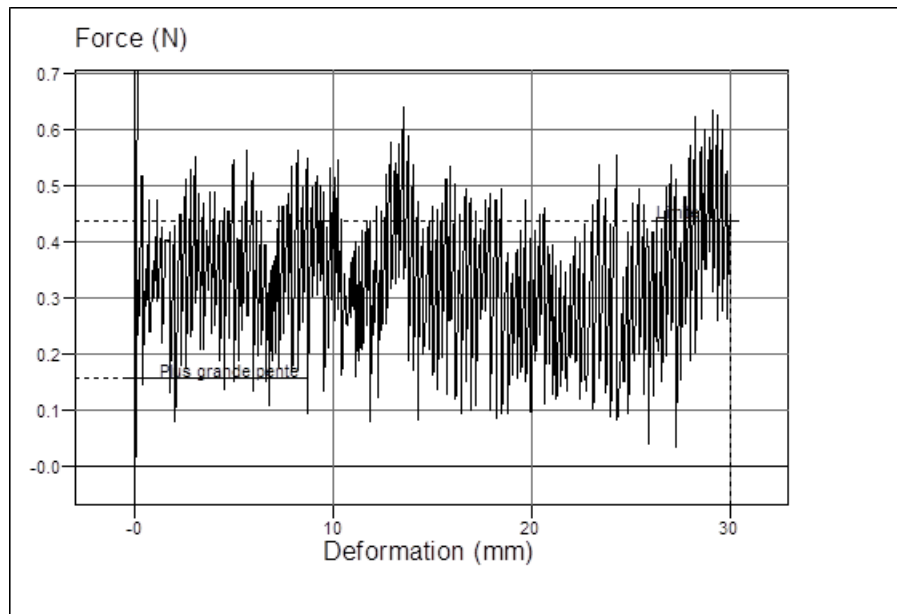


Figure 148. Force versus extension graph obtained for sample code 1

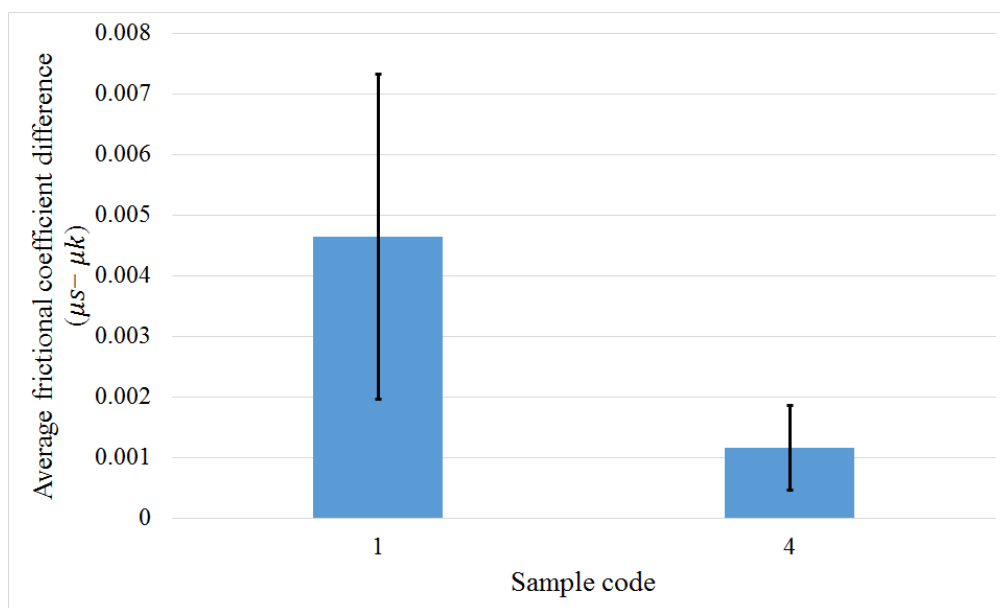


Figure 149. Mean friction coefficient difference values of different sample codes



It was observed that the mean coefficient friction difference values were significantly different for different samples codes as shown in Figure 149. The sample code 1 had elliptical cross-sectional shape while sample code 4 had less elliptical with more regular shape as compared to sample code 1. The mean coefficient friction difference value for sample code 1 was quite high which was due to more surface contact of filaments with each other. As the filament become regular, the frictional contact area reduces. This is the reason that sample code 4 depicted less mean coefficient friction difference values as compared to sample code 1.

### **E Bending characterization**

The bending properties expresses the stiffness of the material to bend. The analysis was performed on Kawabata Evaluation System (KES) using FB2-SH module. This module is specified for single hair bending test by executing bending deformation as a circular arc up to defined curvature at constant rate. The bending rigidity and moment of hysteresis was recorded and given in Table 15.

Table 15. Experimental data of bending properties of different samples

<b>Sample code</b>	<b>Bending rigidity (B) [gf.cm<sup>2</sup>]</b>	<b>Moment of hysteresis (2HB) [gf.cm]</b>	<b>Bending rigidity (B) [mN.mm<sup>2</sup>/tex<sup>2</sup>]</b>
2	0.2902	0.0922	0.0231
4	0.1144	0.0685	0.0146
5	0.3494	0.0896	0.0240
6	0.1417	0.0731	0.0139
8	0.2025	0.0751	0.0264
10	0.0513	0.0799	0.0113
11	0.0352	0.0889	0.0119
12	0.2748	0.1212	0.0367
C-HS	0.0021	0.05	0.0018
C-NHS	0.0058	0.0495	0.0051

The bending curves of different cross-sectional shaped filaments developed between bending moment (M) and curvature (K) are shown in Figure 150. The sample codes 2, 6 and 10 represents elliptical, triangular and rectangular cross-sectional shapes respectively. It was observed that the bending curves obtained for elliptical and triangular shaped filaments were quite different from rectangular shaped filament. The reason behind this fact is that shape have high influence on the bending properties of the material. Moreover, the co-ordinate of bending is highly important in bending of irregular shapes. The bending force required in a particular direction is almost the same as required in any other direction for regular shaped filaments, which is not possible in case of other irregular cross-sectional shaped filaments.

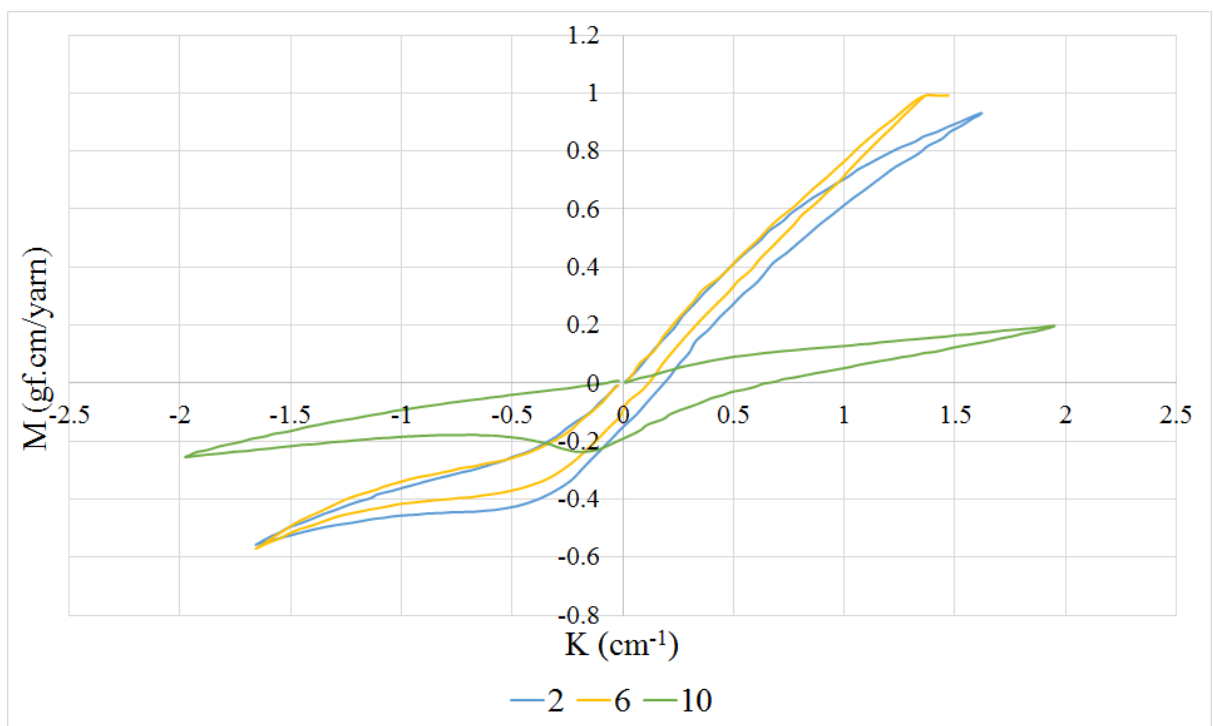


Figure 150. Experimental bending curves of different shaped filaments

The bending curves obtained for regular structures of sample codes 4, 8 and 12 are shown in Figure 151. These codes represent cross-sectional shapes of elliptical, triangular and rectangular. The sample code 11 represents circular cross-sectional shape. The bending curves of copper filaments of thermal treated and non-thermal treated samples are also provided for reference.

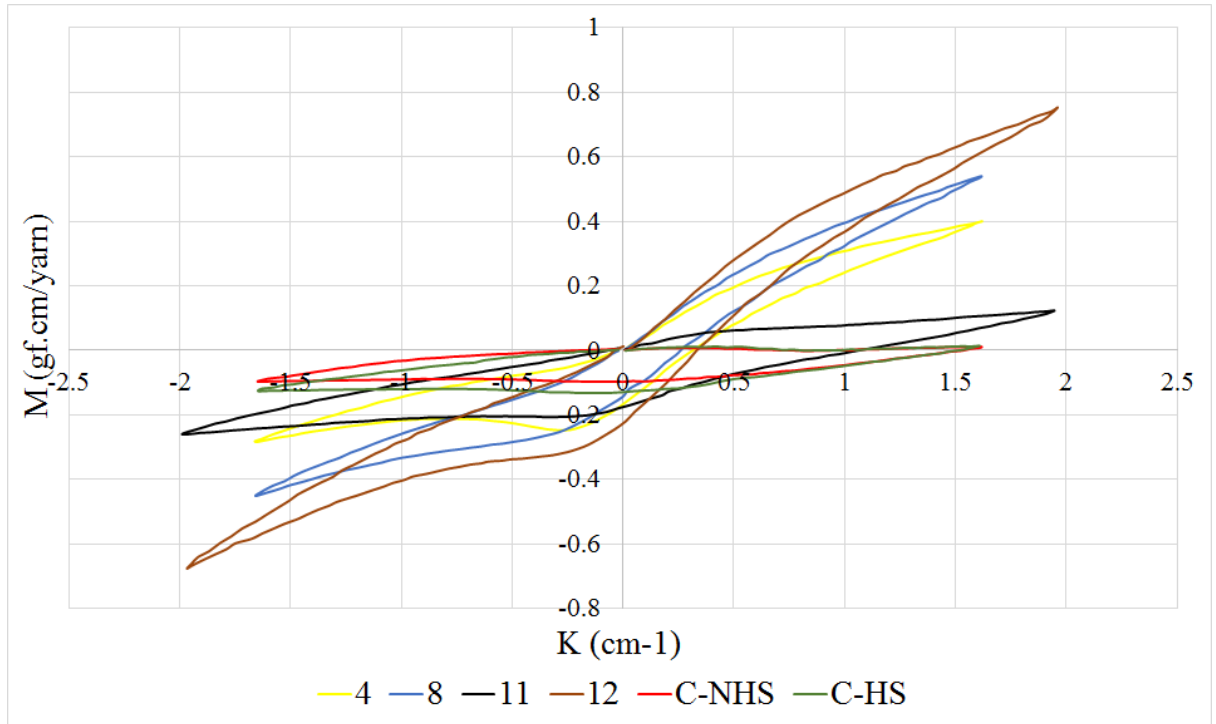


Figure 151. Experimental bending curves obtained for different sample codes

It was observed that the bending rigidity of non-thermal treated copper filament was high comparative to thermal treated filament. It explains that thermal treatment changed the stiffness value of the filament. The results can be comparable by calculating bending modulus. It is ratio of bending rigidity to moment of inertia. The bending rigidity for a circular shaped filament can be calculated using Equation 29.

$$E_B = \frac{B}{I} = \frac{64 B}{\pi D^4} \quad (29)$$

Where  $E_B$  is the bending modulus (GPa),  $B$  is the bending rigidity ( $\text{mN}\cdot\text{mm}^2/\text{tex}^2$ ),  $I$  is the geometrical moment of inertia and  $D$  is the diameter of the filament (mm). The obtained results were shown in Figure 152. It was observed that the filament sample codes having regular cross-sectional structure have higher bending modulus as compared to the other samples. One of the reason is also that the calculation method is for circular section of filament. the other reason may be due to irregular bending rigidity of the filament at different directions. As the distance from the centre point of the filament to the outer boundary changes at every place, therefore due to change in material quantity in particular direction may change the properties associated with them. It was concluded that KES is not proved to be adequate bending stiffness measurement device for irregular shaped metallic composite filaments.

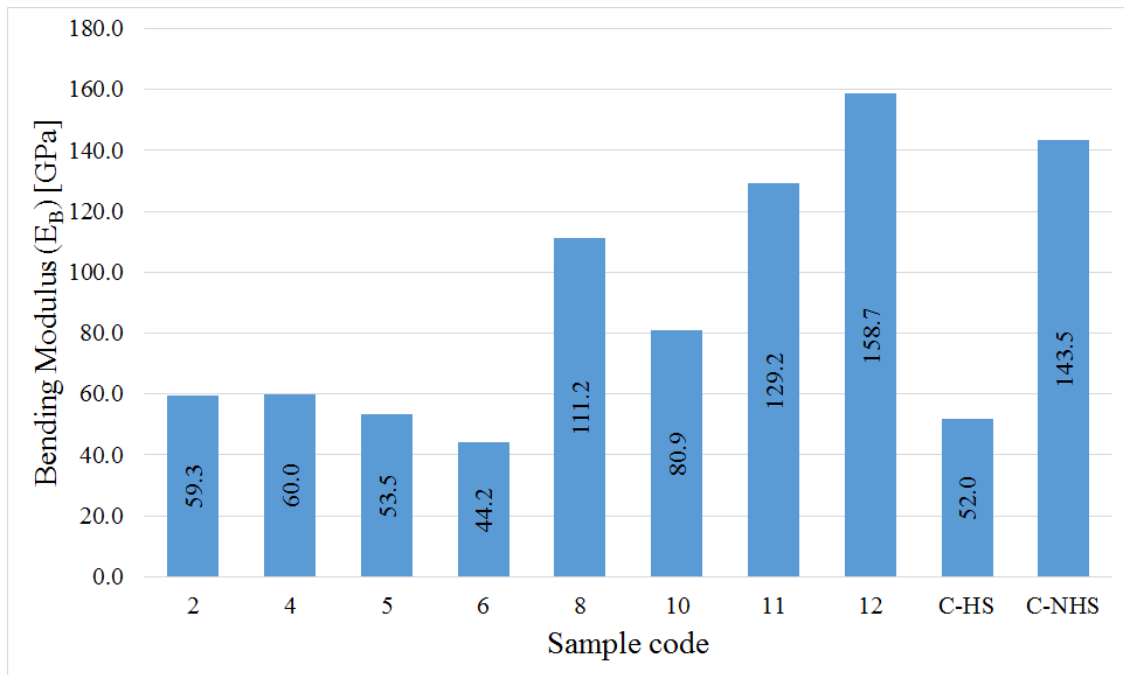


Figure 152. Graphical representation of bending modulus of samples

## ***VI Development of coaxial ferroelectric filament***

One of the application of previously optimized process is in the development of ferroelectric coaxial composite filament for sensor and actuator. To demonstrate the effectiveness of the designed process, coaxial composite filament with PVDF<sub>70</sub>-TrFE<sub>30</sub> copolymer and copper monofilament was developed. The piston end type 3 with optimized spinneret prototype 9 having specifications of 4 holes, 254  $\mu\text{m}$  tube, 2 mm tube position and 1 mm of spinneret exit diameter were used. The increased cooling chamber length enforced with forced counter airflow was employed for cooling of filament. The operating temperature was considered keeping in view the results obtained from DSC and rheology analysis. The extrusion was done at temperature of 320 °C with resident time for polymer in oven was 5 minutes. The spinning parameters, namely piston speed and winding speed were set at 5 mm/min and 35.85 m/min respectively. The drawing was done with homogeneous temperature field drawing technique, which provides constant rate of drawing with necking. The filament drawing was done at temperature of 30 $\pm$ 2 °C. The coaxial composite filament was wound on package with winding system.

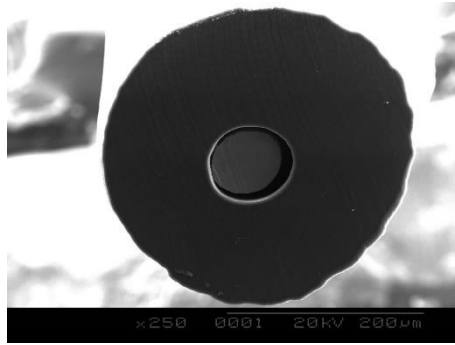


Figure 153. Cross-sectional view of Cu/PVDF-TrFE core/sheath coaxial composite filament

The cross-sectional morphology of the composite filament is shown in Figure 153. It was observed that the developed composite filament had very good positioning of core at central coaxial position. The diameter of the filament obtained were in the range of 315-355 µm. It was observed that the eccentricity of core filament from coaxial position in composite filament was quite low for both samples developed with high and low molecular weight ferroelectric copolymers as shown in Figure 154.

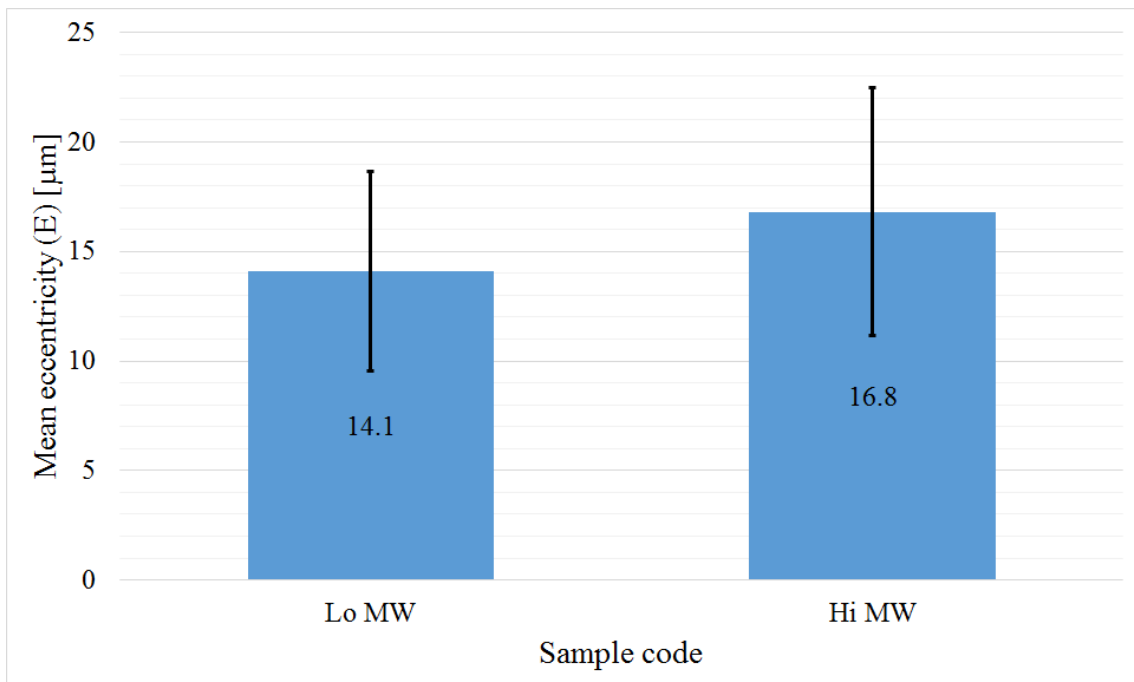


Figure 154. Graphical representation of eccentricity of core in PVDF-TrFE composite filaments

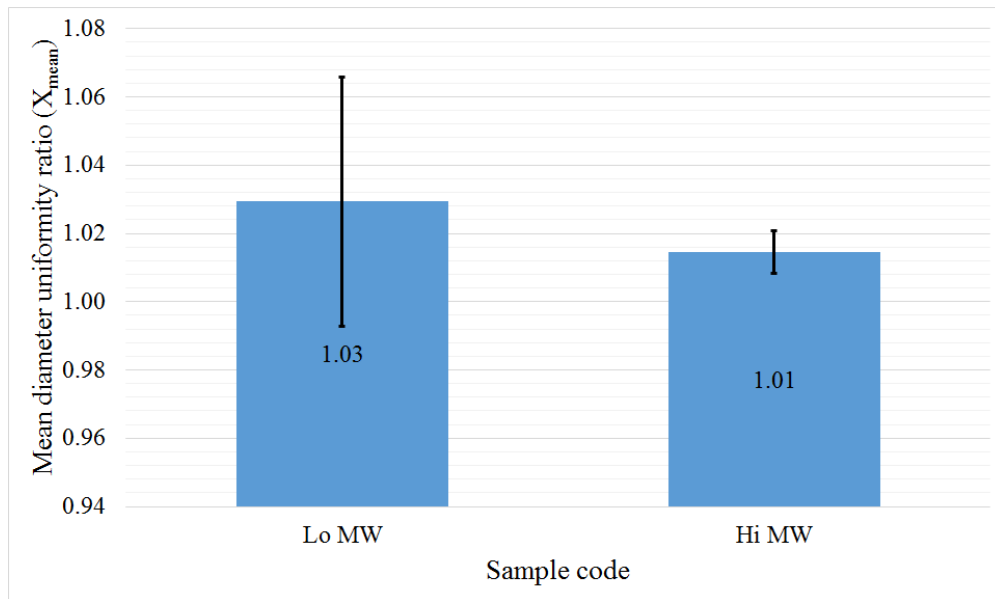


Figure 155. Graphical representation of mean diameter uniformity ratio of PVDF-TrFE composite filaments

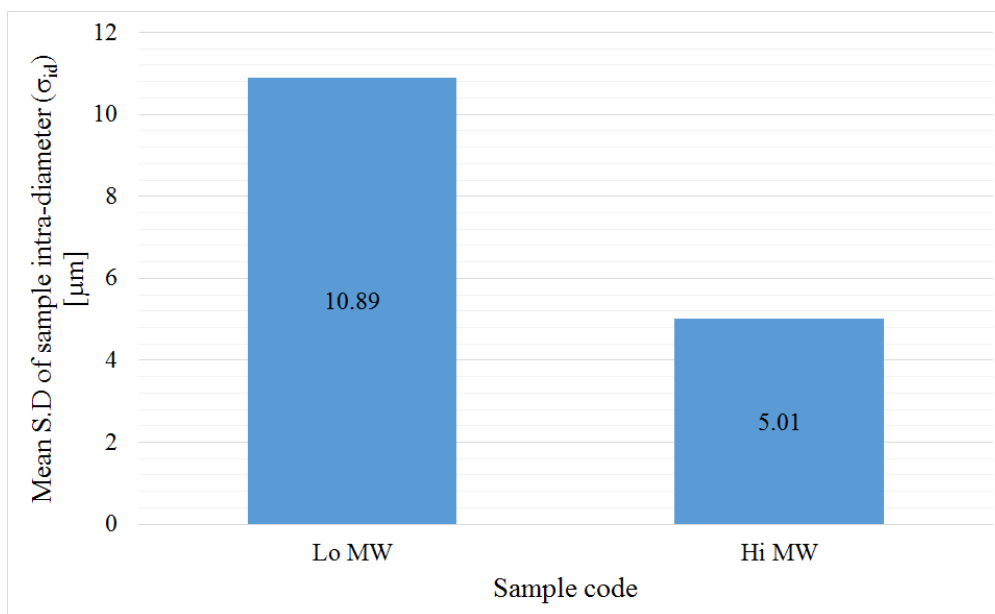


Figure 156. Graphical representation of standard deviation within samples of PVDF-TrFE composite filaments

The results expressed that the core was at very good position in the composite filament. In addition, the mathematical calculations showed that the mean diameter uniformity ratio for both low and high molecular weight samples were regular and circular in nature as shown in Figure 155. Considering both attributes, it is evident that the developed composite filament were in good shape and structure as per required for fabrication of sensor.

The standard deviation obtained within the dataset of sample having 10 replicates each is shown in Figure 156. It was observed that the produced results are reproducible and reliable. The standard deviation obtained for low and high molecular weight composite filaments were 11 and 5 respectively.

### A Characterization of PVDF-TrFE composite filament

Mechanical, tribology and objective characterization of the ferroelectric composite filament were done. The specific stress and elongation percentage graphical representation is shown in Figure 157.

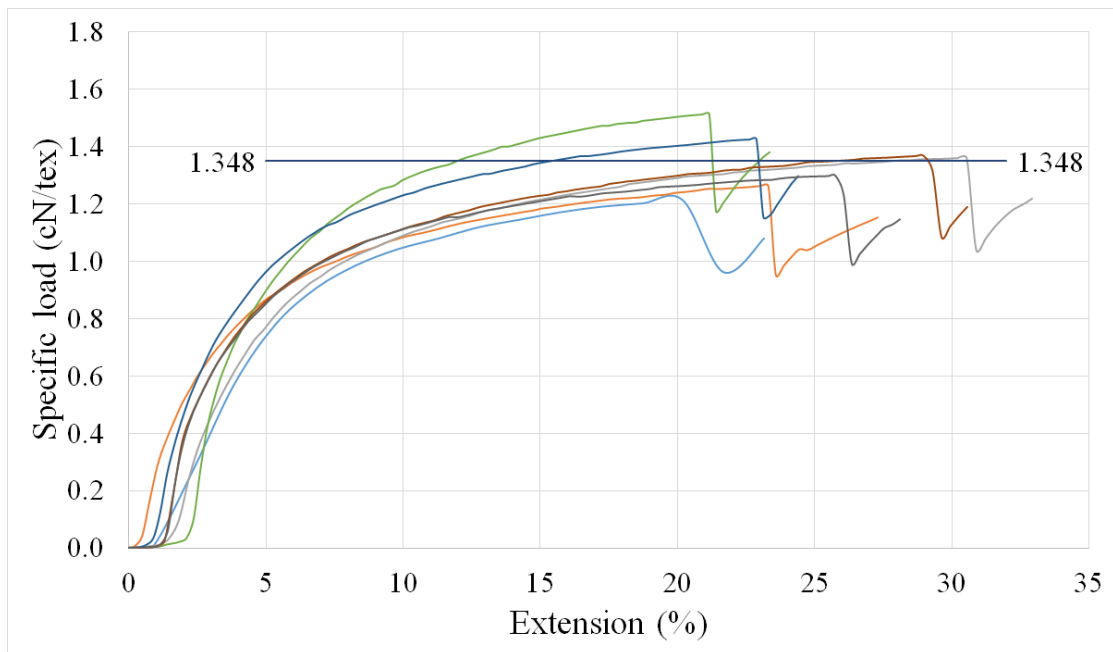


Figure 157. Specific load vs extension curves of Cu/PVDF-TrFE core/sheath coaxial composite filament

It was observed that the elastic region was too small as compared to the plastic region. The specimen start getting elongated plastically after the elastic limit, from where it didn't go back to its initial dimension. The gauge length kept for these analysis was 25 mm with breakage within  $20 \pm 3$  seconds same as per previous tests. The arithmetic mean value of the breaking specific stress is shown as horizontal straight line on the graph.

The test data of the mechanical characterization is shown in Table 16. The reason for reduction in tenacity and modulus is might be due to non-proper adhesion between core and sheath polymer. The weak adhesion was caused due to adsorbed water vapors on

surface of copper filament by high humidity in air, which restricted the development of strong bonding interface between copper core and copolymer sheath.

Table 16. Tensile properties of Cu/PVDF-TrFE core/sheath coaxial composite filament

	<b>Tenacity (cN/tex)</b>	<b>Breaking Extension (%)</b>	<b>Initial Modulus (cN/tex)</b>	<b>Specific work of rupture (<math>\mu\text{J/tex}</math>)</b>
Mean	1.35	24.60	0.66	64.59
S.D	0.10	3.84	0.14	12.56
C.V %	7.51	15.61	21.34	19.45

The tribology characterization was carried out using special arrangement device as shown in Figure 49. The displacement curve obtained during successive up and down picks corresponds to stick and slip of filament with each other is shown in Figure 158. The average frictional coefficient difference ( $\overline{\mu_s} - \overline{\mu_k}$ ) between successive minimum ( $\mu_s$ ) and maximum ( $\mu_k$ ) coefficients corresponding to generated forces in slip ( $F_s$ ) and stick ( $F_k$ ) points of filament was used to compare different samples.

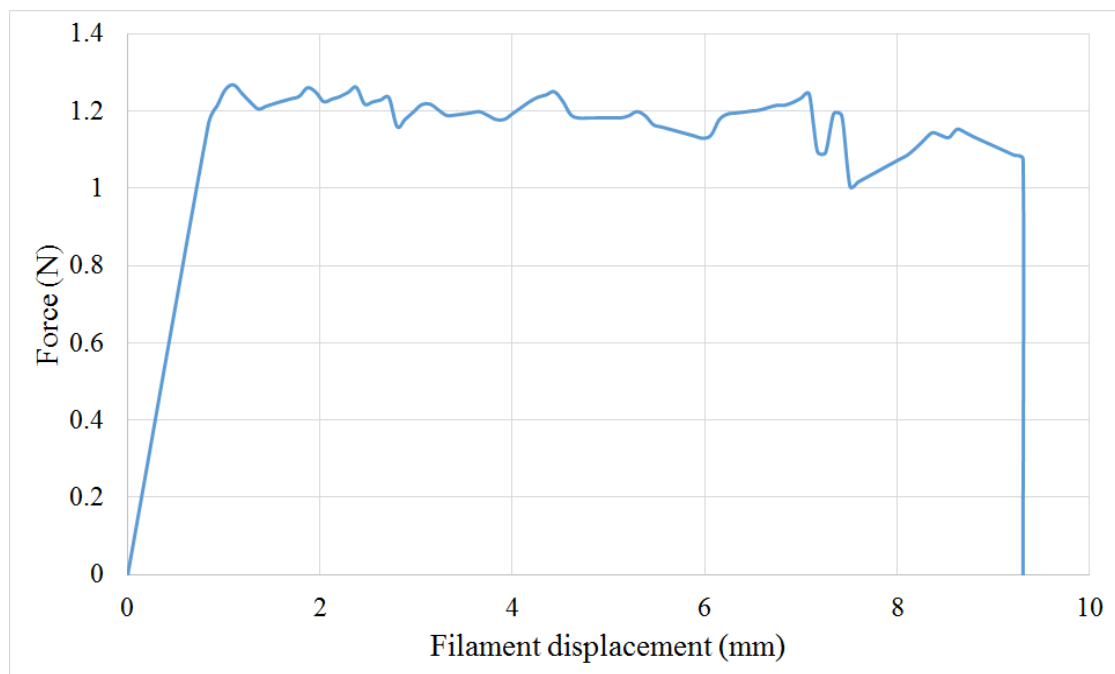


Figure 158. Force versus displacement curve obtained during frictional testing of composite filament



There was no significant difference observed between the mean friction coefficient difference ( $\overline{\mu_s - \mu_k}$ ) values of low and high molecular copolymer composite filaments as shown in Figure 159. It is concluded that low and high molecular weight copolymer composite filaments have same physical attributes irrespective of their molecular arrangements.

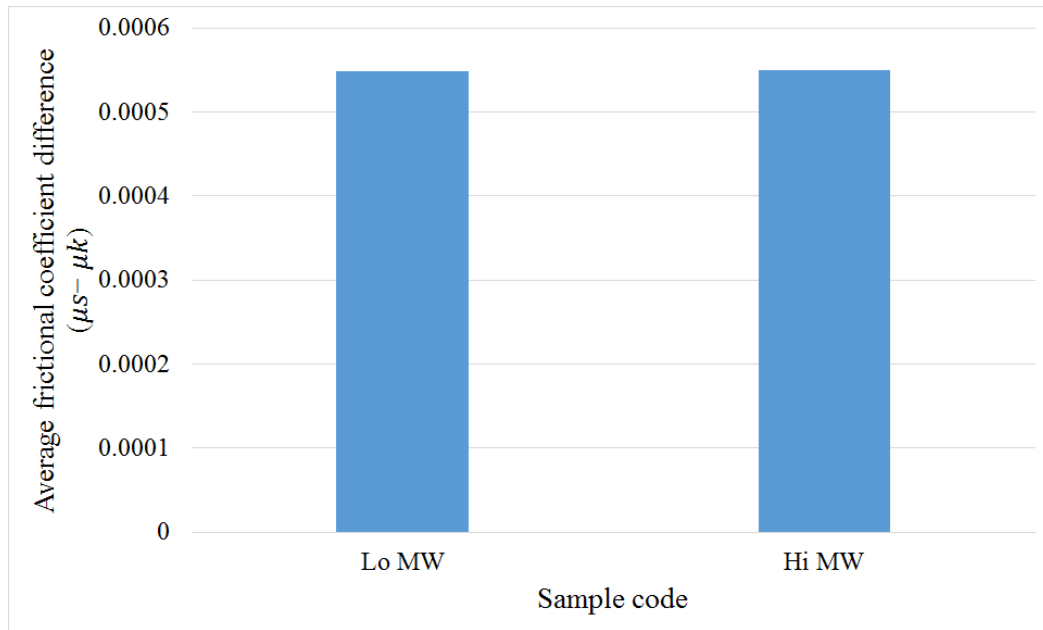


Figure 159. Friction coefficient difference values of low and high molecular weight PVDF-TrFE composite filaments

Table 17. Experimental data of bending properties of PVDF-TrFE coaxial composite filament

Sample code	Bending rigidity (B) [gf.cm <sup>2</sup> ]	Moment of hysteresis (2HB) [gf.cm]
Lo MW	0.2794	0.2683
Hi MW	0.2645	0.1998

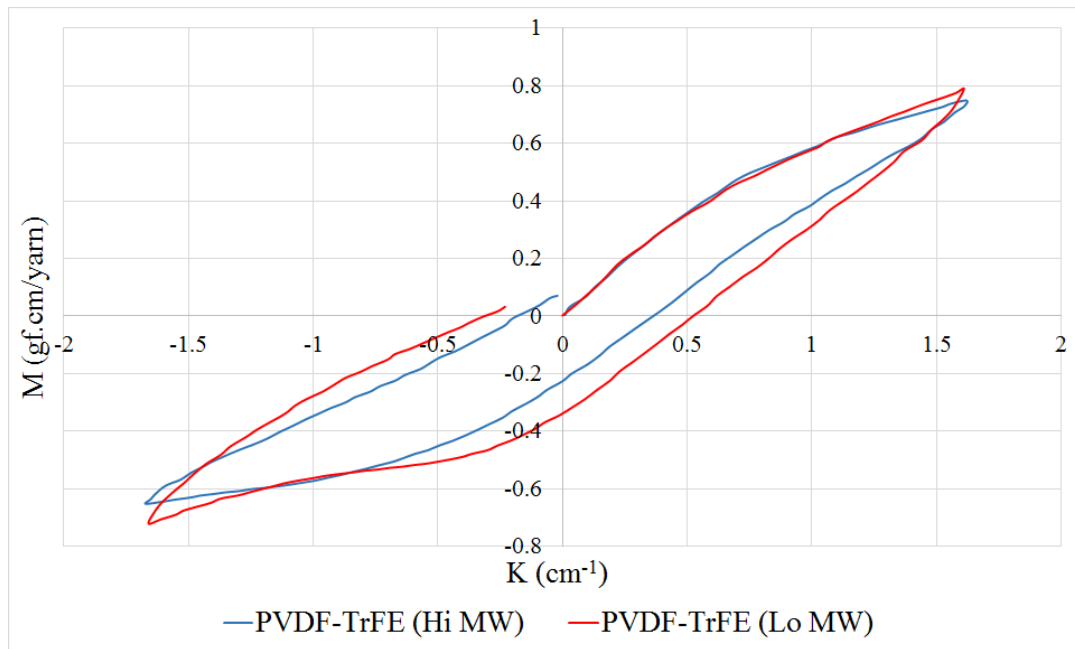


Figure 160. Experimental bending curves for low and high molecular weight coaxial composite Cu/PVDF-TrFE filaments

The objective characterization was done using KES on FB2-SH module. The experimental data is shown in Table 17. The graphical representations of the bending curves are shown in Figure 160. It is observed that the bending rigidity was not much different for high and low molecular weight ferroelectric copolymers, while the moment of hysteresis had a difference of 26 % between them.

## VII Conclusion

It is concluded that the developed spinneret design can be used to fabricate coaxial composite filaments in desired cross-sectional shape including elliptical, triangular, rectangular and circular shape. A number of 10 spinneret prototypes were designed. The parameters of the spinneret design had significant influence on the cross-sectional shape and position of core filament of composite filament. The modification in melt extrusion machine also includes introduction of a separate feeding channel for core filament, piston end modification design and cooling chamber modifications. The tensile strength test showed that the filament having circular cross-sectional shape exhibit highest tenacity value. The work of rupture was also found higher for regular cross-sectional shaped filaments. The developed composite filaments had diameter in range of 350-500  $\mu\text{m}$ . It was observed that the crystallinity of the polymer in filament structure was reduced due to non-stretching and improper alignment of polymer chains during extrusion process. The

ferroelectric copolymer coaxial composite filaments developed with high and low molecular weights were found having almost same values for bending rigidity and mean coefficient of friction difference values. It was concluded that the developed extrusion process and design can be efficiently used for manufacturing required coaxial composite filament structures.

## CHAPTER 5

### CONCLUSION

The aim of this study is to develop a coaxial composite filament for fabrication of sensors and actuators. The core of the filament was selected as metallic filament for obtaining higher performance characteristics for sensors and excellent electrical signal transmission. This work comprises of development of spinneret for manufacturing of coaxial composite filaments, modifications in machine process and design, characterization of coaxial composites filaments and characterization of polymers. The development and optimization of spinneret were initially carried out using polyester polymer followed by development of coaxial composites filaments using other polymeric materials including PVDF<sub>70</sub>-TrFE<sub>30</sub> copolymer and polyamide polymers as sheath material and core of copper filament. It is concluded that the developed spinneret optimized design can be efficiently used for the development of coaxial composite filaments using different polymer matrix and core filaments as per requirement. The particular point to be addressed during extrusion is viscosity of the polymer. The results obtained using polyester, polyamide and polyvinylidene difluoride-co-trifluoroethylene polymer explained that the developed spinneret work efficiently in particular range of polymer viscosity. At very low viscosity, the position of the core shifts from desired coaxial position of composite filament.

There is no spinneret found in literature for the development of coaxial composite filaments using metallic wire in core. Therefore, a number of 10 spinneret prototypes were designed keeping in view of industrial die design rules. Different cross-sectional filament shapes having core at central axial position were obtained including elliptical, triangular, rectangular and circular shapes. The spinneret design was optimized for circular shaped filament. The optimized spinneret design is constructed in two parts. The upper part has tube passage at central position for core filament along with flow channels around the tube passage at equal radial and angular positions. The lower part has conical shape with exit hole. The joining of both parts is done by flange type rigid coupling to ensure proper positioning of core in central axial position of the filament. It was observed that filament cross-sectional shape significantly depends on flow channel's position, geometry of flow and spinneret exit diameter. The position of the core filament was significantly dependent on tube inner diameter, position of tube and polymer viscosity. The spinneret parameters were analysed extensively to reproduce the results with accuracy.

The machine modifications in process and design includes an introduction of separate passage for core filament, hollow piston end type modified design and cooling chamber modifications. It was proved that the separate passage was highly important for the development of coaxial composite filaments in regard of continuity of process and quality of produced filament. The hollow piston end design made it possible to pass the core filament through it without causing any blockage or chocking of core. The cooling chamber modifications include forced counter airflow and change of temperature gradient across chamber length proves regularity and softness in developed composite filament.

The developed composite filament samples were characterized by physical, morphological, mechanical and stiffness aspects. The developed composite filaments were in range of 350-500  $\mu\text{m}$  in diameter. The cross-sectional shape of the filaments changed with change of parameters in spinneret design including number of polymer flow channels, geometry of polymer flow inside spinneret, inner diameter of tube for core and length of interaction of core and melt polymer before spinneret exit. The tensile results suggested that circular cross-sectional shaped composite filaments exhibit higher tenacity value as compared to all developed samples. In addition, work of rupture was also found higher for regular cross-sectional shaped filaments. The bending stiffness was found higher for irregular cross-sectional shaped filaments caused due to irregular material placement across the transversal direction of filament. It was concluded that obtained bending stiffness results were not reliable due to variations in filament cross-sectional shapes on KES.

The polymer characterisation was done including thermal, rheological and structural characterization. Melt flow rate was highly dependent on molecular weight of the polymer and temperature being processed. DSC analysis showed that the degree of crystallization reduces in composite filaments as compared to polymer chips. The reason is that the polymer was quenched at room temperature which was about  $50\pm 2$   $^{\circ}\text{C}$  lower than glass transition temperature of polymer. This restricted the polymer chains to align themselves with each other. Furthermore, the polymer chains were not get stretched as polymer flow along with core filament like a sheath. These factors ultimately reduced the crystallinity percent in the developed filament. The viscosity was found inverse function with temperature. It was found that the viscosity of polyamide dropped steeply at small increase in shear rate. the overall viscosity of polyamide was found very low due to which the sheathing technique was not found effective for it. The PVDF<sub>70</sub>-TrFE<sub>30</sub> copolymer

viscosity was found too high, therefore higher extrusion temperature was required for its processing.

The composite filaments were developed using sheath of polyester, polyamide and polyvinylidene difluoride-trifluoroethylene polymers. Coaxial composite filament developed with PVDF<sub>70</sub>-TrFE<sub>30</sub> copolymer were also characterized. It was found that the developed modified process can be effectively used for the development of coaxial composite filaments. These filaments have higher electrical conductivity values because of introduction of metal filament in them. These filaments prove to be more efficient in electrical signal transmission and in sensitivity of sensors developed from them as compared to results reported in literature. These filaments find their applications in SMART textiles, e-textiles and intelligent textiles. The main application includes for development of sensors, actuators; can be used for electrical signal transmission yarns in wearable electronic textiles and fabrication of electromagnetic shielding effectiveness fabrics.



## **FUTURE PLANS**

1. Improvement of extrusion die design by using electro-polishing method for better flow and maintain consistency in the internal surfaces of the flow channels.
2. Theoretical calculations of polymer flow through the spinneret and its validation from experimental results.
3. Experimentation of prototype 10 and development of better spinneret design.
4. Transformation of this research to screw based mechanism.
5. Modification of industrial melt extruders and its study.
6. Introduction of CNT's in ferroelectric copolymer to develop highly sensitive pressure sensors.





## REFERENCES

1. Hearle, J. W. S., *Fibre structure: its formation and relation to performance*, in *Handbook of Textile Fibre Structure*, S. J. Eichhorn, J. W. S. Hearle, M. Jaffe and T. Kikutani. Vol. 1. 2009, Woodhead Publishing: Oxford, UK. p. 3-21.
2. Youssef, H. A., El-Hofy, H. A. and Ahmed, M. H., *Polymeric Materials and Their Processing*, in *Manufacturing Technology: Materials, Processes, and Equipment*, H. A. Youssef, H. A. El-Hofy and M. H. Ahmed. 2011, CRC Press: New York.
3. Bhargava, A., *Engineering Materials: Polymers, Ceramics and Composites*. 2012, PHI Learning Pvt. Ltd.
4. Akovall, G. and Uyanik, N., *Introduction*, in *Handbook of composite fabrication*, G. Akovall. 2001, Rapra Technology Ltd.: Shropshire, UK. p. 3-20.
5. Kechiche, M. B., Bauer, F., Harzallah, O. and Drean, J. Y., *Development of piezoelectric coaxial filament sensors P(VDF-TrFE)/copper for textile structure instrumentation*. *Sensors and Actuators A: Physical*, 2013. **204**: p. 122-130.
6. Lim, T. H., Lee, S. H. and Yeo, S. Y., *Highly conductive polymer/metal/carbon nanotube composite fiber prepared by the melt-spinning process*. *Textile Research Journal*, 2016. online February 18, 2016.
7. Martins, R. S., Gonçalves, R., Azevedo, T., Rocha, J. G., Nóbrega, J. M., Carvalho, H. and Lanceros-Mendez, S., *Piezoelectric coaxial filaments produced by coextrusion of poly(vinylidene fluoride) and electrically conductive inner and outer layers*. *Journal of Applied Polymer Science*, 2014. **131**(17).
8. Pecora, A., Maiolo, L., Maita, F. and Minotti, A., *Flexible PVDF-TrFE pyroelectric sensor driven by polysilicon thin film transistor fabricated on ultra-thin polyimide substrate*. *Sensors and Actuators A: Physical*, 2012. **185**: p. 39-43.
9. Yildiz, Z., Atak, O., Güngör, A., Önen, A. and Usta, İ., *The effect of various dopant types for chemical oxidation polymerization of pyrrole on electromagnetic shielding, electrical conductivity and thermal properties of cotton fabrics*, in *2nd International Conference on Value Addition and Innovation in Textile (Covitex)*. 2013, National Textile University, Pakistan: Faisalabad, Pakistan. p. 86-94.
10. Güngör, A., Önen, A., Usta, İ., Yildiz, Z. and Atak, O., *Electromagnetic shielding, electrical and thermal properties of conductive polymer coated cotton fabrics*, in *2nd International Conference on Value Addition & Innovation in Textiles*. 2013, National Textile University, Pakistan: Faisalabad, Pakistan. p. 310-316.
11. Schwarz, A., Hakuzimana, J., Westbroek, P., Mey, G. D., Priniotakis, G., Nyokong, T. and Langenhove, L. V., *A study on the morphology of thin copper films on para-aramid yarns and their influence on the yarn's electro-conductive and mechanical properties*. *Textile Research Journal*, 2012. **82**(15): p. 1587-1596.
12. Little, B. K., Li, Y., Cammarata, V., Broughton, R. and Mills, G., *Metallization of Kevlar Fibers with Gold*. *ACS applied materials & interfaces*, 2011. **3**(6): p. 1965-1973.
13. Lee, S., Shin, S., Lee, S., Seo, J., Lee, J., Son, S., Cho, H. J., Algadi, H., Al-Sayari, S., Kim, D. E., and Lee, T., *Ag Nanowire Reinforced Highly Stretchable Conductive Fibers for Wearable Electronics*. *Advanced Functional Materials*, 2015. **25**(21): p. 3114-3121.
14. Hu, C.-C., Chang, S.-S. and Liang, N.-Y., *Preparation and characterization of carbon black/polybutylene terephthalate/polyethylene terephthalate antistatic*

- fiber with sheath–core structure*. The Journal of The Textile Institute, 2015. **107**(8): p. 976-984.
15. Liu, X., Zhou, X., Li, Y. and Zheng, Z., *Surface-Grafted Polymer-Assisted Electroless Deposition of Metals for Flexible and Stretchable Electronics*. Chemistry – An Asian Journal, 2012. **7**(5): p. 862-870.
  16. Kannaian, T., Neelaveni, R. and Thilagavathi, G., *Design and development of embroidered textile electrodes for continuous measurement of electrocardiogram signals*. Journal of Industrial Textiles, 2013. **42**(3): p. 303-318.
  17. Zhiyi, Z., *Electrical conductive Cu/glass fibre composites prepared by electroless plating*. Micro & Nano Letters, IET, 2014. **9**(2): p. 83-86.
  18. Behabtu, N., Young, C. C., Tsentlovich, D. E., Kleinerman, O., Wang, X., Ma, A. W. K., Bengio, E. A., ter Waarbeek, R. F., de Jong, J. J., Hoogerwerf, R. E., Fairchild, S. B., Ferguson, J. B., Maruyama, B., Kono, J., Talmon, Y., Cohen, Y., Otto, M. J., and Pasquali, M., *Strong, Light, Multifunctional Fibers of Carbon Nanotubes with Ultrahigh Conductivity*. Science, 2013. **339**(6116): p. 182-186.
  19. Pant, H. R., Pandeya, D. R., Nam, K. T., Baek, W.-i., Hong, S. T. and Kim, H. Y., *Photocatalytic and antibacterial properties of a TiO<sub>2</sub>/nylon-6 electrospun nanocomposite mat containing silver nanoparticles*. Journal of Hazardous Materials, 2011. **189**(1–2): p. 465-471.
  20. Bhat, N. V., Seshadri, D. T. and Radhakrishnan, S., *Preparation, Characterization, and Performance of Conductive Fabrics: Cotton + PANi*. Textile Research Journal, 2004. **74**(2): p. 155-166.
  21. Reese, G., *Polyester Fibers: Fiber Formation and End-Use Applications*, in *Modern Polyesters: Chemistry and Technology of Polyesters and Copolyesters*, J. Scheirs and T. E. Long. 2004, John Wiley & Sons, Ltd: Chichester, UK. p. 399-433.
  22. Rajendrakumar, K. and Thilagavathi, G., *A study on the effect of construction parameters of metallic wire/core spun yarn based knitted fabrics on electromagnetic shielding*. Journal of Industrial Textiles, 2013. **42**(4): p. 400-416.
  23. Ozkan, I., Baykal, P. D. and Karaaslan, M., *Investigation of electromagnetic polarization properties of silver containing Robotuft carpets*, in *16th Autex World Textile Conference*. 2016: Ljubljana, Slovenia.
  24. Su, C. I. and Leu, C. S., *Cross-Sectional Structure of Composite Yarns*. Textile Research Journal, 1998. **68**(10): p. 715-718.
  25. Wu, W.-Y. and Lee, J.-Y., *Twist in the Spinning of a Composite Yarn*. Textile Research Journal, 1995. **65**(9): p. 522-526.
  26. Okamoto, M. and Watanabe, K., *Spontaneously crimping synthetic composite filament and process of manufacturing the same*. 1973. U. S. Patent, US3718534 A.
  27. Michael, J. and Anthony, J. E., *Polyester Fibers*, in *Handbook of Fiber Chemistry*, M. Lewin. Third ed. Vol. Volume 8. 2006, CRC Press: Boca Raton, FL.
  28. Shyr, T.-W. and Shie, J.-W., *Electromagnetic shielding mechanisms using soft magnetic stainless steel fiber enabled polyester textiles*. Journal of Magnetism and Magnetic Materials, 2012. **324**(23): p. 4127-4132.
  29. David, T., *Splittable composite filament*. 1968. U. S. Patent, US3418200 A.
  30. Han, E., Wang, Y., Chen, X., Shang, G., Yu, W., Niu, H., Qi, S., Wu, D. and Jin, R., *Consecutive Large-Scale Fabrication of Surface-Silvered Polyimide Fibers via an Integrated Direct Ion-Exchange Self-Metallization Strategy*. ACS applied materials & interfaces, 2013. **5**(10): p. 4293-4301.

31. Wei, Q., Yu, L., Wu, N. and Hong, S., *Preparation and Characterization of Copper Nanocomposite Textiles*. Journal of Industrial Textiles, 2008. **37**(3): p. 275-283.
32. Lu, Y., Liang, Q. and Xue, L., *Palladium-free catalytic electroless copper deposition on bamboo fabric: Preparation, morphology and electromagnetic properties*. Applied Surface Science, 2012. **258**(10): p. 4782-4787.
33. Cho, G. and Han, A., *Review of performance evaluation on e-textiles and textile-based keypads*. International Journal of Fashion Design, Technology and Education, 2011. **4**(2): p. 83-89.
34. Neves, A. I. S., Bointon, T. H., Melo, L. V., Russo, S., de Schrijver, I., Craciun, M. F. and Alves, H., *Transparent conductive graphene textile fibers*. Scientific Reports, 2015. **5**: p. 9866.
35. Panhuis, M. i. h., Wu, J., Ashraf, S. A. and Wallace, G. G., *Conducting textiles from single-walled carbon nanotubes*. Synthetic Metals, 2007. **157**(8–9): p. 358-362.
36. Hecht, D. S., Hu, L. and Grüner, G., *Electronic properties of carbon nanotube/fabric composites*. Current Applied Physics, 2007. **7**(1): p. 60-63.
37. Dastjerdi, R. and Montazer, M., *A review on the application of inorganic nanostructured materials in the modification of textiles: Focus on anti-microbial properties*. Colloids and Surfaces B: Biointerfaces, 2010. **79**(1): p. 5-18.
38. Okuhashi, T., *Carpet having durable antistatic properties*. 1971. U. S. Patent, US3582445 A.
39. Zhang, W., Tan, Y. Y., Wu, C. and Silva, S. R. P., *Self-assembly of single walled carbon nanotubes onto cotton to make conductive yarn*. Particuology, 2012. **10**(4): p. 517-521.
40. Huang, C. T., Shen, C. L., Tang, C. F. and Chang, S. H., *A wearable yarn-based piezo-resistive sensor*. Sensors and Actuators A: Physical, 2008. **141**(2): p. 396-403.
41. Huang, C. T., Tang, C. F., Lee, M. C. and Chang, S. H., *Parametric design of yarn-based piezoresistive sensors for smart textiles*. Sensors and Actuators A: Physical, 2008. **148**(1): p. 10-15.
42. Green, J., *Cotton/nylon fiber blends suitable for durable light shade fabric containing carbon doped antistatic fibers*. 1999. U. S. Patent, US5876849 A.
43. Jiang, S., Newton, E., Yuen, C.-W. M. and Kan, C.-W., *Application of chemical silver plating on polyester and cotton blended fabric*. Textile Research Journal, 2007. **77**(2): p. 85-91.
44. Jiang, S. Q., Newton, E., Yuen, C. W. M. and Kan, C. W., *Chemical silver plating and its application to textile fabric design*. Journal of Applied Polymer Science, 2005. **96**(3): p. 919-926.
45. Egusa, S., Wang, Z., Chocat, N., Ruff, Z. M., Stolyarov, A. M., Shemuly, D., Sorin, F., Rakich, P. T., Joannopoulos, J. D. and Fink, Y., *Multimaterial piezoelectric fibres*. Nature Materials, 2010. **9**(8): p. 643-648.
46. Zhu, S., So, J.-H., Mays, R., Desai, S., Barnes, W. R., Pourdeyhimi, B. and Dickey, M. D., *Ultrastretchable Fibers with Metallic Conductivity Using a Liquid Metal Alloy Core*. Advanced Functional Materials, 2013. **23**(18): p. 2308-2314.
47. Shi, X., Hu, Y., Fu, F., Zhou, J., Wang, Y., Chen, L., Zhang, H., Li, J., Wang, X. and Zhang, L., *Construction of PANI-cellulose composite fibers with good antistatic properties*. Journal of Materials Chemistry A, 2014. **2**(21): p. 7669-7673.

48. Lee, H. H., Chou, K. S. and Shih, Z. W., *Effect of nano-sized silver particles on the resistivity of polymeric conductive adhesives*. International Journal of Adhesion and Adhesives, 2005. **25**(5): p. 437-441.
49. Xu, M., Feng, J. Q. and Cao, X. L., *Electrical properties of nano-silver/polyacrylamide/ethylene vinyl acetate composite*. Journal of Shanghai University (English Edition), 2008. **12**(1): p. 85-90.
50. Nicolais, L. and Carotenuto, G., *Metal-Polymer nanocomposites*. 2004, John Wiley & Sons, Inc.: Hoboken, New Jersey.
51. Ma, P. C., Tang, B. Z. and Kim, J.-K., *Effect of CNT decoration with silver nanoparticles on electrical conductivity of CNT-polymer composites*. Carbon, 2008. **46**(11): p. 1497-1505.
52. Kelly, F. M. and Johnston, J. H., *Colored and Functional Silver Nanoparticle–Wool Fiber Composites*. ACS applied materials & interfaces, 2011. **3**(4): p. 1083-1092.
53. Deng, H., Zhang, R., Reynolds, C. T., Bilotti, E. and Peijs, T., *A Novel Concept for Highly Oriented Carbon Nanotube Composite Tapes or Fibres with High Strength and Electrical Conductivity*. Macromolecular Materials and Engineering, 2009. **294**(11): p. 749-755.
54. Yi, W., Wang, Y., Wang, G. and Tao, X., *Investigation of carbon black/silicone elastomer/dimethylsilicone oil composites for flexible strain sensors*. Polymer Testing, 2012. **31**(5): p. 677-684.
55. Jordan, E. G., *Electrically conductive tapes and processes*. 1998. U. S. Patent, US5763069 A.
56. Bahia, H. S., *Electrically conductive materials*. 1990. U. S. Patent, US4902562 A.
57. Tanaka, H., Koseki, T. and Fujii, S., *Antistatic acrylic fiber*. 1978. U. S. Patent, US4107129 A.
58. Dai, K., Xu, X.-B. and Li, Z.-M., *Electrically conductive carbon black (CB) filled in situ microfibrillar poly(ethylene terephthalate) (PET)/polyethylene (PE) composite with a selective CB distribution*. Polymer, 2007. **48**(3): p. 849-859.
59. Zhang, R., Deng, H., Valenca, R., Jin, J., Fu, Q., Bilotti, E. and Peijs, T., *Strain sensing behaviour of elastomeric composite films containing carbon nanotubes under cyclic loading*. Composites Science and Technology, 2013. **74**: p. 1-5.
60. Li, Z., Luo, G., Wei, F. and Huang, Y., *Microstructure of carbon nanotubes/PET conductive composites fibers and their properties*. Composites Science and Technology, 2006. **66**(7–8): p. 1022-1029.
61. Ma, H., Zeng, J., Realf, M. L., Kumar, S. and Schiraldi, D. A., *Processing, structure, and properties of fibers from polyester/carbon nanofiber composites*. Composites Science and Technology, 2003. **63**(11): p. 1617-1628.
62. Liu, X.-M., Huang, Z. d., Oh, S. w., Zhang, B., Ma, P.-C., Yuen, M. M. F. and Kim, J.-K., *Carbon nanotube (CNT)-based composites as electrode material for rechargeable Li-ion batteries: A review*. Composites Science and Technology, 2012. **72**(2): p. 121-144.
63. Thostenson, E. T., Ren, Z. and Chou, T.-W., *Advances in the science and technology of carbon nanotubes and their composites: a review*. Composites Science and Technology, 2001. **61**(13): p. 1899-1912.
64. Taipalus, R., Harmia, T., Zhang, M. Q. and Friedrich, K., *The electrical conductivity of carbon-fibre-reinforced polypropylene/polyaniline complex-blends: experimental characterisation and modelling*. Composites Science and Technology, 2001. **61**(6): p. 801-814.

65. Shen, L., Wang, F. Q., Yang, H. and Meng, Q. R., *The combined effects of carbon black and carbon fiber on the electrical properties of composites based on polyethylene or polyethylene/polypropylene blend*. Polymer Testing, 2011. **30**(4): p. 442-448.
66. Al-Hartomy, O. A., Al-Solamy, F., Al-Ghamdi, A. A., Ibrahim, M. A., Dishovsky, N. and El-Tantawy, F., *Pressure Sensors Based on Polyvinyl Chloride/Graphite/Nickel Nanocomposites*. Journal of Elastomers and Plastics, 2011. **43**(2): p. 137-153.
67. Rusu, M., Sofian, N. and Rusu, D., *Mechanical and thermal properties of zinc powder filled high density polyethylene composites*. Polymer Testing, 2001. **20**(4): p. 409-417.
68. Bauhofer, W. and Kovacs, J. Z., *A review and analysis of electrical percolation in carbon nanotube polymer composites*. Composites Science and Technology, 2009. **69**(10): p. 1486-1498.
69. Deng, H., Skipa, T., Bilotti, E., Zhang, R., Lellinger, D., Mezzo, L., Fu, Q., Alig, I. and Peijs, T., *Preparation of High-Performance Conductive Polymer Fibers through Morphological Control of Networks Formed by Nanofillers*. Advanced Functional Materials, 2010. **20**(9): p. 1424-1432.
70. Li, C., Thostenson, E. T. and Chou, T.-W., *Sensors and actuators based on carbon nanotubes and their composites: A review*. Composites Science and Technology, 2008. **68**(6): p. 1227-1249.
71. Kohler, J. *Inherently conductive polymer* Technology opportunity January 15, 2013 [cited 2016 July 07, 2016]; Available from: [http://www.nasa.gov/pdf/410003main\\_TOPS12190b\\_InherentCondPolym.pdf](http://www.nasa.gov/pdf/410003main_TOPS12190b_InherentCondPolym.pdf).
72. Biron, M., *Plastics Solutions for Practical Problems*, in *Thermoplastics and Thermoplastic Composites*, B. Michel. Second ed. 2013, William Andrew Publishing: New York. p. 831-984.
73. Lin, B., Gelves, G. A., Haber, J. A. and Sundararaj, U., *Electrical, Rheological, and Mechanical Properties of Polystyrene/Copper Nanowire Nanocomposites*. Industrial & engineering chemistry research, 2007. **46**(8): p. 2481-2487.
74. Kim, M. S., Kim, H. K., Byun, S. W., Jeong, S. H., Hong, Y. K., Joo, J. S., Song, K. T., Kim, J. K., Lee, C. J. and Lee, J. Y., *PET fabric/polypyrrole composite with high electrical conductivity for EMI shielding*. Synthetic Metals, 2002. **126**(2-3): p. 233-239.
75. Ye, W., Zhu, J., Liao, X. J., Jiang, S. H., Li, Y. H., Fang, H. and Hou, H. Q., *Hierarchical three-dimensional micro/nano-architecture of polyaniline nanowires wrapped-on polyimide nanofibers for high performance lithium-ion battery separators*. Journal of Power Sources, 2015. **299**: p. 417-424.
76. Lim, T. H., Oh, K. W. and Kim, S. H., *Polypyrrole/MWCNT-gr-PSSA composite for flexible and highly conductive transparent film*. Journal of Applied Polymer Science, 2012. **123**(1): p. 388-397.
77. Hu, C., He, S., Jiang, S., Chen, S. and Hou, H., *Natural source derived carbon paper supported conducting polymer nanowire arrays for high performance supercapacitors*. RSC Advances, 2015. **5**(19): p. 14441-14447.
78. Lim, T. H., Oh, K. W. and Kim, S. H., *Self-assembly supramolecules to enhance electrical conductivity of polyaniline for a flexible organic solar cells anode*. Solar Energy Materials and Solar Cells, 2012. **101**: p. 232-240.
79. Saba, J., Magga, Y., He, D., Miomandre, F. and Bai, J., *Continuous electrodeposition of polypyrrole on carbon nanotube-carbon fiber hybrids as a protective treatment against nanotube dispersion*. Carbon, 2013. **51**: p. 20-26.

80. Priestley, J., *A familiar introduction to the study of electricity*. 3rd ed. Vol. 1. 1777, Oxford University: London. p. 69-70.
81. Zhang, H. and Tao, X.-M., *A single-layer stitched electrotexile as flexible pressure mapping sensor*. Journal of The Textile Institute, 2012. **103**(11): p. 1151-1159.
82. Khoffi, F., Khenoussi, N., Harzallah, O. and Drean, J. Y., *Mechanical behavior of polyethylene terephthalate/copper composite filament*. Physics Procedia, 2011. **21**: p. 240-245.
83. Rujitanaroj, P.-o., Pimpha, N. and Supaphol, P., *Wound-dressing materials with antibacterial activity from electrospun gelatin fiber mats containing silver nanoparticles*. Polymer, 2008. **49**(21): p. 4723-4732.
84. Ma, R., Lee, J., Choi, D., Moon, H. and Baik, S., *Knitted Fabrics Made from Highly Conductive Stretchable Fibers*. Nano letters, 2014. **14**(4): p. 1944-1951.
85. Chen, R.-X., Li, Y. and He, J.-H., *Bubbfil spinning for mass-production of nanofibers*. Thermal Science, 2014. **18**(5): p. 1718-1719.
86. Afzal, A., Drean, J. Y., Khenoussi, N., Akhtar, N. A. and Ahmad, S., *Influence of drawing parameter on the development of composite polymeric technical filaments*, in *3rd International Conference on value addition and innovation in textiles*. 2015, National Textile University: Faisalabad, Pakistan. p. 119-123.
87. Laforgue, A., Champagne, M. F., Dumas, J. and Robitaille, L., *Melt-Processing and Properties of Coaxial Fibers Incorporating Carbon Nanotubes*. Journal of Engineered Fibers and Fabrics, 2012. **7**(3): p. 118-124.
88. Laforgue, A., Rouget, G., Dubost, S., Champagne, M. F. and Robitaille, L., *Multifunctional Resistive-Heating and Color-Changing Monofilaments Produced by a Single-Step Coaxial Melt-Spinning Process*. ACS applied materials & interfaces, 2012. **4**(6): p. 3163-3168.
89. Coleman, J. N., Khan, U. and Gun'ko, Y. K., *Mechanical Reinforcement of Polymers Using Carbon Nanotubes*. Advanced Materials, 2006. **18**(6): p. 689-706.
90. Wang, Z., Ciselli, P. and Peijs, T., *The extraordinary reinforcing efficiency of single-walled carbon nanotubes in oriented poly(vinyl alcohol) tapes*. Nanotechnology, 2007. **18**(45): p. 455709.
91. Zhang, R., Dowden, A., Deng, H., Baxendale, M. and Peijs, T., *Conductive network formation in the melt of carbon nanotube/thermoplastic polyurethane composite*. Composites Science and Technology, 2009. **69**(10): p. 1499-1504.
92. Wu, M., Wang, Q., Li, K., Wu, Y. and Liu, H., *Optimization of stabilization conditions for electrospun polyacrylonitrile nanofibers*. Polymer Degradation and Stability, 2012. **97**(8): p. 1511-1519.
93. El-Salmawy, A., Miyamoto, M. and Kimura, Y., *Preparing a Core-Sheath Bicomponent Fiber of Poly(butylene Terephthalate)/Poly(butylene Succinate-co-L-lactate)*. Textile Research Journal, 2000. **70**(11): p. 1011-1018.
94. El-Salmawy, A. and Kimura, Y., *Structure and Properties of Bicomponent Core-Sheath Fibers from Poly(ethylene Terephthalate) and Biodegradable Aliphatic Polyesters*. Textile Research Journal, 2001. **71**(2): p. 145-152.
95. Hufenus, R., Reifler, F. A., Maniura-Weber, K., Spierings, A. and Zinn, M., *Biodegradable Bicomponent Fibers from Renewable Sources: Melt-Spinning of Poly(lactic acid) and Poly[(3-hydroxybutyrate)-co-(3-hydroxyvalerate)]*. Macromolecular Materials and Engineering, 2012. **297**(1): p. 75-84.
96. Jin Luo, Wang, F.-M., Dan Li and Bugao Xu, *Elasticity of woven fabrics made of polytri-methylene terephthalate/ polyethylene terephthalate bicomponent filaments*. Textile Research Journal, 2011. **81**(8): p. 865-870.

97. Cho, H. H., Kim, K. H., Kang, Y. A., Ito, H. and Kikutani, T., *Fine structure and physical properties of polyethylene/poly(ethylene terephthalate) bicomponent fibers in high-speed spinning. I. Polyethylene sheath/poly(ethylene terephthalate) core fibers*. Journal of Applied Polymer Science, 2000. **77**(10): p. 2254-2266.
98. Tomioka, S. and Kojima, M., *Spinnability and adhesiveness of polypropylene-polyethylene bicomponent fibers*. Sen'i Gakkaishi, 1979. **35**(12): p. T542-T547.
99. Hills, W. H., *Spin pack and method for producing conjugate fibers*. 1983. U. S. Patent, US4406850 A.
100. David, T., *Composite filament*. 1964. U. S. Patent, US3117906 A.
101. Naruse, T., Osagawa, T., Naito, H., Matsui, M. and Okamoto, K., *Conductive composite filaments*. 1980. U. S. Patent, US4216264 A.
102. Wang, H., Jin, X., Mao, N. and Russell, S. J., *Differences in the Tensile Properties and Failure Mechanism of PP/PE Core/Sheath Bicomponent and PP Spunbond Fabrics in Uniaxial Conditions*. Textile Research Journal, 2010. **80**(17): p. 1759-1767.
103. Sancak, E., Yuksek, M., Usta, İ., Akalin, M., Uzun, M. and Isgoren, E., *An investigation of electromagnetic shielding effectiveness of knitting fabrics with different metal wire*, in *2nd International Conference on Value Addition & Innovation in Textiles*. 2013, National Textile University, Pakistan: Faisalabad, Pakistan. p. 46-55.
104. Bedeloglu, A., Sunter, N., Yildirim, B. and Bozkurt, Y., *Bending and tensile properties of cotton/metal wire complex yarns produced for electromagnetic shielding and conductivity applications*. Journal of The Textile Institute, 2012. **103**(12): p. 1304-1311.
105. Liu, Z. and Wang, X., *Relation between shielding effectiveness and tightness of electromagnetic shielding fabric*. Journal of Industrial Textiles, 2013. **43**(2): p. 302-316.
106. Ortlek, H. G., Alpyildiz, T. and Kilic, G., *Determination of electromagnetic shielding performance of hybrid yarn knitted fabrics with anechoic chamber method*. Textile Research Journal, 2013. **83**(1): p. 90-99.
107. Green, J. R., *Yarns suitable for durable light shade cotton/nylon clothing fabrics containing carbon doped antistatic fibers*. 2000. U. S. Patent, US6057032 A.
108. Lund, A. and Hagström, B., *Melt spinning of  $\beta$ -phase poly(vinylidene fluoride) yarns with and without a conductive core*. Journal of Applied Polymer Science, 2011. **120**(2): p. 1080-1089.
109. Lund, A., Jonasson, C., Johansson, C., Haagensen, D. and Hagström, B., *Piezoelectric polymeric bicomponent fibers produced by melt spinning*. Journal of Applied Polymer Science, 2012. **126**(2): p. 490-500.
110. Glauß, B., Steinmann, W., Walter, S., Beckers, M., Seide, G., Gries, T. and Roth, G., *Spinnability and Characteristics of Polyvinylidene Fluoride (PVDF)-based Bicomponent Fibers with a Carbon Nanotube (CNT) Modified Polypropylene Core for Piezoelectric Applications*. Materials, 2013. **6**(7): p. 2642.
111. Hull, D. R., *Synthetic filament having antistatics properties*. 1974. U. S. Patent, US3803453 A.
112. Strååt, M., Rigdahl, M. and Hagström, B., *Conducting bicomponent fibers obtained by melt spinning of PA6 and polyolefins containing high amounts of carbonaceous fillers*. Journal of Applied Polymer Science, 2012. **123**(2): p. 936-943.
113. Schwarz, A., Hakuzimana, J., Kaczynska, A., Banaszczyk, J., Westbroek, P., McAdams, E., Moody, G., Chronis, Y., Priniotakis, G., De Mey, G., Tseles, D.,



- and Van Langenhove, L., *Gold coated para-aramid yarns through electroless deposition*. Surface and Coatings Technology, 2010. **204**(9–10): p. 1412-1418.
114. Alagirusamy, R., Eichhoff, J., Gries, T. and Jockenhoevel, S., *Coating of conductive yarns for electro-textile applications*. Journal of The Textile Institute, 2013. **104**(3): p. 270-277.
  115. Sato, H., Takagi, K., Yu, L. and Nagamine, M., *Metal Core Piezoelectric Complex Fiber and Application for Smart System*, in *MRS Proceedings*. 2005, Cambridge Univ Press.
  116. Cornock, R., Beirne, S. and Wallace, G. G., *Development of a Coaxial Melt Extrusion Printing process for specialised composite bioscaffold fabrication*, in *IEEE/ASME International Conference on Advanced Intelligent Mechatronics (AIM)*. 2013, IEEE: Wollongong, Australia. p. 973-978.
  117. Kechiche, M. B., Khoffi, F., Harzallah, O. and Drean, J. Y., *Mechanical characterization of composite Polyethylene Terephthalate / Copper filaments*, in *Fiber Society Conference*. 2012: Saint Gall, Switzerland.
  118. Kechiche, M. B., Khoffi, F., Harzallah, O. and Drean, J. Y., *The development and characterization of conductive composite filaments*, in *AUTEX International Conference*. 2011, AUTEX: Mulhouse, France.
  119. Lund, A. and Hagström, B., *Melt spinning of poly(vinylidene fluoride) fibers and the influence of spinning parameters on  $\beta$ -phase crystallinity*. Journal of Applied Polymer Science, 2010. **116**(5): p. 2685-2693.
  120. Patel, P. C., Vasavada, D. A. and Mankodi, H. R., *Applications of electrically conductive yarns in technical textiles*, in *IEEE International Conference on Power System Technology (POWERCON)*. 2012: Auckland, New Zealand. p. 1-6.
  121. Hansen, C. M., *The Universality of the Solubility Parameter*. Industrial & Engineering Chemistry Product Research and Development, 1969. **8**(1): p. 2-11.
  122. Harrison, J. S. and Ounaies, Z., *Piezoelectric Polymers*, in *Encyclopedia of Polymer Science and Technology*, H. F. Mark. 2002, John Wiley & Sons, Inc.: New York.
  123. Afzal, A., Drean, J. Y., Khenoussi, N., Ahmad, S. and Akhtar, N. A., *Evaluation of dimensional stability in cutting of coaxial composite filaments*, in *16th AUTEX World Textile Conference*. 2016, University of Ljubljana: Ljubljana, Slovenia.
  124. Walter, M., *Monoextrusion Dies for Thermoplastics*, in *Extrusion Dies for Plastics and Rubber*, M. Walter. 2003, Hanser Publishers: Munich, Germany. p. 141-235.
  125. Walter, M., *Coextrusion Dies for Thermoplastics*, in *Extrusion Dies for Plastics and Rubber*, M. Walter. 2003, Hanser Publishers: Munich, Germany. p. 237-262.
  126. Fitzgerald, W. E. and Knudsen, J. P., *Mixed-Stream Spinning of Bicomponent Fibers I*. Textile Research Journal, 1967. **37**(6): p. 447-453.
  127. Szarvasy, I., *Automatic CAD Model Based Simulation of PVC Extrusion and Calibration*. PhD Thesis, 2005, Swansea University: Wales, UK.
  128. Pittman, J. F. T., *Computer-aided design and optimization of profile extrusion dies for thermoplastics and rubber: a review*. Proceedings of the Institution of Mechanical Engineers, Part E: Journal of Process Mechanical Engineering, 2011. **225**(4): p. 280-321.
  129. Sienz, J., Goublomme, A. and Luege, M., *Sensitivity analysis for the design of profile extrusion dies*. Computers & Structures, 2010. **88**(9–10): p. 610-624.
  130. Lee, C. C. and Stevenson, J. F., *The Face-relief Strategy for Design of Profile Dies*. International Polymer Processing, 1992. **7**(2): p. 186-189.

131. Ettinger, H. J., *Development of optimization and parameter techniques applied to the extrusion die design optimization of PVC profile dies*. Ph.D. Thesis, 2005, Swansea University: Wales, UK.
132. Bird, R. B., Armstrong, R. C. and Hassager, O., *Dynamics of polymeric liquids. Volume 1: Fluid Mechanics*. Second ed. Vol. 1. 1987, John Wiley & Sons, Inc.: New York.
133. Gupta, M., *Effect of elongational viscosity on axisymmetric entrance flow of polymers*. *Polymer Engineering & Science*, 2000. **40**(1): p. 23-35.
134. Zatloukal, M., *A simple phenomenological non-Newtonian fluid model*. *Journal of Non-Newtonian Fluid Mechanics*, 2010. **165**(11-12): p. 592-595.
135. Mahesh, G. and Debabrata, S., *An investigation of the effect of elongational viscosity on entrance flow*, in *CAE and Related Innovations for Polymer Processing*, L. S. Turng, H. P. Wang, K. Ramani and A. Bernard. Vol. 90. 2000, American Society of Mechanical Engineers: Houston, Texas.
136. Denn, M. M., *Extension instabilities and wall slip*. *Annual Review of Fluid Mechanics*, 2001. **33**(1): p. 265-287.
137. Denn, M. M., *Polymer melt processing: foundations in fluid mechanics and heat transfer*. 2008, Cambridge University Press: Cambridge, UK.
138. Malkin, A. Y., *Flow instability in polymer solutions and melts*. *Polymer Science Series C*, 2006. **48**(1): p. 21-37.
139. Agassant, J.-F. and Covas, J. A., *An overview of polymer processing modelling*, in *Advances in Material Forming*, F. Chinesta and E. Cueto. 2007, Springer: New York. p. 37-59.
140. Southern, J. H. and Ballman, R. L., *Additional observations on stratified bicomponent flow of polymer melts in a tube*. *Journal of Polymer Science: Polymer Physics Edition*, 1975. **13**(4): p. 863-869.
141. Schrenk, W. J., Bradley, N. L., Alfrey, T. and Maack, H., *Interfacial flow instability in multilayer coextrusion*. *Polymer Engineering & Science*, 1978. **18**(8): p. 620-623.
142. Han, C. D., *Multiphase Flow in Polymer Processing*, in *Rheology: Volume 3: Applications*, G. Astarita, G. Marrucci and L. Nicolais. 1980, Springer US: Boston, MA. p. 121-128.
143. Hermann, J. K., *Polymer Melt Rheology and Flow Birefringence*. 1983, Springer: Berlin.
144. Pittman, J. F. T., *Finite elements for field problems*, in *Fundamentals of Computer Modeling for Polymer Processing*, M. R. Barone and C. L. Tucker. 1989, Hanser Publishers: Munich, Germany. p. 237-331.
145. Huneault, M. A., Lafleur, P. G. and Carreau, P. J., *Extrudate swell and drawdown effects on extruded profile dimensions and shape*. *Polymer Engineering & Science*, 1990. **30**(23): p. 1544-1550.
146. Zolfaghari, A., Behravesh, A. H., Shakouri, E. and Soury, E., *An innovative method of die design and evaluation of flow balance for thermoplastics extrusion profiles*. *Polymer Engineering & Science*, 2009. **49**(9): p. 1793-1799.
147. Miller, C., *Predicting Non-Newtonian Flow Behavior in Ducts of Unusual Cross Section*. *Industrial & Engineering Chemistry Fundamentals*, 1972. **11**(4): p. 524-528.
148. Walter, M., *Mechanical Design of Extrusion Dies*, in *Extrusion Dies for Plastics and Rubber*, M. Walter. 2003, Hanser Publishers: Munich, Germany. p. 305-327.

149. Lepoittevin, B. and Roger, P., *Poly(ethylene terephthalate)*, in *Handbook of Engineering and Speciality Thermoplastics*, S. Thomas and P. M. Visakh. Vol. 3. 2011, John Wiley & Sons, Inc.: Hoboken, New Jersey. p. 97-126.
150. Elamri, A., Lallam, A., Harzallah, O. and Bencheikh, L., *Mechanical characterization of melt spun fibers from recycled and virgin PET blends*. Journal of Materials Science, 2007. **42**(19): p. 8271-8278.
151. Garg, S., Hurren, C. and Kaynak, A., *Improvement of adhesion of conductive polypyrrole coating on wool and polyester fabrics using atmospheric plasma treatment*. Synthetic Metals, 2007. **157**(1): p. 41-47.
152. Donaldson, L. A., *Analysis of fibres using microscopy*, in *Handbook of Textile Fibre Structure*, S. J. Eichhorn, J. W. S. Hearle, M. Jaffe and T. Kikutani. Vol. 1. 2009, Woodhead Publishing: Oxford, UK. p. 121-153.
153. Chanda, M. and Roy, S. K., *Industrial Polymers, Specialty Polymers, and Their Applications*. 2008, Taylor & Francis.
154. Legrand, J. F., *Structure and ferroelectric properties of P(VDF-TrFE) copolymers*. Ferroelectrics, 1989. **91**(1): p. 303-317.
155. Kawai, H., *The Piezoelectricity of Poly (vinylidene Fluoride)*. Japanese Journal of Applied Physics, 1969. **8**: p. 975-976.
156. Wang, T. T., *Piezoelectricity in  $\beta$ -phase poly(vinylidene fluoride) having a "single-crystal" orientation*. Journal of Applied Physics, 1979. **50**(10): p. 6091-6094.
157. ASTM, *Practice for Conditioning Plastics for Testing*. 2013. ASTM D618-13. ASTM International: West Conshohocken, PA.
158. ASTM, *Standard Test Method for Melt Flow Rates of Thermoplastics by Extrusion Plastometer*. 2013. ASTM D1238-13. ASTM International: West Conshohocken, PA.
159. Karagiannidis, P. G., Stergiou, A. C. and Karayannidis, G. P., *Study of crystallinity and thermomechanical analysis of annealed poly(ethylene terephthalate) films*. European Polymer Journal, 2008. **44**(5): p. 1475-1486.
160. Starkweather, H. W., Zoller, P. and Jones, G. A., *The heat of fusion of poly(ethylene terephthalate)*. Journal of Polymer Science: Polymer Physics Edition, 1983. **21**(2): p. 295-299.
161. Afzal, A., Drean, J. Y., Khenoussi, N., Ahmad, S. and Akhtar, N. A., *Development of composite filament by conventional melt extruder*, in *Fiber Society Spring Conference 2016*. 2016: Mulhouse, France.
162. Afzal, A., Khenoussi, N., Ahmad, S., Drean, J. Y. and Akhtar, N. A., *Development of Composite Technical Filament for Smart Applications*, in *The 13th Asian Textile Conference*. 2015: Geelong, Australia. p. 172-175.
163. Afzal, A., Drean, J. Y., Khenoussi, N., Ahmad, S. and Akhtar, N. A., *Influence of spinning parameter on the development of composite polymeric technical filaments*, in *15th Autex World Textile Conference*. 2015: Bucharest, Romania.
164. Göschel, U., *Thermally stimulated structural changes in highly oriented glassy poly(ethylene terephthalate)*. Polymer, 1996. **37**(18): p. 4049-4059.
165. ASTM, *Standard Test Method for Yarn Number Based on Short-Length Specimens*. 2001. ASTM D1059-01. ASTM International: West Conshohocken, PA.
166. Abràmoff, M. D., Magalhães, P. J. and Ram, S. J., *Image processing with ImageJ*. Biophotonics international, 2004. **11**(7): p. 36-42.

167. ASTM, *Standard Test Method for Tensile Properties of Yarns by the Single-Strand Method*. 2015. ASTM D2256 / D2256M-10. ASTM International: West Conshohocken, PA.
168. Debbabi, F. and Abdessalem, S. B., *Effect of manufacturing conditions on structural and handling properties of braided polyamide suture*. *Journal of Engineered Fibers and Fabrics*, 2015. **10**(3): p. 1-8.
169. Sejri, N., Harzallah, O., Viallier, P. and Ben Nasrallah, S., *Influence of wetting phenomenon on the characteristics of a sized yarn*. *Textile Research Journal*, 2011. **81**(3): p. 280-289.
170. Afzal, A., Drean, J.-Y., Harzallah, O., Khenoussi, N., Ahmad, S. and Akhtar, N.-A., *Development of multifunctional different cross-sectional shaped coaxial composite filaments for SMART textile applications*. *Textile Research Journal*, 2016. Online September 2, 2016.
171. Göschel, U., *Herstellung von Poly(ethylen-terephthalat)-Folienbändchen mit höherer Steifigkeit und Festigkeit durch Orientierungsreckung*. *Acta Polymerica*, 1989. **40**(1): p. 23-31.
172. Hofmann, D., Göschel, U., Walenta, E., Geiß, D. and Philipp, B., *Investigations on supermolecular structure of poly(ethylene terephthalate) samples of higher modulus*. *Polymer*, 1989. **30**(2): p. 242-247.
173. Pakula, T. and Fischer, E. W., *Instabilities of the deformation process in cold drawing of poly(ethylene terephthalate) and other polymers*. *Journal of Polymer Science: Polymer Physics Edition*, 1981. **19**(11): p. 1705-1726.
174. Klyosov, A. A., *Wood-Plastic Composites*. 2007, John Wiley & Sons: New York, USA.
175. Raposo, M., Ferreira, Q. and Ribeiro, P., *A guide for atomic force microscopy analysis of soft-condensed matter*. *Modern research and educational topics in microscopy*, 2007. **1**: p. 758-769.
176. Merchant Research & Consulting, L. *Global PET Supply to Exceed 24.39 Mln Tonnes in 2015*. *Fiber Organon 2014* [cited 2016 07 April]; Available from: <http://mcgroup.co.uk/news/20140117/global-pet-supply-exceed-2439-mln-tonnes-2015.html>.
177. Thomas, S. and Visakh, P. M., *Engineering and Specialty Thermoplastics: Polyethers and Polyesters: State-of-the-art, New Challenges and Opportunities*, in *Handbook of Engineering and Speciality Thermoplastics*, S. Thomas and P. M. Visakh. Vol. 3. 2011, John Wiley & Sons, Inc.: Hoboken, New Jersey. p. 1-14.
178. East, A. J., *The structure of polyester fibers*, in *Handbook of Textile Fibre Structure*, S. J. Eichhorn, J. W. S. Hearle, M. Jaffe and T. Kikutani. Vol. 1. 2009, Woodhead Publishing: Oxford, UK. p. 181-231.
179. Davis, G. T., *Piezoelectric and pyroelectric polymers*, in *Polymers for electronic and photonic applications*, C. P. Wong. 1993, Academic Press. p. 435.
180. Kikutani, T., *Structure development in synthetic fiber production*, in *Handbook of Textile Fibre Structure*, S. J. Eichhorn, J. W. S. Hearle, M. Jaffe and T. Kikutani. Vol. 1. 2009, Woodhead Publishing: Oxford, UK. p. 157-180.
181. Chanda, M. and Roy, S. K., *Industrial polymers, speciality polymers and their applications*. 2008, Taylor & Francis Group: New York, USA.



## ANNEXURE

### Annexure 1

Polyester polymer specifically poly (ethylene terephthalate) is the most widely used polymer in the World with total consumption of more than 60 million metric tons [176, 177]. The other polyester polymers include poly (butylene terephthalate), poly (propylene terephthalate), poly (ethylene naphthalate) and poly (lactic acid). The main reason for such high demand around the World lies in the low cost of production, easy to manufacture and excellent as per demand performance characteristics. The reasons for low production cost lies in the fact that the mixed xylenes are very easily and efficiently converted into terephthalic acid, lower glass transition temperature (at approx. 75 °C) for convenient stabilization in molecular orientation and morphology of the polymer induced during spin-line and melting temperature (approx. 280 °C) being within the range of commercial heating fluids [27]. The major properties of the polyester are given in Table 18 [21, 27, 122].

Table 18. Major properties of polyester polymer

Attribute	Value
Crystal habit	Triclinic: one polymer chain per unit cell
Cell density (g/cm <sup>3</sup> )	1.52
Cell parameters	a = 0.444 nm ; b = 0.591 nm ; c = 1.067 nm ; $\alpha = 100^\circ$ ; $\beta = 117^\circ$ ; $\gamma = 112^\circ$
Heat of fusion (°C)	260-265
Enthalpy of fusion	140 J/g; 33.5 cal/g
Glass transition temperature (°C)	75 °C
Specific gravity (g/cm <sup>3</sup> )	1.33 (undrawn, amorphous), 1.39 (drawn, crystalline)
Tenacity (MPa)	450-750 (textile fibre)
Elongation (%)	10-50
Initial Modulus (MPa)	≤6000 (textile fibre)
Shrinkage at 160 °C	5-15 (textile fibre)
Thermal conductivity (W/m/°C)	0.14

Attribute	Value
Thermal volumetric expansion (1/°C)	$1.6 \times 10^{-4}$ (at 30-60 °C) $3.7 \times 10^{-4}$ (at 90-190 °C)
Moisture regain at 65% RH (%)	0.4
Refractive index	1.58-1.64
Dielectric constant	3.3 (at 60 Hz) 2.8 (1 GHz)
Electric conductivity (ohm cm)	$10^{18}$ (dry) $10^{12}$ (0.5 % moisture)
Solvents	o-chlorophenol, hexafluoroisopropanol, hot alkali
Non solvents	Alcohol, gasoline, most acids

Polyesters are condensation polymers which are developed by polycondensation reaction between terephthalic acid/dimethyl terephthalate and ethylene glycol through esterification/transesterification reaction respectively. It is a linear partially aromatic polymer with a repeating unit of  $C_{10}H_8O_4$ . The chemical structure and plastic identification code is shown in Figure 161 [21].

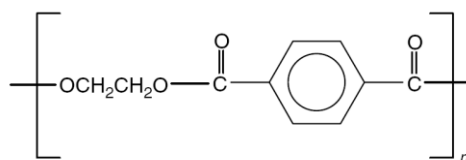


Figure 161. Chemical structure of poly (ethylene terephthalate)

The polymerization process is carried out in different stages in steps while ensuring the completion of the reaction through amount of the released by-products. The polymerization is completed in three main steps including pre-polymerization, polycondensation and solid polymerization [149]. The actual process details are quite complex and also contain highly proprietary information regarding the designs, so only a broad overview of the process description is possible to explain. The continuous process schematic diagram is shown in Figure 162 [178].

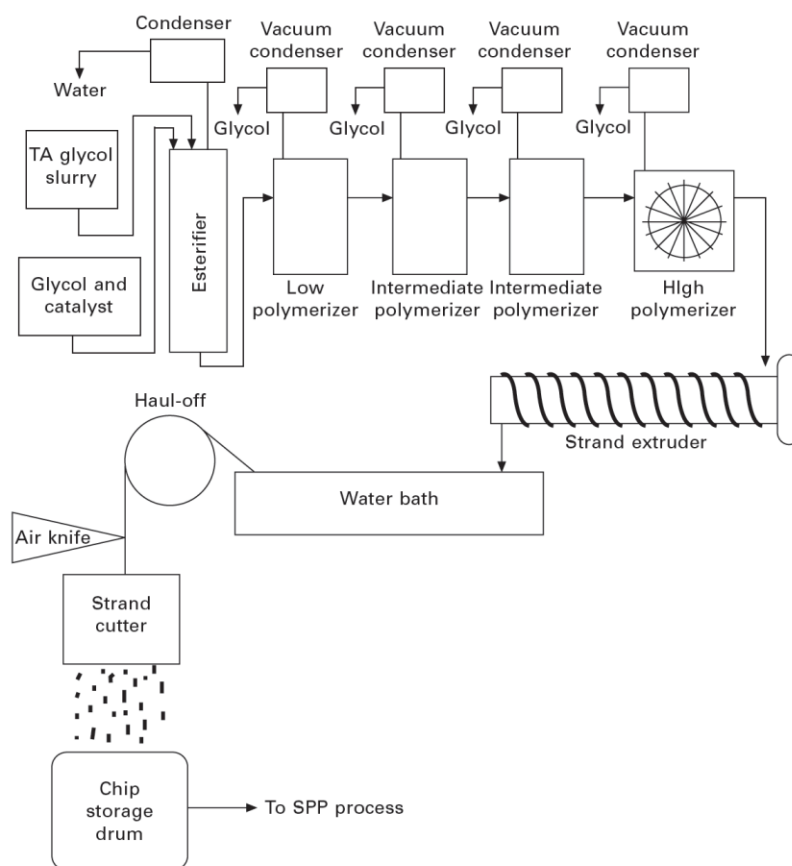


Figure 162. Schematic diagram of continuous polyester manufacturing process

In the first step, the monomers terephthalic acid and ethylene glycol reacted at 150-210 °C by direct esterification reaction or dimethyl terephthalate and ethylene glycol reacted at high temperature by transesterification reaction to formulate bis-(2-hydroxyethyl) terephthalate. the catalyst used for esterification and transesterification reactions are derived metal compounds based on Ca, Mn, Ge, Ti, Sn, Zn etc. the completion of the reaction is estimated by quantity of the eliminated by products. The chemical formulation of this step is shown in Figure 163 [149].

In the second step, bis-(2-hydroxyethyl) terephthalate is heated at 280-300 °C under vacuum (10-50 Pa) for polycondensation by transesterification reaction. Ethylene glycol is eliminated as by product in this step. This step involves in the macromolecular formation; hence high pressure is applied to force the reaction to obtain high molecular weights. The approximate time for both steps varies from 5 to 10 hours. The catalysts are required to speed up the reaction process which includes  $Sb_2O_3$ ,  $Sb(OAc)_3$ ,  $GeO_2$  or  $Ti(OC_4H_9)_4$ . The reaction equation is shown in Figure 164 [149].



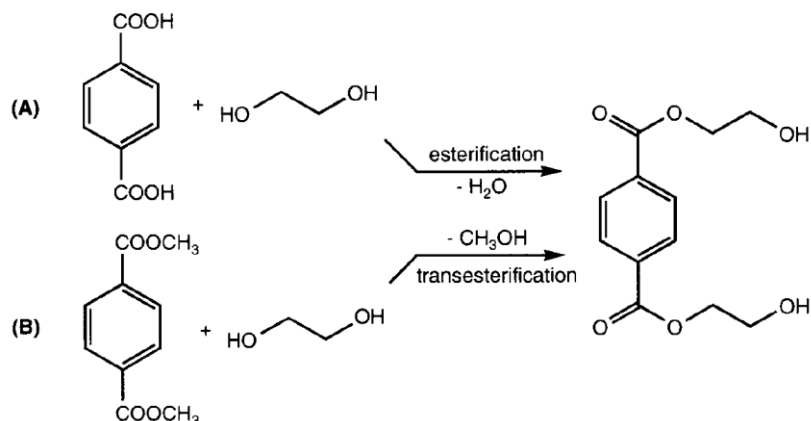


Figure 163. Chemical reactions for the preparation of bis-(2-hydroxyethyl) terephthalate

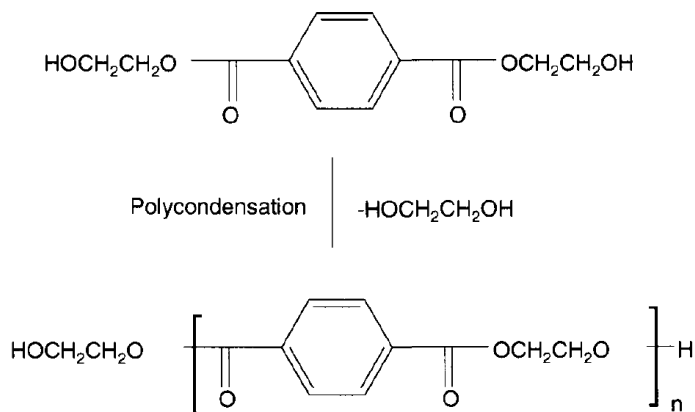


Figure 164. Polycondensation reaction for second step of PET manufacturing

The third step is called as solid state polymerization in which molecular weight (>30,000 g/mol number average molar mass) and viscosity of the polymer is increased [149]. The temperature of the reaction is kept between glass transition and melting temperature at about 220-230 °C to avoid degradation of the polymer chains and also allow the chains mobility to attain the required molecular weight. The polyester obtained by solid state polymerization had higher crystallinity and melting point as compared with conventional polyester [149]. The molten polymer is pumped to the strand extruder and quenched in the water bath after getting the target molecular weight which have usually intrinsic viscosity of 0.65 [178]. The strand cast is cut into chip and dry to store it for further processing.

The textile PET filaments have aesthetics like natural silk. It is widely used in textile and clothing sector [149]. It is also a well-known fibre used in home textiles and nonwovens

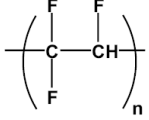
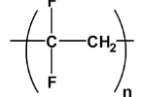
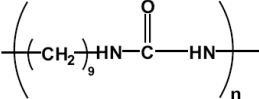
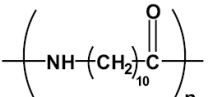
for multiple applications. Industrial filament applications include high strength textile fabrics, hose, ropes, nets, cords and reinforcement in rubber [122, 149].

## Annexure 2

In 1969, Kawai [155] explained that PVDF films have very high piezoelectric coefficient about 6-7 pC/N after electrically poled which is estimated as ten times higher than had been measured for any other polymer. The spatial arrangement of fluorine and hydrogen atoms in a symmetrical manner in the polymer chain cause the generation of polarity in the structure which act upon the dielectric properties, solubility, electromechanical response, much high dielectric constant and crystal morphology. The PVDF is the point of focus for integration into devices due to its higher dielectric constant of about 12 which is four fold as compared with other polymers and therefore yield lower signal to noise ratio. The PVDF is strained and quite flexible at room temperature due to lower glass transition temperature of amorphous phase than room temperature. The PVDF has minimum four crystal phases out of which minimum three are polar in nature and has 50 % to 60 % crystalline phase which depends upon the processing and thermal history of the polymer.

Strong ferroelectric, piezoelectric and pyroelectric effects were observed for the copolymers of polyvinylidene fluoride with tetrafluoroethylene (TFE) and trifluoroethylene (TrFE). These both polymers act in same manner when copolymerized with PVDF and hence can be discussed together. The appealing structural characteristic of the co monomers is that they compel the polymer into all-trans configuration which has a polar crystalline phase due to which mechanical stretching is eliminated for achieving polar phase. The degree of crystallinity is much higher for P(VDF-TrFE) than PVDF providing a good remnant polarization, much sharper hysteresis loop and lower coercive field. The maximum usage temperature is also increased with TrFE to close to 100 °C by twenty degrees. On contrary, copolymers with TFE have lower degree of crystallinity along with lower melting temperature as compared with PVDF. In consideration of the fact that piezoelectric constants for those copolymers are not as much as that of homopolymer, the advantages obtained of P(VDF-TrFE) with higher usage temperature, enhanced crystallinity and process ability makes it encouraging for different applications. Some distinctive values of the piezoelectric constants are already shown in Table 19 [122].

Table 19. Comparison of some semi crystalline polymeric material's properties

Polymer	Structure	$d_{31}$ (pC/N)	$T_g$ (°C)	Max. use temp (C)	$T_m$ (°C)	Ref.
PTrFE		12	32	90-100	150	2
PVDF		20-28	-35	80	175	2
Polyurea-9		-	50	-	180	28
Nylon-11		3 @ 25°C and 14 @ 107°C	68	185	195	22

The PVDF-TrFE is more adaptable due to the reason that it can be crystallizes in its beta form spontaneously on extrusion [154, 155]. While PVDF requires different processes like stretching, rolling followed by polling of polymer for obtaining piezoelectric phenomenon [156].

The characteristics of piezoelectric polymers are different from inorganic materials in such a way that they can be used for special purposes and applications for which the other ceramics and single crystal materials are incapable to perform effectively. The characteristics comparison of standard crystal materials and piezoelectric material are shown in Table 20. It is evident from Table 20 that piezoelectric strain constant ( $d_{31}$ ) for the ceramic is higher than that of the polymer. On contrary, the piezoelectric stress constant of the polymer is much higher than that of the ceramics which indicates the sensitivity level of the polymer is better than ceramics and therefore effectively used as sensor applications. The piezoelectric polymer actuators and sensors are tough, lightweight, promptly produced into big areas and can be cut and mould into complicated patterns, which make then advantageous over the other materials in terms of processing flexibility. Moreover, the polymers also offer high impact resistance and strength [179]. The other distinguished properties of the piezoelectric polymers include low elastic stiffness, low acoustic and mechanical impedance (essential for underwater and medical

applications), low dielectric constant and low density, which accounts for high voltage sensitivity and performed for excellent sensor attributes. Polymers usually have high operating field strength and a high dielectric breakdown which elaborates that they can resist very higher driving fields than that of the ceramics. Electrodes pattern them self on the film surface, which is the ability of the polymers and poles are developed on the selected regions. Considering these characteristics, piezoelectric polymers are employed in technical purposes and practicable device configurations.

Table 20. Comparison of ceramic materials and standard piezoelectric polymer properties

	$k_{31}$	$g_{31}$ (mV-m/N)	$d_{31}$ (pm/V)	<b>Salient Attributes</b>
Lead Zirconium Titanate (PZT)	0.34	11	175	Toxic, heavy, brittle
Polyvinylidene fluoride (PVDF)	0.12	240	28	Low acoustic and mechanical impedance, lightweight, flexible

### Annexure 3

The rate of crystallization increases 6 times when crystallization occurs under the applied stress as compared with quiescent state of filament. This increase in crystallization rate also accompanied by the change in crystal habit, shape of the developed crystalline phase, from spherulitic (spherically symmetric) to columnar habit (shish kabab) structure.

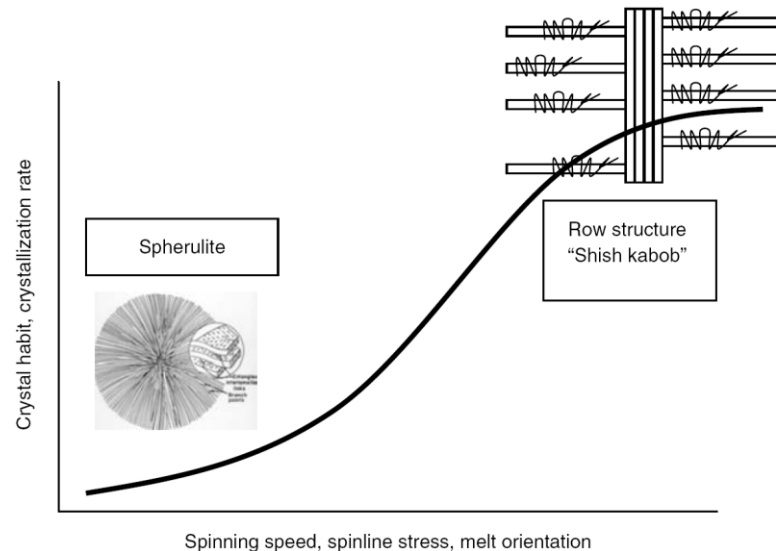


Figure 165. Morphological variations observed by change in spin line parameters during melt spinning

The graphical representation of the change in the morphological structures as a function of key spinning parameters is shown in Figure 165 [27]. It is reported that the transition of crystal habit occurs at the stress of about 0.1g/d. In addition, it is reported that the number of rows increases by the increase in spin-line stress while decreases the diameter of the fibrillary structure. These fibrils are only visible during the spin-line stress and may not be visible in final filament morphology. The spin-line process is divided into three regions to understand these variations in detail as shown in Figure 166 [27].

- Region 1: Increase in global and local molecular orientation
- Region 2: development of fibrils at maximum orientation points (mechanical steady state, transient mesogen)
- Region3: decoration of fibrils (crystal growth in folded chains)

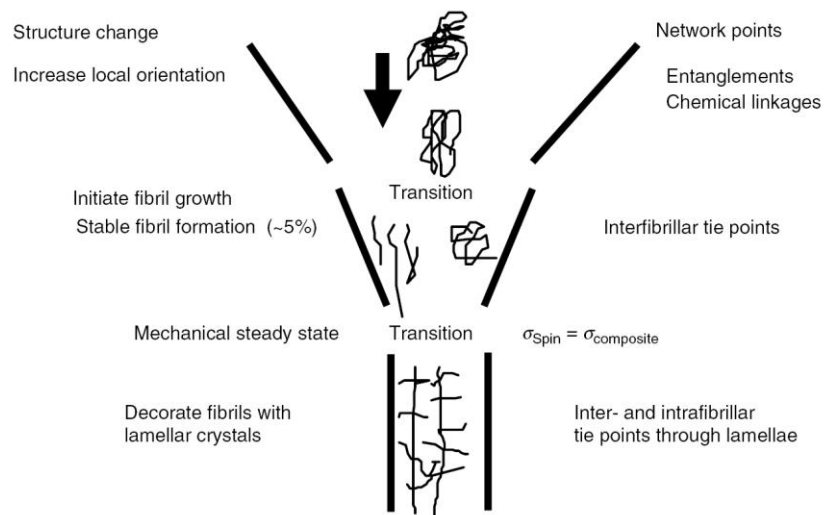


Figure 166. Morphological transformation in filament during spin-line process

The molecular orientation of amorphous and molten polymer increases by filament drawdown due to the applied spin-line stress in region 1. As a consequence of the applied stress, the starting network chains disentangled accompanied by increase in local molecular chain orientation in the proximity of remaining entanglements. In region 2, nematic phase formation occurs as bundle of locally oriented chains grow in aspect ratio, followed by development in biphasic array comprised of dispersed fibrillar mesogenic structures in less oriented amorphous matrix. The fibril formation reduces when the developed fibrillary structures supported the applied spin-line stress hence matrix chains are able to relax. During the spin-line process, the matrix structure enters in lower temperature range which enhances the fibrillar nucleation density for lamellar crystal overgrowth of fibrils. The increase in effective nucleation density leads to increase in effective crystallization rate up to six order in magnitude. These developed fibrils may or may not be evident in the filament final structures, but the high orientation in semicrystalline phase are always prominent. The growth of further structures is based on the developed template of transient fibril structure. The molecular chains may grow while joining different fibril structures together, which provide the stress transfer elements between different fibril structures during filament deformation. These tie molecular chains are classified as three different types, which includes: interfibrillar (joining different fibrillar structures), interlamellar (joining between different lamella on same fibril or on other fibrils) and between lamella and fibril.

The experimental detailed proof of this conceptual model is difficult to obtain, yet the experimental data on melt spinning process supported this concept [27]. The advantage of

the model in predicting process-structure-property relationship is more important than the accuracy of the overall model. The importance conclusions of the model are as under [27]:

- The layout of molecular chain orientation and crystallization sequence in melt extrusion process is critical.
  - The morphological structure is based on the developed transient fibrillar mesophase template which defines the nucleation density for succeeding crystallization.
- The load bearing elements in the developed crystalline network increased by increase in prior formation of chain orientation before crystallization step while the non-crystalline load bearing aspects decreases in the structure.

The chain formation template remains the same for further structure development in all later processing steps. The morphology of partially crystalline polyester fibre is shown in Figure 167 [178]. The spun yarn shrinkage was used to estimate the remaining yarn draw ratio as shown in Figure 168 [27], where DR<sub>max</sub> is considered as the maximum stable draw ratio available to spun yarn. Glassy structures with large chain orientation are achieved at temperature either close or below to glass transition temperature for polyester [164].

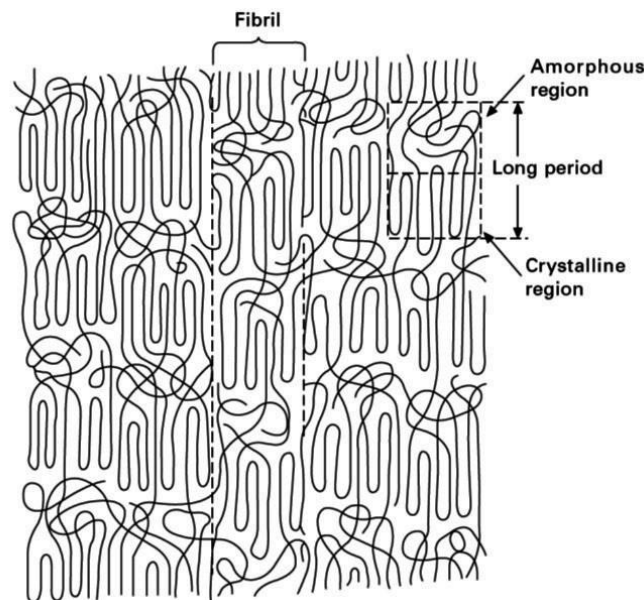


Figure 167. Morphological illustration of polyester fibre showing various features



The melt polymer faces large amount of stress after extrusion from spinneret hole. the filament travel at 100-200 times faster than their exit speed from spinneret hole after freezing point [122]. The acceleration caused considerable stretching in the filament. the forces act on the polymer during this process includes air drag, gravity, rheological drag, surface tension and inertia as shown in Figure 169 [122]. These force balance change rapidly because of the change in temperature and thread-line speed along the thread-line.

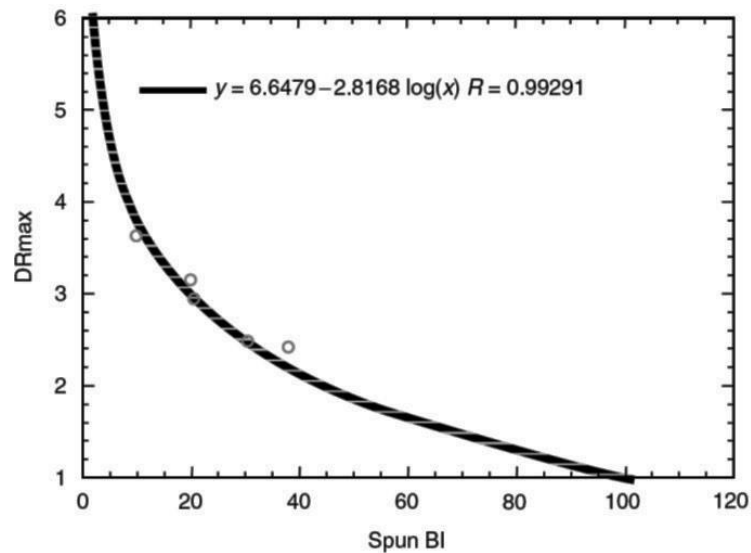


Figure 168. Graphical representation of draw ratio as a function of molecular orientation induced during spinning

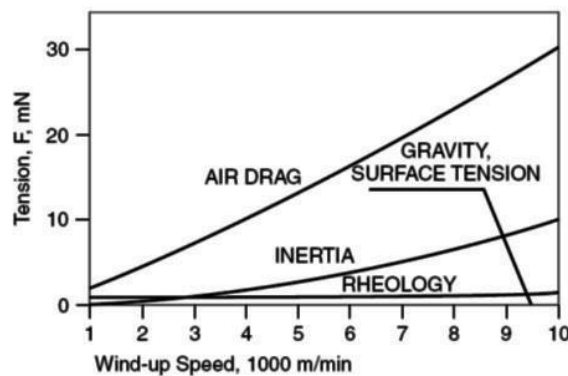


Figure 169. Interactive graph between typical forces acting upon spinning thread-line vs winding speed

The dynamics of thread-line formation are divided into three types based upon take up speed [122]:

- a. In low speeds (<1000 m/min), the spinning thread-line forces are dominated by rheological deformation. The effect of air drag is negligible near spinneret hole at

fibre formation region due to less surface-volume ratios. The acceleration is also so small that inertial forces also do not play role. Thermal disorientation predominates over the orientation effects of fibre elongation and a very small amount of residual orientation is frozen into the thread-line.

- b. In medium speeds spinning (1000-4000 m/min), air movements cause higher drag and faster cooling. The effect of inertia also become prominent and increases proportionally to extensional shear rate and velocity. The increased orientation obtained due to higher stress at freezing point are retained in the frozen filament.
- c. In high speed spinning (beyond 4000 m/min), air drag and inertial forces become the dominant contributors to fibre stress. The higher stress aligns the orientation in the fibre and significant crystallization is achieved in the filament. The structure obtained has highly crystalline regions or relatively low orientation amorphous regions.

The temperature of cooling also effects greatly on the structure and morphology of the filament. The rapid cooling have high impact on the crystallization rate as shown in Figure 170 [180]. It is evident that the fibre cooling process in which the rapid cooling takes place, the crystallization rate does not have any intersection point with cooling rate line and hence amorphous state is obtained in the fibre.

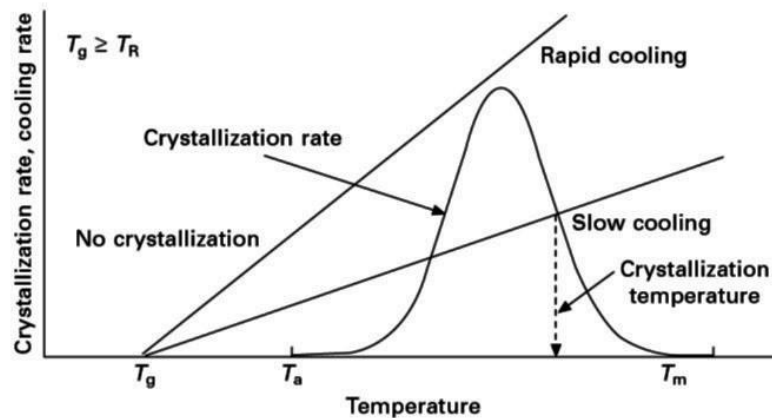


Figure 170. Schematic illustration of relation between cooling rate line of different cooling rates and temperature dependent different crystallization rate curve

Annexure 4

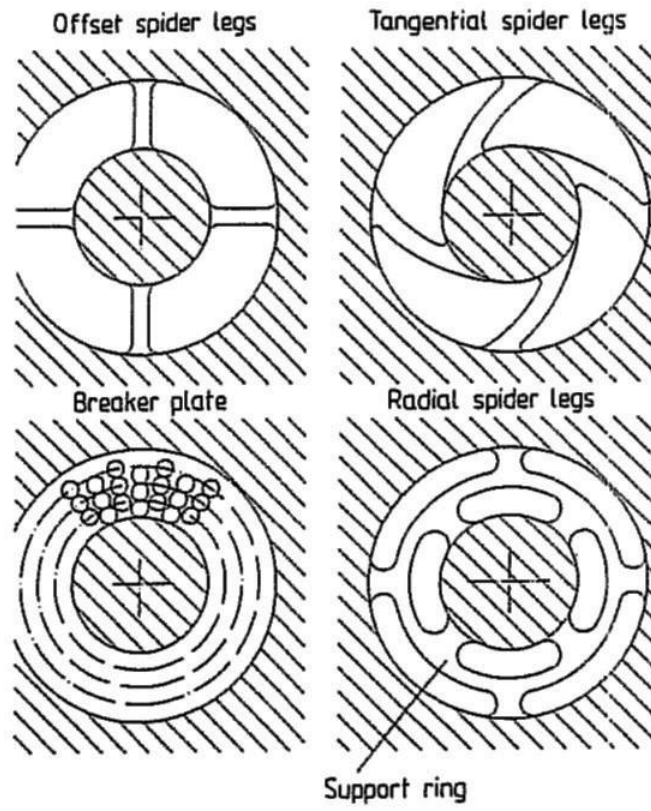


Figure 171. Mandrel support system

## Annexure 5

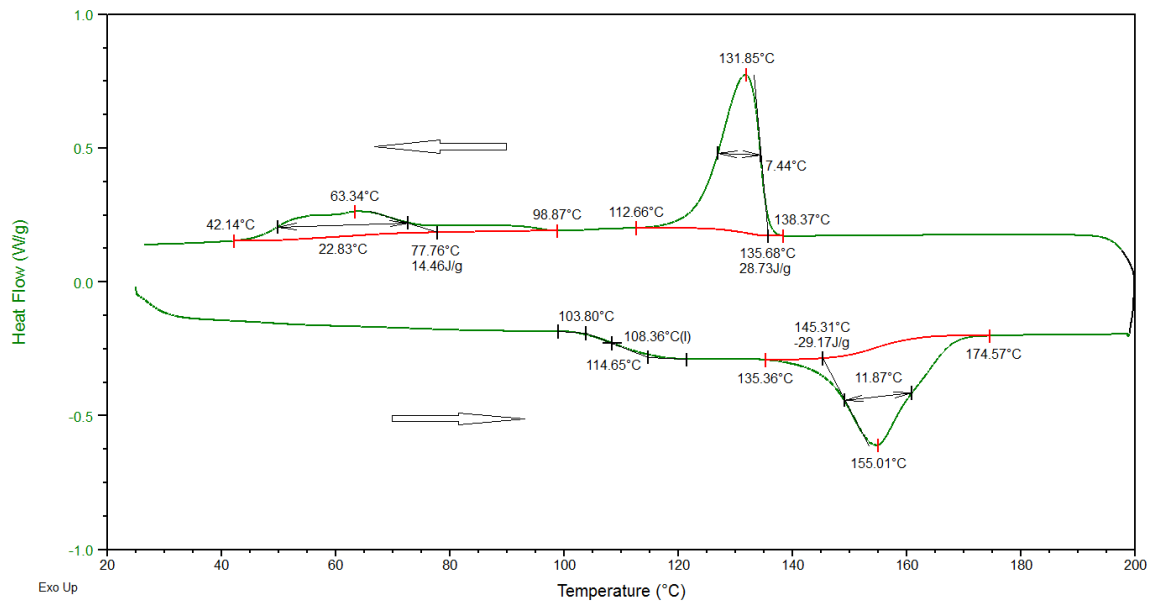


Figure 172. DSC thermogram of high molecular weight PVDF-TrFE copolymer in chips form

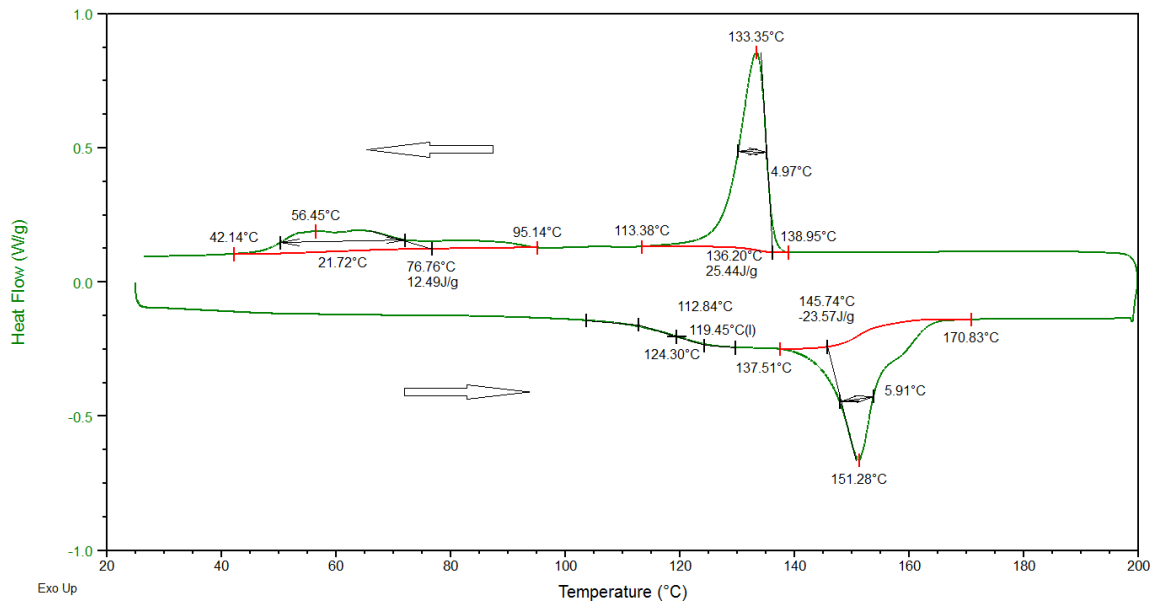


Figure 173. DSC thermogram of high molecular weight PVDF-TrFE copolymer in composite filament

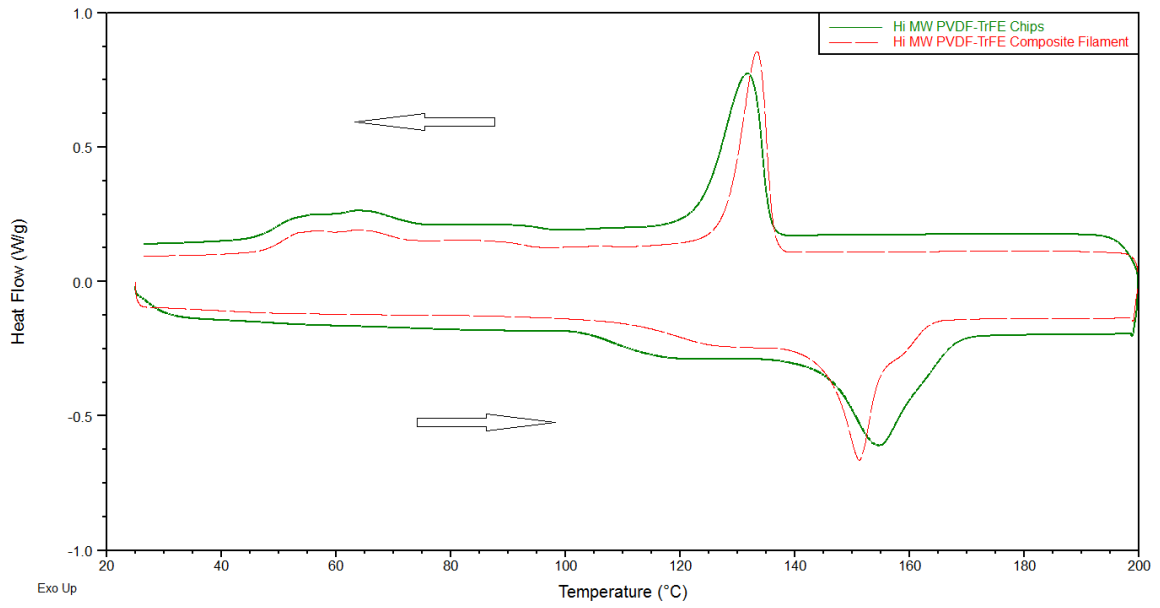


Figure 174. DSC thermogram comparison of high molecular weight PVDF-TrFE copolymer chips and composite filament

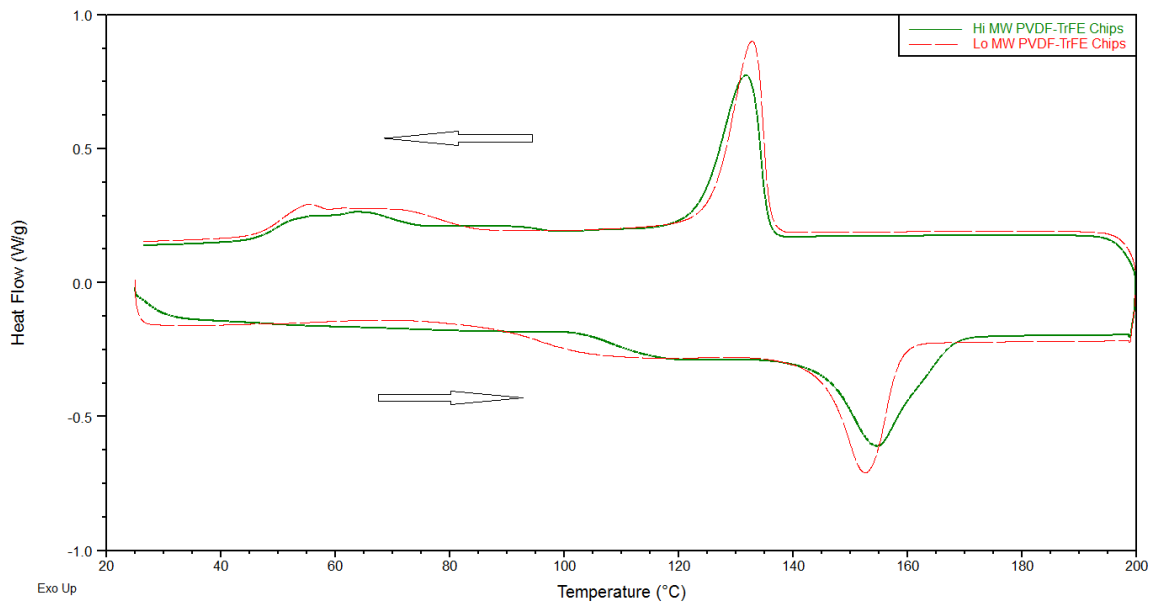


Figure 175. DSC thermogram comparison of high and low molecular weight PVDF-TrFE copolymer in chips form

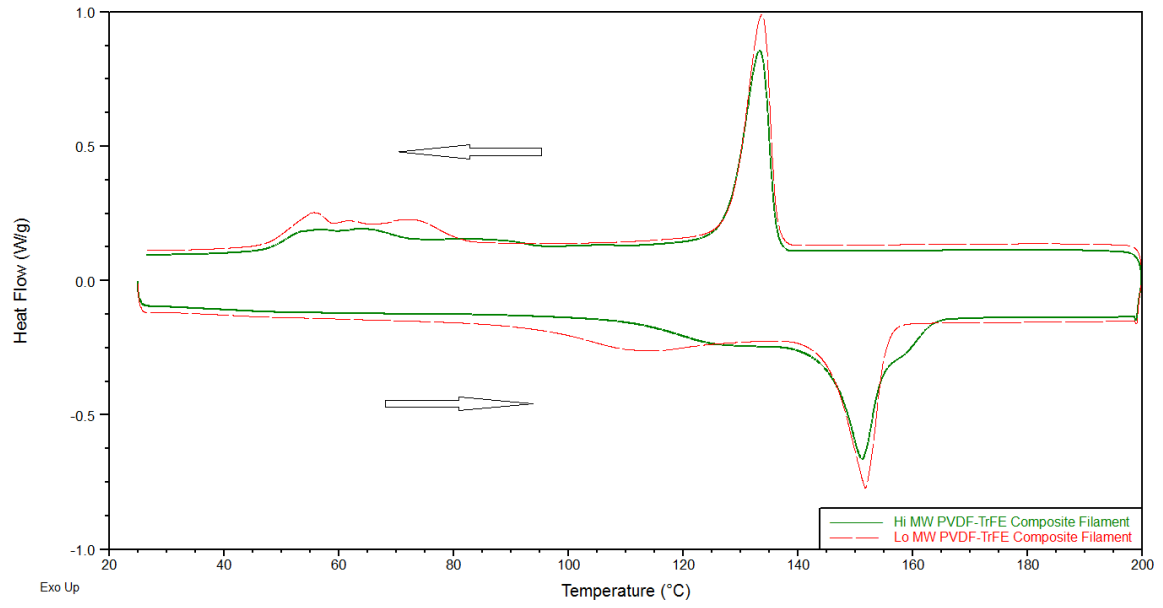


Figure 176. DSC thermogram comparison of high and low molecular weight PVDF-TrFE copolymer in composite filament

**Annexure 6**

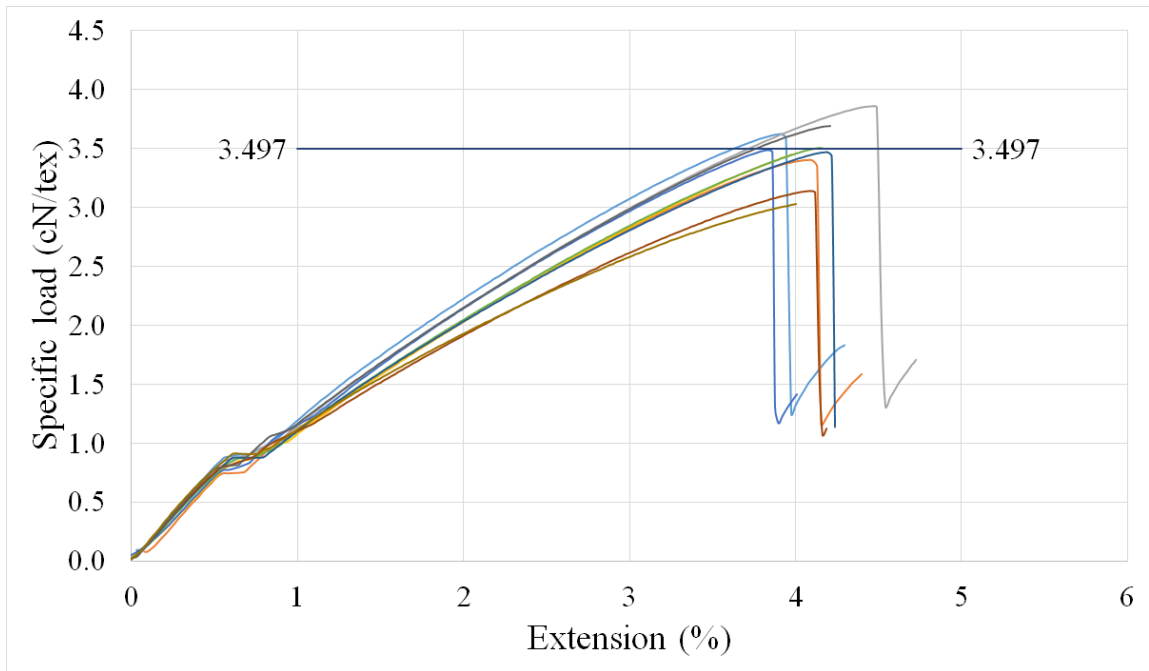


Figure 177. Specific load-extension curves of sample code 2

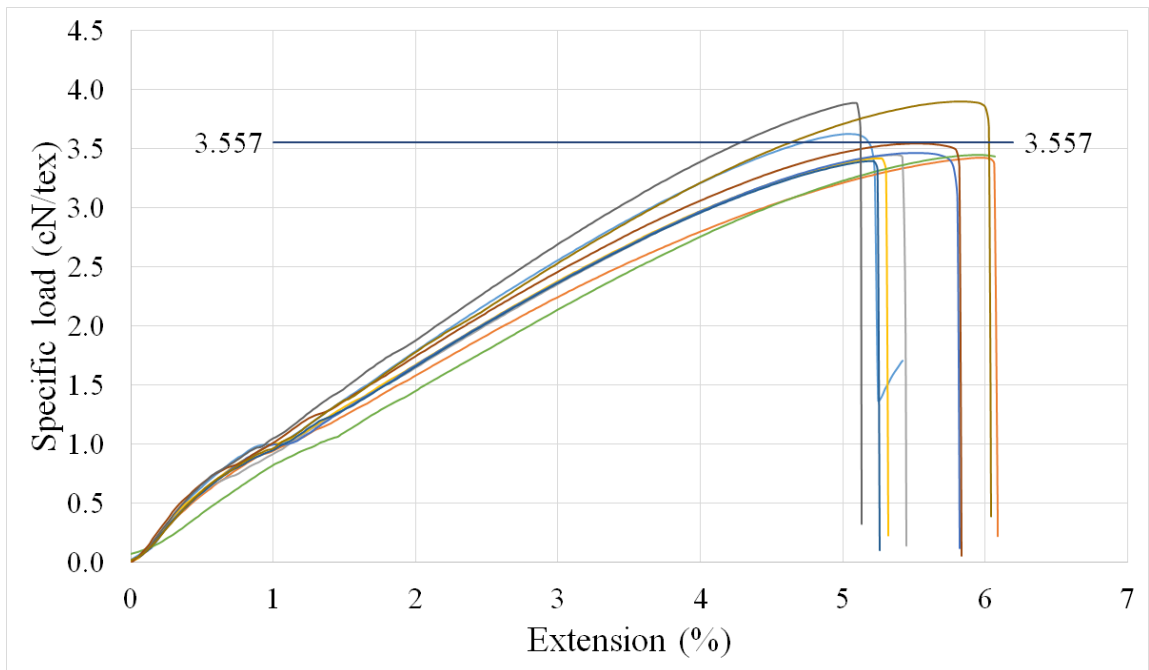


Figure 178. Specific load-extension curves of sample code 3

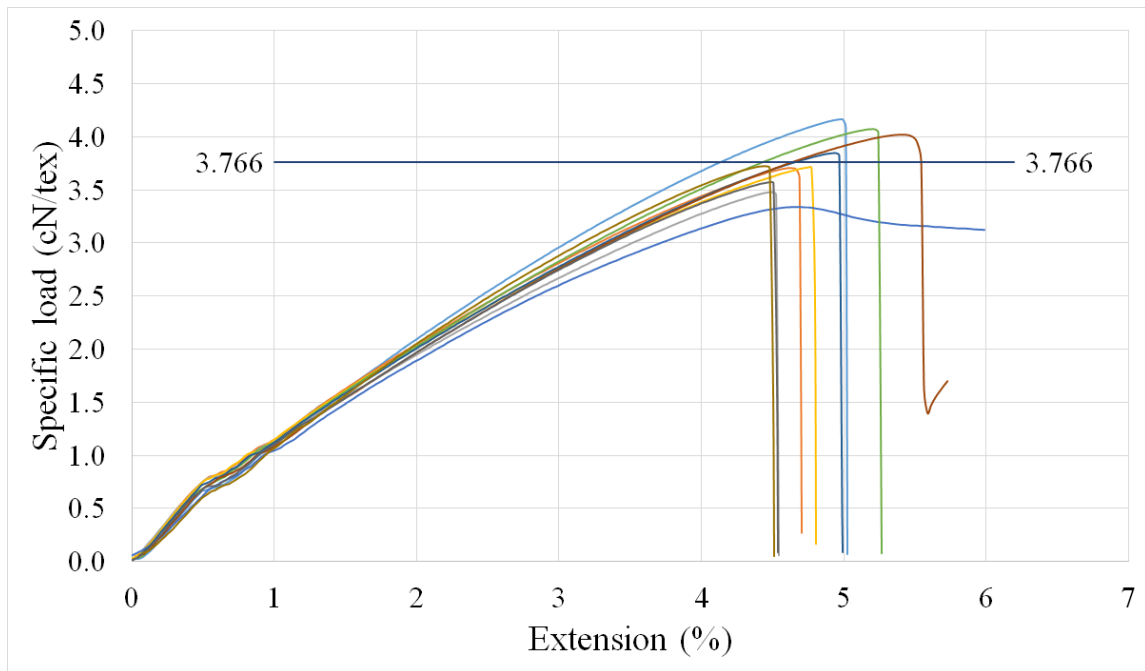


Figure 179. Specific load-extension curves of sample code 4

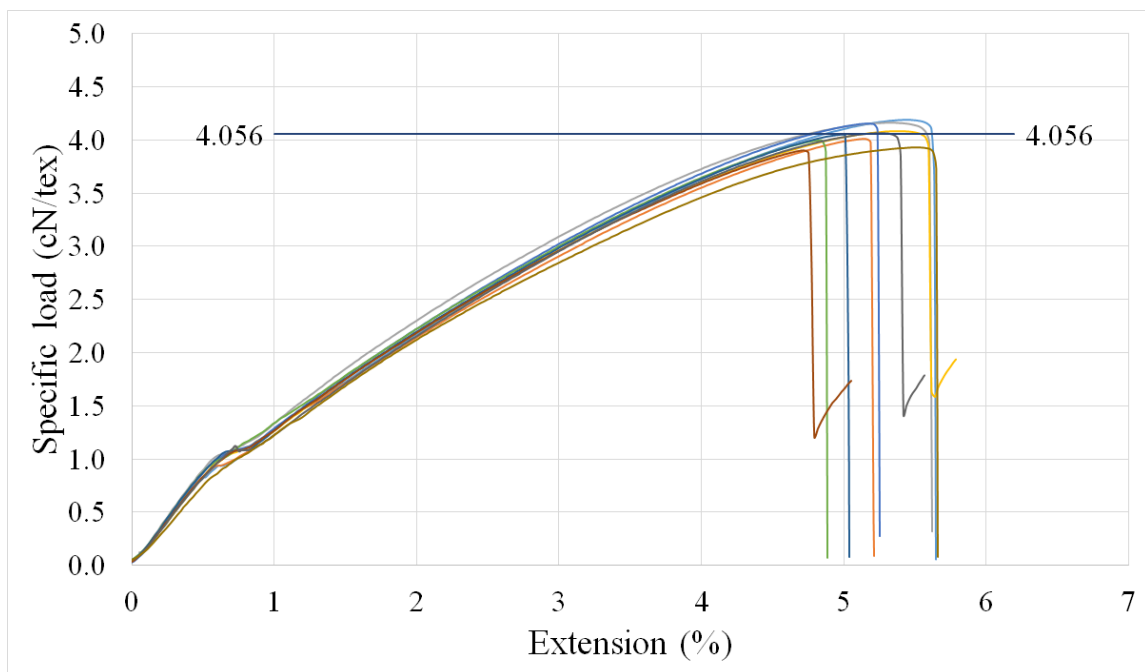


Figure 180. Specific load-extension curves of sample code 5



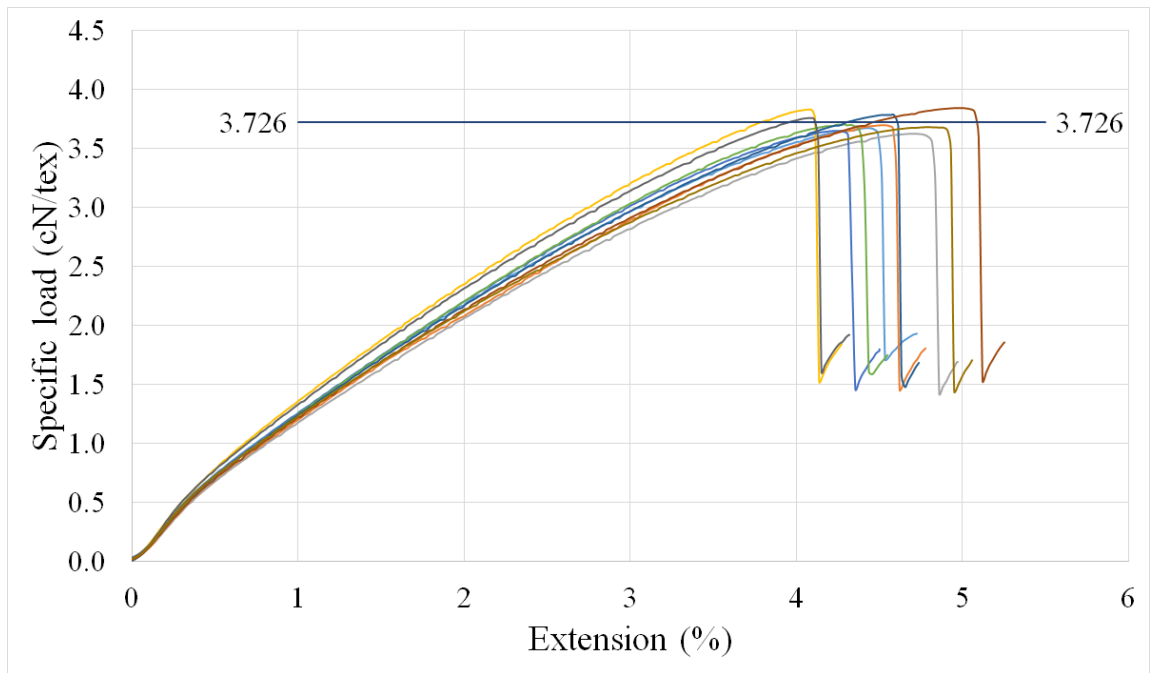


Figure 181. Specific load-extension curves of sample code 6

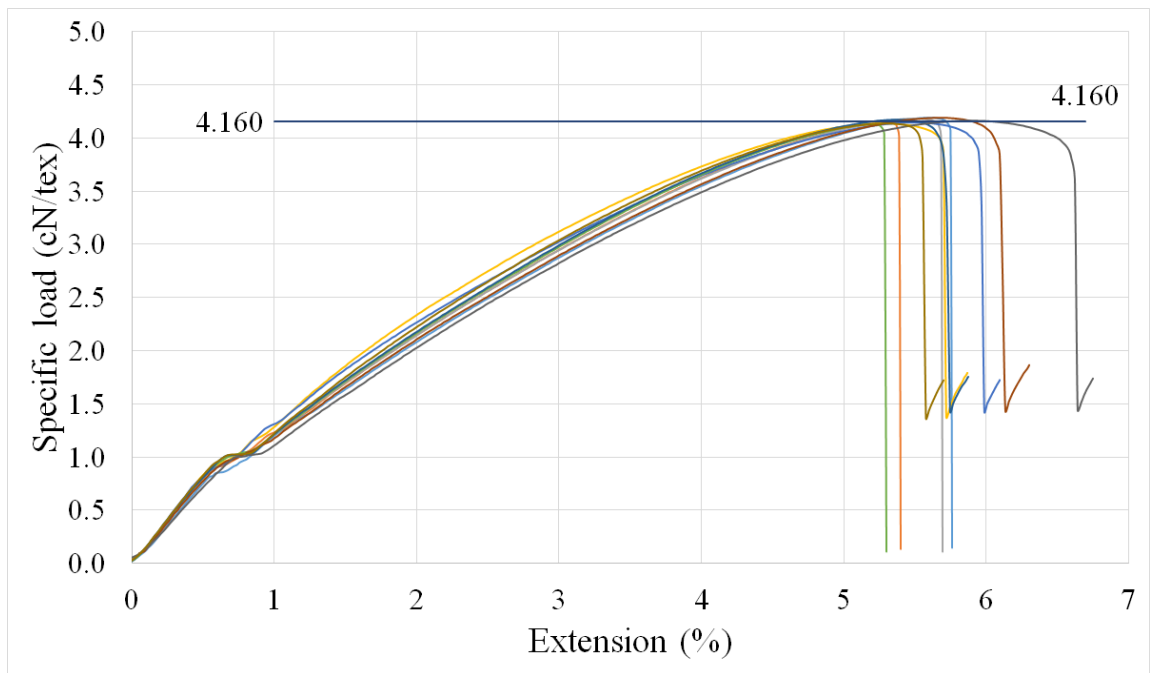


Figure 182. Specific load-extension curves of sample code 7

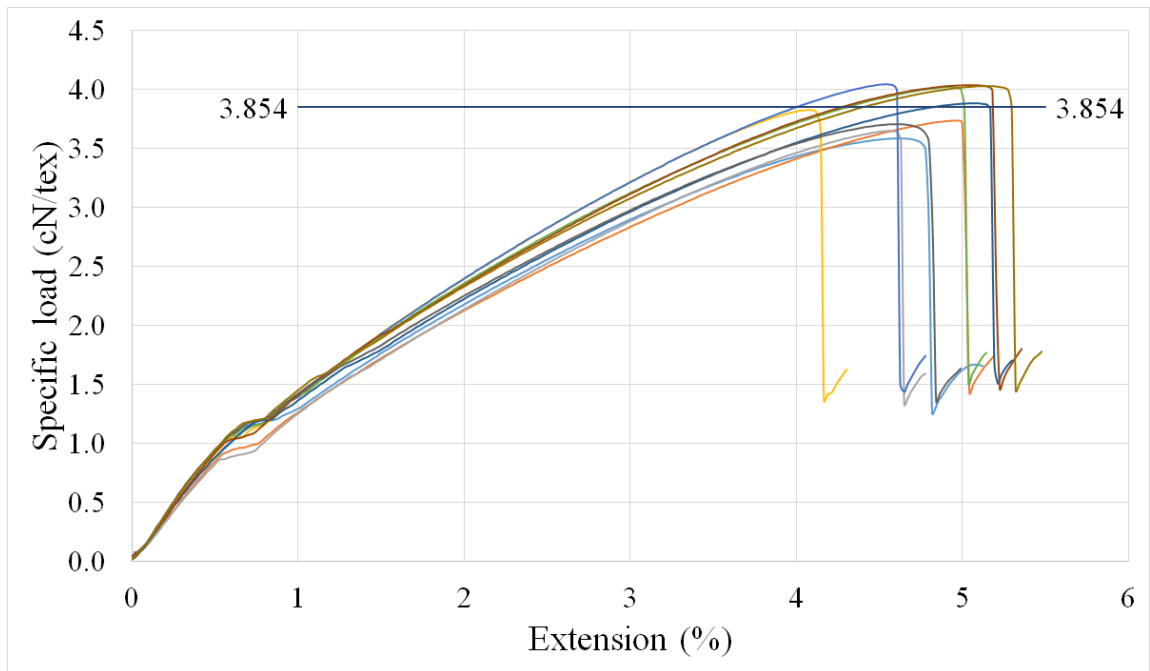


Figure 183. Specific load-extension curves of sample code 8

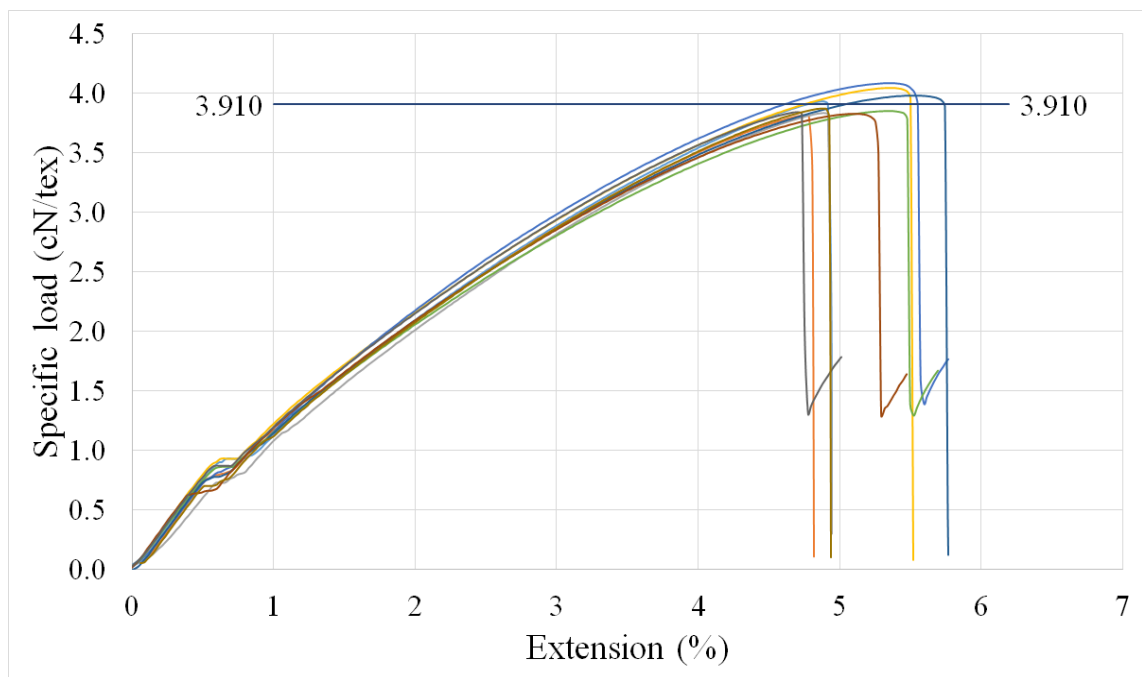


Figure 184. Specific load-extension curves of sample code 9

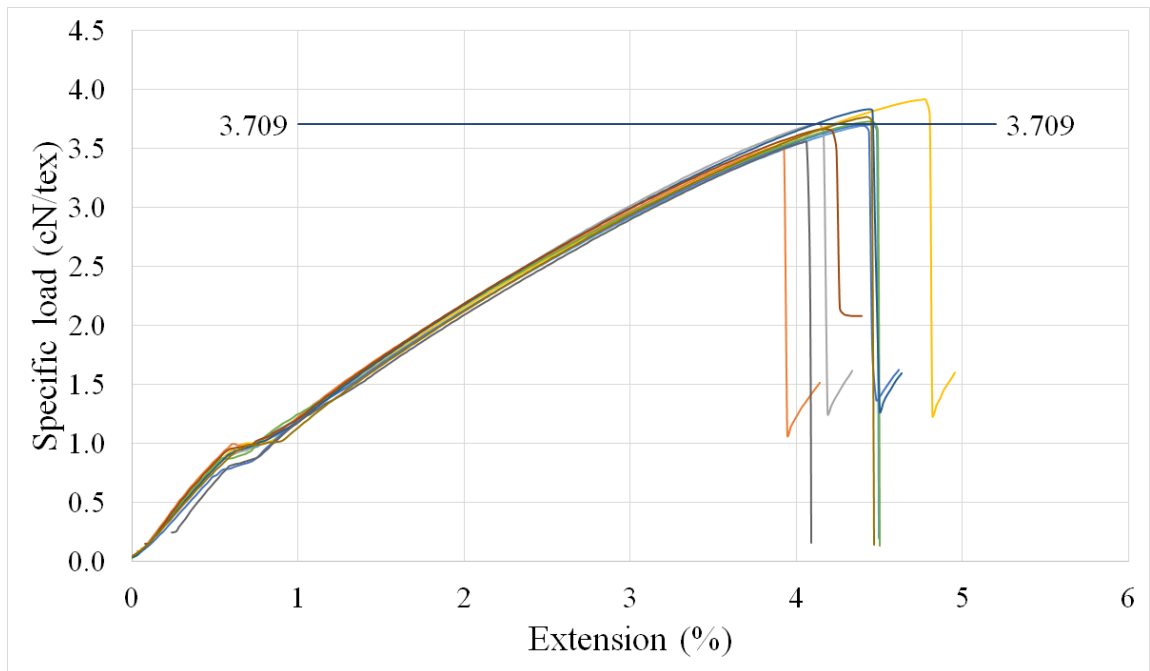


Figure 185. Specific load-extension curves of sample code 10

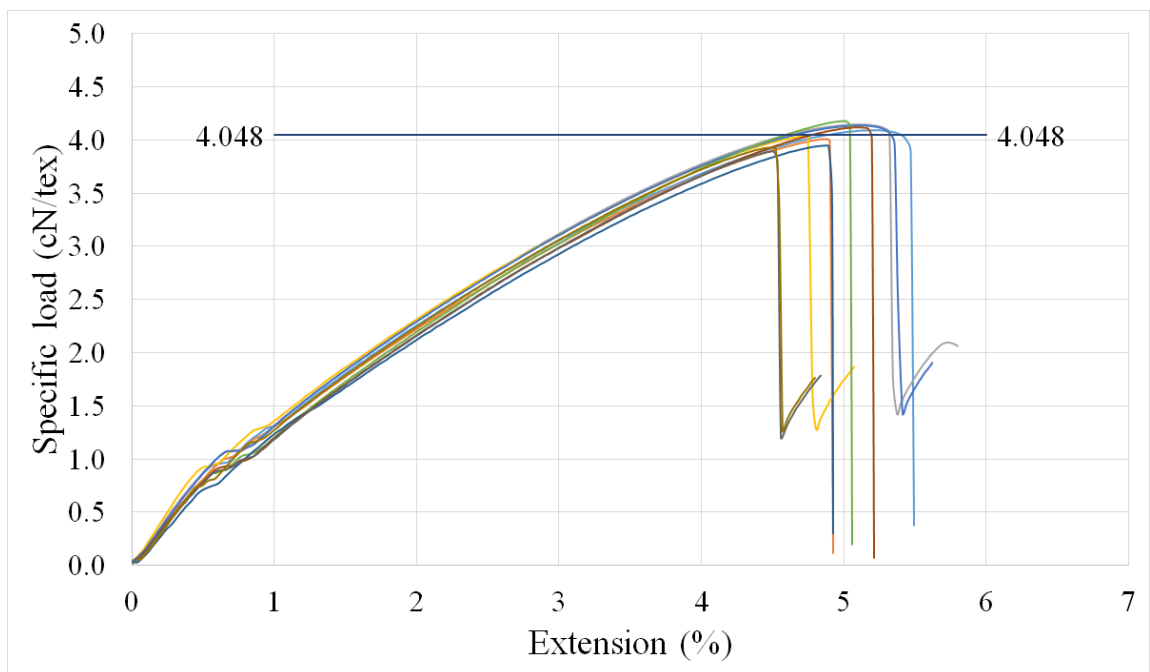


Figure 186. Specific load-extension curves of sample code 11

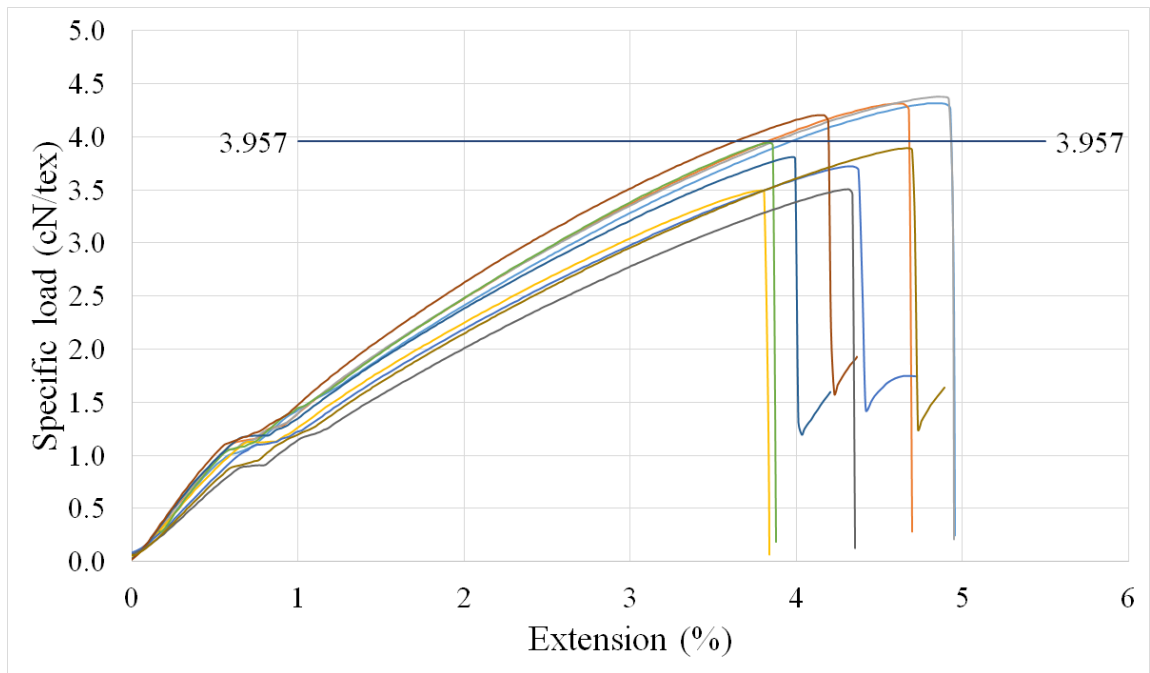


Figure 187. Specific load-extension curves of sample code 12

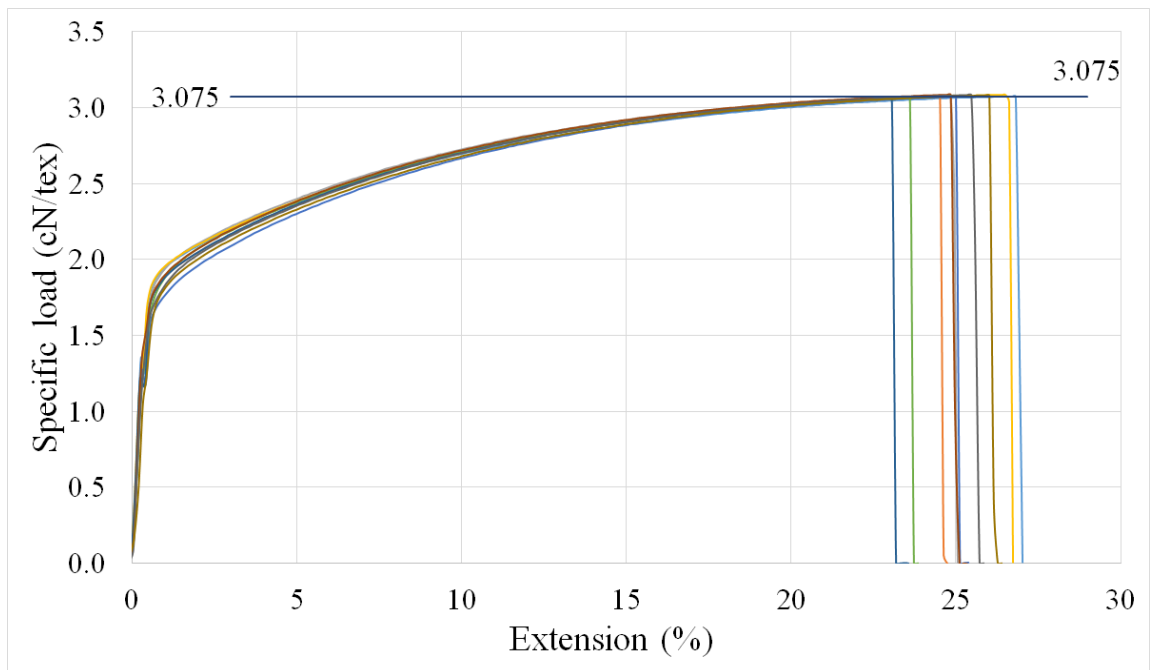


Figure 188. Specific load-extension curves of thermally treated copper filament (C-HS)

## Annexure 7

### Material properties

Nylon 6, 6 is an aliphatic polyamide which was obtained from AIFP Saint Louis, France. It is one of the main industrial polymer which is produced from condensation polymerization. It has high cohesive energy and crystalline nature; therefore, nylon is resistant to most solvents. It is characterized by high toughness, flexibility, abrasion resistance and impact strength. The strength deteriorates by the absorption of moisture at high humidity levels. Some of the particular properties of Nylon 6,6 are elaborated in Table 21 [181].

Table 21. Properties of Nylon 6, 6

Attribute	Value
Specific gravity	1.14
Tensile stress at yield (MPa)	80
Elongation at break (%)	80-100
Tension modulus ( $10^2$ MPa)	30
Impact strength (ft.-lbf/1/2-in. notch)	1.0-1.5
Dielectric constant ( $10^3$ Hz dry)	3.6-6.0
Dielectric strength (kV/cm)	>100

### Characterization of Polyamide polymer

The thermal analysis of polyamide, Nylon 6, 6 was carried out to investigate different parameters. The thermogram of the polymer in chips form is shown Figure 189. The melting point was obtained at 255 °C without any glass transition temperature. This sort of behaviour depicted that the polymer was crystalline in nature. The 100 % crystallinity of Nylon 6, 6 is 230 J/g. The crystallinity obtained for the polymer chips was 33 %.

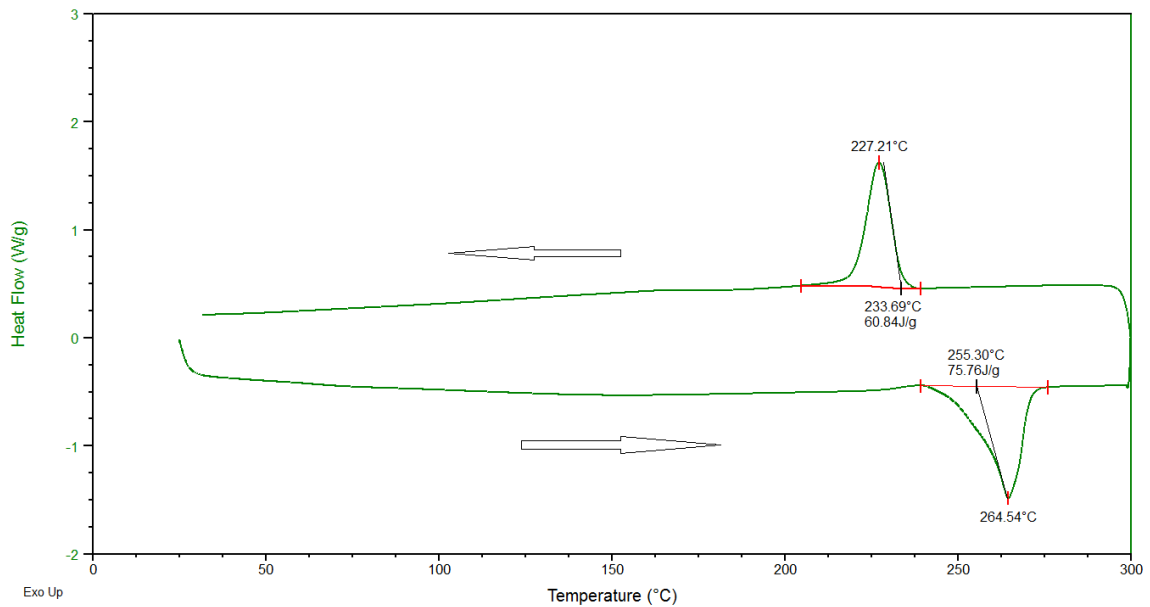


Figure 189. DSC thermogram of Nylon 6,6 in chips form

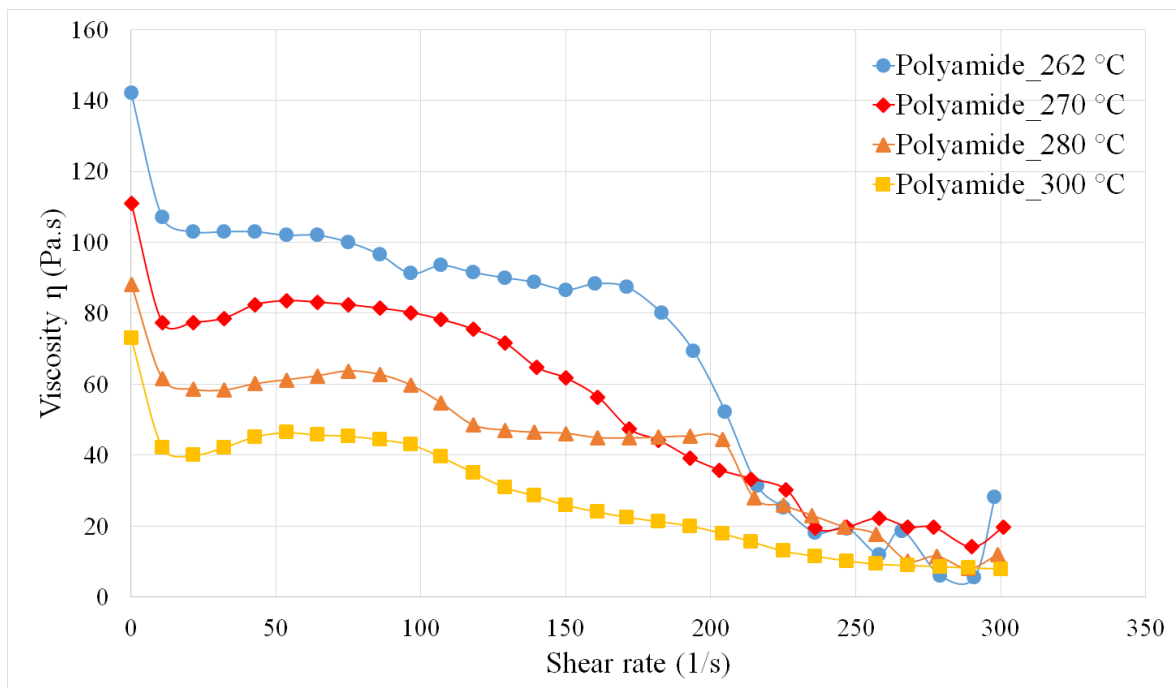


Figure 190. Viscosity vs shear rate curves of polyamide at different temperatures

The rheological properties of polyamide (Nylon 6,6) were analysed and stipulated in graphical form in Figure 190. The zero shear viscosity obtained at temperature of 262 °C, 270 °C, 280 °C and 300 °C are 172 Pa.s, 111 Pa.s, 88 Pa.s and 73 Pa.s respectively. It was observed that viscosity dropped significantly as steep slope by small increase of shear rate. The overall viscosity of the polyamide obtained was very low as compared to polyester.

### Development of core/sheath filament of Cu/Polyamide polymer

Polyamide (Nylon 6,6) polymer was used to develop a coaxial composite filament. The extrusion parameters include temperature of 300 °C and resident time of polymer inside oven of 5 minutes were used for the said test. The spinning parameters including piston and winding speed were set at 5 mm/min and 35.85 m/min (140 rpm) respectively. The spinneret used was prototype 9 with piston end of type 3. The developed filament cross-sectional view is shown in Figure 191. It was observed that core filament was not obtained at coaxial position of the composite filament. the reason behind this abnormality was that the polyamide had very low viscosity value as compared to polyester. During the extrusion process, Nylon 6,6 started flowing on its own way due to very low viscosity rather than attachment/adhesion around copper filament. The flow non-equilibrium with copper filament caused displacement of core from coaxial position of composite filament.

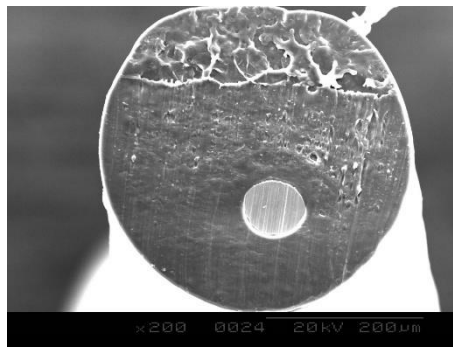


Figure 191. SEM cross-sectional image of Cu/Nylon 6,6 core/sheath composite filament

### Conclusion

It was observed that composite filament developed with Nylon 6,6 polymer and copper filament was a core sheath filament with core at eccentric position. The reason may lie in the fact that viscosity of Nylon 6,6 was low which made it easier to flow in its own path rather than following coating mechanism. The different nature of Nylon 6,6 polymer with respect to other used polymers provide an idea of influence of viscosity on positioning of core at central axial position of the composite filament using the developed process.